

2014

# INTEGRATED GEOPHYSICAL, GEOCHEMICAL AND STRUCTURAL ANALYSIS OF THE MERSIN OPHIOLITE, SOUTHERN TURKEY

OMER, AHMED FATIH

<http://hdl.handle.net/10026.1/3101>

---

<http://dx.doi.org/10.24382/4816>

Plymouth University

---

*All content in PEARL is protected by copyright law. Author manuscripts are made available in accordance with publisher policies. Please cite only the published version using the details provided on the item record or document. In the absence of an open licence (e.g. Creative Commons), permissions for further reuse of content should be sought from the publisher or author.*

**INTEGRATED GEOPHYSICAL, GEOCHEMICAL AND STRUCTURAL  
ANALYSIS OF THE MERSIN OPHIOLITE, SOUTHERN TURKEY**

by

**Ahmed Fatih Omer**

A thesis submitted to the University of Plymouth in partial fulfilment for the  
degree of

**DOCTOR OF PHILOSOPHY**

**School of Geography, Earth and Environmental Sciences**

**July 2014**

## **Copyright statement**

*This copy of the thesis has been supplied on condition that anyone who consults it is understood to recognize that its copyright rests with its author and that quotation from the thesis and no information derived from it may be published without the author's prior consent.*

# Abstract

This study examines the tectonic evolution of the Mersin ophiolite of the central Tauride of Turkey, using palaeomagnetic, structural and geochemical analyses. This ophiolite represents one of the best examples of Tethyan-type ophiolites formed by supra-subduction zone spreading within the northern Neotethyan Ocean basin during the Late Cretaceous. It exposes a 3.0 km section of lower crustal, cumulate rocks, and tectonically separated exposures of the underlying mantle sequence and metamorphic sole, both of which are cut by basaltic dykes.

Stepwise thermal and alternating field demagnetization of ultramafic and gabbroic cumulates from 18 sites mostly identified single components of remanent magnetization characterized by ENE-directed, moderately upwards inclined directions in geographic coordinates with high coercivities/high unblocking temperatures. The slight increase in scattering in remanence directions after tilt correction has been interpreted to be related to local variations in orientation of cumulates layering within the magma chamber. Rock magnetic investigations showed that magnetite is the main magnetic mineral in the majority of ultramafic, gabbro and dyke rock samples, and rock magnetic and demagnetization characteristics suggest that the samples carry thermoremanent magnetizations acquired during crustal accretion.

Net tectonic rotation analyses show that all the units of the Mersin ophiolite, including lower crustal cumulates, dykes in the mantle sequence and dykes in the metamorphic sole have experienced large clockwise rotations around NE-trending, moderately plunging to sub-horizontal axes. Correcting anisotropy of magnetic susceptibility data for the effects of these rotations suggests that magmatic flow in the cumulates had an initial NNE-SSW orientation, which if assumed to relate to seafloor spreading suggests that the Mersin spreading axis was oriented WNW-ESE. This is consistent with regional palaeogeographic reconstructions. The net tectonic rotation data show that dykes in the metamorphic sole are rotated by c. 45°, significantly less than the c. 115° rotations seen in the mantle sequence and in the cumulate sequences of the overlying thrust sheets. These results therefore document an initial stage of intra-oceanic clockwise rotation of the ophiolite that occurred after initial detachment but prior to emplacement of dykes cutting the metamorphic sole. Subsequent additional clockwise rotation (of all units) may be attributed to further intra-oceanic rotation (preferred interpretation) or to later emplacement of the ophiolite onto the Tauride continental margin.

Finally, some new, preliminary data are presented from the Lizard ophiolite of Cornwall in Appendix A, forming the results of a training project undertaken while awaiting permission for fieldwork in Turkey.

## Table of contents

<b>Chapter 1 - General Introduction</b>	<b>1</b>
1.1 Introduction	1
1.2 Brief historical perspective of the ophiolite concept	3
1.3 General explanation of ophiolite units	4
1.4 Ophiolite types	8
1.5 Emplacement of ophiolites	9
1.6 Aims and objectives	11
1.7 Overview of the thesis	11
<b>Chapter 2 - Theoretical Background &amp; Methodologies</b>	<b>13</b>
2.1 Basic characteristics of the Earth's magnetic field	13
2.2 Magnetic behavior of materials	17
2.2.1 Diamagnetism	18
2.2.2 Paramagnetism	19
2.2.3 Ferromagnetism	20
2.3 Rock magnetism	22
2.3.1 Magnetic domains	22
2.3.2 Hysteresis	24
2.3.3 Curie temperature, blocking temperature & relaxation time	25
2.4 Magnetic minerals	27
2.5 Forms of natural magnetization in rocks	30
2.5.1 Thermoremanent magnetization (TRM)	32
2.5.2 Depositional remanent magnetization (DRM)	33
2.5.3 Chemical remanent magnetization (CRM)	34
2.6 Anisotropy of magnetic susceptibility (AMS)	34
2.7 Palaeomagnetic methodologies	36
2.7.1 Palaeomagnetic sampling	36
2.7.2 Anisotropy of magnetic susceptibility (AMS) measurements	39
2.7.3 Anisotropy of anhysteretic remanent magnetization (AARM)	40
2.7.4 Palaeomagnetic measurement & demagnetization techniques	42
2.7.5 Rock magnetic experiments	46

2.7.5.1	<i>Isothermal remanent magnetization (IRM) analyses</i>	46
2.7.5.2	<i>Curie temperature determinations</i>	48
2.7.6	Structural correction of palaeomagnetic data	49
2.7.6.1	<i>Standard tilt corrections</i>	49
2.7.6.2	<i>Net tectonic rotation (NRT) analysis method</i>	50
2.8	Other methods employed	52
2.8.1	Thin section preparation for AMS & petrographic analysis	52
2.8.2	Analytical techniques for geochemistry & X-ray fluorescence (XRF) analysis	54
2.8.2.1	<i>Sample preparation</i>	55
2.8.2.2	<i>Producing pressed powder pellets for trace element measurements</i>	56
2.8.2.3	<i>Producing fused beads for major element measurements</i>	56
 <b>Chapter 3 - The Mersin Ophiolite</b>		59
3.1	Introduction	59
3.2	Outline of Turkish terranes and sutures	60
3.3	The distribution of Turkish ophiolites	64
3.4	Overview of the genesis and root zones of ophiolites in the Turkish area	65
3.5	Geological setting of the Mersin ophiolite	69
3.5.1	General description	69
3.5.2	Origin and development	70
3.5.3	Description of main units and lithologies in the Mersin ophiolite	71
3.5.3.1	<i>Ophiolitic units</i>	71
3.5.3.2	<i>Subophiolitic metamorphic rocks</i>	76
3.5.3.3	<i>Dykes cutting the mantle sequence and the metamorphic sole</i>	78
3.5.3.4	<i>Mersin mélange</i>	80
3.5.4	Ophiolite emplacement	80
3.5.5	Post-emplacement tectonic structures	82
3.6	Previous palaeomagnetic research on eastern Mediterranean Tethyan ophiolites	85
3.6.1	Troodos ophiolite	85
3.6.2	Kizildağ (Hatay) ophiolite	90
3.6.3	Baër-Bassit ophiolite	94

<b>Chapter 4 - Petrography and Geochemistry</b>	<b>97</b>
4.1 Petrography	97
4.1.1 Ultramafic cumulates	97
4.1.2 Gabbroic cumulates	98
4.1.3 Mafic dykes	101
4.2 Whole rock geochemistry	102
4.2.1 Aims of the study	102
4.2.2 General description and field relations of the basaltic veins	103
4.2.3 Geochemical results	103
4.3 Discussion of the origin of the basaltic veins within the layered gabbros	115
4.4 Summary	121
<b>Chapter 5 - Palaeomagnetic study of the Mersin Ophiolite</b>	<b>123</b>
5.1 Introduction	123
5.2 Recap of the context of previous palaeomagnetic results from ophiolites in this region	123
5.3 Fieldwork and palaeomagnetic sampling localities	125
5.4 Rock magnetic analyses and microscopy	133
5.4.1 Isothermal remanent magnetization (IRM) analyses	133
5.4.2 Thermomagnetic analysis	134
5.4.3 Petrographic and SEM analyses	135
5.5 Magnetic fabric analyses and petrofabric observations	146
5.5.1 Anisotropy of magnetic susceptibility results	146
5.5.1.1 <i>Bulk susceptibility and anisotropy parameters</i>	146
5.5.1.2 <i>Distribution of AMS principal axes in the Mersin cumulate                 sequence</i>	150
5.5.1.3 <i>Distribution of AMS principal axes in discrete dykes</i>	154
5.5.1.4 <i>Distribution of AMS principal axes in lavas</i>	158
5.5.1.5 <i>Distribution of AMS principal axes in Miocene sediments</i>	158
5.5.2 Thin section observations of petrofabrics	159
5.5.3 Anisotropy of anhysteretic remanent magnetization (AARM) results	164
5.6 Remanent magnetizations and demagnetization characteristics	168
5.6.1 Demagnetization of NRM	168
5.6.2 Demagnetization characteristics	170

5.6.3	Stepwise demagnetization and palaeomagnetic directions	177
5.7	Tectonic analysis of palaeomagnetic data	188
5.7.1	Expected palaeomagnetic reference direction	188
5.7.2	Discussion of structural corrections and timing of magnetization	188
5.7.3	Net Tectonic Rotation Analysis	190
5.8	Discussion	203
5.8.1	Significance of the magnetic fabric data	203
5.8.2	Tectonic interpretation of the palaeomagnetic data and net tectonic rotation analyses	208
		213
	<b>Chapter 6 - Conclusions</b>	215
6.1	Summary	215
6.2	Recommendations for further work	219
	<b>Appendix A - A pilot palaeomagnetic study of the Lizard ophiolite</b>	221
A1.	Introduction	221
A2.	Overview of the tectonic evolution of the Rheic Ocean	221
A2.1	Initial Rifting and Ocean Opening	222
A2.2	Collision and Ocean Closure	223
A2.3	Models for initial rifting	226
A3.	Geology of the Lizard Ophiolite	228
A3.1	General Overview	228
A3.2	Age and formation of the Lizard ophiolite	229
A3.3	Obduction of the ophiolite	229
A3.4	Description of lithologies	233
A3.4.1	Peridotite	234
A3.4.2	Gabbros	235
A3.4.3	Dykes	235
A4.	Previous Palaeomagnetic Studies	238
A5.	Fieldwork in the Lizard ophiolite	238
A6.	Results	241
A6.1	Petrography	241
A6.2	Rock magnetic results	242

A6.2.1. Isothermal remanent magnetization (IRM) analyses	244
A6.2.2. Thermomagnetic analysis	246
A6.3. Anisotropy of magnetic susceptibility (AMS)	249
A6.4. Remanent magnetization results	254
A7. Interpretation and discussion	261
References	265

## List of figures

Figure 1.1.	Simplified ophiolite sequence	1
Figure 1.2.	Outline tectonic map of the eastern Mediterranean	3
Figure 1.3.	Comparison of selected ophiolite complexes with the idealized ophiolite assemblage	7
Figure 1.4.	Types of ophiolite	8
Figure 1.5.	Types of mechanisms of ophiolite emplacement	9
Figure 2.1.	Convection currents in the Earth's outer core generate the geomagnetic field	13
Figure 2.2.	(a) The main elements of the Earth's magnetic field. (b) The Earth's magnetic field showing field direction either side of the Earth's equator	14
Figure 2.3.	The Earth showing the deviation of the magnetic north pole about 11.5° from the geographic North Pole	15
Figure 2.4.	Schematic of the Earth's magnetic field reversal	16
Figure 2.5.	Magnetism of an atom	18
Figure 2.6.	The essential groups of magnetic behavior	19
Figure 2.7.	Schematic representations of different forms of magnetization against applied field	21
Figure 2.8.	Schematic diagram showing domain formation	23
Figure 2.9.	Hysteresis loop showing the behavior of magnetization of an unmagnetized ferromagnetic mineral	25
Figure 2.10.	Relaxation time of a SD magnetite grain as a function of temperature	27
Figure 2.11.	FeO-TiO <sub>2</sub> -Fe <sub>2</sub> O <sub>3</sub> ternary compositional system showing the two important solid solution series	29
Figure 2.12.	Schematic figure showing the changes in the magnetic status of ferromagnetic grains from paramagnetic to ferromagnetic during cooling	32
Figure 2.13.	Schematic diagram of magnetic fabric ellipsoids showing the three principal susceptibility axes	35
Figure 2.14.	Core sample collection in the field	36
Figure 2.15.	Sampling technique used in the field	37

Figure 2.16. Orientation system for core samples	38
Figure 2.17. Laboratory techniques for preparation of the palaeomagnetic specimens	38
Figure 2.18. Palaeomagnetic laboratory instruments	41
Figure 2.19. Degree of anisotropy $P_j$ , versus shape parameter $T$ diagram	42
Figure 2.20. Illustration of the principle of orthogonal projections	44
Figure 2.21. Equal-area stereographic projection of the same data shown in Figure 2.20, with NRM intensity diagram	45
Figure 2.22. Schematic diagram illustrating the process of isothermal remanent magnetization acquisition	47
Figure 2.23. An example of the palaeohorizontal case of the method of Allerton and Vine (1987) using data from site MC04	51
Figure 2.24. Photos illustrating the method of thin section preparation	53
Figure 2.25. Rock powder preparation using the teamer mill	54
Figure 2.26. Pressed pellet preparation in the laboratory	55
Figure 2.27. Laboratory equipment used for preparing fused beads	57
Figure 2.28. Fusion machine used in melting the powder mixtures for preparing fused beads	57
Figure 2.29. Fusion steps	58
Figure 3.1. Simplified map showing the distribution of main Tethyan ophiolites	59
Figure 3.2. A view of the Mediterranean palaeogeography showing the Northern Neotethyan, Southern Neotethyan and the main Turkish continental fragments during the Early Cretaceous (100 Ma)	61
Figure 3.3. Tectonic map of Turkey and surrounding regions showing the main sutures and continental fragments	61
Figure 3.4. Distribution of ophiolite complexes in Turkey	64
Figure 3.5. Ophiolite single root-zone interpretation for Turkey	66
Figure 3.6. Alternative tectonic models for the genesis of Turkish ophiolitic suture zones during Late Palaeozoic to Early Mesozoic time	67
Figure 3.7. Palaeogeographic sketch map showing the genesis of the Latest Cretaceous ophiolites in the eastern Mediterranean region	68
Figure 3.8. Simplified geological map of the Mersin	69
Figure 3.9. Tectonostratigraphic setting of the Mersin ophiolite	70

Figure 3.10.	Field photograph showing the locations of columnar basalt together with the pillow lava along Fındıklı valley section	72
Figure 3.11.	(a) Field photographs of pillow lava at Fındıklı; (b) field photograph illustrating the overturned pillow lava at Fındıklı	72
Figure 3.12.	Field photographs of (a) Ultramafic rocks along main Sorgun valley section, (b) brownish colour due to alteration with lamination within the ultramafic layers and (c) grain-size grading in ultramafic cumulates	74
Figure 3.13.	(a) Rhythmic layering in cumulate gabbros along the Sorgun Valley, indicating overturned layering; (b) grain-size grading in cumulates along the Sorgun Valley	75
Figure 3.14.	Cumulate layering along the main Sorgun Valley section, cross-cut by thin basaltic veins	75
Figure 3.15.	Google image showing the localities of the exposed dykes at the Fındıklı valley area	76
Figure 3.16.	Field photographs of (a) Metamorphic sole rocks intruded by thin dolerite dyke at Fındıklı and (b) Metamorphic sole rocks with deformation structures at Fındıklı	77
Figure 3.17.	Field photographs of (a) Massive doleritic dyke cross-cutting harzburgite at Fındıklı and (b) Thin dolerite dyke intruding the metamorphic sole at Fındıklı	79
Figure 3.18.	Field photograph showing the boundary between metamorphic sole and the mélangé at Fındıklı together with the Miocene sedimentary cover on the top	81
Figure 3.19.	Stereographic projections of structural data from early ductile fabrics in the metamorphic sole of the Mersin Ophiolite	83
Figure 3.20.	Simplified geological map of the southern Turkey showing the locations of Cretaceous Tauride ophiolites and the Ececiğ fault	84
Figure 3.21.	Outline geological map of Cyprus showing the Troodos ophiolite and Arakapas Fault Belt	86
Figure 3.22.	Palaeomagnetic results from the sedimentary cover of the Troodos ophiolite showing the progressive anticlockwise rotation of the underlying ophiolite during the Late Cretaceous and Palaeogene	89
Figure 3.23.	Possible alternative mechanisms to account for the deviation in dyke trend near the Southern Troodos Transform Fault	89
Figure 3.24.	Simplified geological map of the Kizıldag (Hatay) ophiolite	92
Figure 3.25.	Stereonet of site mean remanence directions from sites in sheeted dykes, layered sequences and extrusives of the Hatay ophiolite	93

Figure 3.26.	Results of net tectonic analyses of palaeomagnetic data from sites in sheeted dyke complex of the main massif of the Hatay ophiolite	93
Figure 3.27.	Results of net tectonic analyses of palaeomagnetic data of the main massif of the Hatay ophiolite	94
Figure 3.28.	Simplified geological map of the Baër-Bassit ophiolite NW of Syria	95
Figure 4.1.	Ultramafic cumulate sample from the Mersin ophiolite showing phenocrysts of clinopyroxene	98
Figure 4.2.	Photomicrographs (under crossed polars and in plane polarized light) of selected gabbro samples from the Mersin ophiolite	100
Figure 4.3.	Photomicrographs (under crossed polars and in plane polarized light) of selected dolerite dyke samples from the Mersin ophiolite	101
Figure 4.4.	Field photographs of site MC10	104
Figure 4.5.	MgO vs Sr diagram for the basaltic veins and gabbroic rocks from the Mersin ophiolite (including the data from Parlak et al., 1995, 1996c and Çelik, 2008)	109
Figure 4.6.	Selected major element variations for the basaltic veins and gabbroic rocks from the Mersin ophiolite (including the data from Parlak et al., 1995, 1996c and Çelik, 2008)	110
Figure 4.7.	Variation of selected major oxides with Zr for the basaltic veins and gabbroic rocks from the Mersin ophiolite (including the data from Parlak et al., 1995, 1996c and Çelik, 2008)	111
Figure 4.8.	TiO <sub>2</sub> –MnO–P <sub>2</sub> O <sub>5</sub> discrimination diagram (Mullen, 1983) for basaltic vein rocks and gabbros from the Mersin ophiolite, compared with data from Parlak et al., 1995, 1996c; Çelik, 2008	113
Figure 4.9.	Ti vs V (after Shervais, 1982) diagram for basaltic vein rocks and gabbros from the Mersin ophiolite compared with data from Parlak et al., 1995, 1996c; Çelik, 2008	113
Figure 4.10.	AFM composition of the samples of the current study (basaltic veins and gabbros) and gabbros with ultramafic cumulates from Parlak et al. (1996c)	115
Figure 4.11.	Photomicrographs (under crossed polars and in plane polarized light) of a cross-cutting basaltic vein within the host gabbro of the Mersin ophiolite.	118
Figure 4.12.	Microstructural shear zone indicators in cross-cutting vein samples from Mersin ophiolite	119
Figure 4.13.	Hand specimen from the cross-cutting vein of Mersin ophiolite showing a sigmoidal fabric in the host gabbro	120

Figure 5.1.	Stereographic projections of mean remanence directions from other Late Cretaceous ophiolites	125
Figure 5.2.	Google Earth images of the northern and southern sections of the Sorgun Valley	126
Figure 5.3.	Google Earth image of the Fındıklı valley area showing the localities of the dykes	128
Figure 5.4.	Simplified geological map of the western part of Mersin ophiolite showing the studied area and cumulate and dyke sampling localities	129
Figure 5.5.	Fieldwork in the Sorgun valley	131
Figure 5.6.	(a) Massive lava flow sampled at Fındıklı, with columnar jointing visible on the left hand side of the image; (b) sub-horizontally bedded Miocene carbonates exposed at Arslanlı	132
Figure 5.7.	Isothermal remanent magnetization (IRM) curves and backfield demagnetization curves for representative samples of the Mersin Ophiolite Complex and Miocene sedimentary cover	136
Figure 5.8.	Curie temperature results from representative samples of Mersin Ophiolite Complex and its Miocene sedimentary cover	139
Figure 5.9.	Photomicrographs of an ultramafic cumulate sample (MC0203B) from the Mersin ophiolite showing secondary magnetite produced by serpentinization of olivine	142
Figure 5.10.	SEM photograph and energy-dispersive X-ray (EDX) spectral analysis of sample MC0203B, confirming presence of secondary magnetite within olivine grains	143
Figure 5.11.	Optical photomicrographs of a gabbro sample (MC1505C) from the Mersin ophiolite showing the Fe-Ti oxide minerals along with clinopyroxene and plagioclase	143
Figure 5.12.	SEM photograph and EDX spectral analysis of gabbro sample MC1505C, showing variations in Ti content within a titanomagnetite grain	144
Figure 5.13.	SEM images of a gabbro sample (MC1505C) from the Mersin ophiolite showing the concentrations of the Fe, Ti, S and Si	144
Figures 5.14 (above) and 5.15 (below).	SEM photograph and EDX spectral analysis of gabbro sample MC1804B and dyke sample MD0708B.	145
Figure 5.16.	Degree of anisotropy $P_j$ , versus shape parameter $T$ diagram for rocks from the Mersin ophiolite.	147

Figure 5.17. (a) Stereoplots of AMS ellipsoid principal axes, together with planes of the layering of ultramafic and gabbroic cumulates from the Mersin ophiolite; (b) diagrammatic cross-section showing the status and the dip direction of the layering for the sites within the Sorgun Valley	151
Figure 5.18. Stereoplots of AMS ellipsoid principal axes together with dyke orientations from the Mersin ophiolite	156
Figure 5.19. Stereoplots of AMS ellipsoid principal axes from: (a) lava flow samples from site ML01, together with plane perpendicular to columnar jointing (that provides the best estimate of the orientation of the flow). (b) Miocene sediments, together with subhorizontal bedding plane	158
Figure 5.20. Images of ultramafic cumulate sample MC0203B showing a banding caused by serpentinization	160
Figure 5.21. Images of cumulate gabbro sample MC1505C showing a good agreement of both magnetite and plagioclase crystal alignments with $k_1$	161
Figure 5.22. Images of gabbroic cumulate sample MC0703C showing a good agreement of both pyroxene and plagioclase crystal alignments with $k_1$	162
Figure 5.23. Images of gabbroic cumulate sample MC1206C illustrating both exsolved inclusions of oriented magnetite and intergrowths of composite lamellae of orthopyroxene in clinopyroxene phenocrysts	163
Figure 5.24. SEM photograph and EDX spectral analysis of sample MC1206C, indicating the presence of exsolved magnetite.	164
Figure 5.25. Comparison of AMS and AARM results for ultramafic and mafic cumulates from Mersin ophiolite	166
Figure 5.26. Degree of anisotropy $P_j$ , versus shape parameter $T$ diagrams of AARM and AMS ellipsoids for ultramafic and mafic cumulates from Mersin ophiolite	168
Figure 5.27. Shapes of AF demagnetization curves of a 0.1 mT TRM in magnetite over a broad range of grain sizes, extending from SD to large MD	171
Figure 5.28. Normalized intensity against applied field diagrams illustrating the different types of magnetic behavior obtained during AF demagnetization of the gabbroic and ultramafic samples from the Mersin ophiolite	173

Figure 5.29. Normalized intensity against temperature diagrams illustrating the different types of magnetic behavior obtained during thermal demagnetization of the gabbroic and ultramafic samples from the Mersin ophiolite	174
Figure 5.30. Normalized intensity against applied field diagrams illustrating the different types of magnetic behavior obtained during AF demagnetization of the dyke samples from the Mersin ophiolite	175
Figure 5.31. Normalized intensity against temperature diagrams illustrating the different types of magnetic behavior obtained during thermal demagnetization of the dyke samples from the Mersin ophiolite	176
Figure 5.32. Normalized intensity against demagnetization level diagrams illustrating the magnetic behavior obtained during AF and thermal demagnetization of the lava flow samples from the Mersin ophiolite	177
Figure 5.33. Zijdeveld and intensity decay plots of AF and thermal demagnetization data from gabbroic and ultramafic samples of the Mersin ophiolite	180
Figure 5.34. Zijdeveld and intensity decay plots of AF and thermal demagnetization data from dyke samples of the Mersin ophiolite	182
Figure 5.35. Zijdeveld and intensity decay plots of AF and thermal demagnetization data for selected samples showing viscous overprints	184
Figure 5.36. Zijdeveld and intensity decay plots of AF and thermal demagnetization data from Miocene sediments	185
Figure 5.37. Schematic diagrams with stereoplots illustrating the classical palaeomagnetic fold test	190
Figure 5.38. Results of the net tectonic analysis at each site in the gabbroic and ultramafic cumulate section of the Mersin ophiolite	194
Figure 5.39. Overall net tectonic analysis for the ultramafic and gabbroic cumulate section in the Sorgun Valley section of Mersin ophiolite	197
Figure 5.40. Results of net tectonic analyses for each site within the discrete dykes cutting the mantle sequence of the Mersin ophiolite (preferred solutions only)	200
Figure 5.41. Results of net tectonic analyses for each site within the discrete dykes cutting the metamorphic sole of the Mersin ophiolite (preferred solutions only).	201
Figure 5.42. Examples of alternative net tectonic rotation solutions from dykes of the Mersin ophiolite	202
Figure 5.43. Summary of net tectonic analysis results for both groups of dykes from Findıkpınarı section of Mersin ophiolite	202

Figure 5.44.	Restoration of anisotropy of magnetic susceptibility (AMS) k1 axes using the overall net tectonic rotation determined for lower crustal cumulates of the Sorgun Valley, Mersin ophiolite	206
Figure 5.45.	Palaeogeographic reconstruction of the eastern Mediterranean region in the latest Cretaceous.	207
Figure 5.46	AMS data from the gabbros of the Troodos ophiolite, from Granot et al. (2011), showing presence of two contrasting fabric domains	207
Figure 5.47.	Schematic tectonic map of Turkey and adjoining region showing the pattern of declinations of mean palaeomagnetic vectors affected by Neotectonic rotations	209
Figure 5.48.	Comparison of net tectonic rotation parameters for the Mersin cumulate section (left), dykes cutting the mantle sequence (middle) and dykes cutting the metamorphic sole (right)	210
Figure 5.49.	Schematic tectonic model illustrating the net tectonic rotation of the Mersin ophiolite	214
Figure A1.	Palaeozoic reconstruction showing the evolution of the Iapetus and Rheic Oceans and location of Laurentia - Baltica – Avalonia–Carolinia	222
Figure A2.	Palaeogeographic maps showing the position of the UK in the southern hemisphere during the Devonian (380 Ma – 400 Ma)	224
Figure A3.	Simplified map showing the location of Rheic suture in western and central Europe, and Lizard ophiolite in the south west of Britain	225
Figure A4.	A map of the major tectonic zones of the Variscan Orogen in Europe	226
Figure A5.	Cross section illustrating the main structures from South Wales to South Cornwall, and the locations of the Lizard ophiolite and Rheic Suture	227
Figure A6.	Simplified map showing the location of the Lizard ophiolite complex, Cornwall	228
Figure A7.	Schematic block diagram illustrating formation of the Lizard Complex-Gramscatho pull-part basin during the Emisian-Eifelian period	230
Figure A8.	Schematic cross-sections illustrating emplacement steps of the Lizard complex	231
Figure A9.	Deformation and emplacement history of the Lizard ophiolite	232
Figure A10.	Simplified geological map of the Lizard complex, Cornwall	233

Figure A11.	Geological map of the Coverack area, showing the interdigitation of gabbro and peridotite, and NW-SE trending dykes	234
Figure A12.	Schematic cross-section from Coverack to Porthoustock, showing the formation stages of the three sets of dolerite dykes	237
Figure A13.	Geological map showing the studied area with indication of sampled dykes and gabbros localities	239
Figure A14.	Outcrop photograph of site GC05 with location of drilled samples labelled	240
Figure A15.	Photographs of studied localities.	241
Figure A16.	Photomicrographs (cross-polars) of the gabbro samples from the Lizard ophiolite	242
Figure A17.	Photomicrographs of the dolerite dyke samples from the Lizard ophiolite showing plagioclase phenocrysts in a groundmass of mostly clinopyroxene, chlorite and opaque minerals	243
Figure A18.	Photomicrographs of the dolerite dyke samples from the Lizard ophiolite showing alteration of the clinopyroxene to chlorite and alignments of plagioclase phenocrysts with the flow direction	243
Figure A19.	Isothermal remanent magnetization (IRM) curves and backfield demagnetization curves for representative samples of the Lizard ophiolite	245
Figure A20.	Curie temperature experiments on representative samples from the Lizard ophiolite	247
Figure A21.	Representation of AMS of the dykes from the east coast of the Lizard	252
Figure A22.	Representation of AMS of the gabbros from the east coast of the Lizard	253
Figure A23.	Zijderveld diagrams (orthogonal vector plots) of demagnetization data for selected samples	255
Figure A24.	Zijderveld plots, stereographic projections and great circle demagnetization trends for selected samples	258
Figure A25.	Zijderveld plots, stereographic projections and thermal demagnetization trends for sample	259
Figure A26.	Schematic summary of remanence data from the Lizard ophiolite	

## List of tables

Table 2.1	Selected magnetic minerals and their magnetic properties	30
Table 2.2	Some different types of natural remanent magnetizations (NRM)	31
Table 4.1	Whole rock major oxide (wt%) and trace element (ppm) data of basaltic veins analysed from the Mersin ophiolite	105
Table 4.2	Whole rock major oxide (wt%) and trace element (ppm) data for gabbros of the Mersin ophiolite	107
Table 4.3	Average values of the major oxides and trace elements of rock from the current study compared to the previous studies on the Mersin ophiolite sample	116
Table 5.1	Summary of the number of samples collected during fieldwork	130
Table 5.2	Magnetic fabric results for ultramafic and gabbroic cumulates of the Mersin ophiolite	148
Table 5.3	Magnetic fabric results for dykes of the Mersin ophiolite	149
Table 5.4	Average intensities of natural remanent magnetization (NRM) for sampled lithologies	170
Table 5.5	Palaeomagnetic data from the ultramafic and gabbroic cumulates of the Mersin ophiolite	186
Table 5.6	Palaeomagnetic data from the dykes of the Mersin ophiolite	187
Table 5.7	Net tectonic rotation parameters for ultramafic and gabbroic cumulates of the Mersin ophiolite	193
Table 5.8	Net tectonic rotation parameters for dykes of the Mersin ophiolite	198
Table A1	Magnetic fabric results	251
Table A2	Palaeomagnetic results from sites	260
Table A3	Net tectonic rotation parameters for restoration of dykes at site GC01 using the remanence direction of their host at site GC02	264

## **Dedication**

This thesis is dedicated to:

The memory of my beloved father, Sayed Fatih, whom I lost many years ago. It is your shining example that I try to emulate in all that I do, and I am sure he is somewhere out there always watching me closely.

The memory of my brother in law, Kadri Al-Khateeb. He was very proud of my development as a person and my scientific and professional progress.

My cherished mother, whose prayers always make me strong and safe throughout my life.

My lovely wife, who has always been with me through the hard times.

## ACKNOWLEDGEMENTS

First of all I am thankful to the God who blessed me with courage, patience and confidence to complete this research work. After that I am very grateful to my supervisors from Plymouth University, Professor Antony Morris and Dr. Mark Anderson for all their considerable help and generous guidance, and for training both in the field, the laboratory and help with analytical techniques throughout the duration of study.

I would like to express my sincere thanks to Ministry of Higher Education and Scientific Research-Iraq, for providing me the scholarship and all the financial support for my stay in Plymouth and study expenses. I am also so grateful to the Iraqi Cultural Attaché-London for their support.

I wish to express my hearty gratitude to Professor Osman Parlak from Çukurova University-Turkey, for his considerable logistical support and for his guidance in the field. I would also express my thanks to several Turkish students from Çukurova University for their help in the fieldwork.

I would like to thank Professor Ian Croudace from the Southampton University for his help whilst using equipment at the Southampton Geochemistry Laboratory. I would like to thank Dr. Arjan Dijkstra (Plymouth University) for helpful discussions about interpretation of petrographic and geochemical results.

Thanks also to the professional support staff in Earth Sciences at Plymouth University, including Sally Greenwood and Ian King for all their kind help, and to all staff at the Plymouth University SEM unit for their expert help in analysing my thin sections. I benefitted from many useful discussions with my fellow PhD students, especially Matthew Meyer, and from guidance and advice in the laboratory from Dr Marco Maffione.

I thank my all colleagues from the Technical Institute of Kirkuk, especially who sponsored me during my study.

My thanks go to all of my family both in Iraq and in Australia for their encouragement over the period of this research, most particularly my mother for listening to me and supporting me through many conversations via net. Also my special appreciation and gratitude goes to my brother-in-law Yujel Najee, who has been very kind, supportive and accommodating with most of my family affairs through the duration of my PhD.

I am grateful extremely to my wonderful wife Tulay Najee, and my daughters Maryam and Maysam, and my son Mohamed Fatih, for their endless support and encouragement, which made this study easier.

Finally, I appreciate the role of all those at Plymouth University, who helped me during my study.

## AUTHOR'S DECLARATION

At no time during the registration for the degree of Doctor of Philosophy has this author been registered for any other University award without prior agreement of the Graduate Committee.

This study was financed with the aid of a scholarship from the Ministry of Higher Education and Scientific Research (MOHESR), Iraq.

Throughout working on this thesis, many conferences, workshops, field trips and training courses were attended as well as several postgraduate courses for generic research skills.

### **Conferences attended:**

- Magnetic Interactions Annual Meeting / Plymouth University, 7<sup>th</sup> – 8<sup>th</sup> Jan. 2010.
- Magnetic Interactions Annual Meeting / University of Oxford, 6<sup>th</sup> – 7<sup>th</sup> Jan. 2011.
- CRES Research Conference / Plymouth University, Nov. 2011.
- The postgraduate Society Conference Series/ Plymouth University, June 2012.
- CRES Research Conference / Plymouth University, Nov. 2013.
- Magnetic Interactions Annual Meeting / University of Cambridge, 8<sup>th</sup> – 9<sup>th</sup> Jan. 2014.

### **Presentations:**

- CRES Research Conference **oral presentation**, title: “Integrated Geophysical, Geochemical and Structural analyses of the Mersin ophiolite, Turkey”. Plymouth University, Nov. 2010.
- The postgraduate Society Conference Series **poster presentation**, titled as above / Plymouth University, June 2011. (**Second prize winner**).
- Magnetic Interaction Annual Meeting **poster presentation**, title: “New palaeomagnetic results from the Lizard ophiolite, Cornwall, UK” / University of Liverpool, 4<sup>th</sup> – 5<sup>th</sup> Jan. 2012.

- CRES Research Conference **poster presentation**, titled as above. Plymouth University, Nov. 2012.
- Ussher Society Conference **oral presentation**, title: “New palaeomagnetic results from the Lizard ophiolite, Cornwall-insights into Palaeotectonics of the Rheic Ocean / Tregenna Castle, St Ives, UK, 3<sup>rd</sup> - 5<sup>th</sup> Jan. 2013.
- Magnetic Interaction Annual Meeting **poster presentation**, title: “First Palaeomagnetic results from the Mersin ophiolite (Turkey)” / University of Lancaster, 7<sup>th</sup> – 8<sup>th</sup> Jan. 2013.
- European Geosciences Union (EGU) General Assembly **poster presentation**, title: “First Palaeomagnetic results from the Mersin ophiolite (Turkey)” / Vienna, Austria, 7<sup>th</sup> -12<sup>th</sup> April 2013.
- The postgraduate Society Conference Series **poster presentation**, titled as above / Plymouth University, June 2013.

#### **Training courses:**

- Health and Safety Awareness modules, Plymouth University, May, 2011.
- Learning and Teaching for General Teaching Associates course (GTA). Plymouth, University, May, 2012.
- Postgraduates who teach Geography, Earth and Environmental Sciences (GEES) with (IRG). The Education Centre, Royal Geographical Society, London, March, 2012.
- X- Ray fluorescence analysis (XRF) - Sample preparation and measurements. University of Southampton, 24<sup>th</sup> – 27<sup>th</sup> June 2013.
- GRADSchool: residential development opportunity for PhD researchers. Buckland Hall, Brecon, Wales, UK, 1<sup>st</sup> – 4<sup>th</sup> July 2013.

#### **Postgraduate Research Skills attended (Plymouth University):**

- Preparing Effective Poster Presentation, 10 / May 2010.
- Overview to searching and accessing information resources, 11 / May 2010.
- Word: Proofing and Tracking changes, 28 / May 2010.
- Introduction to Endnote, 9 / June 2010.
- Introduction to My sites, 12 / Jan. 2011,
- Excel Conditional Formatting and Charts, 9 / March 2011.

- Creating Web Pages using SharePoint Designer, 16 / March 2011.
- Research Owing and Using, 5 / May 2011.
- Overview of the Intranet of PGR's, 21 / May 2011.
- The Transfer Process, 24 / June 2011.
- Geographical Information System (GIS) an introduction, 14 / Nov. 2012.

**Participation in field trips:**

- 12<sup>th</sup> – 23<sup>th</sup> April 2010 EOE5002/GLY5206/ Troodos ophiolite –Cyprus.
- 21<sup>th</sup> Feb. 2011 EOE1102/ Lyme Regis Dorset, UK.
- 29<sup>th</sup> – 1<sup>st</sup> April 2011 EOE2102/ The Lizard complex and associated tectonic boundaries, UK.
- 24<sup>th</sup> – 30<sup>th</sup> March 2012 EAR112/ St Ives-Portreath/ West Cornwall, UK.
- 16<sup>th</sup> – 22<sup>th</sup> March 2013 EAR115/ EAR117/ St Ives/ West Cornwall, UK.
- 13<sup>th</sup> – 19<sup>th</sup> April 2013 EAR 210/ Advanced geological field skills/ North Devon and Cornwall, UK.

Word Count of main body of thesis: 43076

Signed .....

Date .....

## List of symbols, units and abbreviations

$\alpha_{95}$	Semi-angle of 95% cone of confidence
$\mu\text{m}$	1 micron=0.001 mm
AARM	Anisotropy of anhysteretic remanent magnetization
AF	Alternating field
AMS	Anisotropy of magnetic susceptibility
APWP	Apparent polar wander path
c.	Circa
CAB	Calk-alkaline basalt
ChRM	Characteristic remanent magnetisation
CRM	Chemical remanent magnetization
Cpx	Clinopyroxene
D	Dip angle
DD	Dip direction
Dec	Declination
DRM	Depositional remanent magnetization
GAD	Geocentric axial dipole
IAT	Island arc tholeiites
Inc	Inclination
IRM	Isothermal remanent magnetization
LOI	Loss on ignition
Ma	Millions of years
MD	Multidomain
MORB	Mid-Oceanic ridge basalts
Mt	Magnetite
mT	milliTesla
NRM	Natural remanent magnetization

OIA	Ocean island alkali basalts
OIB	Oceanic island basalts
OIT	Ocean island tholeiites
OI	Olivine
Opx	Orthopyroxene
Pl	Plagioclase
PPM	Part(s) per million
PSD	Pseudo-single-domain
pDRM	Post Depositional Remanent Magnetization
SD	Single-domain
SEM	Scanning electron microscope
s.l.	Sensu lato (Latin: in the broad sense)
s.s.	Sensu stricto (Latin: in the strict sense)
SSZ	Supra-subduction zone
TRM	Thermoremanent Magnetization
$T_b$	Blocking temperature
$T_c$	Curie temperature
VRM	Viscous remanent magnetization
XRF	X-ray Fluorescence Spectrometry

# Chapter 1

## General Introduction

### 1.1 Introduction

Ophiolites are fragments of oceanic lithosphere that were thrust (obducted) onto the continental crust during collisional orogenesis. They represent igneous rock complexes that include an upper basaltic unit, a middle gabbroic unit and lower peridotite unit (Figure 1.1). Ophiolites provide opportunities to study the architecture and evolution of the oceanic crust in three dimensions, including the processes responsible for the formation of the lower oceanic crust, and to determine regional tectonic development during plate convergence (i.e. successive phases of intraoceanic, emplacement-related and post-emplacement deformation).

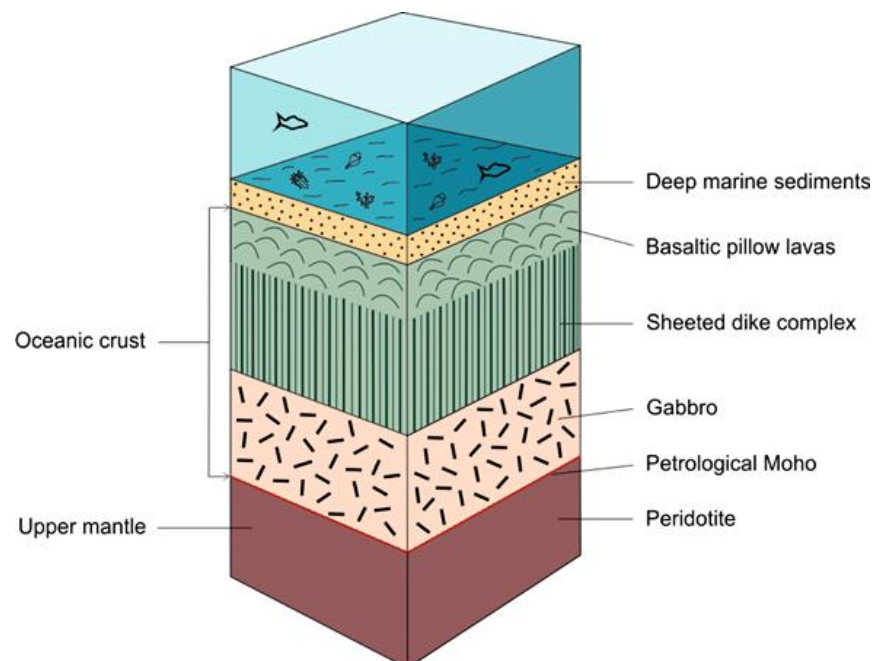


**Figure 1.1.** Simplified ophiolite sequence (modified from Monroe and Wicander, 2009).

The eastern Mediterranean and Middle Eastern orogenic belt is marked by several discontinuous lines of ophiolites that were generated in several narrow Neotethyan strands of the Tethys Ocean (e.g. Robertson, 2004). Of these ophiolites, two have formed the focus of international research for the last 40 years: the Semail ophiolite of Oman, which formed at a fast spreading axis, and the Troodos ophiolite of Cyprus, which is inferred to have formed at a slow-intermediate spreading axis. These lie at opposite ends of the so-called “peri-Arabian ophiolite crescent (Ricou, 1971) (Figure 1.2). Palaeomagnetic research within these units (e.g. Moores and Vine, 1971; Luyendyk and Day, 1982; Allerton and Vine, 1987; Morris et al., 1990, 1998; Weiler, 2000; Perrin et al., 2000) has documented substantial tectonic rotations. Other eastern Mediterranean ophiolites of the same chain (Hatay; Baer-Bassit) have also been studied palaeomagnetically (Morris et al., 2002; Inwood, 2005; Inwood et al., 2009), leading to recognition of a regionally significant rotation of oceanic crust in the southern Neotethyan ocean (e.g. Morris et al., 2006). However, other ophiolites in this region have received less attention from the geological community and have not been studied palaeomagnetically.

This thesis, therefore, describes new palaeomagnetic, structural and geochemical data from the Mersin ophiolite of Turkey. This occupies a key position in the regional context, since it is believed to have formed in a different strand of the Neotethyan ocean located to the north of previously studied ophiolites. Given the ubiquitous nature of major rotations documented in other ophiolites in this region, an assessment of the rotation history of the Mersin ophiolite may shed further light on the regional tectonic evolution of the eastern Mediterranean Tethys.

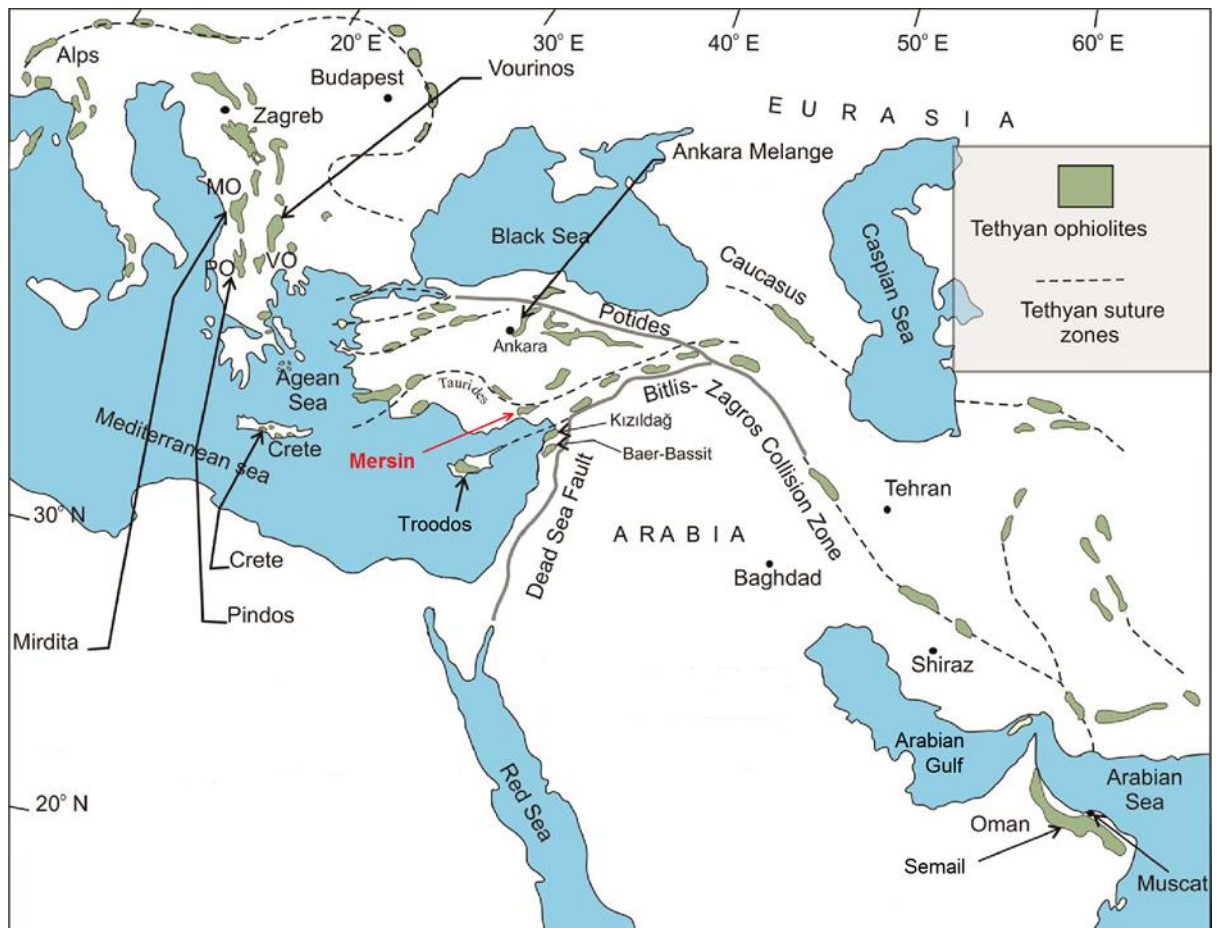


**Figure 1.2.** Outline tectonic map of the eastern Mediterranean showing the location of major Tethyan ophiolites (modified from Karaoglan *et al.*, 2013).

## 1.2 Brief historical perspective of the ophiolite concept

The classification and interpretation of ophiolitic rocks began in the nineteenth century, where Brongniart in 1813 interpreted ophiolites as an essential combination of rocks “with a matrix of serpentine enveloping iron oxide or other disseminated accessory minerals, with compact (as opposed to sheet like) structure” (Moores, 1982), but making no distinction between igneous rocks and metamorphic rocks. However in 1827, Brongniart started to distinguish between these two main groups of rocks, placing ophiolites with igneous rocks in his classification, together with ‘granitoids,’ ‘porphyritics,’ and ‘trachytes’ because of their mostly unstratified, massive appearance (Moores, 1982). At the beginning of the twentieth century, Steinmann expressed several notable ideas

about ophiolites that influenced future research. Steinmann (1927) noted the presence generally of three types of rocks in a sequence, from bottom to top, ultramafic peridotites, gabbro and finally diabase-spilite on the top (Figure 1.1). This combination later became known as the 'Steinmann trinity'. After Steinmann, almost all workers in this field accepted this interpretation and realized its importance, until the end of 1960, when the true significance of ophiolite sequences began to be realized (Moore, 1982).

By the end of 1960, Brunn clarified important issues related to ophiolites, where he visualized an ophiolite as a broad influx of magma onto the floor of geosynclines, with this magma subsequently producing ophiolites by gravitational separation (Robertson, 2004).

Finally, the Penrose Conference in 1972 (Anonymous, 1972), served as the foundation stone for understanding the true development and evolution of ophiolites based on plate tectonics, and defined the ideal ophiolite sequence used today, i.e. ultramafic complex, gabbroic complex, mafic sheeted dyke complex and mafic volcanic complex (Dilek and Furnes, 2011). Since then, ophiolites have become the key for understanding the formation and evolution of the Earth's oceanic crust and to determine the nature of tectonic processes associated with seafloor spreading.

### **1.3 General explanation of ophiolite units**

A typical complete ophiolite sequence includes the following units from base to top:

1- Ultramafic tectonite

Ultramafic tectonites are rocks that show no cumulate features and were not formed by crystallization from a magma. They represent depleted mantle, i.e. mantle that has had basaltic melt extracted from it (Moore, 1982). This unit is generally comprised of harzburgite (olivine + orthopyroxene), but may also include lherzolite (olivine + orthopyroxene + clinopyroxene), dunite (more than 90% olivine) and chromitite (a rock with high concentrations of chrome spinel). The rocks of this unit often show deformed, foliated fabrics resulting from ductile deformation during mantle flow. These fabrics can be seen under the microscope by presence of a preferred orientation of olivine crystals and by pyroxene and spinel laminar concentrations (Moore and Twiss, 1995). Overlying these rocks are ultramafic and mafic cumulates, which formed by partial melting and fractional crystallization. The boundary between the tectonites and the overlying cumulate rocks is known as the petrological Moho, and represents the base of the crust.

## 2- Ultramafic and mafic cumulates

These represent stratified plutonic rocks that formed by fractional crystallization and accumulation of crystals in a magma chamber, fed from below by the delivery of basaltic melts derived from partial melting of the mantle peridotites. These rocks display obvious compositional layering and cumulus textures (Condie, 2005). The cumulate section starts from the base with ultramafic layered cumulates, which are predominantly composed of olivine and pyroxene and grade upward into more plagioclase-rich gabbroic layers (Moore and Twiss, 1995). In the upper part of the gabbroic unit, layering is no longer seen and the gabbros become structureless. The upper gabbros have variations in crystal-size as a result of hydrous fluids in the melt, and these varitextured gabbros are

often interpreted as representing a fossil melt lens located at the top of the gabbro section (MacLeod *et al.*, 2000).

### 3- Sheeted dyke complex

In a typical ophiolite, the gabbros are overlain by a sheeted dyke complex, which generally consists of multiple doleritic dykes. These dykes display variable thickness but mostly ranging between 1 to 3 m in width (Kidd, 1977). Cross-cutting relationships lead to the majority of dykes displaying one-sided chilled margins (Moore, 1982), as successive dykes are intruded into a host rock consisting of previously formed dykes. These dykes represent the conduits for transport of magma from the underlying (gabbroic) magma chamber up to the seafloor, where they feed the overlying extrusive section.

### 4- Extrusive section

The rocks of this section overlie the sheeted dyke complex and represent the uppermost unit of the igneous rocks within an ophiolite sequence. This unit consists of extrusive volcanic rocks in the form of pillow lavas or massive, sheet flows. However, the transition from sheeted dyke complex to extrusive lavas generally does not happen suddenly, but it occurs over a depth range of 50 - 100 m (Moore, 1982; Condie, 2005).

### 5- Marine sediments

In a typical ophiolite, the igneous sequence is commonly overlain by various sedimentary rocks reflecting marine depositional environments (i.e. abyssal, bathyal or arc-related deposition environments). These sediments generally include: metalliferous sediments (umber; Robertson, 1975), radiolarian cherts, carbonates and sulphide layers (Moore, 1982).

However, many ophiolite outcrops are missing one or more units of the Penrose ophiolite sequence outlined above, because of tectonic deformation during emplacement, and the thickness of each unit varies significantly between different ophiolites (Clague and Straley, 1977). Figure 1.3 shows the comparison of some ophiolite complexes with the idealized ophiolite stratigraphy.

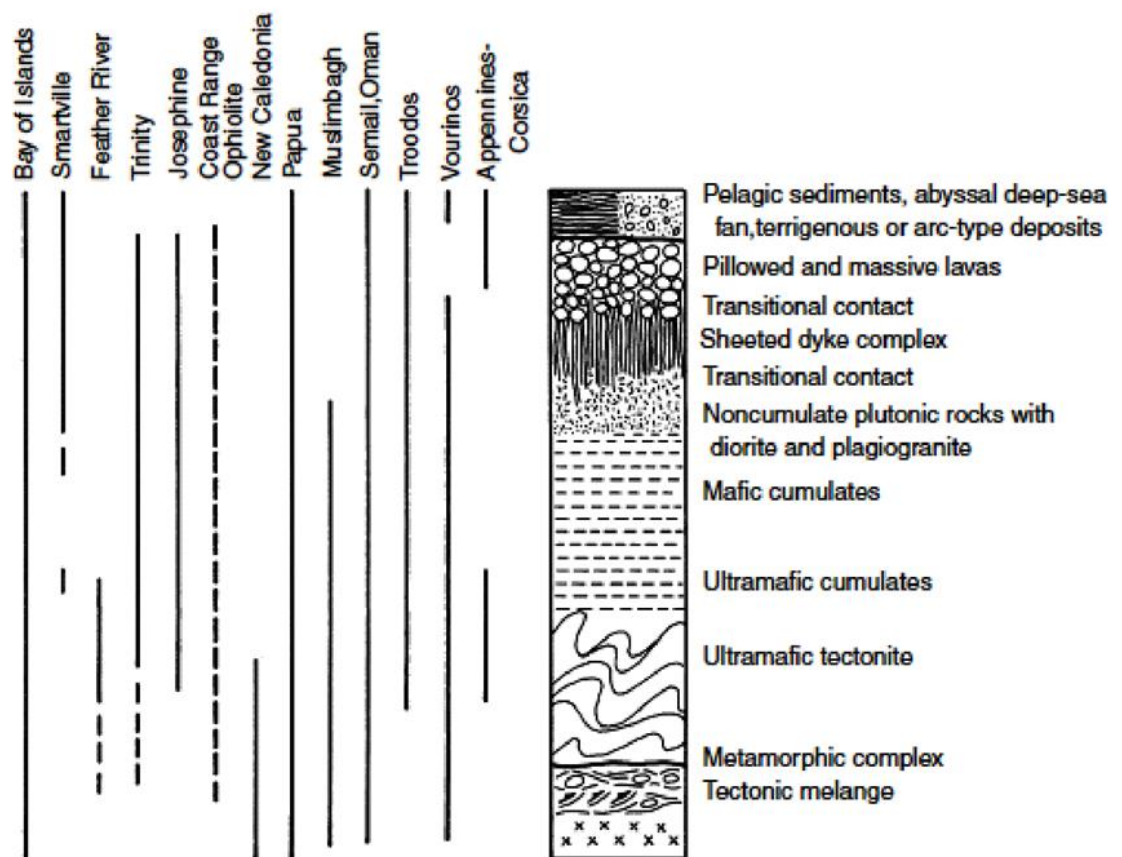


**Figure 1.3.** Comparison of selected ophiolite complexes with the idealized ophiolite assemblage (from Condie, 2005, after Moore, 1982).

## 1.4 Ophiolite types

There are numerous studies about the classification of ophiolites from different geological settings. In general, ophiolites can be divided into two main sets: mid-oceanic ridge (MOR) type generated at divergent plate boundaries through seafloor spreading, and supra-subduction zone (SSZ) type generated above convergent plate boundaries through the closure of ocean basins (Figure 1.4). These types are distinguished by geochemical characteristics. For example, SSZ-type ophiolites are characterized by island-arc tholeiites, more depleted mantle (predominantly harzburgite) sequences, and they may have boninitic lavas, whereas MORB-type ophiolites are characterized by mid-oceanic ridge basalts, and the mantle sequences are both harzburgites and lherzolites (Pearce *et al.*, 1984; Metcalf and Shervais, 2008).

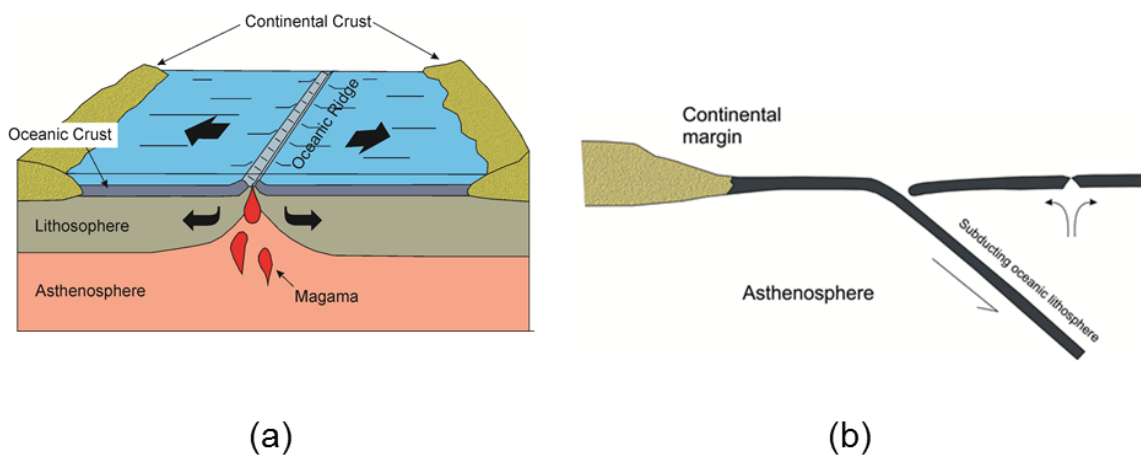


**Figure 1.4.** Types of ophiolite. (a) Mid-oceanic ridge (MOR) type. (b) Supra-subduction zone (SSZ) type.

In a more recent classification, Dilek and Furnes (2011) divide ophiolites into two main subgroups as follows: subduction-related ophiolites (which comprise subduction-zone and volcanic-arc types), and subduction-unrelated ophiolites (which comprise continental margin, mid-ocean ridge and plume-type ophiolites).

## 1.5 Emplacement of ophiolites

There is still extensive debate on the mechanisms of ophiolite emplacement onto the continental crust. According to Condie (2005), there are three main mechanisms in arcs or collisional orogens (Fig 1.5). The first model involves emplacement onto a passive continental margin by collision of a continental margin with a subduction zone leading to obduction by thrusting. The second model involves the separation of the top section of a down-going plate and its emplacement as a thrust sheet onto a former arc. The third model involves underthrusting of a sheet of oceanic lithosphere within an accretionary prism.

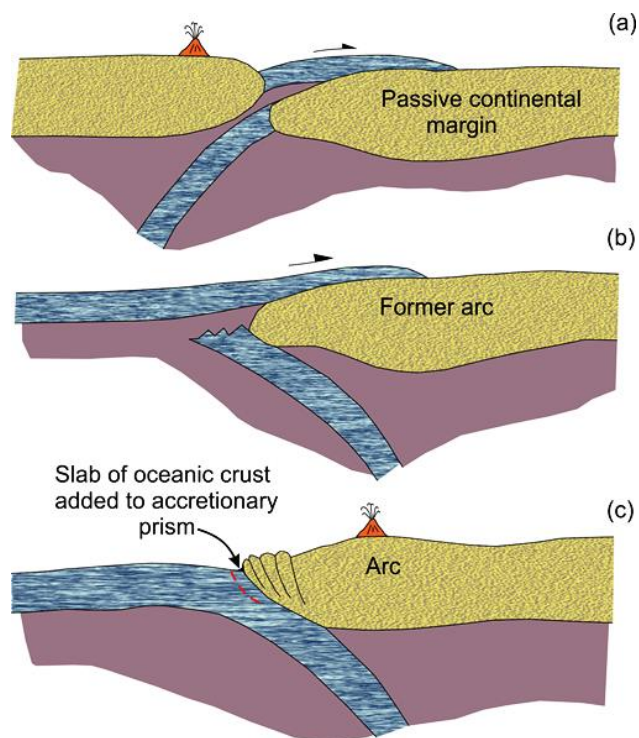


**Figure 1.5.** Types of mechanisms of ophiolite emplacement (modified from Condie, 2005). (a) Obduction onto a passive continental margin. (b) Obduction onto a former arc. (c) Addition of a sheet of oceanic lithosphere to an accretionary prism.

On the other hand, Wakabayashi and Dilek (2003) classified the emplacement of ophiolites depending on their various emplacement mechanisms; these are:

(1) Tethyan ophiolites, (2) Cordilleran ophiolites, (3) ridge-trench intersection ophiolites and (4) Macquarie Island-type ophiolite.

The first and second ophiolite types have been defined since the Penrose Conference (1972); also they have been identified by many researchers as the two major subgroups (Moores, 1982; Pearce *et al.*, 1984; Wakabayashi and Dilek, 2003; Beccaluva *et al.*, 2004). In the case of Tethyan-type ophiolites, they are tectonically characterized as located above passive continental margins, mostly in the form of intact oceanic sheets within major collision belts, and have the entire rock sequence of an ideal ophiolite structure (Wakabayashi and Dilek 2003; Beccaluva *et al.*, 2004). This type of ophiolite is widely found in the eastern Mediterranean area (e.g. Troodos in Cyprus, Semail in Oman, Baër-Bassit in Syria, Hatay and Mersin in Turkey, etc.). Cordilleran ophiolites were structurally emplaced on subduction zone accretionary complexes and this type of ophiolite has no relationship with a passive continental margin and is commonly characterized by having incomplete ophiolite sections (Wakabayashi and Dilek 2003; Beccaluva *et al.*, 2004). Examples of this type are the Coast Range ophiolite of California, and the Caribbean ophiolites of Guatemala, Cuba and Venezuela (Beccaluva *et al.*, 2004).

As for the third type (ridge-trench intersection ophiolites), Wakabayashi and Dilek (2003) have described these as resulting from the interaction of a subduction zone and a spreading ridge (e.g. Resurrection Bay and Knight Island ophiolites in Alaska and the Taitao ophiolites in Chile) (Wakabayashi and Dilek, 2003).

Finally, the Macquarie Island ophiolite is located along the transform border between the Indo-Australian and Pacific Plates (Varne *et al.*, 1969; 2000) and

consists of a complete ophiolite sequence. It is tectonically dissimilar from Tethyan and Cordilleran types, as it overlies either in situ oceanic crust or suboceanic mantle, instead of a continental margin or an accretionary complex (Wakabayashi and Dilek, 2003).

## **1.6 Aims and objectives**

The primary aim of this project is to study the Mersin Ophiolite of southern Turkey, in order to determine the amount of tectonic rotation experienced during its evolution. Therefore, this project uses a combination of palaeomagnetic, magnetic fabric, geochemical and structural analyses to investigate the following principal topics and to achieve its objectives:

The nature of fabrics within the layered gabbros of the Mersin ophiolite, using petrofabric and geochemical data to provide information on magmatic processes during crustal accretion

The amount of net tectonic rotation of the Mersin ophiolite experienced during seafloor spreading and tectonic emplacement

In addition, some new palaeomagnetic results from the much older Lizard ophiolite of SW England are also presented (Appendix A). These data were acquired as part of a smaller, discrete study undertaken at the start of the PhD, while permission to undertake palaeomagnetic sampling in Turkey was been sought.

## **1.7 Overview of the thesis**

This thesis consists of six chapters, including this overview of some general concepts about ophiolites and the aims of this research project. Chapter Two

presents a basic account of the theoretical background of palaeomagnetism and magnetic fabric analysis and describes the methodologies and equipment used in this study. Chapter Three includes a more detailed overview of the genesis of ophiolites in the Turkish area and, more specifically, of the Mersin ophiolite and the study area. Chapter Four presents a petrographic study of the ultramafic-mafic cumulates and dyke samples of the Mersin ophiolite with a geochemical investigation of cross-cutting veins within the cumulate (layered) gabbros and their relationship with the host gabbros. Chapter Five presents the new data and analyses of produced in this study, including palaeomagnetic and rock magnetic results interpreted in the regional context of previous palaeomagnetic investigations. Chapter Six presents a summary of the main conclusions of the thesis and recommendations for future work. Finally, Appendix A presents preliminary palaeomagnetic results from the subsidiary study of the Lizard ophiolite.

## Chapter 2

### Theoretical Background & Methodologies

#### 2.1 Basic characteristics of the Earth's magnetic field

Theoretical and experimental studies of the Earth's magnetic field have shown that the major portion of the field observed at the Earth's surface is generated by electromagnetic dynamo processes in the iron-nickel alloy fluids of the outer core (Figure 2.1). This internal source generates more than 90% of the total geomagnetic field (Butler, 1992; Tauxe, 2009).

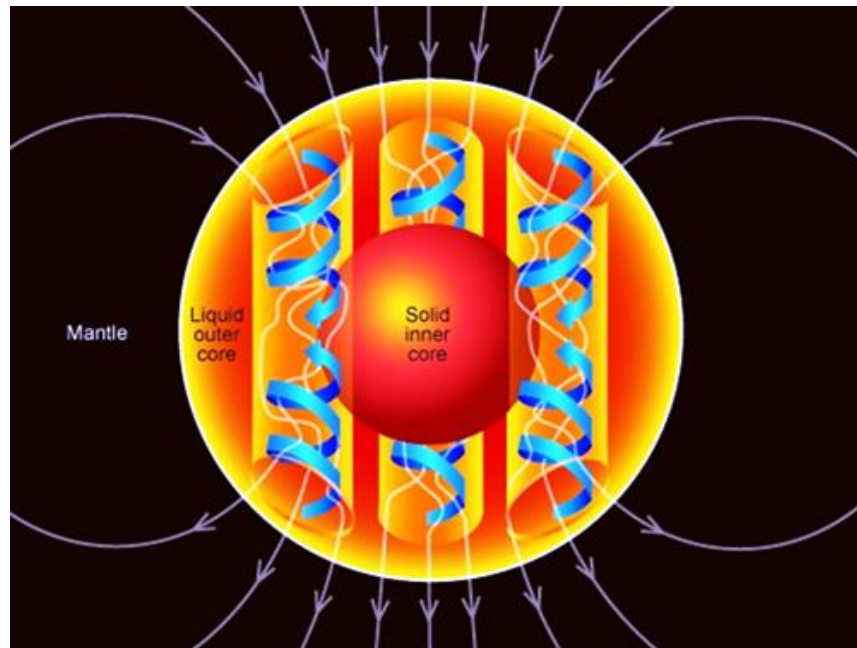


**Figure 2.1.** Convection currents in the Earth's outer core generate the geomagnetic field (from Reeve, 2010).

Remaining components of the field arise from the crustal field (produced by induced currents in ferromagnetic materials in the Earth's crust and the mantle) and the external field caused by electric currents in the atmosphere (Knecht, 1972; Merrill *et al.*, 1996).

There are two components for specifying the orientation of the geomagnetic field ( $H$ ): (1) Declination ( $D$ ): The angle between the geographical north pole and the field in the horizontal plane. Declination is always measured clockwise from geographical north, ranging from  $0^\circ$  to  $360^\circ$ . (2): Inclination ( $I$ ): The angle measured from the local horizontal surface, ranging between  $0^\circ$  and  $\pm 90^\circ$  (Figure 2.2a), with positive/negative inclinations indicating downward/upward directed fields respectively (Figure 2.2b).

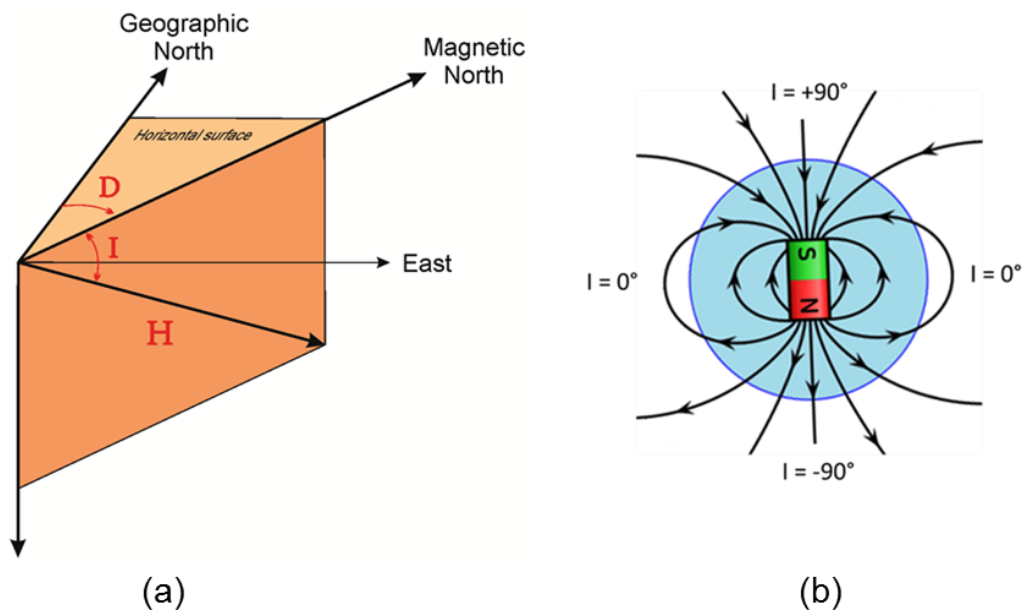


**Figure 2.2.** (a) The main elements of the Earth's magnetic field. The declination ( $D$ ) represents the angle between the magnetic field and the true north, measured in the horizontal plane. The inclination ( $I$ ) is the angle between the horizontal and  $H$ , where  $H$  is the total magnetic field vector. (b) The Earth's magnetic field showing field direction either side of the Earth's equator.

The geometry of the majority of the present day field may be modeled by a simple dipole placed at the centre of the Earth and tilted about  $11.5^\circ$  from the rotation axis of the Earth (i.e. the magnetic poles do not coincide with the geographical poles) (Figure 2.3), with a more minor contribution from non-dipole field elements. The intensity of the field varies on the Earth's surface, from

about 62000 nT at the magnetic poles (where the field lines are dense and perpendicular to the Earth's surface) to about 23000 nT at the magnetic equator, where the field lines are parallel to the Earth's surface (Gunnarsdóttir, 2012).

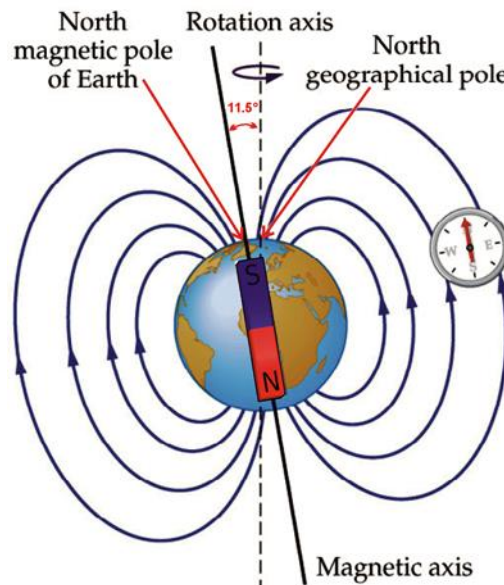


**Figure 2.3.** The Earth showing the deviation of the magnetic north pole about 11.5° from the geographic North Pole.

In general, the intensity of the Earth's field – dipole plus non-dipole (the remaining portion of the Earth's magnetic field after removal of the dipole and external fields) – has in recent times continuously decreased with time, falling by 1.4% during the period from 1970 to 2000 (Humphres, 2002). Furthermore, the geomagnetic poles are not constant in location, but instead move slowly around the rotation axis of the Earth (the geographical pole). This phenomenon is known as secular variation, and results from changes in fluid flow in the outer core of the Earth. Secular variations affects the direction (declination, inclination) and intensity of the field (Butler, 1998; Lowrie 2007). Palaeosecular variation studies by geomagnetists indicate that when the field is averaged over  $10^4$  or  $10^5$  years, the geomagnetic field at the Earth's surface can be modelled as that created by a geocentric axial dipole (GAD) (Butler, 1998; Tauxe, 2009). In this

longer-term model, the magnetic field matches that generated by a single magnetic dipole located at the centre of the Earth and coincident with the rotation axis (Butler, 1998). For a GAD field, the declination of the field,  $D = 0^\circ$  at any point on the Earth's surface and the inclination is related to latitude by the simple equation:

$$\tan I = 2 \tan \lambda$$

where  $\lambda$  = geographic latitude, ranging from  $-90^\circ$  at the geographic south pole to  $+90^\circ$  at the geographic north pole (Figure 2.2b).

Furthermore, the geomagnetic field also switches its polarity over the long periods ranging between  $10^4$  and  $10^7$  yr. The present arrangement of the field in which the magnetic North Pole of the Earth is close to the geographic North Pole is called a normal polarity field, whereas the opposite arrangement is called a reverse polarity field (Butler, 1998) (Figure 2.4).

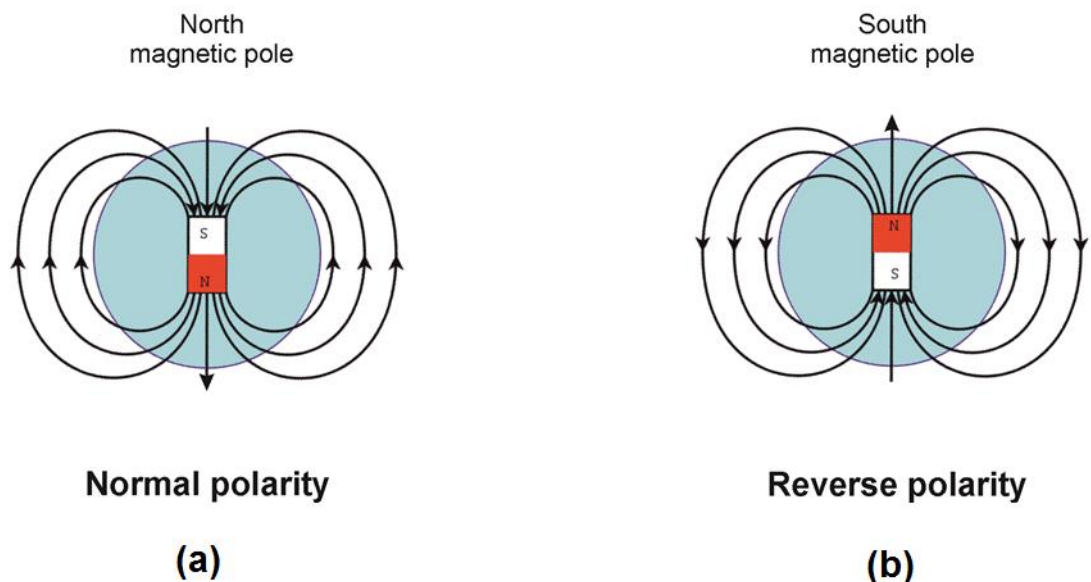


**Figure 2.4.** Schematic of the Earth's magnetic field reversal. (a) Normal polarity. (b) Reverse polarity.

The study of the history and behavior of the natural remanent magnetization (NRM) recorded in rocks which acquired their magnetization in ancient geomagnetic fields over geological time is termed palaeomagnetism. As a result of the long-term geocentric axial dipolar geometry of the geomagnetic field, palaeomagnetists are able to use the direction of magnetization of rocks and sediments to establish palaeolatitudes of sampled units and determine whether they have been affected by rotations (around vertical, horizontal or inclined axes). Thus, palaeomagnetism is a powerful tool for investigating tectonic processes.

Rocks may acquire different components of magnetization at various times during their geological history. A primary objective in all palaeomagnetic investigations is to identify and isolate these different components of remanent magnetization, using palaeomagnetic analyses and demagnetization techniques. The types of NRM are described in the section 2.5.

## **2.2 Magnetic behavior of materials**

All materials have magnetic properties at the atomic scale, and this property arises through the motion of electrons as they spin on their axes and orbit around atomic nuclei (Figure 2.5) (Tarling and Hrouda, 1993). Thus, there are various kinds of spin interactions, which give rise to different magnetic effects.

The magnetic behavior of materials can be classified on the basis of magnetic susceptibility (how they respond to an external magnetic field) into three main groups: diamagnetism, paramagnetism and ferromagnetism.

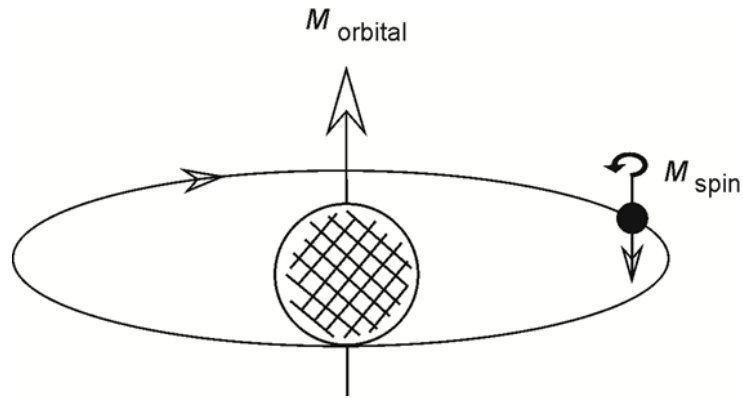


**Figure 2.5.** Magnetism of an atom. The magnetization arises from the spin of an electron about its axis and from the orbital motion of the electron about its nucleus (redrawn after Tarling 1971).

### 2.2.1 Diamagnetism

Diamagnetism is a property of all matter. In purely diamagnetic materials all the orbital shells are complete (i.e. all the orbital shells are paired in the structure of atoms). When a magnetic field is applied to any diamagnetic material, a small magnetization is produced with direction opposite to the applied field. This induced magnetization relates linearly to the applied field, and vanishes as soon as the external applied magnetic field is removed (Butler, 1998) (Figure 2.6a) and (Figure 2.7a). The magnetic susceptibility ( $k$ ) of diamagnetic materials is negative and independent of temperature. Examples of this type of material are quartz and calcite, which are important constituents of many kinds of rocks.

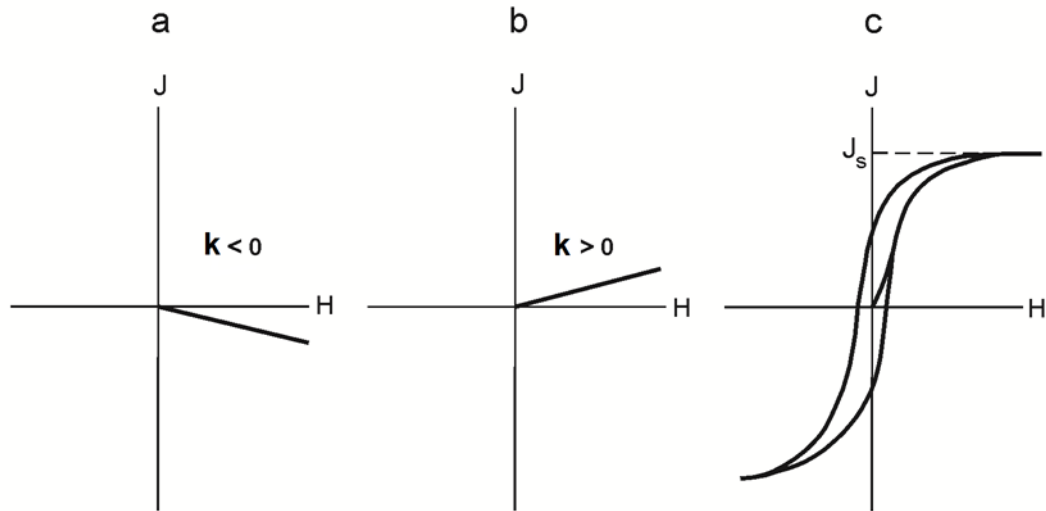


**Figure 2.6.** The essential groups of magnetic behavior. All three illustrations show the magnetization,  $J$ , against the magnetizing field,  $H$ , for: (a) diamagnetic; (b) paramagnetic; and (c). ferromagnetic materials.  $k$  represents magnetic susceptibility, which is a negative/positive constant for diamagnetic/paramagnetic materials respectively. For ferromagnetic materials, the path of magnetization exhibits hysteresis, and the magnetic susceptibility is not a simple constant (redrawn after Butler, 1998).

### 2.2.2 Paramagnetism

Paramagnetic materials have incomplete electron shells. Therefore, when a magnetic field is applied, they acquire induced magnetization by spinning their orbitals and electrons, thus producing a weak magnetization in the same direction as the applied field. Like diamagnetic materials, the magnetization depends linearly on the applied field and the induced magnetization disappears when the external applied magnetic field is removed (Figure 2.6b) and (Figure 2.7b). Thus, the magnetic susceptibility,  $k$ , of paramagnetic materials is low and positive, but dependent on temperature, and it can only be observed below the Curie temperature for each mineral (Butler, 1998). Examples of paramagnetic

materials include many of the iron-containing minerals, such as fayalite, pyroxene, biotite and hornblende (Tarling and Hrouda, 1993).

### 2.2.3 Ferromagnetism

Unlike diamagnetic and paramagnetic materials, ferromagnetic materials have very strong atomic moment interactions caused by electronic exchange forces. Thus these materials possess much stronger magnetic susceptibilities. Magnetic moments display either parallel or antiparallel alignment. The relationship of magnetization with the applied field is not linear, but forms a hysteresis loop and the magnetic susceptibility is not a simple constant (Butler, 1998) (Figure 2.6c). Like paramagnetic materials, the magnetization is lost at temperatures above the Curie temperature for each mineral. The term "ferromagnetism" (in some sources "ferromagnetism *sensu lato*"), is a broad expression, but more precisely, this group is divided into three subdivisions depending on classes of spin alignment; these are: true ferromagnetism (in some sources ferromagnetism *sensu stricto*), antiferromagnetism and ferrimagnetism.

The true ferromagnetic materials (s.s.) display a parallel alignment of magnetic moments in the same direction (i.e. positive exchange interaction) (Figure 2.7c), leading to a very strong spontaneous magnetism which can remain even after the external field has been removed, causing a remanent magnetization (Tarling and Hrouda, 1993; Butler, 1998). Ferromagnetic materials include iron, nickel and cobalt, and these materials rarely exist naturally in the Earth's crust (Kearey *et al.*, 2002).

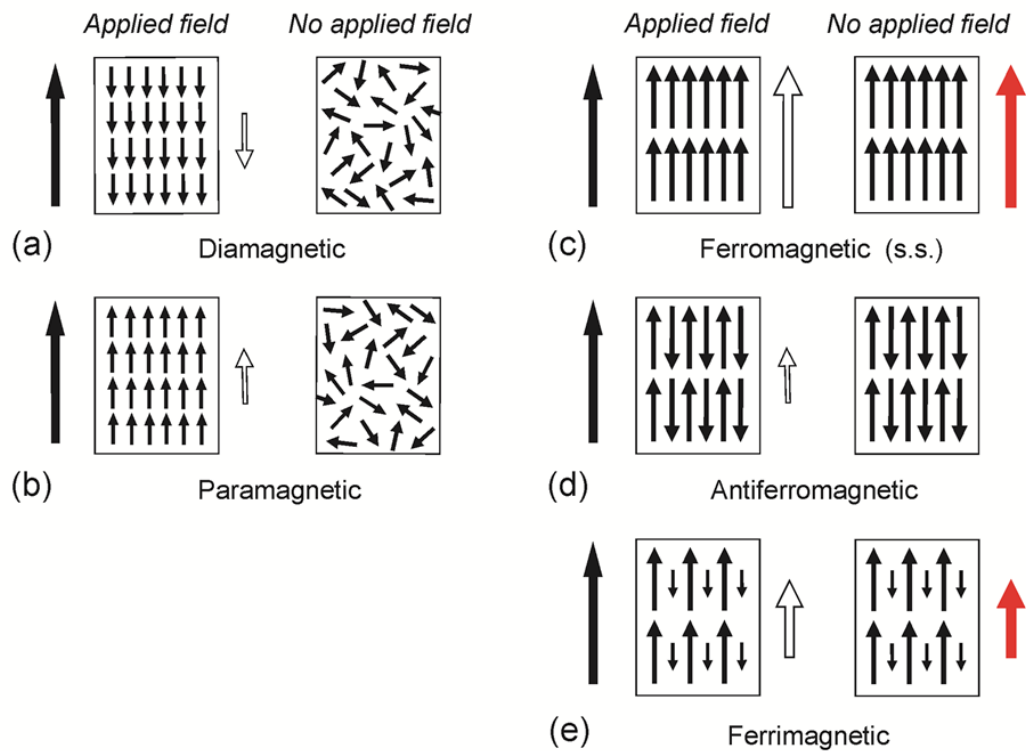


**Figure 2.7.** Schematic representations of different forms of magnetization against applied field. All the solid arrows on the left-hand side on a pair of diagrams in these illustrations refer to the applied field, whereas the hollow arrows represent the acquired magnetization when the applied magnetic field exists. Red arrows refer to the remanent magnetization after removal of the external magnetization. (a) Diamagnetic materials; showing a small magnetization in the opposite direction of the applied field, but the magnetic moment alignments become randomized upon removal of the applied field. (b) Paramagnetic materials; showing a small magnetization in the same direction of the applied field, but also become randomized upon removal of the applied field. c, d and e. Ferromagnetic materials (s.l.) are sub-divided to ferromagnetic (s.s.), antiferromagnetic and ferrimagnetic materials depending on the order of the magnetic moment alignments after removal of the applied field and all display paramagnetism above their Curie temperature (modified from Tarling and Hrouda, 1993).

In antiferromagnetic materials the exchange interaction occurs within crystal sub-lattices. These sub-lattices have equal magnitude of magnetic moments but in an anti-parallel spin manner (i.e. negative exchange interaction) (Figure 2.7d). However, when all the spins are completely anti-parallel, there will be no net magnetization (an example is ilmenite,  $\text{FeTiO}_3$ ), whereas if the spins of magnetic moments are not perfectly anti-parallel (or canted) the configuration yields a weak magnetization as occurs in hematite ( $\text{Fe}_2\text{O}_3$ ) (Tauxe, 2009).

Ferrimagnetic materials also possess anti-parallel alignments of the magnetic moments, but unlike antiferromagnetic materials, the magnetic moment alignments within the sub-lattices are not of the same strength. Therefore, ferrimagnetic materials retain a remanent magnetization after removal of the applied field. Moreover, ferrimagnetic materials also behave paramagnetically above the Curie temperature for each mineral (Tarling and Hrouda, 1993) (Figure 2.7e). The most important example is magnetite ( $\text{Fe}_3\text{O}_4$ ).

## **2.3 Rock magnetism**

Rock magnetism involves the study of magnetic minerals in rocks and the stability of natural remanences. Generally, magnetic minerals represent at most a few percent of the rock volume, and usually occur in the form of ferromagnetic iron oxides (most commonly magnetite  $\text{Fe}_3\text{O}_4$ ) or iron sulphides. During rock formation, the intrinsic magnetization of grains of magnetic minerals become statistically aligned with the direction of the ambient magnetic field, providing a fossil record of the field direction that may then persist on geological timescales (Kearey et al., 2002).

### **2.3.1 Magnetic domains**

Domains are small regions inside ferromagnetic minerals in which the magnetization is uniform and aligned in a specific direction (Tarling and Hrouda, 1993).

Each magnetic particle has a magnetostatic energy that arises from the distribution of magnetic charges on its surface (Butler, 1998). For example, in a spherical ferromagnetic particle with uniform magnetization, charges of opposite polarity occur on opposite hemispheres. As a result, there is energy stored

within the distribution of the charges resulting from the work required to keep opposite charges apart (Figure 2.8a). This magnetostatic energy decreases with the formation of magnetic domains, because in this way the proportion of the surface covered by magnetic charge is reduced, and the distance between opposite charges is reduced (Butler, 1998). The grain will divide into a number of domains of uniform magnetization if this results in an overall reduction in magnetostatic energy.

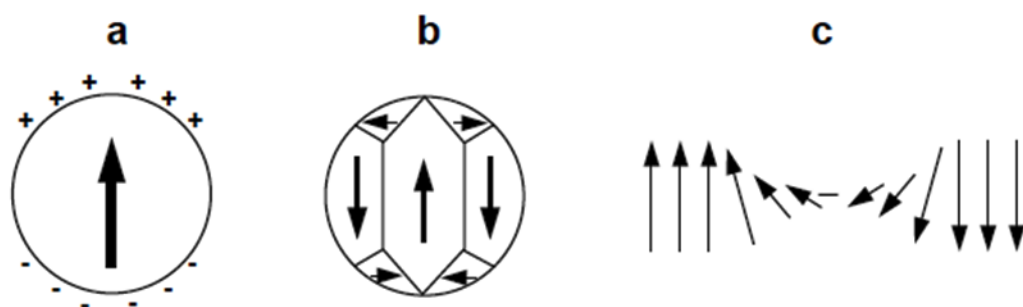


**Figure 2.8.** Schematic diagram showing domain formation. (a) Spherical grain of ferromagnetic mineral showing uniform magnetization, the arrow indicates the direction of magnetization. (b) Spherical ferromagnetic grain subdivided into magnetic domains. The arrows indicate the domain magnetization direction; the planes between magnetic domains refer to domain walls. (c) Gradual changes in magnetization direction within the domain wall (from Butler, 1998).

The number of the magnetic domains depends on the size of the ferromagnetic grain. For example, a small magnetite grain ( $<1 \mu\text{m}$ ) tends to form one domain, and is termed a single domain (SD) grain. Larger grains of magnetite with a diameter  $> 10 \mu\text{m}$ , consist of many domains and are called multidomain (MD) grains (Butler, 1992) (Figure 2.8b). Each domain is separated from its neighbours by a narrow boundary called a domain wall. The estimated thickness of domain walls ranges from ca.  $0.01$  to  $0.1 \mu\text{m}$  (Piper, 1987). In domain walls, the orientation of the atomic-level magnetizations changes from the direction in one domain to that of the adjacent domain (Tarling and Hrouda, 1993; Butler, 1998) (Figure 2.8c). In fact the transition between a large single

domain and small multidomain grain does not occur suddenly. Instead, there is a range of grain sizes that exhibit intermediate behaviour of magnetization within this interval. These grains of intermediate size are called pseudo-single domain (PSD) grains (Butler, 1998). Domain state does not fall in a constant range of grain sizes for all ferromagnetic minerals. For example, the interval of single domain sizes for equidimensional grains of magnetite falls within ca. 0.03 to 0.1  $\mu\text{m}$  and reaches ca. 1  $\mu\text{m}$  for elongate grains, whereas, in hematite, the single domain size ranges between the interval ca. 0.03 to 15  $\mu\text{m}$  (Lowrie, 2007).

### **2.3.2 Hysteresis**

When a demagnetized ferromagnetic specimen is subjected to an external magnetized field, the specimen becomes magnetized and follows the magnetization curve starting from the origin. As the field increases, the specimen eventually reaches a maximum level of magnetization, termed the saturation magnetization, where there is no further increases in magnetization occur (Figure 2.9). If the applied field reduced to zero, the magnetization does not relax back to zero, but instead the specimen will retain some remanent magnetism, which is an isothermal remanent magnetization (IRM) (Tarling, 1971; McElhiny and McFadden, 2000).

In order to reduce this remanence back to zero, a reverse direction field is required. The amount of a reverse magnetic field required to reduce *IRM* to zero is called coercivity or coercivity force ( $H_c$ ) (Butler, 1998; McElhiny and McFadden, 2000).

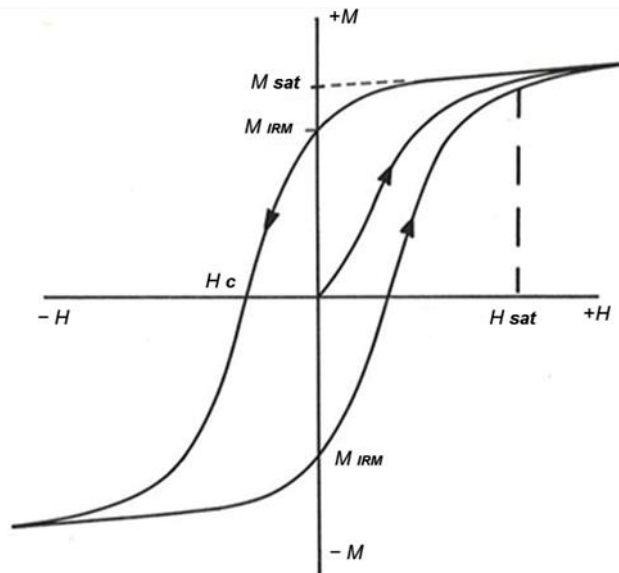


**Figure 2.9.** Hysteresis loop showing the behavior of magnetization of an unmagnetized ferromagnetic mineral.  $H$  is applied magnetic field.  $M$  is the magnetic intensity (magnetization).  $M_{sat}$  is the saturation magnetization of the ferromagnetic mineral.  $M_{IRM}$  is isothermal remanent magnetization (remanence).  $H_c$  is coercivity force (modified from Tarling, 1971).

### 2.3.3 Curie temperature, blocking temperature & relaxation time

All ferromagnetic materials lose their intrinsic magnetization at a temperature known as the Curie temperature, which varies with mineralogy. Above the Curie temperature, thermal energy is too great to allow interactions between adjacent atomic magnetic moments, and hence the material is incapable of holding a permanent, remanent magnetization and behaves paramagnetically. Of greater significance, however, is the blocking temperature of a ferromagnetic grain, which is the temperature below which its net magnetic moment becomes blocked in and becomes stable. In the interval between the Curie temperature ( $T_c$ ) and blocking temperature ( $T_b$ ), the ferromagnetic grain behaves superparamagnetically and the magnetization relaxes quickly after removal of applied field. The blocking temperature is dependent on the timescale or relaxation time ( $\tau$ ) of interest.

The essential assessment of the influence of time on magnetization came from the studies carried out by Louis Néel, where he defined the relaxation time by the following equation: (Tarling and Hrouda, 1993):

$$\frac{1}{\tau} = \frac{1}{C} \exp - \left( \frac{v B_c J_s}{2kT} \right)$$

Where

$\tau$  = relaxation time

$v$  = volume of the grain

$C$  = frequency factor  $\approx 10^{10} \text{ s}^{-1}$

$T$  = absolute temperature

$k$  = constant

$J_s$  = spontaneous magnetization of the ferromagnetic mineral

$B_c$  = coercivity

The equation demonstrates that the relaxation time has a strong relationship with ambient temperature, in addition to the importance of the size and composition of the grain in every magnetic process (Tarling and Hrouda, 1993; Butler, 1998). This is shown graphically in Figure 2.10 for the example of an elongated SD magnetite grain with dimensions of 0.1  $\mu\text{m}$  length and 0.02  $\mu\text{m}$  width.

The figure shows, at a relaxation time of 100 s (typical of the measurement time for a remanence determination), this specific grain will change from superparamagnetic to stable single domain at 550°C, corresponding to the blocking temperature ( $T_b$ ). However, when the temperature decreases below 550 °C, the relaxation time increases exponentially accordingly, so that by 510°C the relaxation time becomes more than the age of the Earth (Butler, 1998). It is this drastic increase in relaxation time over a narrow temperature

interval that produces the great stability of thermally controlled remanences in igneous rocks.

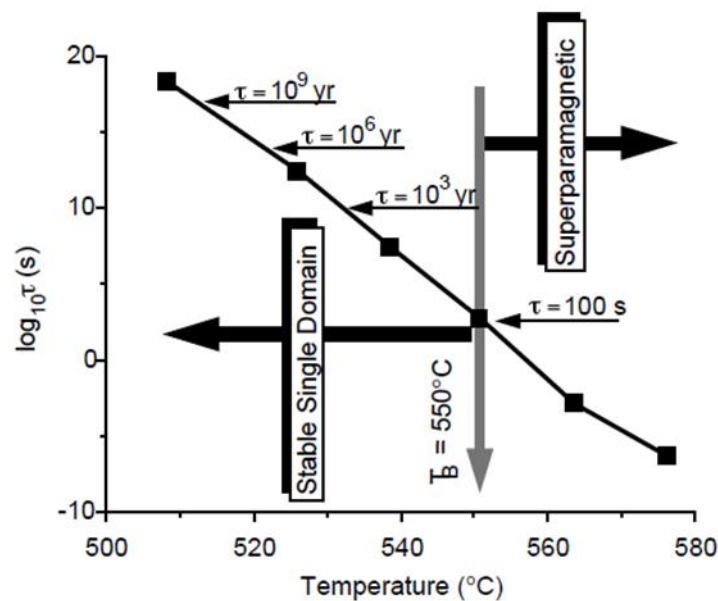


**Figure 2.10.** Relaxation time of a SD magnetite grain as a function of temperature. The grey arrow indicates the blocking temperature ( $T_b$ ), which for this grain is  $550\text{ }^\circ\text{C}$  when  $\tau = 100\text{ s}$  (the typical timescale of a remanence measurement). The grain behaves superparamagnetically when the temperature is greater than the blocking temperature ( $T_b$ ), and becomes stable SD when the temperature is less than  $T_b$  (after Butler, 1998).

## 2.4 Magnetic minerals

The majority of minerals that contain magnetic elements are not interesting in palaeomagnetic studies because of their low Curie temperatures. Even desirable ones like free iron and nickel-iron alloys, are very rare within the rocks of the Earth's crust, and these materials are only important in the study of meteorites or other planet's rocks (Tarling, 1971). However, the majority of ferromagnetic minerals that are important in palaeomagnetism and may carry remanence are present in the form of accessory minerals in terrestrial rocks, either as iron oxides or iron titanium oxides and may be shown in a ternary oxide diagram with rutile ( $\text{TiO}_2$ ), wustite ( $\text{FeO}$ ), and hematite ( $\text{Fe}_2\text{O}_3$ ) at the apexes (Butler, 1998) (Figure 2.11). These magnetic minerals belong to two

solid-solution series. The first group is known as the titanomagnetite (or ulvöspinel-magnetite) series, and comprises a continuous series of solid solutions that lie between magnetite ( $\text{Fe}_3\text{O}_4$ ) and ulvöspinel ( $\text{Fe}_2\text{TiO}_4$ ). The minerals of this series are opaque and cubic, and crystallize in the spinel structure (Butler, 1998). Magnetite is an important ferrimagnetic example from this group, that has a significant role in carrying the natural remanent magnetization for the majority of terrestrial rocks, forming a common constituent of igneous rocks and some sedimentary and metamorphic rocks. As shown in Figure 2.11, magnetite represents the right corner of this series and it has a Curie temperature  $580^\circ\text{C}$ . Curie temperature decreases linearly from right to left (with increasing amount of titanium), and consequently becomes nearly  $-150^\circ\text{C}$  for antiferromagnetic ulvöspinel (Merrill *et al.*, 1996). Magnetite sometimes can be oxidized at low temperatures to produce another ferrimagnetic mineral called maghemite ( $\gamma\text{Fe}_2\text{O}_3$ ) (Tarling, 1971). Furthermore, magnetite can be found as a primary mineral in igneous rocks, whereas in sediments, it often appears as detrital component, or is produced either by bacteria or authigenically during diagenesis (Tauxe, 2009).

The second important series of magnetic minerals is called the titanohematite (or ilmenite-hematite) series. The members of this group are also considered to be important carriers for remanence in some terrestrial rocks, where hematite can represent a dominant ferromagnetic mineral within highly silicic and/or highly oxidized igneous rocks. However, generally, in most igneous rocks the titanomagnetite minerals (including their oxidation products) comprise a more dominant part than titanohematite minerals and their oxidation products (Butler, 1998). Hematite is the most common antiferromagnetic mineral in this group, which is characterized by a black or red color, and it has Néel temperature

(analogous to Curie temperature) of approximately 680°C. Hematite is an important carrier of remanence in terrestrial rocks, particularly in red bed sediments (Tauxe, 2009). Hematite occupies the right corner of this series and Curie temperature decreases linearly from right to left (with increasing amount of ilmenite) (Figure 2.11), and becomes -223 C° for ilmenite (Merrill *et al.*, 1996). Moreover, hematite can originate as a result of oxidation of titanomagnetites or by exsolution of ilmeno-hematite. Also it can be found in igneous rocks by decomposition processes of other iron-bearing minerals like olivine, pyroxene and amphibole (Tarling, 1971). In addition, there are two iron-sulfide minerals which are important ferromagnetic minerals in palaeomagnetic studies; these are pyrrhotite ( $\text{Fe}_7\text{S}_8$ ) and greigite ( $\text{Fe}_3\text{S}_4$ ), and both these minerals originate in reducing environments (Tauxe, 2009). Table 2.1 displays some magnetic minerals that exist in rocks and summarises their magnetic properties.

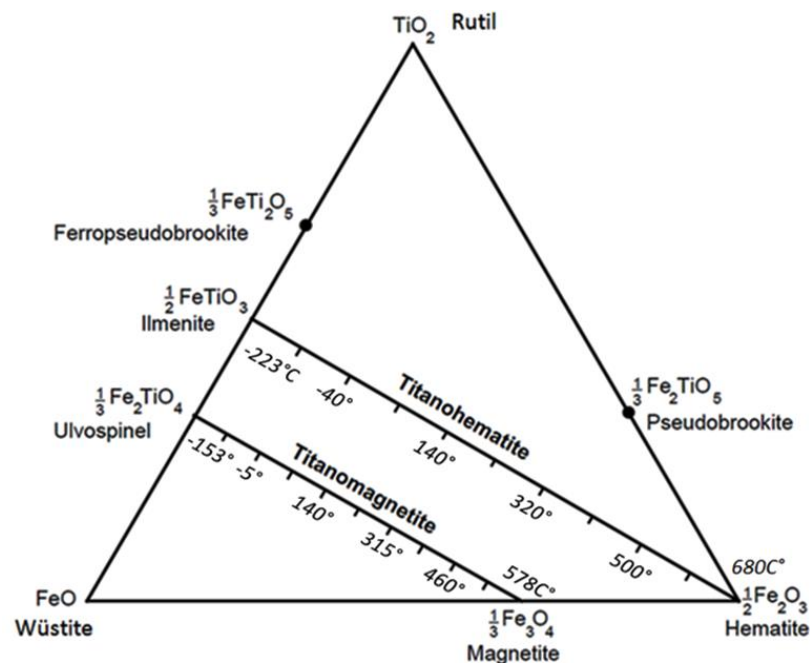


**Figure 2.11.** FeO-TiO<sub>2</sub>-Fe<sub>2</sub>O<sub>3</sub> ternary compositional system showing the two important solid solution series (combined from Butler, 1998 and McElhiny and McFadden, 2000).

**Table 2.1.** Selected magnetic minerals and their magnetic properties (modified from Harrison and Feinberg 2009).

Mineral	Formula	Magnetic structure	Curie/Néel temperature (°C)	Saturation magnetization (Am <sup>2</sup> /kg)
<b>OXIDES</b>				
hematite	$\alpha\text{-Fe}_2\text{O}_3$	canted antiferromagnetic	675	0.4
maghemite	$\gamma\text{-Fe}_2\text{O}_3$	ferrimagnetic	~600	70–80
ilmenite	$\text{FeTiO}_3$	antiferromagnetic	-233	0
magnetite	$\text{Fe}_3\text{O}_4$	ferrimagnetic	575–585	90–92
ulvöspinel	$\text{Fe}_2\text{TiO}_4$	antiferromagnetic	-153	0
<b>SULPHIDES</b>				
pyrrhotite	$\text{Fe}_7\text{S}_8$	ferrimagnetic	320	20
greigite	$\text{Fe}_3\text{S}_4$	ferrimagnetic	~333	~25
<b>OXYHYDROXIDES</b>				
goethite	$\alpha\text{-FeOOH}$	Antiferromagnetic weak ferromagnetic	~120	<1
lepidocrocite	$\gamma\text{-FeOOH}$	antiferromagnetic?	-196	?
tetraenaite	$\text{FeNi}$	ferromagnetic	550	?

## 2.5 Forms of natural magnetization in rocks

In general, natural magnetizations may be of two types: induced magnetization, which is present in a material exposed to an external ambient field and disappears when this external field is removed, and remanent magnetization, which remains after removal of the applied field (Tauxe, 2009). Palaeomagnetism mainly deals with the measurement of natural remanent magnetization (NRM), i.e. the magnetization which was recorded naturally in a rock over its history as a fossil magnetism before any laboratory treatment (Butler, 1998; Van der Voo, 1993).

The NRM of a rock generally is composed of several magnetization components acquired over its geological history. The NRM component produced in a rock by an ancient field at the time of formation of the rock is

referred to as the primary NRM component, and is the component desired in most palaeomagnetic studies. Components acquired after formation are known as secondary components. These may be removed by laboratory demagnetization, allowing recovery of primary components.

Table 2.2 summarizes the various forms of natural remanence in rocks, and there follows a brief account of the most significant processes that give rise to these remanences.

**Table 2.2.** Some different types of natural remanent magnetizations (NRM) (combined from Butler, 1992 and McElhinny and McFadden, 2000).

Type of remanence	Acronym	Magnetization process	Rock types
<b>Thermoremanent magnetization</b>	TRM	Magnetization acquired during cooling below the Curie temperature in an external field	Igneous and metamorphic rocks
<b>Depositional remanent magnetization</b>	DRM	Magnetization acquired during deposition of ferromagnetic detrital grains in an external field	Sedimentary rocks
<b>Post-depositional remanent magnetization</b>	pDRM	Magnetization acquired due to realignment of magnetic grains in wet sediments in an external field	Sedimentary rocks
<b>Chemical remanent magnetization</b>	CRM	Magnetization acquired through chemical changes within a magnetic material at low temperature in an external field	All rock types
<b>Isothermal remanent magnetization</b>	IRM	Magnetization acquired instantaneously due to a strong magnetic field (e.g. lightning strikes)	All rock types
<b>Viscous remanent magnetization</b>	VRM	Kind of natural secondary magnetization acquired over time due to exposure to ambient geomagnetic field	All rock types

### 2.5.1 Thermoremanent magnetization (TRM)

Thermoremanent magnetization (TRM) is a type of NRM acquired by most igneous rocks during cooling down below the Curie and blocking temperatures of its constituent ferromagnetic grains in the presence of an Earth magnetic field. In the absence of an ambient magnetic field, thermal energy randomises the magnetization of grains and no significant net magnetization is produced. However, the presence of an ambient magnetic field acts to bias this randomization process, resulting in statistically more grains having their magnetization blocked in along an easy axis of magnetization that is close to the direction of the magnetic field at that time (Butler, 1998; Lowrie, 2007; Tauxe, 2009) (Figure 2.12).

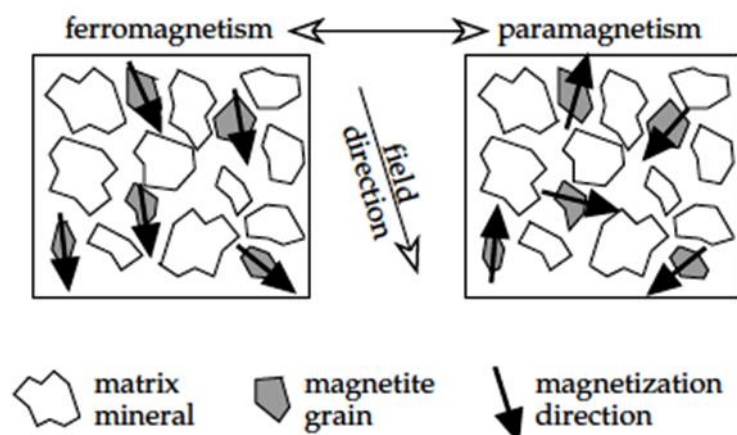


**Figure 2.12.** Schematic figure showing the changes in the magnetic status of ferromagnetic grains from paramagnetic to ferromagnetic during cooling (from Lowrie, 2007).

During the cooling process from the Curie Temperature ( $T_c$ ) of an individual SD grain to the blocking temperature ( $T_b$ ), the grain is ferromagnetic but remanent magnetization of the grain is unstable and it behaves paramagnetically. Below  $T_b$ , the remanent magnetization is effectively blocked, becomes stable and remains after removal of the magnetizing field (Butler, 1998). In a rock

containing an assemblage of grains, each with its own  $T_b$  (determined principally by grain size), TRM acquisition will not occur solely at the Curie point but over a distinct blocking temperature interval starting from the Curie temperature down to room temperature. The total TRM acquired in this process can be considered as the sum of the TRM components that were acquired in different temperature intervals, known as partial TRMs (pTRMs). Also, as a rock cools, the relaxation times of its ferromagnetic grains increase exponentially, eventually potentially exceeding the age of the Earth. Hence, TRM can be considered as a very stable magnetization that remains in the rock for a long period of geological time.

### **2.5.2 Depositional remanent magnetization (DRM)**

Depositional remanent magnetization (DRM) is acquired during deposition of detrital sedimentary rocks. During settlement of detrital magnetic grains through water, they are affected by the ambient geomagnetic field and tend to align with this field. However there are hydromechanical forces related to water currents that act to disturb the grains alignment with the field during settlement. In addition, as non-spherical grains are deposited, they rotate so that their long axes are sub-parallel to the sediment surface giving rise to an inclination error. Magnetic grains are also subject to other physical alignment processes after deposition caused by organisms, compaction and diagenesis. The magnetization which is acquired after deposition but before lithification is called post-depositional remanent magnetization (pDRM) (Butler, 1998; Lowrie, 2007; Tauxe, 2009). pDRM is usually acquired in the top of accumulated sediments within the first 10-20 cm (Butler, 1998).

### **2.5.3 Chemical remanent magnetization (CRM)**

Chemical remanent magnetization (CRM) is acquired during mineralogical changes within a rock at low temperatures (below the Curie temperatures of the magnetic minerals) in the presence of a magnetizing field. In general, CRM has properties similar to TRM, but unlike TRM, during the formation of CRM the volume of magnetic grains progressively grows and consequently the acquisition process is related to the volume changes of the magnetic grains. The smallest grains are superparamagnetic, have short relaxation times, and cannot carry a stable remanence. As magnetic grains grow, their volume increases and their relaxation time increases until their domain state changes from superparamagnetic to stable single domain at a certain critical point called the blocking volume ( $V_b$ ) (Piper, 1987; Butler, 1998; Lowrie, 2007; Tauxe, 2009).

CRM may form a primary CRM in chemical sediments, but more often represents a secondary component in a rock acquired during diagenesis and alteration (Butler, 1998).

### **2.6 Anisotropy of magnetic susceptibility (AMS)**

Anisotropy of magnetic susceptibility (AMS) is used to infer the alignment of elongate magnetic minerals by defining the magnetic fabric of rocks. Hence AMS can give information about processes related to different geological phenomena, e.g. flow directions in dykes and lava flows or structural features related to tectonic forces (Tarling and Hrouda, 1993). As a result of its very high magnetic susceptibility, the AMS signal in most rocks is dominated by the preferred alignment of magnetite grains. The AMS method depends on measuring the variation in low field magnetic susceptibility in different directions in a standard volume of rock sample under a weak magnetic field ( $\sim 10^{-4}$  T).

These variations can be expressed as a symmetric second rank tensor, which can be represented by a triaxial ellipsoid. The principal axes of the ellipsoid are defined in magnitude and direction by the maximum ( $K_1$ ), intermediate ( $K_2$ ) and minimum ( $K_3$ ) susceptibilities. When  $K_1 = K_2 = K_3$ , the shape of the anisotropy ellipsoid is a sphere and the magnetic susceptibility is described as isotropic. When  $K_1 \approx K_2 > K_3$ , the ellipsoid is oblate (disc-shaped). When  $K_1 > K_2 \approx K_3$ , the shape is prolate (cigar-shaped). Finally when  $K_1 > K_2 > K_3$  the shape of the ellipsoid is triaxial (Tauxe, 1998; Morris, 2003) (Figure 2.13).

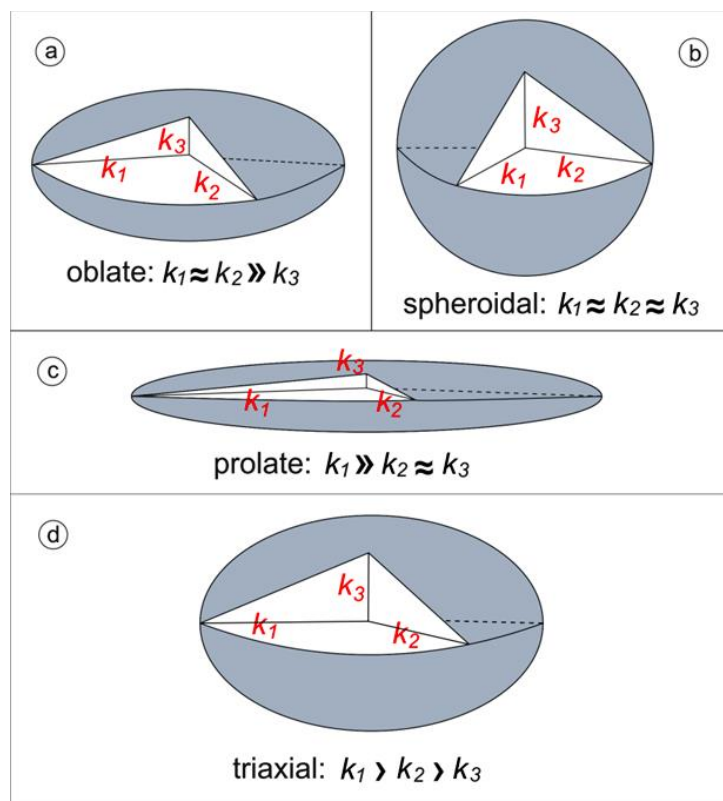


**Figure 2.13.** Schematic diagram of magnetic fabric ellipsoids showing the three principal susceptibility axes (modified after Winkler *et al.*, 1997).

The  $K_1$  axis normally represents the magnetic lineation, and its alignment describes the palaeo-flow direction, both in igneous rocks and in sedimentary current deposits (i.e. they show prolate ellipsoids). In oblate ellipsoids the  $K_3$

axis is usually perpendicular to the magnetic foliation plane which contains both the  $K_1$  and  $K_2$  axes, which is common in foliated rocks (Morris, 2003).

## 2.7 Palaeomagnetic methodologies

### 2.7.1 Palaeomagnetic sampling

In all localities of the Mersin and Lizard ophiolites, sampling was carried out using a gasoline-powered portable drill with a water-cooled diamond bit, following standard palaeomagnetic practice (Butler, 1998; Tauxe, 2009) (Figures 2.14 and 2.15).



**Figure 2.14.** Core sample collection in the field. (a) Field photograph illustrating core drilling. (b) Portable gasoline-powered drill with water-cooled diamond bits. (c) A pump used to inject water into the drill hole to lubricate the drill. (d) Sun compass as a part of non-magnetic slotted tube with an adjustable platform around the sample, used to orient drill cores.



**Figure 2.15.** Sampling technique used in the field. (a) Collecting drilled samples. (b) *In situ* marking of a permanent arrow on the upper side of the drilled core in the direction of drilling and labeling the sample with the sample name.

At least eight samples with an average length of 7 cm were taken at each site and independently oriented using both magnetic and sun compasses. Heavily fractured exposures were avoided during drilling, and weathered surfaces were cleared prior to drilling. The right-handed Cartesian coordinate system was used to specify the orientation of core samples *in situ* (Figure 2.16). In addition to core samples, some oriented block samples were also collected and subsequently drilled in the laboratory (Figure 2.17).

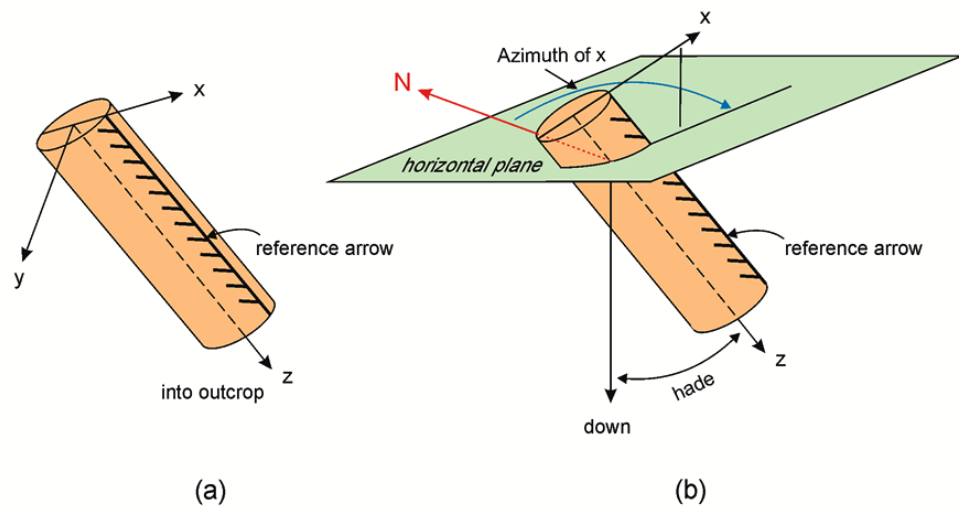


**Figure 2.16.** Orientation system for core samples. (a) A schematic diagram representing of drilled core sample *in situ*. (b) Diagram showing orientation angles for drilled core sample. The measured angles are: hade of the z axis (angle between z axis and vertical) and geographic azimuth of the horizontal projection of the +x axis measured clockwise from geographic north (modified from Butler, 1998).



**Figure 2.17.** Laboratory techniques for preparation of the palaeomagnetic specimens. (a) Drilling the hand samples. (b) Arrows drawn on the side of the drilled cores. (c) Preparing the specimens by cutting the core samples. (d) Numbering the specimens for measuring.

## 2.7.2 Anisotropy of magnetic susceptibility (AMS) measurements

AMS of all specimens was measured before application of palaeomagnetic demagnetization techniques. All AMS measurements were conducted at Plymouth University using an AGICO KLY-3 Kappabridge (Figure 2.18a) using the control program SUSAR. Each specimen was measured in three positions to determine differences in susceptibility in the plane of measurement, with a fourth measurement used to determine the bulk susceptibility. The program SUSAR then automatically combined these measurements and calculated a best-fit anisotropy ellipsoid for each specimen described by a second-order tensor, with principal axes corresponding to the maximum ( $K_1$ ), intermediate ( $K_2$ ) and minimum ( $K_3$ ) susceptibilities. In addition to the direction and magnitude of each of these axes, the principal susceptibilities were used to calculate two standard AMS statistics (using the AGICO program ANISOFT v. 4.2). The corrected anisotropy degree  $P_J$ , (Jelinek, 1981) describes the strength of the anisotropy, with a  $P_J$  value of 1.00 indicating zero anisotropy (isotropic), and, for example,  $P_J = 1.05$  indicating 5% anisotropy. The shape parameter,  $T$ , (Jelinek, 1981) describes the shape of the anisotropy ellipsoid, with  $T$  values ranging from +1 to -1, where positive values indicate oblate magnetic fabric shapes (disks) and negative values indicate prolate magnetic fabric shapes (rods or cigars) (Figure 2.19). These parameters are calculated from the principal susceptibilities using the following equations (Tarling and Hrouda, 1993):

$$P_J = \exp 2 [(\eta_1 - \eta_m)^2 + (\eta_2 - \eta_m)^2 + (\eta_3 - \eta_m)^2]$$

where  $\eta_1 = \ln K_1$ ,  $\eta_2 = \ln K_2$ ,  $\eta_3 = \ln K_3$  and  $\eta_m = (\eta_1 + \eta_2 + \eta_3)/3$

$$T = [2 \ln (K_2 / K_3) / \ln (K_1 / K_3)] - 1$$

### 2.7.3 Anisotropy of anhysteretic remanent magnetization (AARM)

AMS includes contributions from all minerals in a specimen (e.g. silicates and oxides in gabbroic rocks). In order to determine the anisotropy of just the oxides (principally magnetite), a different form of magnetic anisotropy is used. Anisotropy of anhysteretic remanent magnetization (AARM) yields the preferred fabric of ferromagnetic minerals *sensu lato* only, as only these phases are capable of retaining a remanent magnetization after removal of a magnetic field. The concept of AARM measurement is similar to AMS measurement, and produces a second rank tensor represented by the AARM ellipsoid. An uncertainty in AMS studies is introduced by a domain-state effect that can give rise to inverse fabrics in rocks dominated by SD magnetite. This is because the  $K_1$  axes of SD grains are perpendicular to their long axes whereas  $K_1$  of larger MD grains is aligned with grain long axes. This is not the case for remanence anisotropy, however, and theoretically both SD and MD magnetite grains preferentially will have a maximum intensity of remanence parallel to their long axes, thus eliminating the problem of inverse fabrics inherent in AMS studies (Jackson, 1991). Therefore, it is useful to compare AMS results with AARM results from the same samples in order to test for the presence of inverse AMS fabrics (Rochette *et al.*, 1999) and allow unambiguous interpretation of AMS data in terms of preferred orientations of crystals.

The AARM measurement consists of imparting an anhysteretic magnetization to a previously demagnetized specimen in several directions. Accordingly, this procedure was started by cleaning the specimen using AF demagnetization at a peak field of 100 mT. The specimen was then magnetized by applying an alternating field of 80 mT in the presence of a direct (bias) field of the 50  $\mu$ T.

The specimen was then measured for remanent magnetization using the JR-6A spinner magnetometer and the ARM6 program. For each specimen, this process was repeated for 12 different positions (i.e. orientation of the applied field). The AARM ellipsoids and corresponding principal axes (AARMmax, AARMint and AARMmin) were then calculated by using the Jelinek method using the AGICO program ANISOFT v. 4.2, (in the same way as for the AMS measurements). In order to avoid any problems during the measurements, all the specimens that were selected for this analysis were intact and with standard sizes (2.5 mm in diameter and 22 mm in height).

In this study, all AARM measurements were conducted at Plymouth University using an AGICO LDA-3 Demagnetizer with an AGICO JR-6 Spinner Magnetometer, using an alternating demagnetizing field of 100 mT and a biasing field of 50  $\mu$ T (Figure 2.18b).

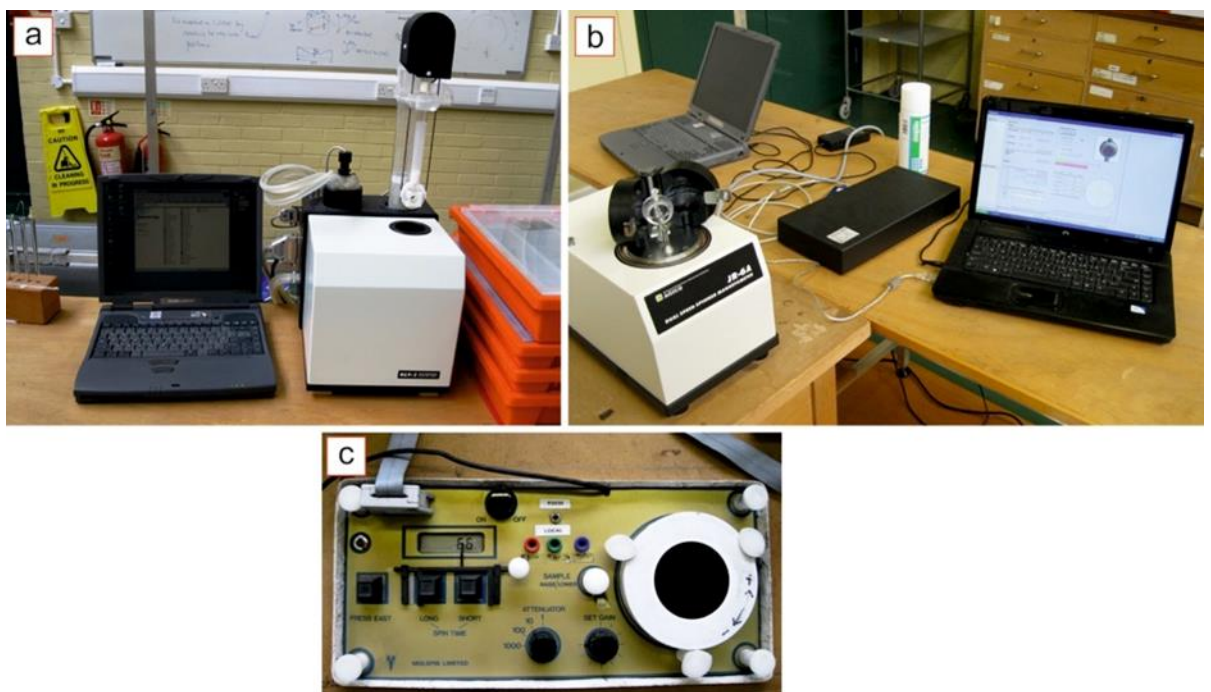


**Figure 2.18.** Palaeomagnetic laboratory instruments. (a) AGICO Kappabridge KLY-3 - Magnetic susceptibility/anisotropy system. (b) AGICO dual speed spinner magnetometer Model JR6A. (c) Molspin fluxgate spinner magnetometer.

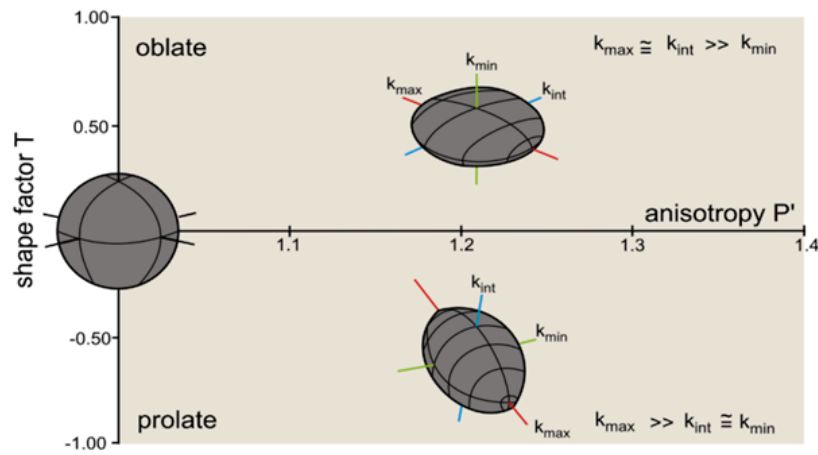


**Figure 2.19.** Degree of anisotropy  $P_j$ , versus shape parameter  $T$  diagram (Jelinek, 1981). Note: positive values of  $T$  represent oblate fabric shapes and negative values of  $T$  represent prolate fabric shapes (after Stefan Schöbel and Helga de Wall, 2011).

#### 2.7.4 Palaeomagnetic measurement & demagnetization techniques

The natural remanent magnetization (NRM) of a rock is usually a mixture of a primary component acquired at the time of its formation, and secondary components acquired at different stages afterwards through its history. In most palaeomagnetic investigations, the primary component is the component which is required, so the removal of the secondary components by demagnetization (magnetic cleaning) is necessary. There are two common techniques used for separation of the various components of magnetization. The first one is alternating field (AF) demagnetization which is implemented by exposing the specimen to a progressively decaying alternating magnetic field in a zero direct magnetic field environment, and the second technique is thermal demagnetization, which is performed by heating the specimen to high temperature and cooling back to room temperature in zero magnetic field, progressively increasing the temperature between measuring steps. There is a difference in the efficiency of thermal and AF techniques due to the difference in the composition of the remanence-carrying grains, whereby AF

demagnetization is often ineffective in removing secondary components carried by hematite, which usually has coercivities more than the peak demagnetizing field (Butler, 1998; Morris, 2003). Thermal demagnetization can effectively demagnetize all hematite grains, but some problems may appear due to the mineralogical alteration in the specimen by increasing the temperature. Therefore, in order to monitor such alteration, it is necessary to measure the magnetic susceptibility of the specimen after each temperature step (Tarling, 1983; Morris, 2003).

In this study, both thermal and AF demagnetization were used and both techniques were carried out at Plymouth University. AF demagnetization was performed using an AGICO LDA-3 AF-demagnetizer with a maximum peak field of 100 mT, whereas thermal demagnetization was performed using a Magnetic Measurements Ltd Thermal Demagnetizer – MMTD oven with a maximum temperature of 580 °C. At each heating step the specimens were held at the specified temperature for 40 minutes before cooling.

All remanent magnetization measurements were carried out using an AGICO JR-6 spinner magnetometer or a Molspin fluxgate spinner magnetometer inside a low field environment produced by a set of Helmholtz coils (Figure 2.18).

There are two principal ways for presenting the stepwise magnetization data: orthogonal diagrams (also called Zijderveld diagrams, or vector component diagrams), and equal area stereographic projections (Butler, 1998; Tauxe, 2009) (Figures 2.20 and 2.21). Orthogonal plots allow both the direction and intensity of the three-dimensional magnetization vector to be present on the two-dimensional diagram. On these two-dimensional diagrams, the remanence at each demagnetization step is projected on to both the horizontal plane and

either the N-S or E-W vertical plane, allowing depiction of the declination and apparent inclination simultaneously. The distance from the origin to any point is then proportional to the intensity in that projection plane.

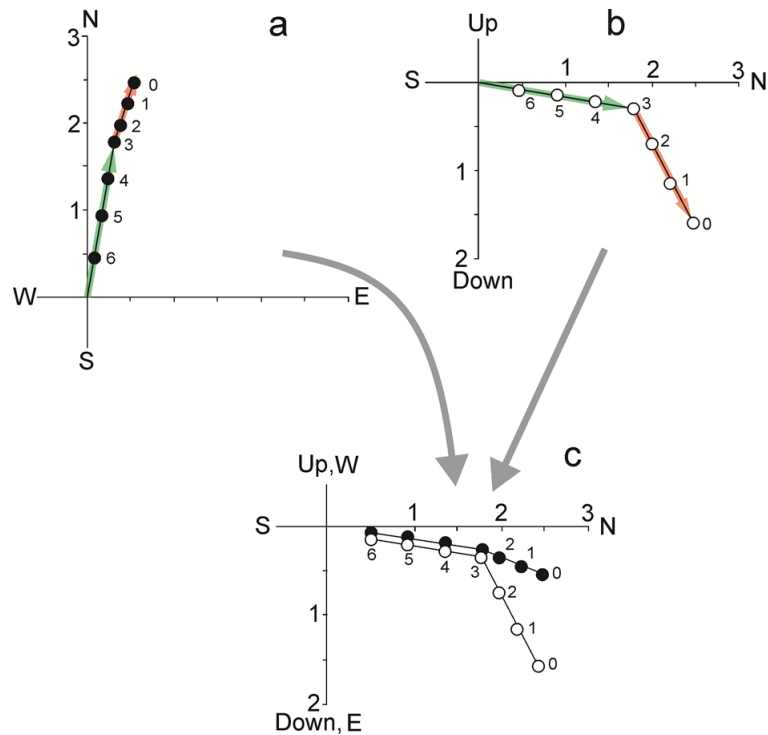


**Figure 2.20.** Illustration of the principle of orthogonal (vector component) projections. (a) Projection of the NRM vector produced during progressive demagnetization onto the horizontal plane. The light red arrow represents the horizontal projection of the low-stability component of NRM removed in the interval 0-3; the light green arrow represents the horizontal projection of the stable characteristic component of magnetization (ChRM) remaining at step 3. (b) Projection of the NRM components onto a vertical plane. The light red arrow represents the vertical projection of the low-stability component of NRM removed in the interval 0-3; the light green arrow is the vertical projection of the ChRM remaining at step 3. (c) Combination of horizontal and vertical projections of NRM vectors in one single diagram (modified from Butler, 1998)

Equal-area projections also display the direction of an NRM, but the intensity of NRM needs to be presented separately (Butler, 1998; Figure 2.21). Figure 2.20 is an example, and also illustrates the usual procedure for isolating the primary component from the data from progressive demagnetization experiments. Directions of NRM components can be determined numerically using principal

component analysis (Kirschvink, 1980). Directions of magnetization determined in this way may then be combined using vector averaging to yield the mean direction of each component at the site-level, together with the associated Fisher statistics.

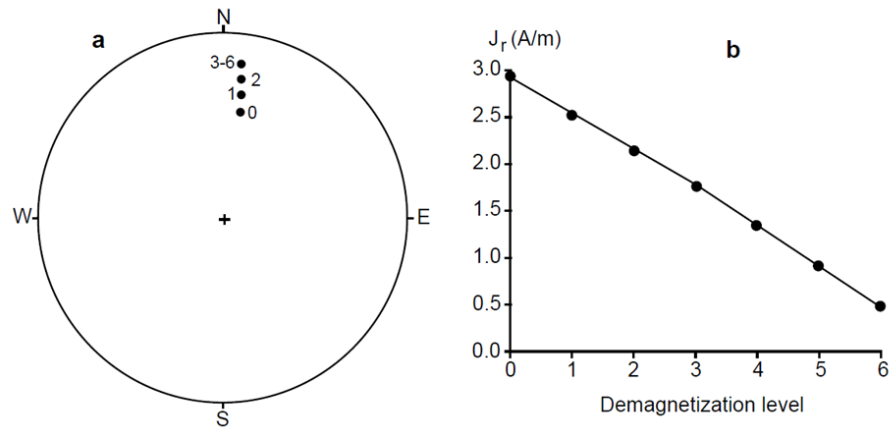


**Figure 2.21.** Equal-area stereographic projection of the same data shown in Figure 2.20, with NRM intensity diagram displaying stepwise demagnetization at levels 0 through 6 (from Butler, 1998).

Fisher (1953) derived a probability density function for vectors considered as points on a sphere, known as the Fisher distribution, which is used to statistically define the dispersion of a set of magnetization vectors around the mean direction and to perform statistical tests. The theoretical precision parameter,  $k$ , for the Fisher distribution varies from zero if all vectors in the total population are randomly distributed to infinity if they are all identical to the mean. The best estimate,  $k$ , of this precision parameter (based on the finite number of samples drawn from the total population) is simply given by:

$$k = \frac{N - 1}{N - R}$$

for  $N > 7$  and  $k > 3$ :

where  $R$  is the length of the resultant vector of the  $N$  individual magnetization

vectors. Values of  $k > 10$  indicate that the observed mean direction is close to the true mean of the total population.

The Fisherian confidence limit associated with a calculated mean direction of magnetization is usually quoted for the 0.95 probability level and is given by:

$$\alpha_{95} = \cos^{-1} \left[ 1 - \frac{N - R}{R} \left( 20^{\frac{1}{N-1}} - 1 \right) \right]$$

which, if  $k > 7$ , can be approximated by:

$$\alpha_{95} \approx \frac{140}{\sqrt{kN}}$$

There is a 95% probability that the true mean direction of the total population of magnetic vectors (from which the sampled population of magnetic vectors was drawn) will lie within this cone. A well-defined mean direction of magnetization will have a high value of  $k$  ( $>10$ ) and a small  $\alpha_{95}$  angle ( $< 15^\circ$ ).

## 2.7.5 Rock magnetic experiments

### 2.7.5.1 Isothermal remanent magnetization (IRM) analyses

Isothermal remanent magnetization (IRM) acquisition is a useful technique for identification of ferromagnetic minerals, which are responsible for carrying remanence and recording an ancient magnetic field in a rock (Butler, 1998; Morris, 2003; Tauxe, 2009). The standard procedure involves exposing a previously demagnetized specimen in the laboratory to incrementally increasing direct magnetic field pulses along its z axis, followed by measurement of the resulting IRM after each field application (Figure 2.22). IRM intensity is then plotted against applied field to produce an IRM acquisition curve for each specimen. The shape of the IRM curve is controlled by the ferromagnetic

mineralogy. For example, magnetite, titanomagnetite or maghemite show rapid IRM acquisition, followed by flattening of the curve as a result of saturation by applied fields of up to 300 mT. In contrast, the IRM curve of a sample containing hematite does not saturate until applied fields of 1.5 - 5.0 T (Morris, 2003).

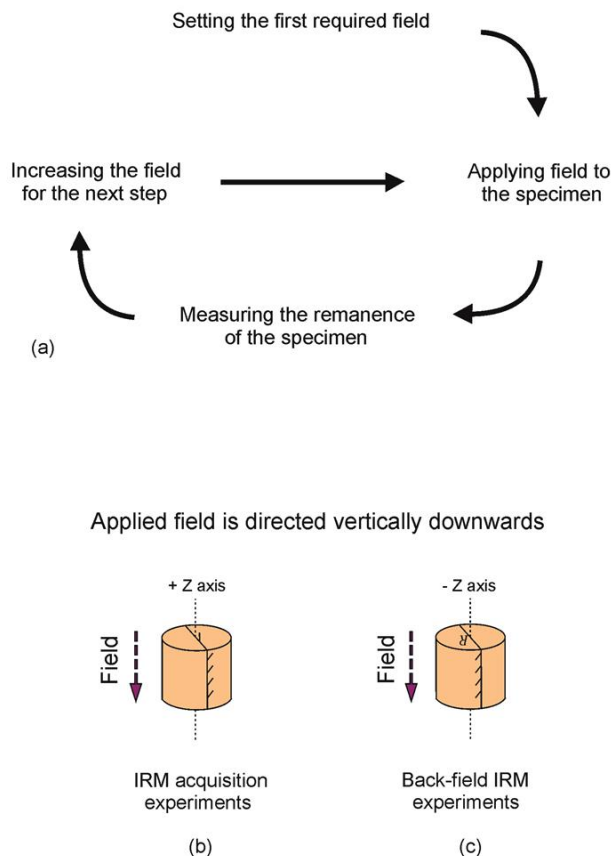


**Figure 2.22.** Schematic diagram illustrating the process of isothermal remanent magnetization acquisition. (a) Steps in the process. (b) Exposing the specimen to a magnetic field along the +z axis. (c) Exposing the specimen to a back field along the -z axis.

After applying the maximum field of 800 mT for the final step of this experiment, the procedure was then repeated using back-fields (i.e. field applied along -z axis of the specimen as shown in Figure 2.22). Application of progressively higher back-fields gradually reduces the IRM from its saturation value in the forward (+z) direction to saturation in the reverse (-z) direction. The back-field that reduces the IRM to zero is called the coercivity or remanence, which is

controlled by magnetic grain-size. Hence, determining the coercivity of remanence provides additional information that complements that obtained from the initial IRM acquisition experiment (Dunlop and Özdemir 1997).

All IRM measurements were conducted at Plymouth University using a Molspin pulse magnetizer (with a maximum peak field of 800 mT) and an AGICO JR-6 spinner magnetometer.

#### *2.7.5.2 Curie temperature determinations*

The Curie temperature is the temperature at which a magnetic substance loses its ferromagnetic properties and behaves paramagnetically. During heating, the interatomic distances will increase and the strength of interaction between magnetic moments will decrease. When a ferromagnetic material reaches its Curie temperature, the magnetic coupling between adjacent atomic moments breaks down due to thermal vibrations and the material becomes paramagnetic (Butler, 1998; Morris, 2003).

Curie temperature is directly controlled by magnetic mineralogy; therefore, the determination of this value in thermomagnetic experiments provides a useful indicator for identifying different kinds of ferromagnetic minerals. Table 2.1 shows the typical values of Curie temperature for selected magnetic minerals.

In order to determine the Curie temperature of samples in this study, the rocks were crushed to a powder suitable for use in the furnace attachment to the AGICO KLY-3S Kappabridge. This device is used to heat the powder to a maximum temperature of 700°C followed by cooling to room temperature while simultaneously measuring temperature and magnetic susceptibility. In addition, to prevent the oxidation of the sample, powders were heated in an argon

atmosphere. To determine the Curie point, we used the program Cureval 8 from Agico Inc. using the method of Petrovský and Kapička (2006).

## **2.7.6 Structural correction of palaeomagnetic data**

### *2.7.6.1 Standard tilt corrections*

In palaeomagnetic studies, standard corrections for tectonic tilting involve rotating palaeohorizontal/vertical planes of sampled units back to horizontal/vertical about a strike-parallel axis. This procedure decomposes the total deformation at a site into components of tilting around a horizontal axis and a vertical axis rotation. In simple geological terrains this approach may give interpretable results, but in complicated orogenic zones, where in general most fold axes are not horizontal, this procedure may result in extreme declination anomalies (MacDonald, 1980). In such cases, it is more appropriate to describe the total deformation at a site by a single rotation about an inclined axis, which returns both the palaeohorizontal/vertical to its original orientation and the site magnetization vector to an appropriate palaeomagnetic reference direction (Allerton and Vine, 1987; Morris *et al.*, 1998). This alternative net tectonic rotation approach has been used extensively in this study.

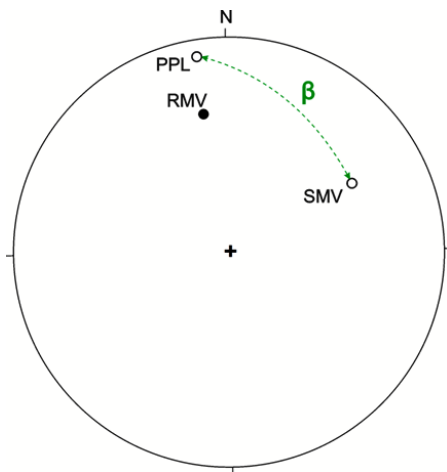
### *2.7.6.2 Net tectonic rotation (NRT) analysis method*

Net tectonic rotation analysis represents an important technique for structural correction in ophiolitic terranes, as it avoids arbitrarily dividing the total deformation at a site into components of rotation around horizontal and vertical axes. Moreover, a net tectonic rotation approach is the only way of assessing components of rotation of dykes around axes perpendicular to their margins (Allerton and Vine, 1987; Borradaile, 2001; Morris and Anderson, 2002).

The net tectonic rotation approach involves finding the single rotation (generally around an inclined axis) that simultaneously restores an observed magnetization direction back to an expected (reference) direction and a geological structure (e.g. bedding, dyke margin etc) back to its original orientation. The specific methodology employed in this thesis is that first proposed by Allerton and Vine (1987) and subsequently modified to incorporate uncertainties by Morris *et al.*, (1998). This is based on the assumption that the angle between the initial magnetization direction and the pole to the dyke/layering has not been changed. The deformation at a site in this case is interpreted in terms of a single rotation about an inclined axis; accordingly, this method provides an appropriate way to restore both the present dyke/layering pole to its initial orientation and the site magnetization vector (SMV) to the proper palaeomagnetic reference direction (Allerton and Vine 1987; Morris *et al.*, 1998). The palaeomagnetic reference direction used is usually found from an appropriate apparent polar wander path (e.g. Besse and Courtillot, 2002).

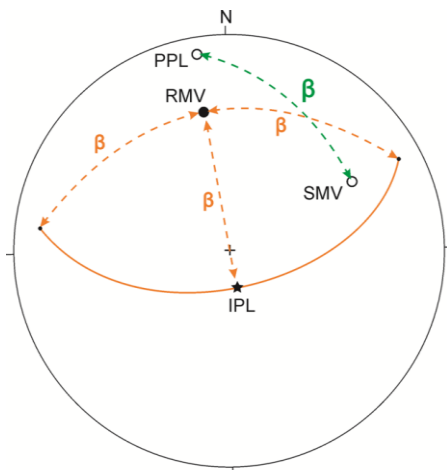
According to Allerton and Vine (1987), there are four fundamental assumptions inherent in this method:

- 1) The observed stable magnetization was acquired prior to occurrence of any structural deformation.
- 2) A reference magnetization direction can be found that represents the Earth's magnetic field direction at the time of magnetization was acquired.
- 3) Dykes/layers are restored as close to vertical/horizontal as possible.

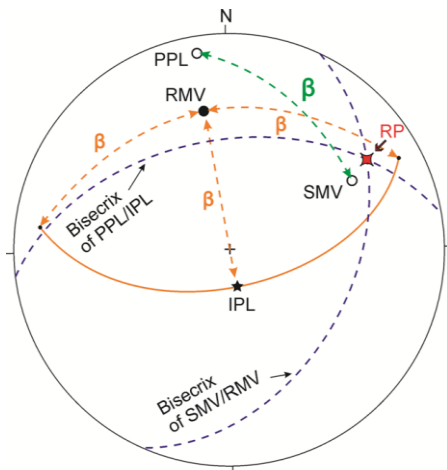


RMV: Reference Magnetization Vector (reference direction = 351/34)  
 SMV: Sample Magnetization Vector (*in situ* remanence = 062/-34)  
 PPL: Present Pole to Layering (352/-08)  
 IPL: Initial Pole to Layering  
 $\beta$ : Angle between SMV and PPL ( $69^\circ$ )  
 RP: Pole of net tectonic rotation (058/24)

Plot RMV, SMV, and PPL. Determine the angle  $\beta$ .



Construct a circle of radius  $\beta$  centred on the RMV. This gives the position of all possible initial poles to layering. The chosen initial pole (IPL) is that which is nearest to the centre of the stereonet, corresponding to the shallowest possible initial dip of the layering.



Construct the great circle bisectrix of the SMV and RMV. This gives the locus of all possible rotation poles that can restore the SMV to the RMV. Likewise, construct the great circle bisectrix of the PPL and IPL. The intersection of both great circle bisectrices gives the position of the net tectonic rotation pole (RP). The angle of rotation is then easily found using an auxiliary rotation method.

**Figure 2.23.** An example of the palaeohorizontal case of the method of Allerton and Vine (1987) using data from site MC04.

4) There is no internal deformation of the sampled rock body and thus the angle  $\beta$  between the pole to the dyke/layering and the magnetization vector remains constant throughout deformation.

Figure 2.23 illustrates the net tectonic analysis method used for the layered cumulates in this study.

The modification to this method proposed by Morris *et al.* (1998) involves performing multiple calculations of the net tectonic rotation parameters using input vectors distributed around their respective  $\alpha_{95}$  cones of confidence. An envelope surrounding the resulting distribution of rotation poles then represents the best estimate of the 95% confidence limit on possible rotation axes, and the associated rotation angles can be represented using a histogram (see Figure 5 of Morris *et al.* (1998) for an example).

## **2.8 Other methods employed**

### **2.8.1 Thin section preparation for AMS & petrographic analysis**

To determine the relationship between AMS principal axes and preferred mineral alignment (i.e. grain shape preferred orientation for the minerals within the rocks), thin sections were prepared that were cut along the plane defined by  $K_1$  and  $K_3$  axes (Figure 2.24). In addition, these thin sections also were used to examine the mineralogy of sampled lithologies, such as ultramafic cumulates, gabbros, dykes, basaltic lavas and carbonate sedimentary rock, using both optical microscopy microscope and SEM analyses. A suite of 30 polished thin sections was prepared in this way.

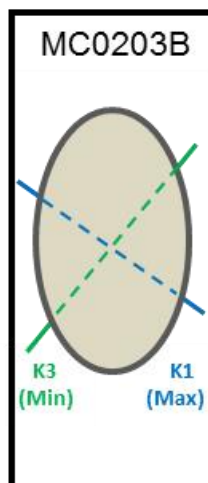


Figure 2.24. Photos illustrating the method of thin section preparation

## 2.8.2 Analytical techniques for geochemistry & X-ray fluorescence (XRF) analysis

X-Ray fluorescence analysis is a powerful analytical method used in a wide spectrum of studies, and in most situations is non-destructive. The relative ease and stability of use of X-ray spectrometers, low cost of sample preparation and the little amount of the sample required for analysis make this one of the most common methods to determine the major and trace (ppm-level) element content of rocks minerals, sediment and liquids. The XRF method depends on the interaction of X-rays with a material to determine its elemental composition. There are two main XRF methodologies: (i) by preparing pressed pellets; and (ii) by preparing fused beads, with the former generally used for determination of trace elements, and the latter used for determination of major elements.



**Figure 2.25.** Rock powder preparation using the teamer mill.

### 2.8.2.1 Sample preparation

Firstly, fresh chips of the samples were dried in the open air and then pulverized using a tungsten carbide crusher machine, T 100/G (Tema machinery Ltd / Germany). Each sample was milled to a powder for two minutes (each approximately 50 g), and between samples the device was cleaned thoroughly, starting by cleaning with alcohol and then grinding with clean glass followed by cleaning with acetone. After that, the milled samples were saved inside plastic bags, ready for analysis at the University of Southampton (Figure 2.25).



**Figure 2.26.** Pressed pellet preparation in the laboratory. (a) Aluminum cups. (B) Pressed pellets. (c) Hydraulic press machine. (d) Oven.

### *2.8.2.2 Producing pressed powder pellets for trace element measurements*

Approximately 12 g of sample powder was weighed into a small plastic mixing jar with 14 drops of PVA glue (polyvinyl alcohol 8% in water), and mixed very well for 5 minutes. The mixed powders are emptied into aluminium cups of 40 mm diameter. The filled cups were then pressed using a 250 kilo-Newton hydraulic press, type: Herzog / SIMATIC C7-621 / SIMENS. Finally, before measurement, the pressed cups were placed inside an oven at 75°C for 12 hours for drying (Figure 2.26). Pressed pellets were then loaded into the XRF spectrometer type MAGIX-PRO / Philips for measurement.

### *2.8.2.3 Producing fused beads for major element measurements*

For major element measurement, 3 g of sample powder was weighed into small glass bottles and dried at 100°C for 24 hours in an oven. To prevent absorption of the moisture after heating, glass bottles were then immediately transferred to a desiccator until the temperature of the samples dropped to room temperature (Figure 2.27a). After cooling, exactly 0.5 g of each sample powder was weighed (using a high sensitivity balance; Figure 2.27b) into platinum crucibles and mixed with exactly 5.0 g of pure Di-lithium Tetraborate flux. In order to get a good and homogeneous mixture for fusion, a small vibrator was used, type IKA VORTEX / GENIUS 3 (Figure 2.27c).

The mixture was then fused in a platinum crucible at 1100°C using a Raddic fusion machine / HD Elektronik und Elektrotechnik GmbH (Figure 2.28) This device works automatically so that after the completion of melting the device starts casting the fluid in a platinum mould with a flat base and then squirts with air to cool and solidify. The cooled beads were then labeled with a marker on

their top surface (Figure 2.29). The fused beads were then loaded into the XRF spectrometer type MAGIX-PRO / Philips for measurement.



**Figure 2.27.** Laboratory equipment used for preparing fused beads. (a) Desiccator. (b) Sensitive balance. (c) Mini vibrator.



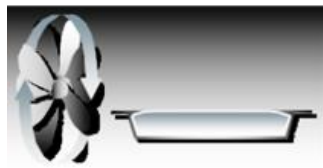
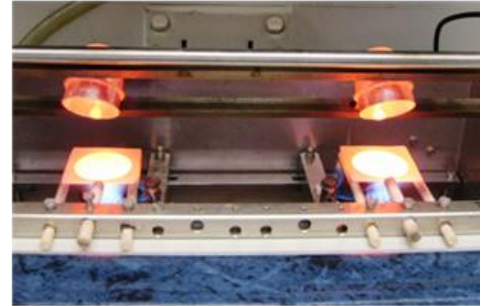
**Figure 2.28.** Fusion machine used in melting the powder mixtures for preparing fused beads.



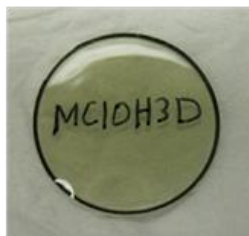
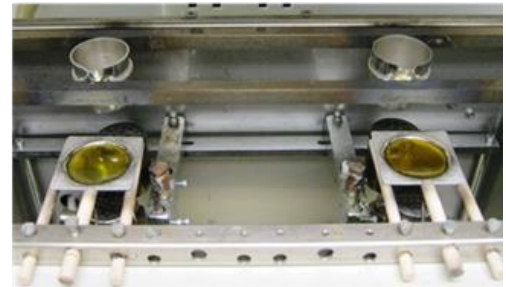
(a)



(b)



(c)



(d)

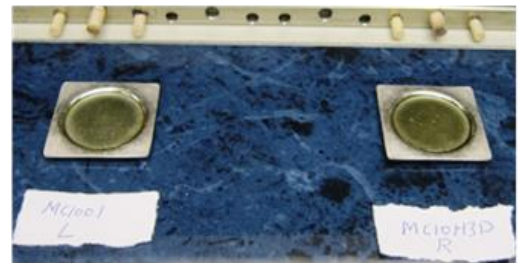


**Figure 2.29.** Fusion Steps. (a) Melting the mixture. (b) Casting. (c) Cooling. (d) Bead retrieval and labeling.

# Chapter 3

## The Mersin Ophiolite

### 3.1 Introduction

The ophiolites of Turkey represent a part of the Tethyan ophiolite belt, which is considered one of the longest ophiolite belts in the world, extending from Spain to the Himalayas (Figure 3.1). The tectonic setting of the Turkish ophiolite belt is a direct result of the closure of the Tethyan Sea. The Tethyan suture zones in the Turkish area are characterised by numerous oceanic lithologies such as ophiolite bodies, ophiolitic melanges, other oceanic magmatic rocks (i.e. seamounts) and pelagic deposits, in addition to active and passive continental margins with intensely deformed structures in some places, resulting from collisional episodes.

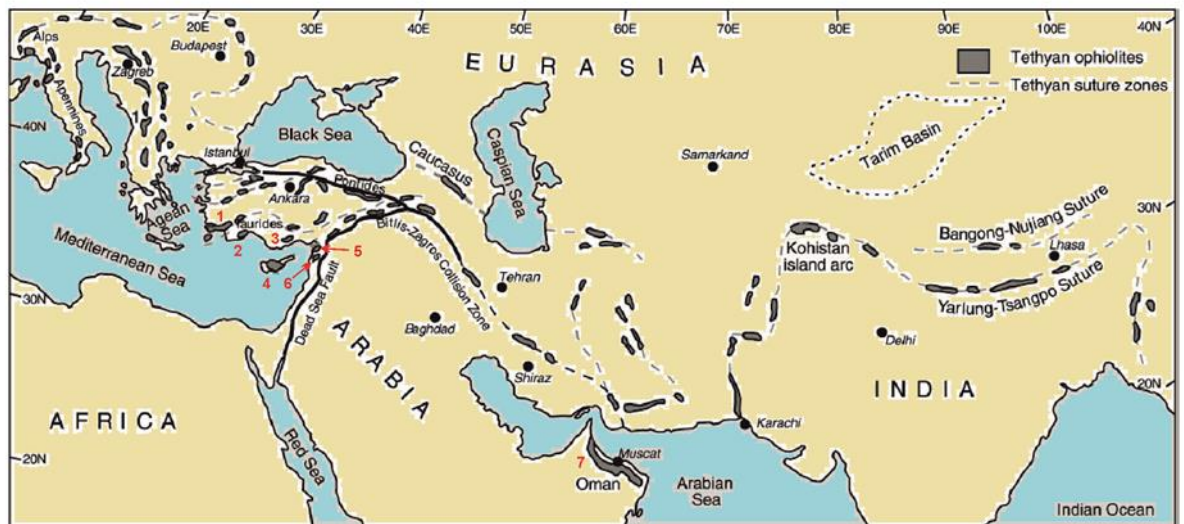


**Figure 3.1.** Simplified map showing the distribution of main Tethyan ophiolites together with suture zones within the Alpine-Himalayan orogeny system (modified from Dilek and Flower, 2003). Key numbers (from west to east): 1- Lycian ophiolite, 2- Antalya ophiolite, 3- Mersin ophiolite, 4- Troodos ophiolite, 5- Kizilirmak (Hatay) ophiolite, 6- Baer-Bassit ophiolite, 7- Semail (Oman) ophiolite.

This chapter introduces the general distribution of the Turkish ophiolites, their origin and root zones, and provides a description of the geology of the Mersin ophiolite. This review helps to explain the structural and the geological development of the studied area, providing the context for the results that have been obtained from palaeomagnetic and structural analyses.

### **3.2 Outline of Turkish terranes and sutures**

Turkey (Anatolia or Asia Minor) represents an east-west bridge that links Asia with Europe, lies within the Alpine-Himalayan mountain belt, and forms the geological boundary between Gondwana and Eurasia. During most of the Phanerozoic period, Turkey was not a single continent, but was composed of several continental fragments that were separated by oceans (Figure 3.2). They assembled to form a single landmass during the Late Cretaceous-Tertiary period through a complex series of geological events which led to the collision of Gondwana in the south with Eurasia in the north and the closure of different Tethyan oceanic basins that now mark the sutures between these continental fragments (Robertson, 1998; Bozkurt and Mittwede, 2001; Moix *et al.*, 2008; Okay and Whitney, 2010; Robertson *et al.*, 2012; Robertson *et al.*, 2013 b).

According to Yılmaz and Yılmaz (2013), the collision of these continental fragments initially started from the north and then gradually moved to the south and down towards south-eastern Anatolia, where the final amalgamation of these continental fragments into a single land mass occurred during the Tertiary period through continental collision between the Arabian and Anatolian plates (Bozkurt and Mittwede, 2001). Turkey is therefore characterized by a very complex geology and can be geologically divided into six major segments



**Figure 3.2.** A view of the Mediterranean palaeogeography showing the Northern Neotethyan, Southern Neotethyan and the main Turkish continental fragments during the Early Cretaceous (100 Ma) (after Okay, 2008).

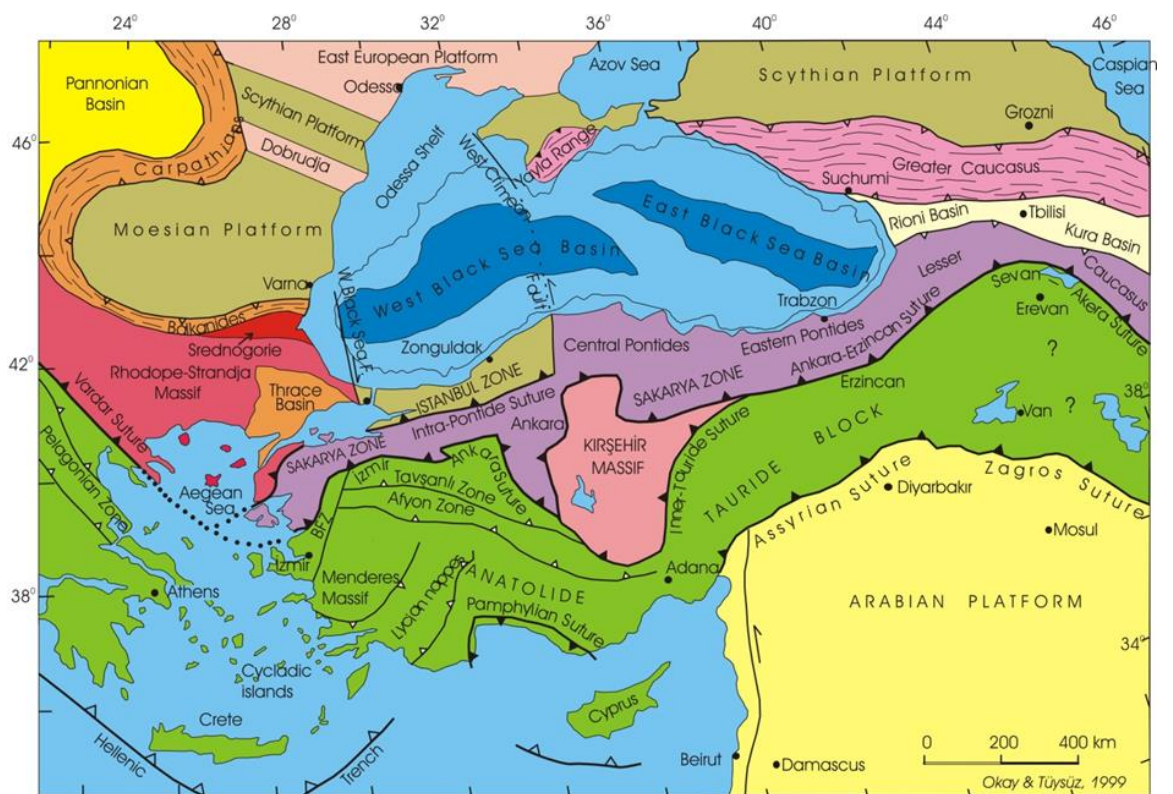


**Figure 3.3.** Tectonic map of Turkey and surrounding regions showing the main sutures and continental fragments (from Okay and Whitney, 2010).

(Şengör and Yılmaz, 1981; Okay and Tüysüz, 1999). These are: (1) The Strandja Zone, (2) The Istanbul Zone, (3) The Sakarya Zone, (4) The Central Anatolian Crystalline Complex (Kırşehir Massif), (5) The Anatolide-Tauride Block, and (6) the Arabian Platform (Figure 3.3).

The first three zones are collectively called the Pontides, which show Eurasian affinities (Okay, 2008; Bozkurt and Mittwede, 2001) and retain indications of Variscan (Carboniferous) and Cimmeride (Triassic) orogenies with little sign of the effects of the Alpine orogeny, which led to folding and faulting but without metamorphism (Okay, 2008). These Pontic zones are separated from the Kırşehir Massif and the Anatolide-Tauride Block by the c. 2000 km long east-west trending Izmir-Ankara-Erzincan suture, which is believed to be the main geological boundary between Eurasia and Gondwana in the Turkish region during the Carboniferous to Paleocene (Okay and Tüysüz, 1999). This suture zone comprises ophiolitic rocks along with accretionary mélangé rocks, and the ophiolites generally display incomplete ophiolitic sequences and are mostly peridotite massifs (Moix *et al.*, 2008). The Kırşehir Massif is a zone of metamorphic and massive granitic rocks of Cretaceous ages (Okay and Tüysüz, 1999; Whitney and Hamilton, 2004). This zone is located in central Turkey between the Pontides to the north and the Anatolide-Tauride Block. It is believed to have rifted from the Anatolide-Tauride Block and then moved to the north (Robertson *et al.*, 2013b). The Anatolide-Tauride Block represents the bulk of southern Turkey and is considered as a continental platform located between the Neotethyan Izmir-Ankara-Erzincan Ocean to the north and the southern section of the Neotethys Ocean. The Anatolide-Tauride Block in fact, consists of two platforms, the Anatolides, which includes the Bornova flysch zone (BFZ), Tavşanlı zone and Afyon zone (Figure 3.3), and the Taurides,

which represent the eastern part of the block (Bozkurt and Mittwede, 2001). However, they are treated together as a single block because there are some common elements of stratigraphy in all zones within the Anatolide-Tauride Block. These are a Pan-African crystalline basement, a discontinuous Cambrian to Devonian succession dominated by siliciclastic rocks, a Permian-Carboniferous sequence of intercalated limestones, shales and quartzites, and a thick Late Triassic to Late Cretaceous carbonate sequence (Okay and Whitney, 2010). The Anatolide-Tauride zone shows Gondwanan affinities, and in contrast to the Pontides was extremely deformed and partially metamorphosed during the Alpine Orogeny because it was in a footwall position during continental collision events in the Late Cretaceous-Palaeocene (Okay and Tüysüz, 1999; Okay, 2008; Okay and Whitney, 2010). During obduction and subduction episodes in the Senonian (the early part of the Late Cretaceous), thrust sheets and large bodies of ophiolite and accretionary complexes were emplaced from north to the south over the Anatolide-Tauride Block. Therefore the northern margin of this block has experienced high pressure-low temperature (HP/LT) metamorphism at depths of more than 70 km (Okay and Tüysüz, 1999; Okay and Whitney, 2010; Robertson *et al.*, 2013a). The Arabian platform is located to the south east of Anatolia and represents the northern Gondwanan passive margin. Throughout the period from the Mesozoic to the Tertiary, the Arabian platform was separated from the Anatolide-Tauride Block by the southern branch of the Neotethys ocean (Şengör and Yılmaz, 1981) (Figure 3.3). The Arabian platform consists mainly of rocks deposited during the Palaeozoic to Mesozoic on a craton assembled during the Pan-African orogeny (Bozkurt and Mittwede, 2001).

### 3.3 The distribution of Turkish ophiolites

Ophiolitic rocks in Turkey are classified according to their genesis and characteristics into three belts or groups (Juteau, 1980; Billor and Gibb, 2002) (Figure 3.4). These are: (1) the Northern ophiolite belt, which comprises a series of E-W trending ophiolite bodies in northern Turkey, such as Orhaneli (Bursa) Ophiolite and Izmir- Ankara- Erzincan zone ophiolites; (2) the Tauride belt. This includes numerous ophiolitic thrust sheets emplaced onto

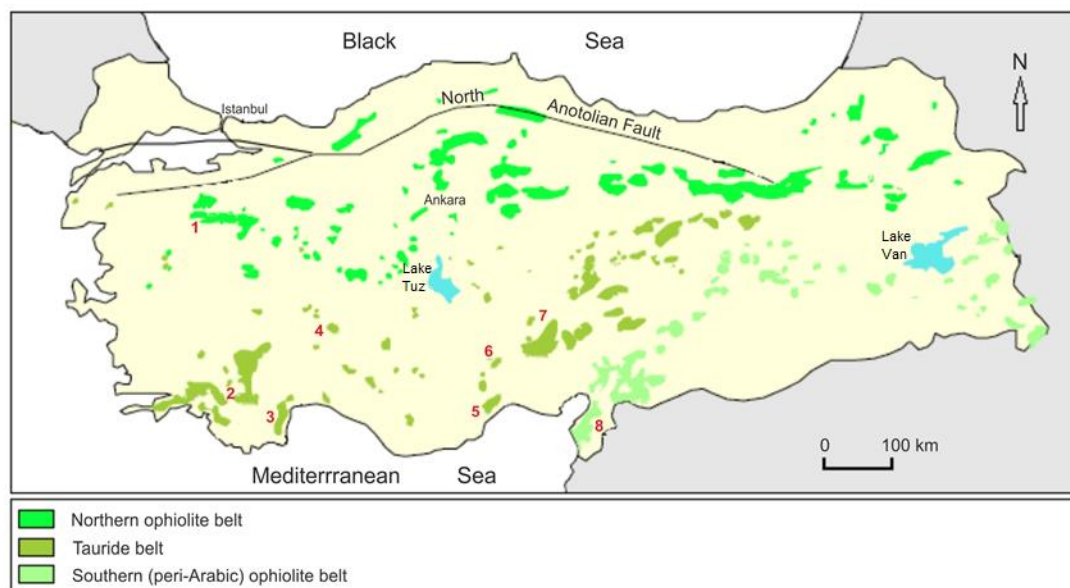


**Figure 3.4.** Distribution of ophiolite complexes in Turkey (modified from Billor and Gibb 2002). Key numbers (from west to east): 1- Orhaneli (Bursa) Ophiolite, 2- Lycian ophiolitic nappe, 3- Antalya ophiolite complex, 4- Beyşehir ophiolite nappe, 5- Mersin ophiolite, 6- Alihoca ophiolite, 7- Posanti- Karsanti ophiolite, 8- Hatay ophiolite.

the Tauride carbonate platforms during the Late Cretaceous, such as Posanti-Karsanti ophiolite, Mersin ophiolite, Alihoca ophiolite, Beyşehir ophiolite and Lycian ophiolite (Robertson, 2002); (3) the Southern (peri- Arabic) ophiolite belt. This includes the largest eastern Mediterranean ophiolites and extends for over 1000 km long, from the Semail ophiolite of Oman in the east to the Troodos ophiolite in the west, including the Hatay ophiolite in Turkey and Baër-Bassit

ophiolite in Syria (Robertson, 2002) (Figure 3.1). The north Anatolian and Tauride ophiolites (except the Antalya ophiolite which is believed to be formed from the Southern Neotethyan basin emplaced as a result of a strike-slip faulting) are interpreted to have formed from the northern section of the Mesozoic Neotethys, whilst the Peri-Arabic belt ophiolites were derived from the southern section of the Neotethyan ocean basin (Robertson and Dixon, 1984; Dilek and Moores, 1990).

### **3.4 Overview of the genesis and root zones of ophiolites in the Turkish area**

In constructing a tectonic model for the Turkish area, a number of questions have been raised about the number and location of the root zones in the region. For example, Ricou *et al.* (1984) and Stampfli *et al.* (1991) proposed derivation of all Turkish and eastern Mediterranean ophiolites, including the Troodos and Hatay/Baër-Bassit units, from a single basin in North Anatolia. In contrast, Şengör *et al.* (1984) and Robertson and Dixon (1984) suggested that the ophiolites were derived from separate oceanic basins through variable tectonic processes. The Ricou *et al.* (1984) interpretation contradicts reconstructions that suggest the existence of at least a separate southern strand of the Neotethys (e.g. Robertson and Woodcock, 1980) and those that propose the existence of multiple micro-continental slivers and basins within a complex palaeogeography (Şengör and Yilmaz 1981). Ricou *et al.*'s (1984) model is based on the similarity between marginal sedimentary units that exist in the ophiolite bodies which led them to interpret all of the allochthonous ophiolite bodies as being derived from a single root zone in North Anatolia. This model shows the progressive northwards subduction of the passive northern margin of Gondwana (Tauride-Anatolide Platform) under the Pontides (Eurasia) from the

middle Cretaceous onwards, followed by southward ophiolite nappe emplacement on the top of the Tauride-Anatolide Platform in stages starting from the Late Cretaceous to the Miocene (Figure 3.5).

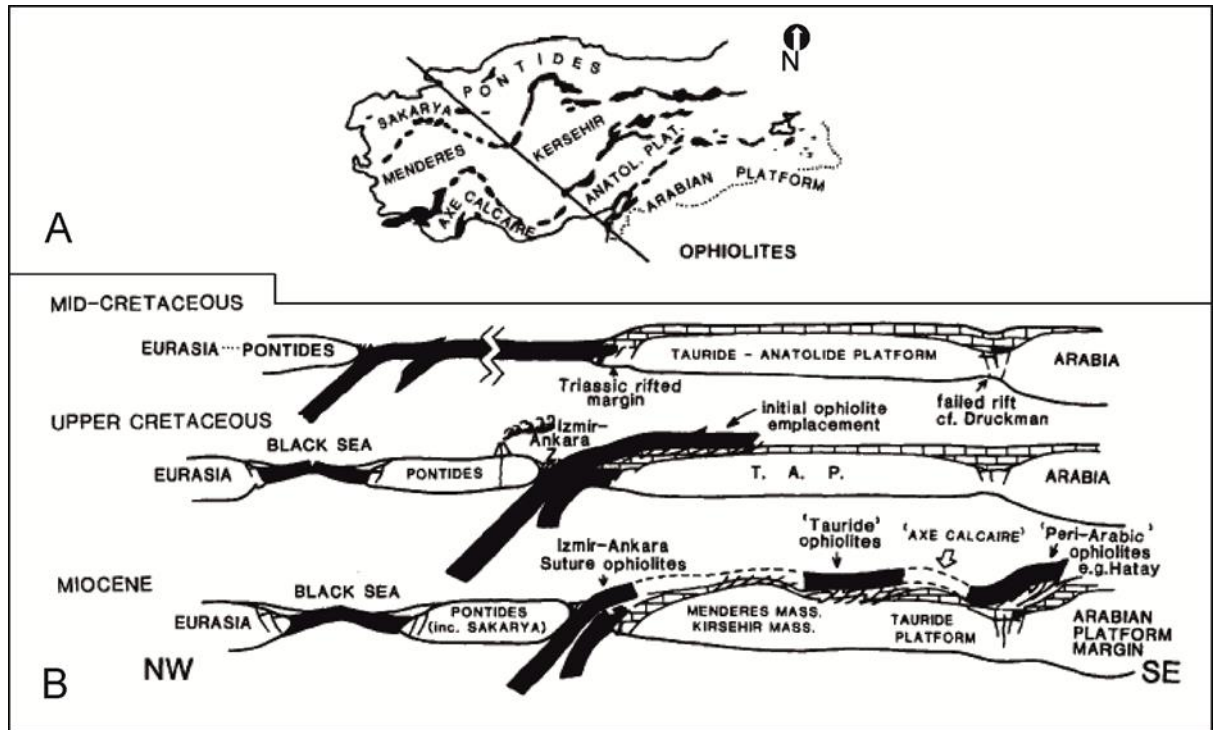


**Figure 3.5.** Ophiolite single root-zone interpretation for Turkey. (a) The major ophiolite belts. (b) Schematic cross-section illustrating the main characteristics of the single-northern-root-zone model and the major ophiolite nappe emplacement (from Robertson and Dixon, 1984).

The alternative tectonic model of Şengör *et al.* (1984) suggests formation of the ophiolites in multiple small basins and prefers southward subduction of the Palaeotethyan oceanic crust with opening of the Neotethys in the south (Figure 3.6a), whereas, Robertson and Dixon (1984) revised this model to incorporate a northward-dipping subduction zone.

On the other hand, Stampfli *et al.* (1991) proposed a model involving derivation of all the eastern Mediterranean ophiolites from a single root zone (northerly suture) adjacent to Eurasia, similar to the Ricou *et al.* (1984) model (Figure 3.6b).

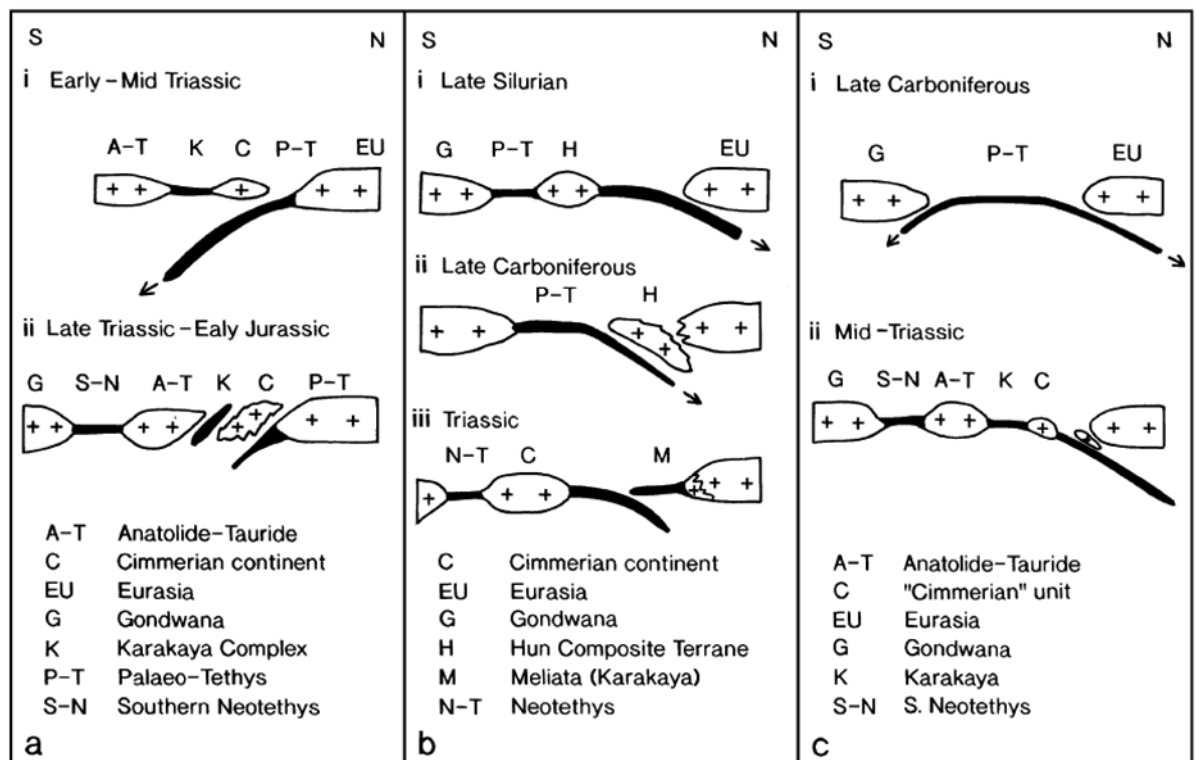


**Figure 3.6.** Alternative tectonic models for the genesis of Turkish ophiolitic suture zones during Late Palaeozoic to Early Mesozoic time (from Robertson, 2004). (a) Model of southward subduction (Şengör *et al.*, 1984). (b) Model of northward subduction (Stampfli *et al.*, 1991). (c) Model of a variable subduction polarity (Robertson *et al.*, 1999).

Robertson (2002) and Robertson *et al.* (2013b) suggest that some of the Cretaceous ophiolites from the eastern region of Turkey (e.g. Hatay, Kocali, Guleman, Ispendere and Kömürhan), including Troodos and Baer-Basit, were derived from a separate southern Neotethyan basin (Figure 3.7). This basin opened in the Triassic-Jurassic and started to close during the Late Cretaceous, but remained partly open until the Middle Miocene (Robertson *et al.*, 2013b).

The derivation of the ophiolites of southeastern Turkey from a separate basin is more compatible with different lines of geological evidence that cannot be easily reconciled with models involving formation of ophiolites in a single northerly Tethys and subsequently thrust for hundreds of kilometers over the Tauride-Anatolide platform to their present positions. For example, the sedimentary units in the central Tauride platforms (e.g. Isparta Angle region) show unbroken

successions from late Mesozoic to Early Tertiary time, and show no trace of ophiolite emplacement (Şengör and Yılmaz, 1981). Additionally, the ophiolites and related marginal sections within the Isparta Angle region through the SW margin of the Bey Dağları platform show westward emplacement and therefore, cannot be correlated with the large-scale Lycian nappes which show southward emplacement (Robertson, 2004).

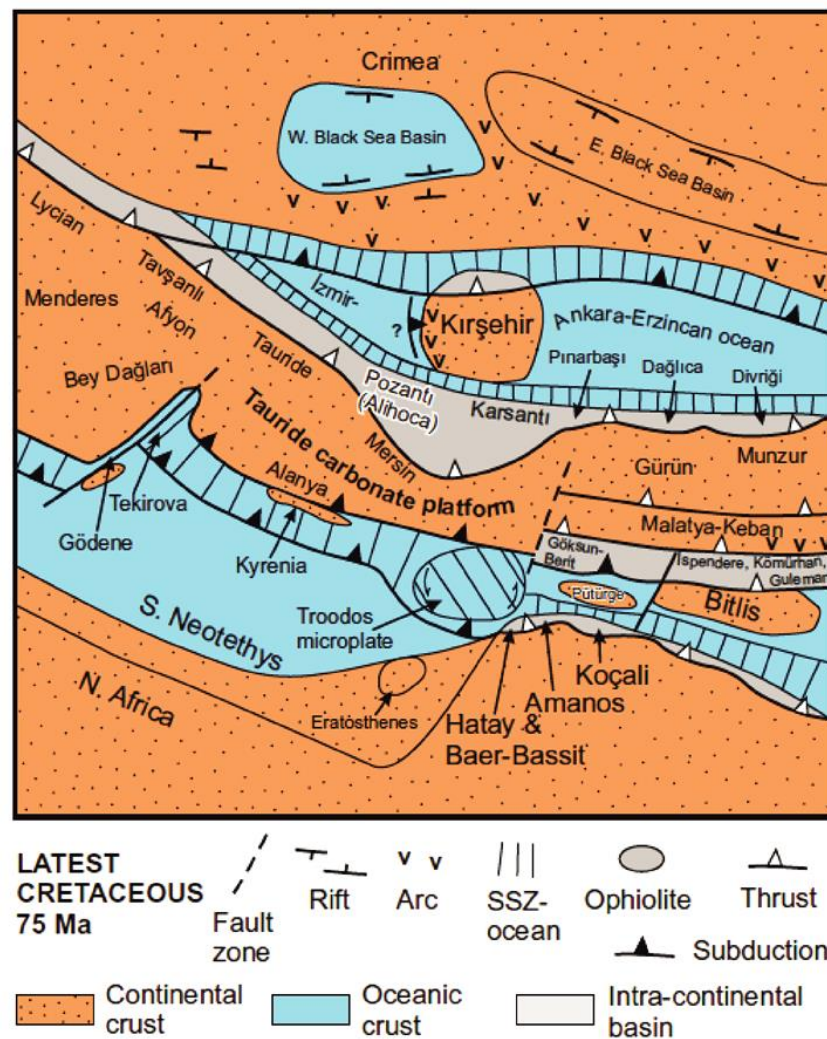


**Figure 3.7.** Palaeogeographic sketch map showing the genesis of the Latest Cretaceous ophiolites in the eastern Mediterranean region, where some of ophiolites were derived from the İzmir-Ankara-Erzincan ocean (equivalent to the Northern Neotethyan basin), whereas some others generated in separate basin of the southern branch of the Neotethys. Note that all the ophiolites are southward obduction of supra-subduction zone type (after Robertson *et al.*, 2013b).

In general, there is growing acceptance of a diverse Mesozoic Tethyan palaeogeography of microcontinents isolated by oceanic strands that increases the probability that ophiolites were generated from numerous oceanic basins by different tectonic processes (Robertson, 2004).

### 3.5 Geological setting of the Mersin ophiolite

#### 3.5.1 General description

The Mersin ophiolite complex of the southern Turkey is bounded by the sinistral Ecemiş fault to the east, the Bolkardağ metamorphic rocks to the north, and is covered by Miocene carbonates to the west and the south (Figure 3.8). It outcrops over a 60 km long, 25 km wide area and represents an approximately 6 km thick oceanic crustal sequence (Parlak *et al.*, 1995).

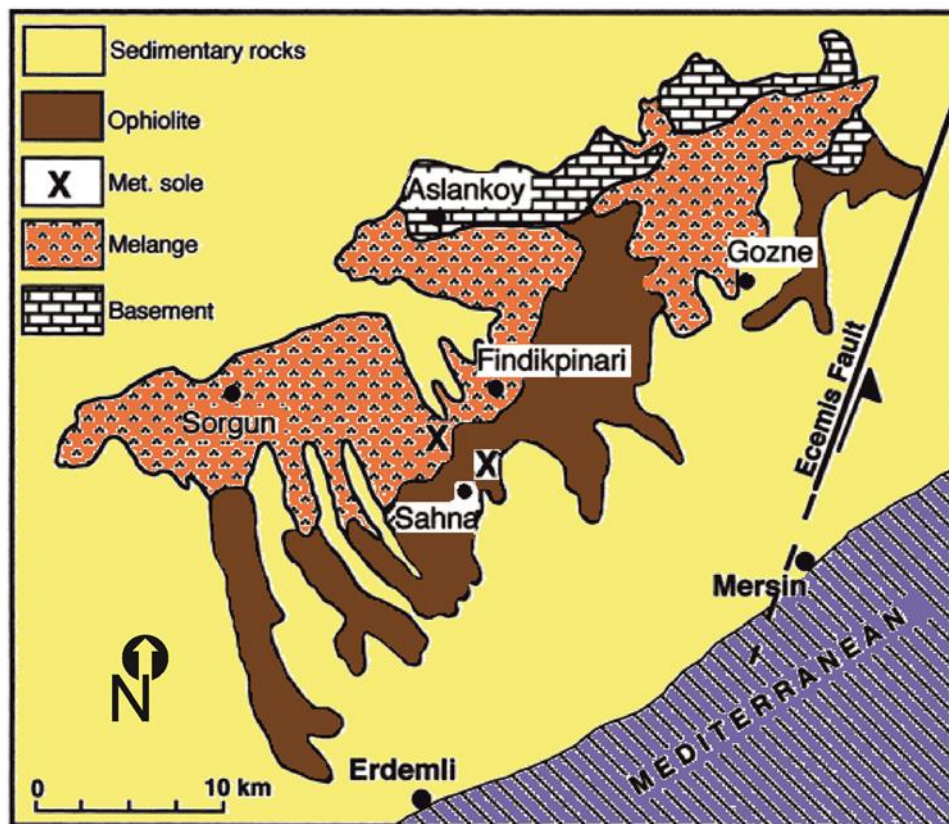


**Figure 3.8.** Simplified geological map of the Mersin ophiolite (modified from Parlak and Delaloye, 1999).

The Mersin ophiolite complex includes three distinct nappe sheets. From bottom to top, these are: the Mersin ophiolitic mélange, the metamorphic sole rocks and the Mersin ophiolite (Figure 3.9) (Juteau, 1980; Parlak and Delaloye, 1999 and Parlak *et al.*, 1995, 1996a).

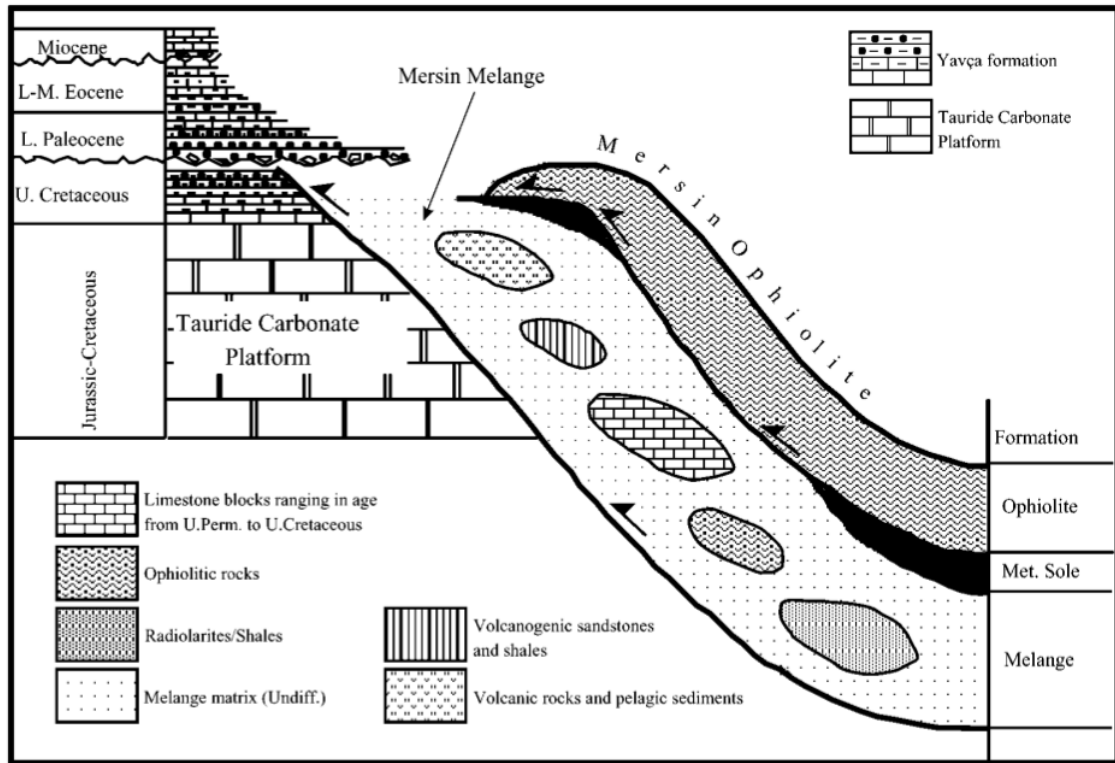


**Figure 3.9.** Tectonostratigraphic setting of the Mersin ophiolite (from Parlak and Robertson, 2004)

### 3.5.2 Origin and development

The Mersin ophiolite represents one of the best exposures in the central Taurides of Turkey, potentially providing insights into the formation and emplacement characteristics of Tethyan-type ophiolites during intra-oceanic subduction. Following the formation of the Cretaceous ophiolites inside the northern Neotethyan ocean basin, they were emplaced over the Tauride/Bolkardag Mesozoic carbonates in the Campanian-Maastrichtian period (Robertson, 2002). However, there are various points of view regarding the

intra-oceanic subduction/obduction processes responsible for the creation of the Tauride Belt ophiolites and their metamorphic sole rocks (Çelik, 2008). Lytwyn and Casey, (1995); Dilek *et al.* (1999) proposed that the development of the Tauride Belt ophiolites happened along a mid-ocean ridge in the Neotethyan ocean, while others (e.g., Pearce *et al.*, 1984; Parlak *et al.*, 1996c, 2000, 2002, and 2006; Robertson, 2002; Bağcı *et al.*, 2006; Çelik *et al.*, 2006; Robertson *et al.*, 2013b) suggested that the development of the ophiolites took place in a supra-subduction zone setting.

Parlak *et al.* (1995) proposed that during Albian-Cenomanian time, intraoceanic subduction along the southern section of the Neotethyan Ocean was started, leading to formation of the Mersin ophiolite in a supra-subduction environment. By the Late Cretaceous the obduction of the oceanic crust onto the Tauride belt had occurred, whereas through the Late Paleocene period the ophiolites were unconformably covered by detritus, derived from the underlying ophiolites.

### **3.5.3 Description of main units and lithologies in the Mersin study area**

#### *3.5.3.1 Ophiolitic units*

The limited extrusive rocks of the Mersin ophiolite are seen within the Fındıklı valley area near the village Zeybekler, located down-slope to the south of the dyke localities discussed later. These extrusive basalt rocks are exposed in two localities and are represented by pillow lavas and dolerites with columnar jointing (Figures 3.10 and 3.11), and are thought to be Late Cretaceous in age. Both cover a limited area on the side of the road leading to the village of Zeybekler. The pillows show clearly overturned structures with radii of nearly 50 cm (Figure 3.11). In the field, some secondary minerals within

these pillows have been observed, such as pyrite and few crystals of calcite that fills the vesicles of the pillow basalts.



**Figure 3.10.** Field photograph showing the locations of columnar basalt together with the pillow lava along Fındıkpinarı valley section.

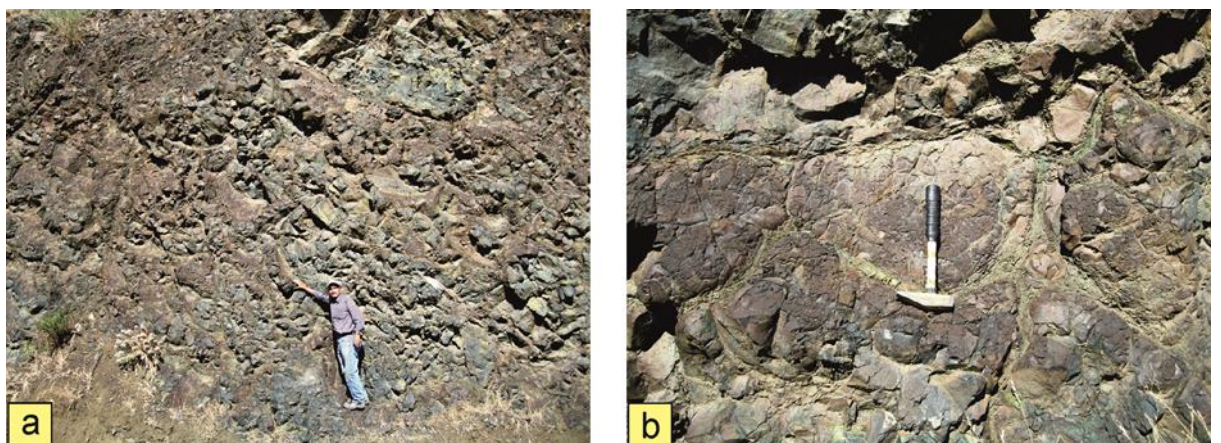


**Figure 3.11.** (a) Field photographs of pillow lava at Fındıkpinarı; (b) field photograph illustrating the overturned pillow lava at Fındıkpinarı.

The majority of the ophiolite is exposed further to the west along the Sorgun valley, one of several deep valleys cutting through the Miocene sedimentary cover of the Adana Basin, in the area between the villages of Sorgun and Arsalanlı. Here mantle rocks and overlying ultramafic and mafic cumulates occupy an area of approximately 15 km<sup>2</sup>, with a total thickness over 3 km (Parlak, 1996). This unit starts with over 800 m of ultramafic rocks at the bottom and continues into nearly 2500 m of gabbroic rocks (Parlak *et al.*, 1996b). The ultramafic rocks of the Mersin ophiolite are composed mainly of clinopyroxenite, wehrlite and dunite (Parlak *et al.*, 1996c). Igneous lamination and in some places grain-size grading has been seen in the ultramafic cumulates in the form of successive accumulation of large crystals (Figure 3.12b). In the field, the rocks generally show greenish colour when they are fresh, but in some places, the colour is yellowish brown due to alteration (Figure 3.12c).

The mafic cumulates consist essentially of gabbro, leucogabbro, olivine gabbro and anorthosite (Parlak *et al.*, 1996c). The age of these rocks is  $82.8 \pm 4.0$  Ma based on crystallization age of the cumulate gabbros of the Mersin ophiolite (Parlak *et al.*, 2013). The orientation of the cumulate layering in the gabbros along the Sorgun Valley was observed to vary, with dip directions mainly to the south but with some sections dipping to the north. In all cases the layering is moderately to steeply dipping. Careful examination of the section identified a number of way-up criteria, including scouring at the base of layers and mineralogical grading within layers (see Figure 3.13). These prove that the north-dipping sections are overturned relative to the south-dipping sections.



**Figure 3.12.** Field photographs of (a) Ultramafic rocks along main Sorgun valley section, (b) brownish colour due to alteration with lamination within the ultramafic layers and (c) grain-size grading in ultramafic cumulates.

In places, the cumulate layers are cross-cut by thin (<1cm) fine-grained basaltic veins. Samples were collected from these veins to attempt to use geochemistry to relate them to the cumulate host. For example, have these formed by compaction of a crystal mush and upwards migration of melt? In this case, the geochemical compositions of the veins and inter-cumulus phases should be similar. Figure 3.14 shows an example of these cross-cutting veins.

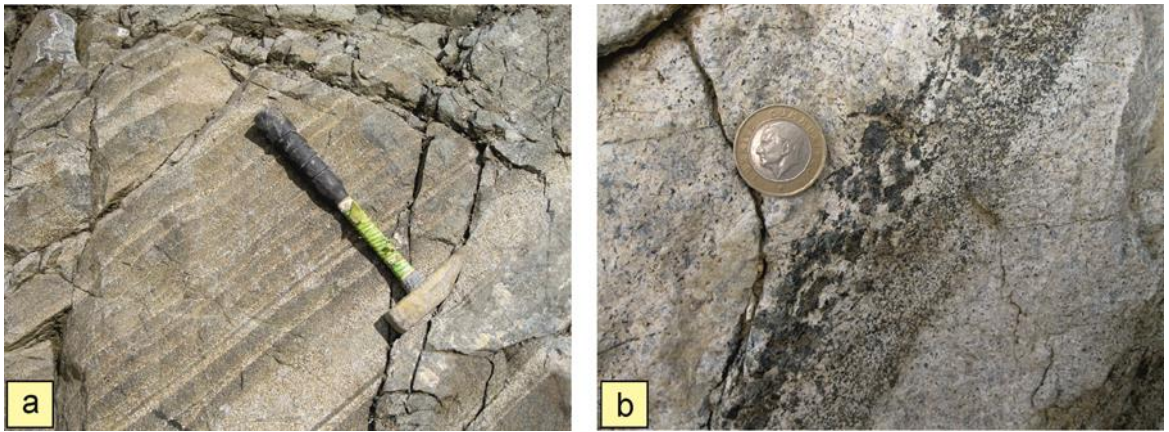


**Figure 3.13.** (a) Rhythmic layering in cumulate gabbros along the Sorgun Valley, indicating overturned layering; (b) grain-size grading in cumulates along the Sorgun Valley, again indicating overturning of the section.



**Figure 3.14.** Cumulate layering along the main Sorgun Valley section, cross-cut by thin basaltic veins (visible as dark grey patches to the left of the image).

The second major section of the Mersin ophiolite occurs in the Fındıklıpınarı valley area (Figure 3.15), which lies nearly 20 km NE from the mafic and ultramafic cumulates section (Sorgun valley). This provides a large section of the mantle sequence of the ophiolite, consisting predominantly of tectonized harzburgites and dunites. This section also exposes the metamorphic sole of the ophiolite and two generations of dykes that cut the mantle sequence and sole rocks (that were targeted for palaeomagnetic sampling).



**Figure 3.15.** Google image showing the localities of the exposed dykes at the Fındıklıpınarı valley area.

### 3.5.3.2 Subophiolitic metamorphic rocks

The well-developed metamorphic sole rocks of the Mersin ophiolite complex are located beneath the ophiolite unit and have a thickness of about 50-70 m (Parlak *et al.*, 1995), and up to 100 m at the base of the mantle tectonites (Çelik, 2008). The sole rocks are intensively deformed (with fold and imbricate structures), and are exposed together with intact dolerite dykes in the Fındıklıpınarı area (Figure 3.16). They are also exposed at other localities within

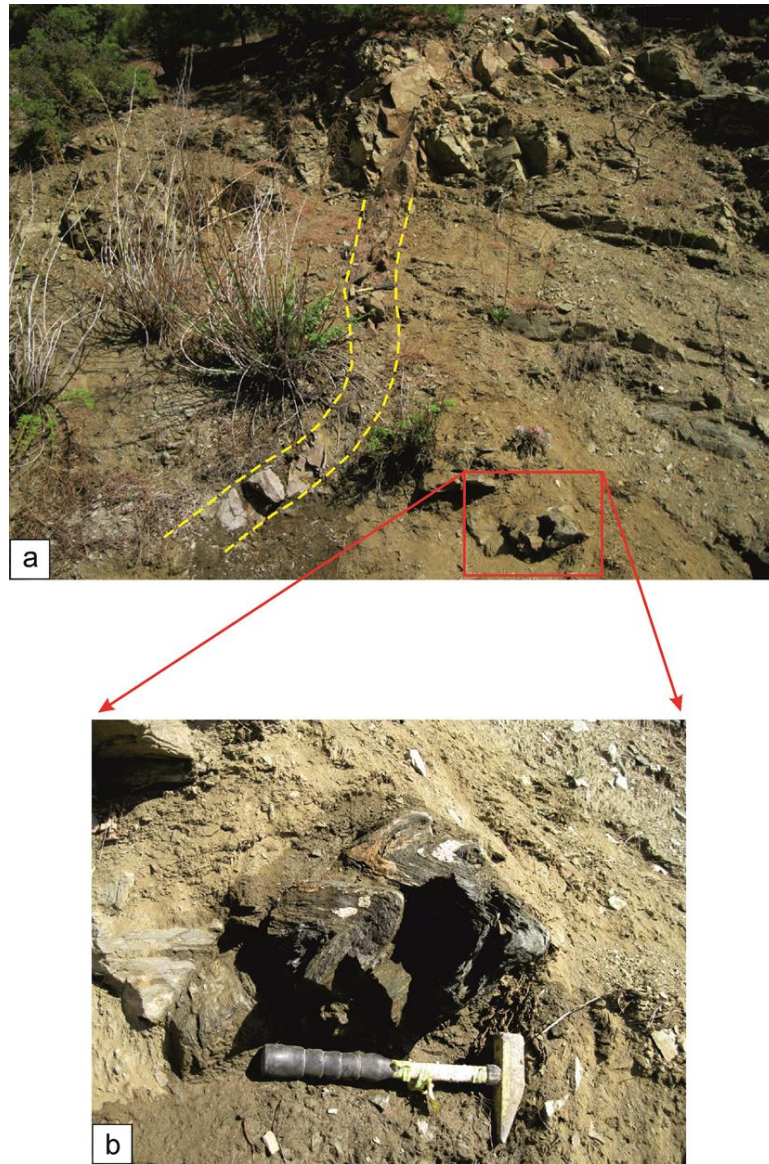


**Figure 3.16.** Field photographs of (a) Metamorphic sole rocks intruded by thin dolerite dyke at Fındıkpınarı and (b) Metamorphic sole rocks with deformation structures at Fındıkpınarı.

the Fındıkpınarı area, such as along the Şahna valley and along the road between Gözne and Aslanköy (Parlak *et al.*, 1996a; Çelik, 2008).

Field observations and published studies (e.g. Parlak *et al.*, 1995; Moix *et al.*, 2007) suggest that these metamorphic sole rocks were folded and thrust-imbricated prior to being intruded by microgabbroic-doleritic dykes. The metamorphic sole rocks are predominantly made of amphibolites, amphibolitic schists, epidote-amphibolite schists, mica schists, calcschists, marble and quartzite (Paralak *et al.*, 1995, 1996a; Çelik, 2008). K-Ar and  $^{40}\text{Ar} / ^{39}\text{Ar}$  dates of

the metamorphic sole yield ages ranging from ~ 91 Ma to 93 Ma (Parlak *et al.*, 1995; Parlak *et al.*, 1996a; Parlak and Delaloye, 1999; Çelik, 2008), which are interpreted to date the initial detachment of Mersin ophiolite during closure of the Neotethys in the eastern Mediterranean (Parlak *et al.*, 1995).

#### 3.5.3.3 Dykes cutting the mantle sequence and the metamorphic sole

In the eastern part of the Fındıklı valley area, thick dykes (each up to 5m thick or more) are hosted by tectonized harzburgite (mantle), whereas in the western part of the study area dykes are hosted by the metamorphic sole and are characteristically thinner (less than 1 m) (Figure 3.17). However, in both sub-areas the doleritic and micro-gabbroic dykes have a common NE-SW trend.

Dykes cutting the mantle sequence are believed to have been generated during seafloor spreading (Parlak, 1996) and are inferred to be older than those cutting the metamorphic sole. There are different estimates of the age of the dolerite dykes that cut the metamorphic sole rocks, ranging from  $84.4 \pm 3$  Ma (Çelik, 2008) based on K-Ar method to  $63.8 \pm 0.9$  to  $89.6 \pm 0.7$  Ma (Parlak and Delaloye, 1996), to  $91.0 \pm 0.6$  Ma (Dilek *et al.*, 1999) based on the  $^{40}\text{Ar} / ^{39}\text{Ar}$  method, with differences probably reflecting the different dating methods (with the  $^{40}\text{Ar} / ^{39}\text{Ar}$  ages considered to be the most reliable). They exhibit the geochemical signatures of island arc tholeiites (Parlak and Delaloye, 1996; Çelik, 2007, 2008), suggesting a subduction influence during the generation of the mafic dykes. They do not show any structural folding or metamorphism, so this indicates that the injection of the dykes occurred in an oceanic setting before the final obduction of the ophiolite but after the structural deformation of the metamorphic sole rocks (Parlak and Delaloye, 1999; Dilek *et al.*, 1999; Çelik and Delaloye, 2003). In general, the dykes exhibit subophitic and microgranular

textures, and are composed essentially of plagioclase, clinopyroxene and amphibole (see Chapter Four). Some of the dykes underwent considerable hydrothermal alteration, whereas others are fresher. Predominantly, the dolerite dykes show weak chilled margins suggesting that at the time of dyke intrusion the main ophiolite body was still hot. This suggestion is supported by the limited time interval between the formation of the ophiolite (based on K-Ar ages from the underlying metamorphic sole) and inception of dyke emplacement (Parlak, 1996).

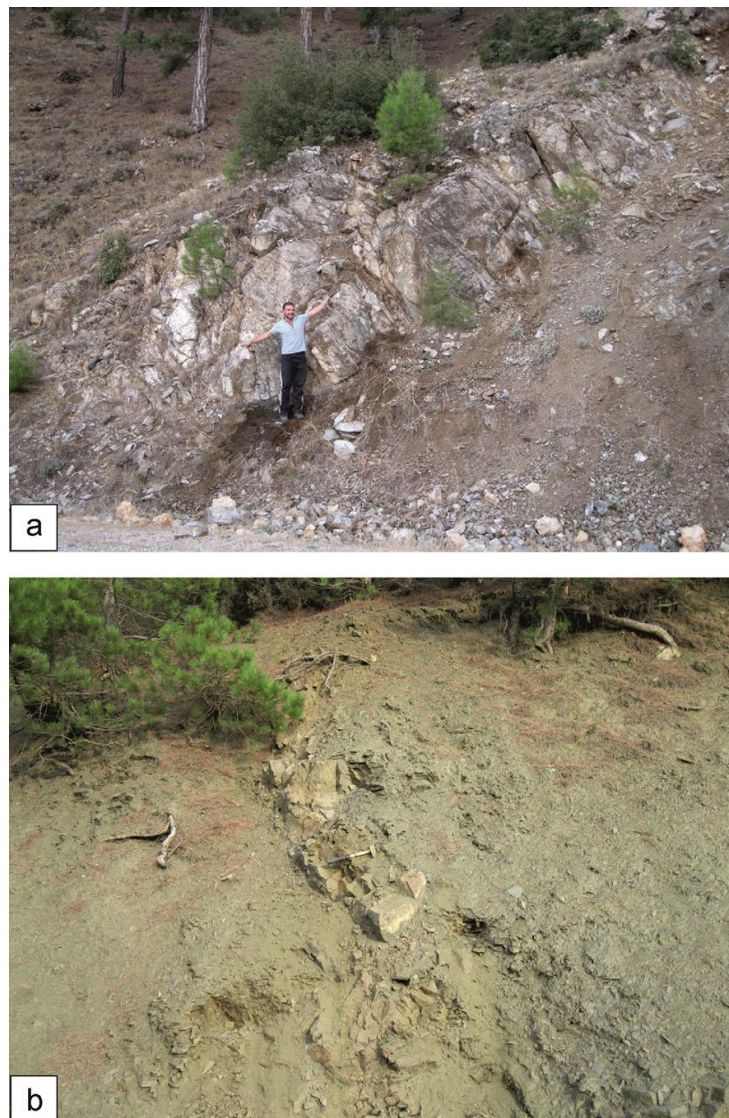


**Figure 3.17.** Field photographs of (a) Massive doleritic dyke cross-cutting harzburgite at Findipinari and (b) Thin dolerite dyke intruding the metamorphic sole at Findikpinari.

#### 3.5.3.4 Mersin mélange

The Mersin mélange underlies the Mersin ophiolitic unit and its metamorphic sole. It is located to the south of the Mesozoic carbonate platform of the southern flank of the Bolkardağ and is exposed over an area about 40 km long by 15 km wide (Parlak and Robertson, 2004). The boundary between the metamorphic sole and melange, which is dipping to SE, is well seen at the Fındıklı section, together with the Miocene sedimentary cover on the road NW of the dyke localities (Figure 3.18). According to Parlak and Robertson (2004), the mélange consists of four distinctive lithological assemblages. These are: (1) shallow-water carbonate assemblage mostly of Late Palaeozoic-Early Cretaceous age; (2) rift-associated volcanogenic-terrigenous-pelagic assemblage; (3) basalt-radiolarite-pelagic limestone assemblage of Late Jurassic-Early Cretaceous age with pelagic carbonates of Late Cretaceous age; (4) ophiolite-originated assemblage, which includes parts of the Upper Cretaceous Mersin ophiolite and pieces from the metamorphic sole. K-Ar analyses on granites from the ophiolitic mélange yielded an age of  $375.7 \pm 10.5$  Ma (Late Devonian) (Parlak and Robertson, 2004).

#### 3.5.4 Ophiolite emplacement

The Mersin ophiolite of southern Turkey represents just one of the Late Cretaceous ophiolites exposed along the northern margin of Tauride-Anatolide carbonate platform, which also includes the Lycian, Beyşehir and Posantı-Karsantı ophiolites. These have similar chemical characteristics and kinematic histories (Robertson, 2004), and have all generally experienced south-directed emplacement onto the Tauride platform (Dilek *et al.*, 1999; Robertson *et al.*, 2013b). Although the consensus is that these ophiolites were emplaced in the

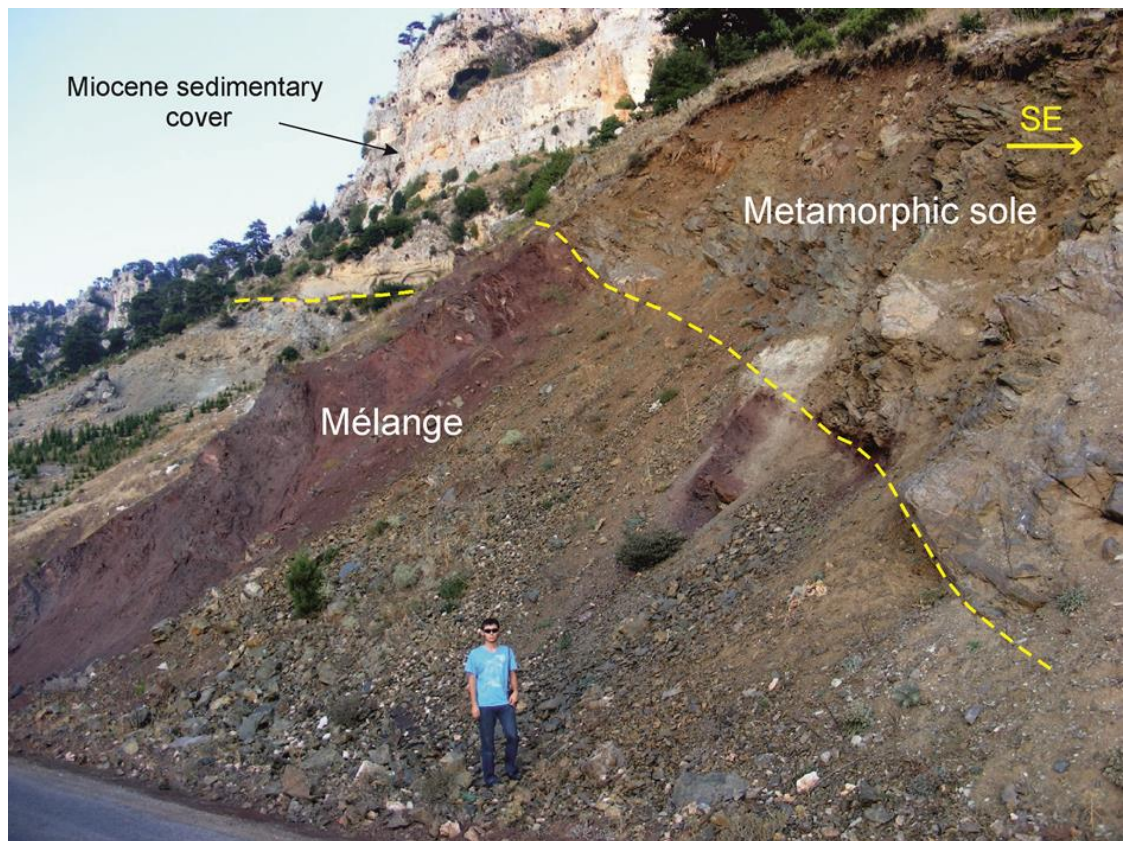


**Figure 3.18.** Field photograph showing the boundary between metamorphic sole and the mélange at Fındıklı together with the Miocene sedimentary cover on the top.

Late Cretaceous (e.g. Parlak and Robertson, 2004), new biostratigraphic evidence from the Mersin mélangé reported by Koç *et al.* (2013) suggests that emplacement was post-Danian. This led Koç *et al.* (2013) to propose two hypotheses for the final emplacement of the ophiolite: (1) the emplacement happened during latest Palaeocene time, directly after formation of the mélangé, or (2) it happened in Late Eocene time prior the deposition of the Miocene sedimentary cover.

The emplacement direction of the ophiolite remains controversial, in part because of a lack of sufficient field structural data reported in the literature. Parlak *et al.* (1996a) reported that the Mersin ophiolite was emplaced to the NW from a southerly Neotethyan basin and obducted over the passive platform margin of the central Taurides, based on fold vergence in the metamorphic sole.

Parlak and Robertson (2004) then revised this interpretation using field data from some of the same localities. Stretching lineations in the amphibolites of the metamorphic sole were reported to plunge moderately to the east on average (Figure 3.19), but have substantial scatter with trends ranging from NNE to ESE. Data from folds within the amphibolites were reported graphically as poles to axial planes (Figure 3.19), suggesting axial planes dipping moderately to the NE or E, but were inferred to have mainly northward vergence. This apparent discrepancy is difficult to resolve without further structural analyses. Overall, however, Parlak and Robertson (2004) favour an E-W or W-E sense of emplacement in current geographic coordinates (based on the lineation data), but they note that structures in the sole may have experienced later intraoceanic or emplacement related tectonic rotation.

### **3.5.5 Post-emplacement tectonic structures**

The central Taurus mountains have been subjected to several geological events during post-Eocene time, and these events can be assigned to four compressional episodes (Akay and Uysal, 1988):

- 1) Late Eocene – Early Oligocene compressional period. During this period the first major movements of the Ecemiş and Beyşehir faults occurred as a result of N - S compression.
- 2) Langhian compressional period. In this period, the Lycian nappes were emplaced from NW to SE over the Beydağları, and this tectonic event weakly affected the Antalya and Adana basins.

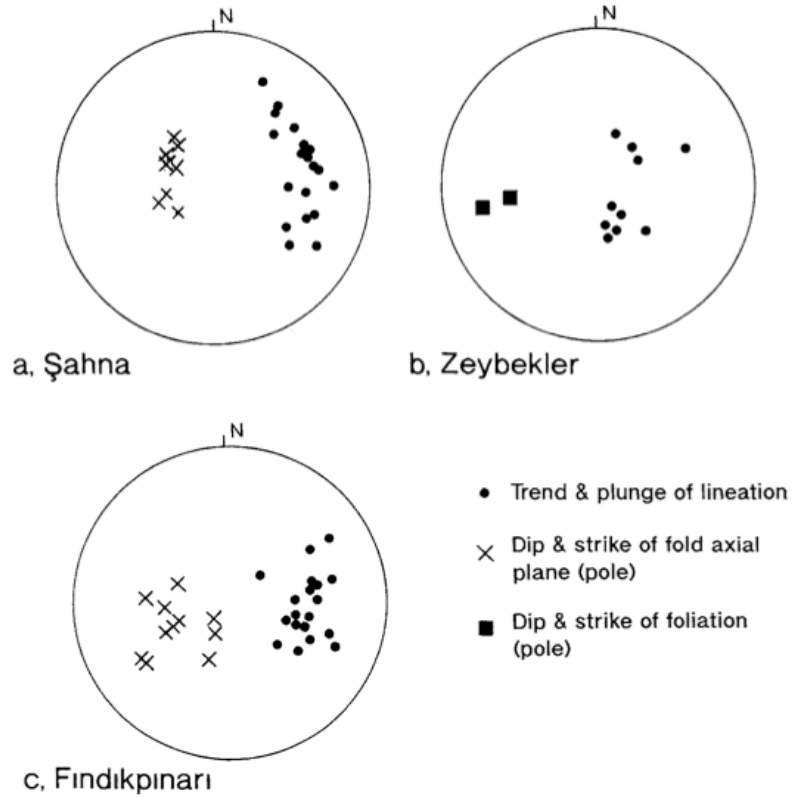


**Figure 3.19.** Stereographic projections (equal area, lower hemisphere) of structural data from early ductile fabrics in the metamorphic sole of the Mersin Ophiolite (from Parlak and Robertson, 2004). (a) Data from amphibolites exposed in the stream below Şahna village; (b) road section, 2 km N of Zeybekler village (between Fındıkpınarı and Şahna); (c) road section between Fındıkpınarı and Tepekoy villages (5 km N of Fındıkpınarı).

3) Late Tortonian compressional period. During this period, the entire area was subject to severe compression forming several significant structural features such as the Aksu thrust, Kirkkavak oblique-slip reverse fault, Koprucay syncline, Beskonak anticline, etc. (Akay and Uysal, 1988). These structural features were covered by Antalya basin deposits of the post-compressional stage through the Messinian-Pliocene period.

4) Late Pliocene to recent compressional period. This period is characterized by development of some mesoscopic faults in the central Taurus region as a whole.

The Ecemiş fault zone of the central Taurides follows a nearly 90 km long, NNE-trending valley, and is bounded to the east by the Posantı-Karsantı

ophiolite, the Alihoca ophiolite to the west and the Mersin ophiolite to the SW (Figure 3.20). The Ecemiş fault is a sinistral strike-slip fault system with total displacement about 60 km (Jaffey and Robertson, 2001).

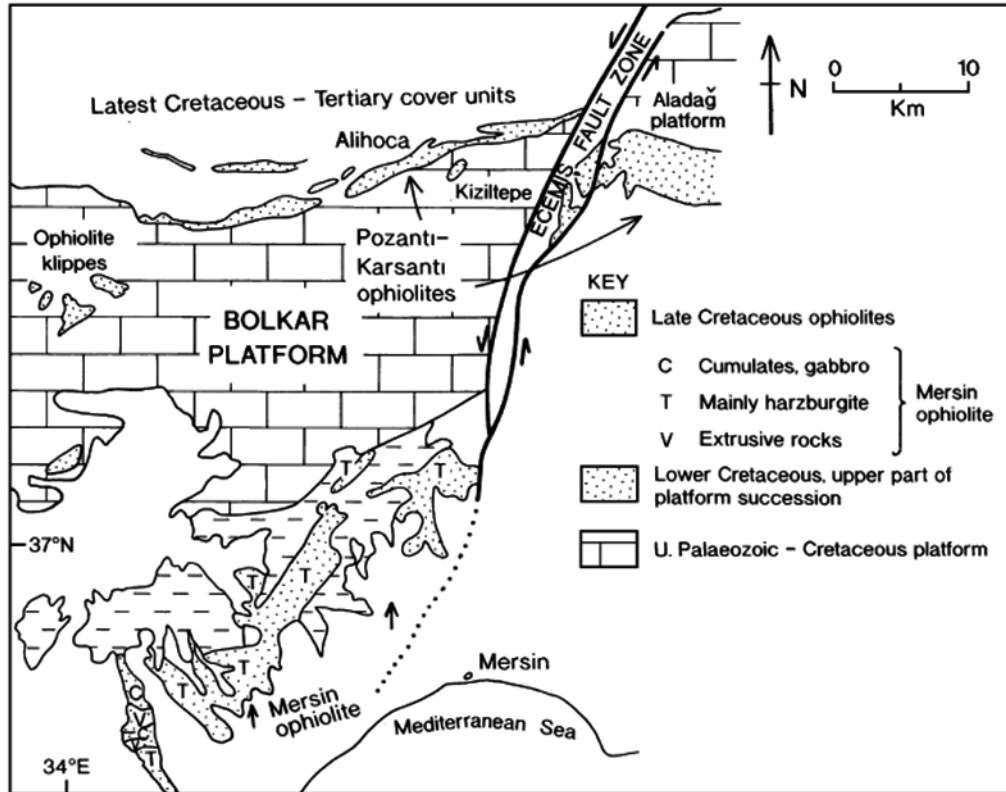


**Figure 3.20.** Simplified geological map of the southern Turkey showing the locations of Cretaceous Tauride ophiolites and the Ecemiş fault (from Robertson, 2002).

There are various arguments about the timing of initiation of the Ecemiş fault ranging from Mid-Miocene or slightly earlier (Jaffey and Robertson, 2001), based on subsidence analysis, to the pre-Lutetian (i.e. during the Early Eocene) (Yetiş, 1984), based on the difference in the stratigraphy of the age of the pre-Eocene from both sides of the Ecemiş fault zone compared with younger sediments and the obvious demise of displacement in the deposits of Middle Eocene and younger ages within the same area. Jaffey and Robertson (2001) indicate that the major strike-slip displacement of the Ecemiş fault zone occurred during pre-Pliocene time and was followed by east-west extension

with minor displacement during the Pliocene and Quaternary. In terms of the effectiveness of the Ecemiş fault zone at the present time, Westaway (2002) argues that the Ecemiş fault zone is currently inactive, whereas Akay and Uysal (1988) found that the Ecemiş fault zone is still active based on field evidence for an active fault within the fault zone lying in the fault trend direction for 10 km.

### **3.6 Previous palaeomagnetic research on eastern Mediterranean Tethyan ophiolites**

The main focus of this thesis is the first palaeomagnetic analysis of the Mersin ophiolite, representing also the first such analysis of any of the ophiolites formed in the northern strand of the Neotethys Ocean. In order to place the new results into the regional context of tectonic rotations in the evolving Neotethyan system, however, it is necessary to provide an overview of previous palaeomagnetic studies that have been conducted on ophiolites of the southern Neotethyan Ocean. The key overarching result of these studies (see below) is that these ophiolites have all rotated anticlockwise during their tectonic evolution.

#### **3.6.1 Troodos ophiolite**

The Troodos ophiolite complex on the island of Cyprus is the most extensively studied ophiolite in the world (e.g., Gass, 1968; Moores and Vine, 1971; Allerton and Vine, 1987, 1991; Morris *et al.*, 1990; Robertson and Xenophontos, 1993; MacLeod and Murton, 1995; Morris *et al.*, 1998; Robertson, 2000). The ophiolite represents a fragment of oceanic lithosphere which formed in a supra-subduction zone (SSZ) environment (Robertson, 2000) within the Southern Neotethyan basin (Robertson and Dixon, 1984; Robertson, 1998, 2002) during the Late Cretaceous (Cenomanian–Turonian) around 90-92 Ma, based on U -

Pb isotopic dating of plagiogranites (Mukasa and Ludden 1987). The ophiolite includes an entire Penrose (Anonymous, 1972) pseudostratigraphy appearing in the form of a dome structure formed as a result of Late Pliocene-Recent uplift, which led to a broadly concentric outcrop pattern, with upper mantle and lower crustal units exposed around the central topographic high (Figure 3.21). The ophiolite has not experienced major thrusting and uplift has preserved original seafloor relationships and structures.

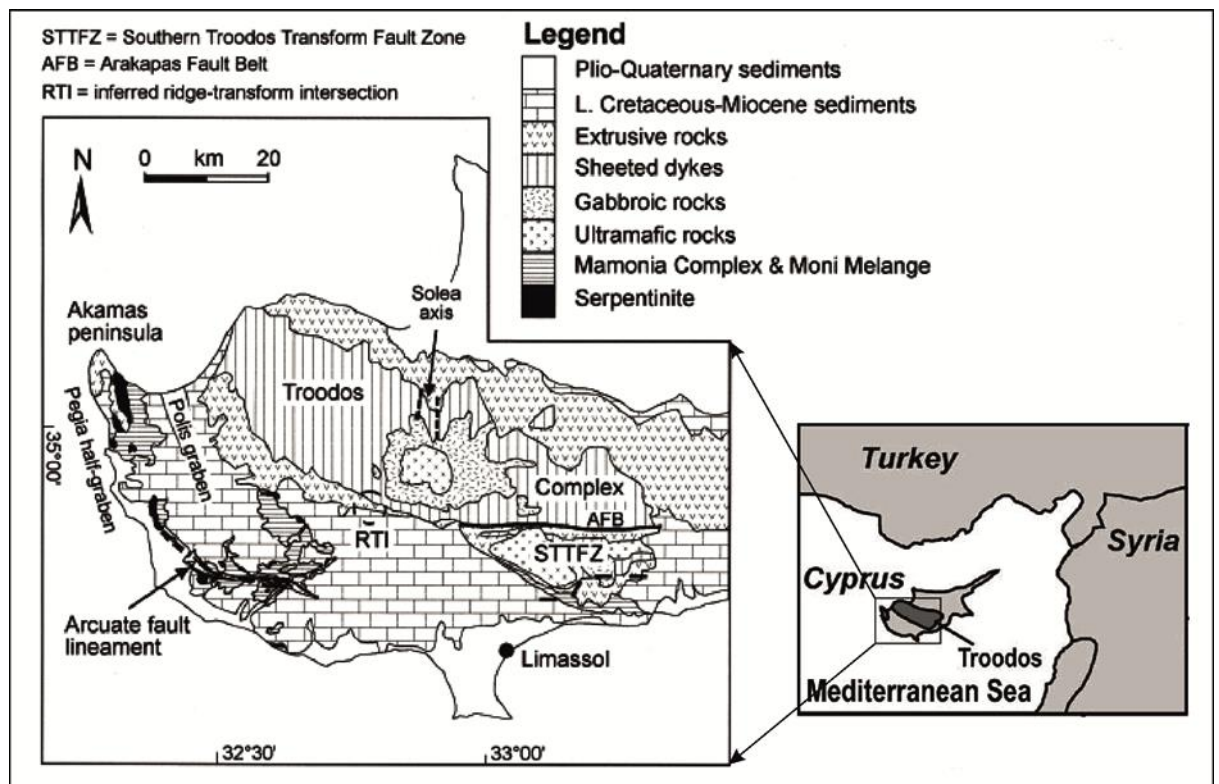


**Figure 3.21.** Outline geological map of Cyprus showing the Troodos ophiolite and Arakapas Fault Belt (combined from Morris *et al.*, 1998 and Morris, 2003).

The plutonic section comprises gabbros and layered cumulates that are cut by gabbroic intrusions, providing evidence for the existence of multiple small magma chambers under the Troodos spreading axis (Robinson and Malpas, 1990). The upper massive gabbros are locally covered by small plagiogranite masses which in some places penetrate into the sheeted dyke complex (Gillis,

2002). The sheeted dyke complex crops out in an area over 80 km wide and generally has nearly N-S striking dykes (current coordinates) (Robertson and Xenophontos, 1993). In places these dykes are rotated to low angles and intruded by later dykes (Dietrich and Spencer, 1993). The sheeted dyke complex passes up into a superbly exposed sequence of extrusive igneous rocks (pillow lavas and sheet flows), containing massive sulphide bodies formed by hydrothermal alteration at the spreading axis. The southern margin of the ophiolite is characterized by the E-W trending Arakapas Fault Belt, that represents the northern boundary of a zone formed within a fossil oceanic transform fault (Moores and Vine, 1971; Simonian and Gass, 1978; Allerton and Vine, 1991; MacLeod and Murton, 1995). The ophiolite is covered by a continuous sequence of Late Cretaceous-Recent sedimentary rocks (Robertson and Xenophontos, 1993).

Palaeomagnetic research on the Troodos ophiolite began with the pioneering work of Vine and Moores (1969), who demonstrated that the remanent magnetization of lavas in the extrusive series is directed to the present-day west, providing evidence for large-scale anticlockwise rotation of the so-called "Troodos microplate". Since then, numerous palaeomagnetic studies have been conducted (see Morris, 1996, for a review), aimed either at establishing the timing of this microplate rotation or seafloor deformational processes during crustal formation. The most accepted model for microplate rotation mechanism is that of Clube and Robertson (1986), who suggested that rotation occurred as a result of combination of continental margin-trench collision and anticlockwise torque produced by northward subduction beneath Troodos. The timing of this rotation has been constrained by palaeomagnetic studies on the sedimentary cover through Late Cretaceous to Recent (Clube, 1985; Clube and Robertson,

1986; Morris et al., 1990). Clube (1985) observed that there are indistinguishable westward-directed remanence directions within hydrothermal sediments (umbers) and underlying extrusives of the ophiolite, indicating that the rotation of the ophiolite complex started after the deposition of the earliest sedimentary rocks. Morris et al. (1990) established that 30° of rotation was complete by the time of deposition of radiolarites overlying the umbers. Remanence directions within the chinks of the overlying Lefkara Formation and shallow water facies of the Pakhna Formation (Clube *et al.* 1985; Clube and Robertson, 1986; Morris *et al.*, 1990) indicated that the rotation of the microplate was completed by the end of the Early Eocene. Overall, these studies clearly show that the Troodos Complex has experienced a prolonged rotation through the period from Campanian to Eocene (Figure 3.22), at a rate of approximately 2°/Ma (Morris et al., 2006).

Within the Troodos microplate, localised tectonic rotations have been documented that result from seafloor spreading processes (e.g. Allerton and Vine, 1987; Morris *et al.*, 1990). The most significant studies have concerned a controversy over the sense of displacement along the fossil Southern Troodos transform zone (STTFZ), preserved in the Arakapas and Limassol Forest areas. Here, the Troodos sheeted dyke complex shows a progressive change in dyke trend as the northern boundary of the transform zone is approached. These changes were believed to have occurred either due to dyke injection into a sigmoidal stress field, which means these dykes are in their initial orientations relative to a sinistrally slipping transform or as a result of vertical axis clockwise rotations of fault blocks caused by dextral slip (Figure 3.23).

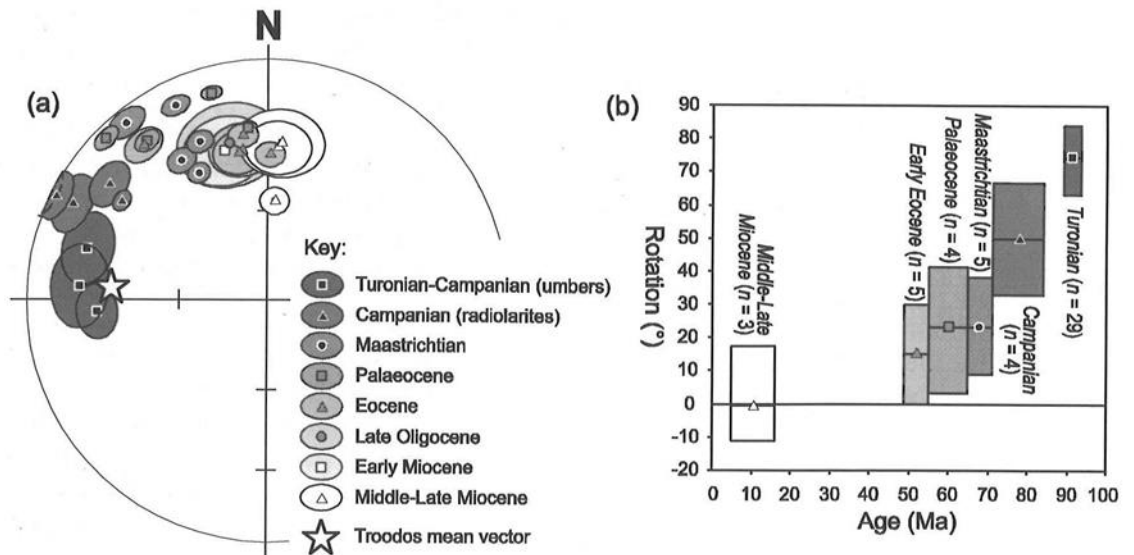


**Figure 3.22.** Palaeomagnetic results from the sedimentary cover of the Troodos ophiolite showing the progressive anticlockwise rotation of the underlying ophiolite during the Late Cretaceous and Palaeogene. (a) Lower hemisphere stereographic projection of tilt-corrected site-level palaeomagnetic data obtained from the *in situ* sedimentary cover of the Troodos ophiolite, showing the timing of rotation of the Troodos ophiolite. (b) Variation of rotation angle through time (from Morris *et al.*, 2006).

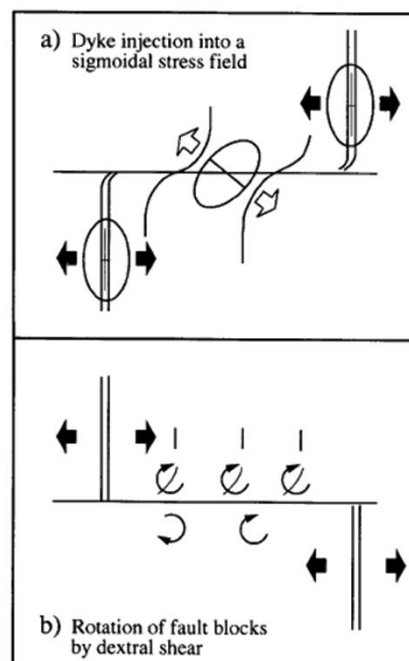


**Figure 3.23.** Possible alternative mechanisms to account for the deviation in dyke trend near the Southern Troodos Transform Fault (from Morris *et al.*, 1990).

Several attempts were made to resolve this controversy, but the first attempt was conducted by Clube, (1985), Clube and Robertson, (1986). Their studies focused on the samples from pillow lava and interlava sediments along the Arakapas fault. In contrast to the westerly Troodos directed remanences, the majority of these sites showed NW directed magnetizations, and these findings were considered as support for the block rotation model. After that, Bonhommet *et al.* (1988) provided additional evidence for clockwise rotation of dykes within the sheeted dyke complex itself. Further support for clockwise localised rotations due to dextral shear along the transform zone was provided by Allerton and Vine (1990), MacLeod *et al.* (1990) and Morris *et al.* (1990). Importantly, these authors were able to apply the net tectonic rotation technique of Allerton and Vine (1987) to sets of cross-cutting units to prove that rotations associated with the transform occurred during magmatic activity, rather than relating to later reactivation of the fault zone.

### **3.6.2 Kizildağ (Hatay) ophiolite**

The NE–SW trending Kizildağ (Hatay) ophiolite is one of the best preserved remnants of the Late Cretaceous SSZ oceanic lithosphere of the southern Neotethys. It is located in the southern Amanos mountains of south-east Turkey (Figure 3.24) and represents a part of the same Peri-Arabian ophiolite belt that includes the Troodos ophiolite (to the west) and the Baër-Bassit ophiolite (to the south). The Kizildağ (Hatay) ophiolite is 25 km wide, 45 km long, up to 7 km thick and covers an area of approximately 950 km<sup>2</sup> (Tekeli and Erendil, 1986). It represents a thrust sheet emplaced tectonically onto the Arabian carbonate platform in the Maastrichtian (Dilek *et al.*, 1999; Yılmaz, 1993). The ophiolite is structurally split into two distinct massifs by high angle NW-striking Tahtaköprü

Fault (Figure 3.24) (Tekeli and Erendil, 1986; Dilek *et al.*, 1999; Dilek and Thy, 1998, 2009). The ophiolite is structurally split into two distinct massifs by the high angle NW-striking Tahtaköprü Fault. The main southwestern massif to the south of the Tahtaköprü Fault is separated from the underlying Arabian platform by a limited *mélange* zone without a metamorphic sole (Robertson, 2002). In general the ophiolite displays a nearly complete Penrose assemblage comprising, from bottom to top, serpentinitised peridotite, ultramafic to mafic cumulates, isotropic and layered gabbros, a sheeted dyke complex that consists of diabase dykes, and extrusive rocks of pillowed and massive basalt lava flows (Delaloye and Wagner, 1984; Tekeli and Erendil, 1986; Dilek *et al.*, 1991; Bağcı *et al.*, 2005, 2008). The gabbroic rocks in this part are separated from the underlain peridotites by a shear zone of 50-100 m thick (Dilek and Thy, 1998). The second massif of the ophiolite is located northeast of the Tahtaköprü Fault and includes faulted blocks of extrusive rocks, gabbros and sheeted dykes. This part of ophiolite does not show consistent internal structure, and the plutonic rocks in this part directly overlie the serpentinitised peridotite (Dilek and Thy, 2009).

The oldest sedimentary rocks covering the volcanic rocks of the ophiolite are clastic rocks of the upper Maastrichtian age and include conglomerate and sandstone which pass upwards into carbonate rocks (Boulton *et al.*, 2006; Dilek and Thy, 2009; Inwood *et al.*, 2009a).

A palaeomagnetic investigation conducted on the Kizildağ ophiolite and its sedimentary cover by Inwood *et al.* (2009) has shown that this ophiolite also rotated in an anticlockwise sense subsequent to its formation by sea floor spreading, and the largest component of this rotation (c. 62°) happened in an

intra-oceanic setting and/or during emplacement. Site mean remanence directions and results of net tectonic analyses from Hatay ophiolite are given in Figure 3.25, 3.26 and 3.27.

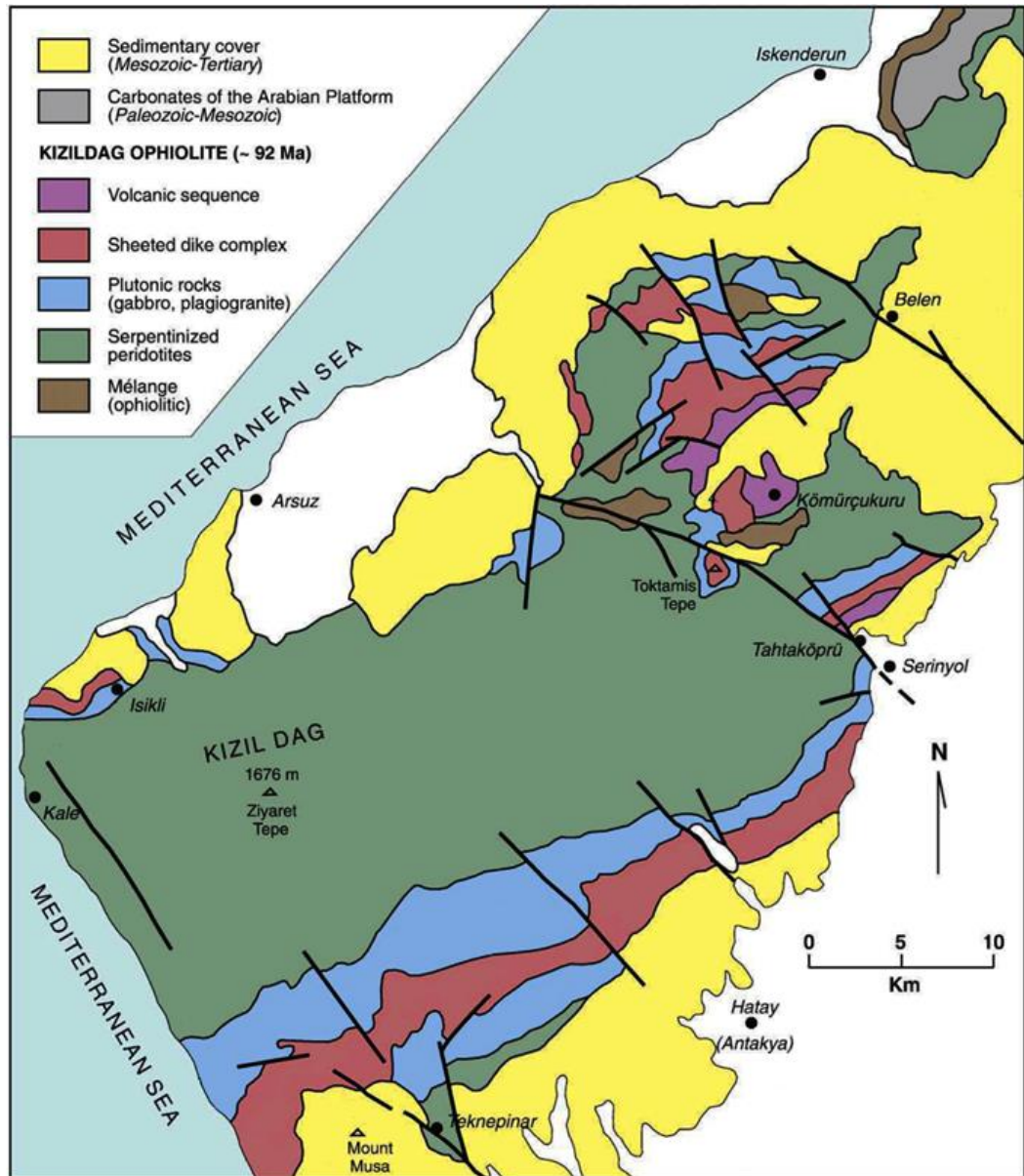


**Figure 3.24.** Simplified geological map of the Kizildağ (Hatay) ophiolite showing the main outcrops of the ophiolite and the location of Tahtaköprü Fault (modified from Dilek and Thy, 2009).

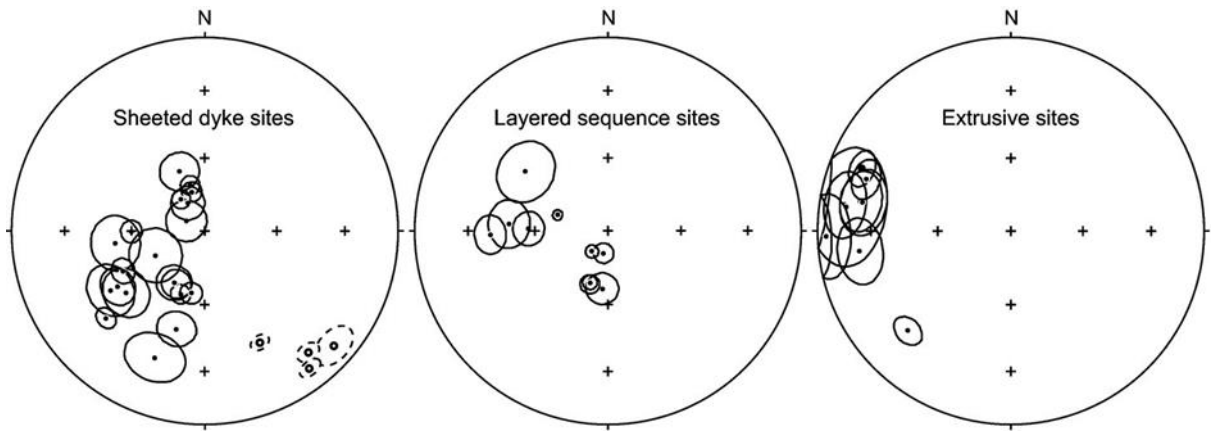


**Figure 3.25.** Stereonets of site mean remanence directions from sites in sheeted dykes, layered sequences and extrusives of the Hatay ophiolite with associated  $\alpha_{95}$  cones of confidence around site mean remanences. Note that all these units show anticlockwise rotation (from Inwood *et al.*, 2009).

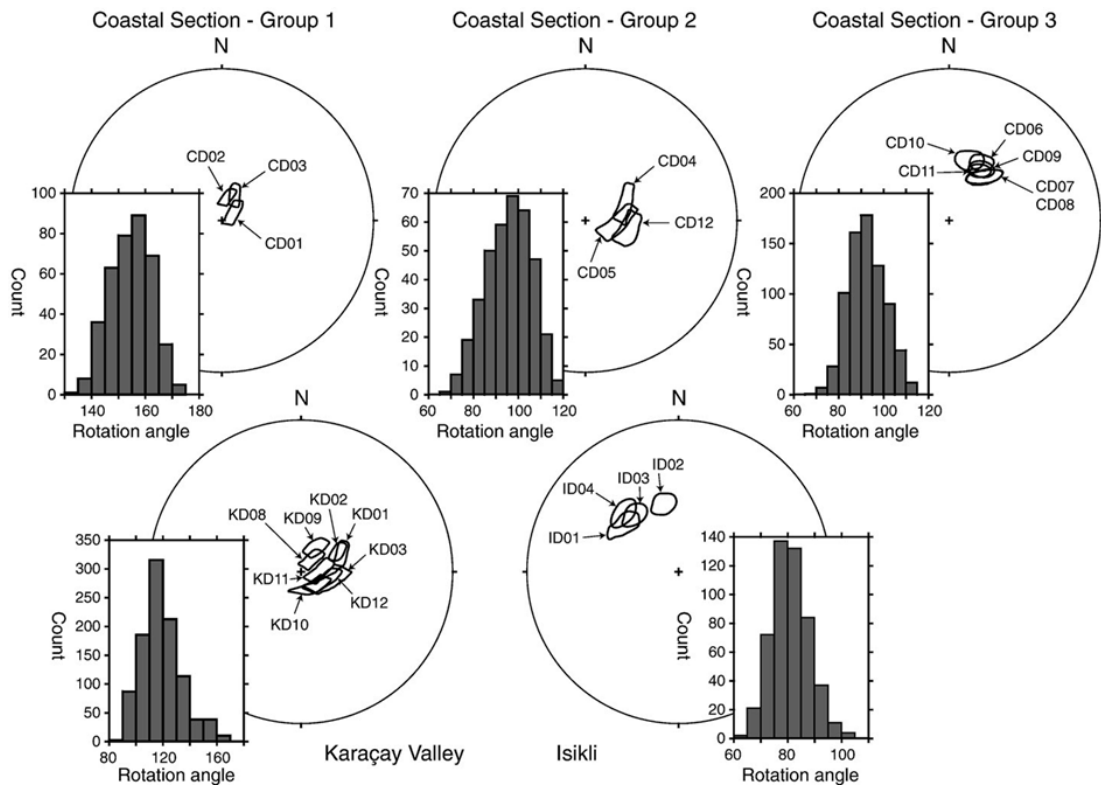


**Figure 3.26.** Results of net tectonic analyses of palaeomagnetic data from sites in sheeted dyke complex of the main massif of the Hatay ophiolite, demonstrating application of a net tectonic rotation method (Allerton and Vine, 1987; Morris *et al.*, 1998). Enclosed areas represent a first-order approximation of the  $\alpha_{95}$  cones of confidence of true rotation pole obtained from 125 estimates of the net tectonic rotation pole for each preferred solution. The inset histograms illustrate the associated distribution of net tectonic rotation angles (from Inwood *et al.*, 2009).

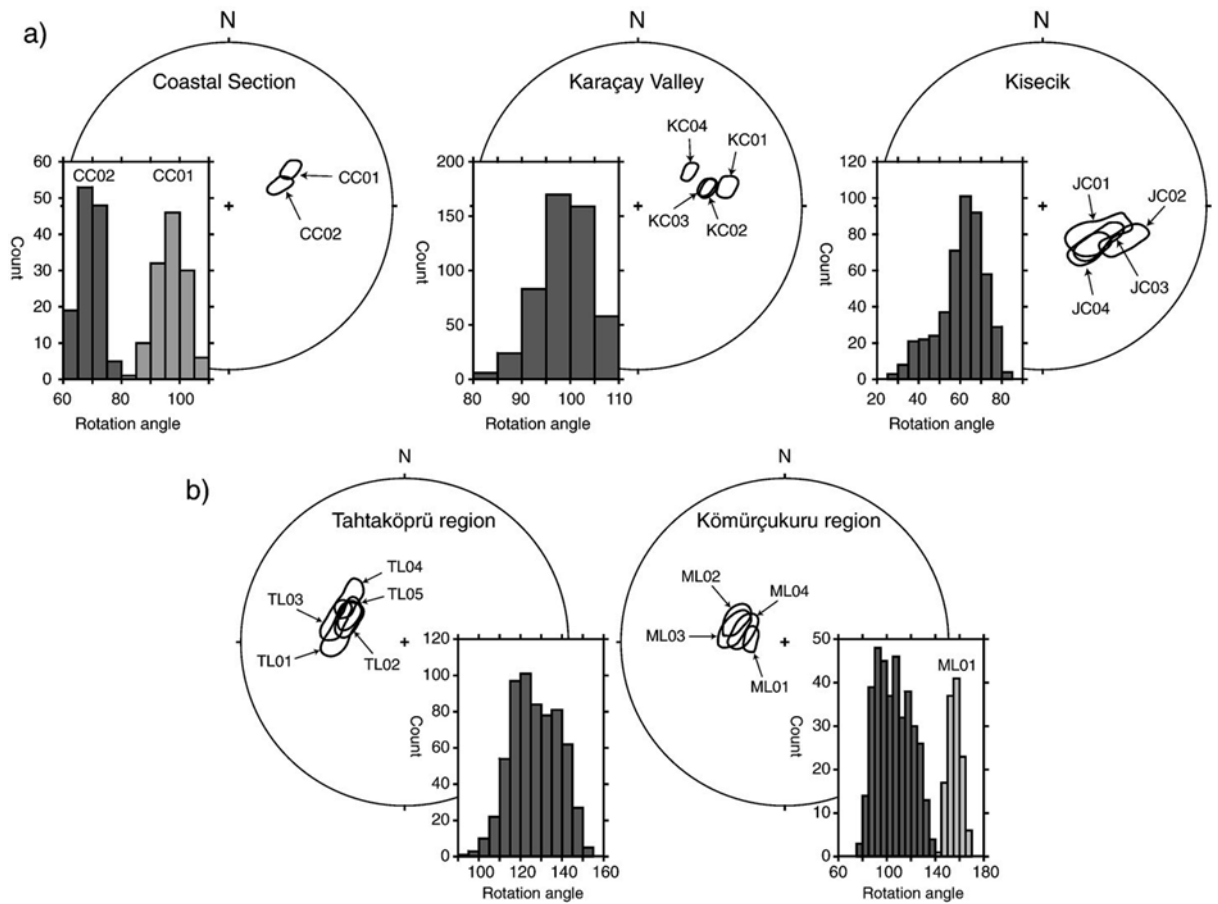


**Figure 3.27.** Results of net tectonic analyses of palaeomagnetic data. (a) Results from sites in the lower crustal layered sequence (ultramafic and gabbroic cumulates) of the main massif of the Hatay ophiolite; (b) Results from sites in the extrusive sequences of the northeastern massif of the Hatay ophiolite, demonstrating application of a net tectonic rotation method (Allerton and Vine, 1987; Morris *et al.*, 1998). Enclosed areas represent a first-order approximation of the  $\alpha_{95}$  cones of confidence of true rotation pole obtained from 125 estimates of the net tectonic rotation pole for each preferred solution. The inset histograms illustrate the associated distribution of net tectonic rotation angles (from Inwood *et al.*, 2009).

### 3.6.3 Baër-Bassit ophiolite

The dismembered Baër-Bassit ophiolite of Late Cretaceous age is located in the NW of Syria, less than 50 km south of the Kizildağ ophiolite (Figure 1.2 and 4.1). It contains a complete Penrose sequence, but, unlike Kizildağ, is underlain by the "Baër-Bassit Mélange" (Al-Riyami and Robertson, 2002), which comprises deformed Mesozoic rocks of continental margin and oceanic affinities. The ophiolitic outcrop includes two main groups: The Baër massif in the NE (inland) and the Bassit massif in the NW (near the coast), with smaller outcrops of highly

dismembered ophiolitic bodies to the SE (Figure 3.28). The Baër massif is almost structurally intact and comprises harzburgites, overlain by cumulate ultramafic rocks, layered gabbros and dolerite dykes (Parrot, 1977). The Bassit massif includes a lower sequence of depleted mantle peridotites and gabbros, which are overthrust by a slice of mélangé, which consists of a Late Triassic to mid-Cretaceous deep-water passive margin succession (Robertson, 2002), and then by thin (< 100 m thick) imbricate thrust sheets of gabbro, sheeted dykes and pillow lavas (Morris *et al.*, 2002).

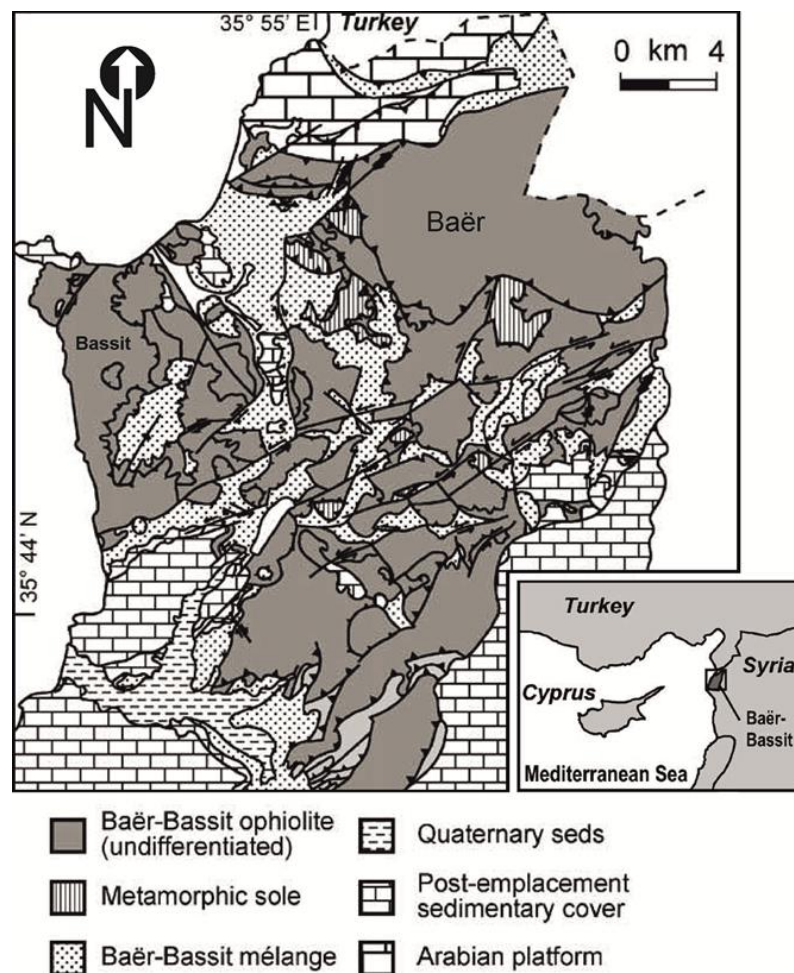


**Figure 3.28.** Simplified geological map of the Baër-Bassit ophiolite, NW of Syria, showing the distribution of the ophiolitic units, Baër-Bassit mélangé and metamorphic sole (modified from Morris, 2003).

The ophiolite represents the leading edge of the Kizildağ ophiolite thrust sheet and was overthrust onto the Arabian carbonate platform during the middle Maastrichtian (c. 70 Ma), together with the metamorphic sole and Baër–Bassit Mélange. The timing of emplacement is constrained by the ages of the youngest sequences of the Arabian platform carbonate beneath the allochthon and the oldest post-emplacement sedimentary cover rocks. The emplacement has been proposed to be related to the inception of the palaeorotation of the Troodos microplate to the west (Clube and Robertson, 1986).

Post-emplacement late Miocene sedimentary rocks are cut by a generally ENE-WSW trending sinistral strike-slip fault. This fault system forms part of the extension of the current plate boundary zone between the African plate and the Turkish microplate, which extends offshore, eastwards from south of Cyprus as a zone of deformation and then continues to pass from Baër–Bassit region until converges with the Dead sea Transform Fault system to the east (Robertson, 1998; Al-Riyami *et al.*, 2002).

Palaeomagnetic research on Baër-Bassit ophiolite and its sedimentary cover (Morris *et al.*, 2002; Morris and Anderson, 2002) have shown that this ophiolite has experienced extreme anticlockwise rotations on a kilometric scale during its development by intra-oceanic detachment and emplacement, in addition to more localised rotations caused by later neotectonic deformation (Morris *et al.*, 2002).

## Chapter 4

# Petrography and Geochemistry

### 4.1 Petrography

As discussed in Chapter Three, petrographic characteristics of some lithologies in the studied area such as the cumulates and the Mersin melange have been reported elsewhere (Parlak, 1996; Parlak *et al.*, 1996b; Parlak and Robertson, 2004). However the current study aims to examine the mineralogy of the samples from both gabbros and dykes in thin section, primarily to identify alteration that may influence the interpretation of the palaeomagnetic or geochemical characteristics of these rocks.

To achieve this, one oriented sample from each site in the different types of lithology was chosen for thin section analysis, with extra samples taken from selected sites. This analysis supplements field observations which were recorded during the sampling.

#### 4.1.1 Ultramafic cumulates

Ultramafic rocks of the Mersin ophiolite are composed mainly of clinopyroxenite and dunite with grain sizes up to 15mm (Figure 4.1a). In thin section, ultramafics generally display an adcumulate texture represented by large crystals of clinopyroxene with small amounts of orthopyroxene, amphibole and olivine, but with no plagioclase (Figure 4.1b). In some samples, olivine underwent variable degrees of serpentinisation and produced secondary magnetite (Figure 5.9 and 5.10; Section 5.4.3).

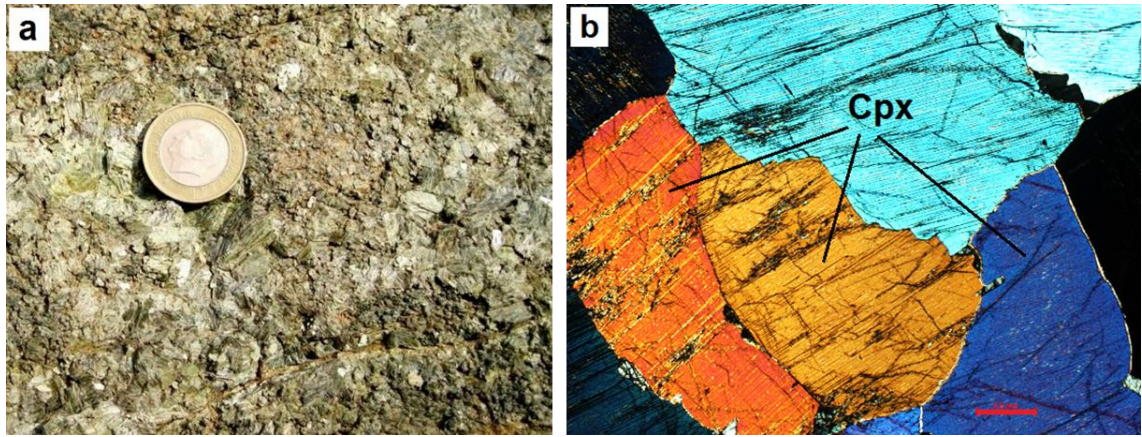


**Figure 4.1.** Ultramafic cumulate sample from the Mersin ophiolite showing phenocrysts of clinopyroxene (a) Field view. (b) Microscopic view (under crossed polars), showing adcumulate texture; Scale bar: 0.5 mm; Cpx = clinopyroxene.

As described in Section 3.5.3, field observations indicate that these ultramafic rocks in some places show grain-size grading, suggesting a gravitational control to the accumulation of minerals during crystallisation within the magma chamber (Parlak et al., 1996b).

#### **4.1.2 Gabbroic cumulates**

Cumulate gabbroic rocks within the study area display a very well-defined rhythmic and graded layering; therefore, they also indicate some gravitational control on the deposition of these cumulates (Figure 3.13; Section 3.5.3.1).

Generally, the gabbros show sub-ophitic to granular textures and are represented by subhedral clinopyroxene, orthopyroxene and plagioclase, ranging from 0.2 to 1 mm in size, with lesser/or no olivine crystals (Figure 4.2), and some samples showed abundant opaque minerals (Figure 5.11; Section 5.4.3).

Many plagioclase crystals in these samples contain fresh clinopyroxene inclusions, suggesting the crystallization order olivine → clinopyroxene → plagioclase, which indicates a suprasubduction zone (SSZ) origin, where olivine comes in first in both SSZ and MORB crystallization orders (Pearce et al. 1984). The delay in the crystallization of the plagioclase is often taken to indicate hydrous characteristics of the magma (Garcia et al., 2003; Yanagi, 2011). In MORB ophiolites, a crystallization order with pyroxene crystallizing after plagioclase is more typical (Pearce et al. 1984; Burns, 1985). In SSZ ophiolites this crystallization sequence also indicates accumulation towards the base of the magma chamber under relatively high pressures (Burns, 1985; Coleman, 1986). However, Yanagi (2011) indicates that an increase of water in the magma tends to cause simultaneous crystallisation of plagioclase and magnetite. It is possible, therefore, that some of the magnetite identified in these rocks may be primary rather than secondary, with important consequences for interpretation of palaeomagnetic results (Section 5.6).

In general, all samples showed limited evidence of alteration, although one sample (at site MC18) showed a high degree of clinopyroxene alteration to chlorite and talc, which is typical of hydrothermal alteration (Figure 4.2 e and f).

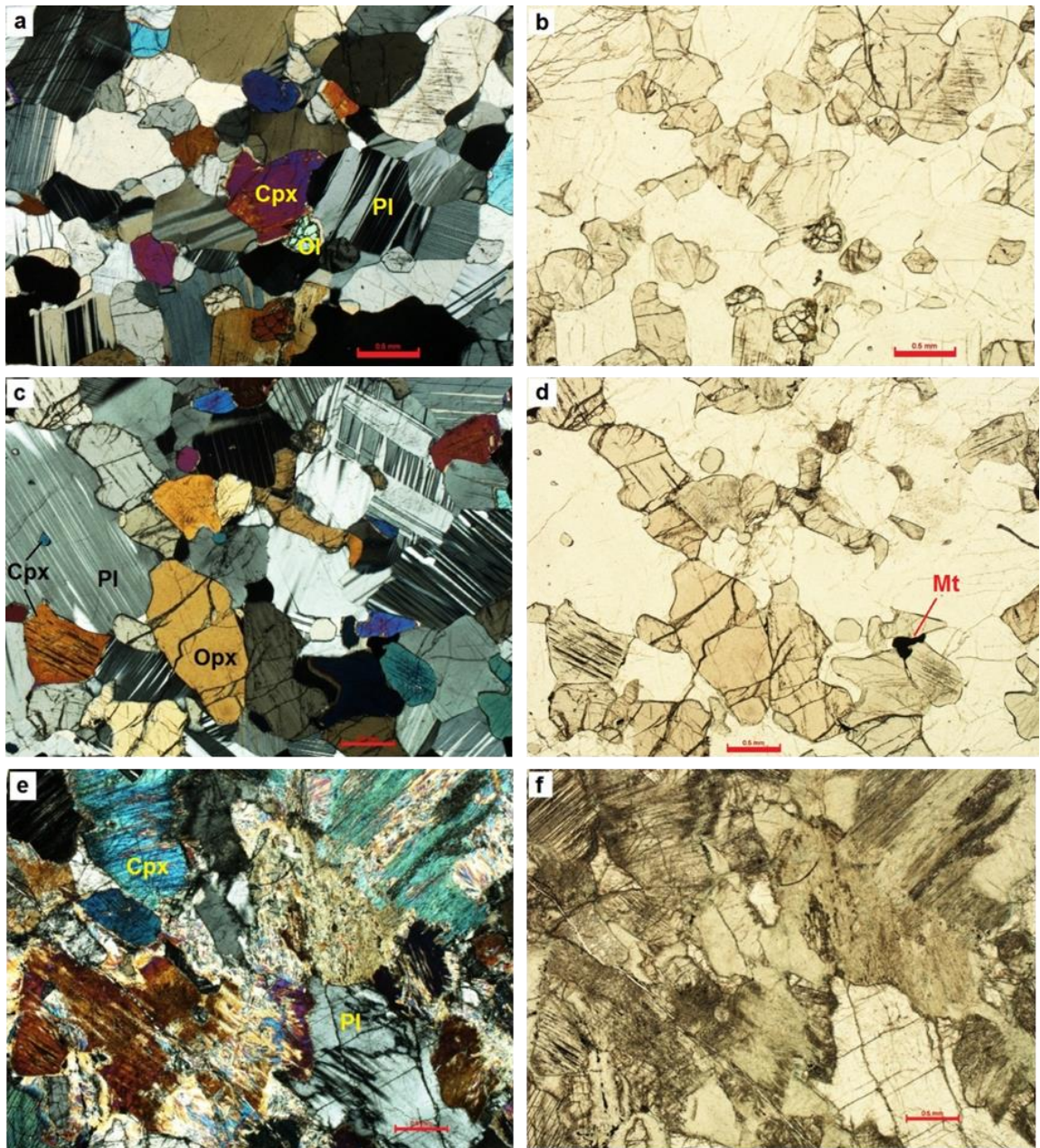


**Figure 4.2.** Photomicrographs (under crossed polars and in plane polarized light) of selected gabbro samples from the Mersin ophiolite. (a-d) Large plagioclase crystals enclose the clinopyroxene and orthopyroxene. (e-f) Gabbroic rock displaying alteration of the clinopyroxene to chlorite. Length of scale bar is 0.5 mm. (Mt = magnetite; Ol = olivine; Opx = orthopyroxene; Cpx = clinopyroxene; Pl = plagioclase).

### 4.1.3 Mafic dykes

A suite of discrete dykes is observed in the Findıkpınarı valley section of the Mersin ophiolite. In thin section these dykes display subophitic or intergranular textures and mainly consist of subhedral clinopyroxene, plagioclase, amphibole and opaque minerals (mostly magnetite), ranging from very fine-grained crystals to 0.5 mm in size. Some dyke samples showed variable degrees of hydrothermal alteration, in which the clinopyroxene crystals have been replaced by chlorite (Figure 4.3a and b).

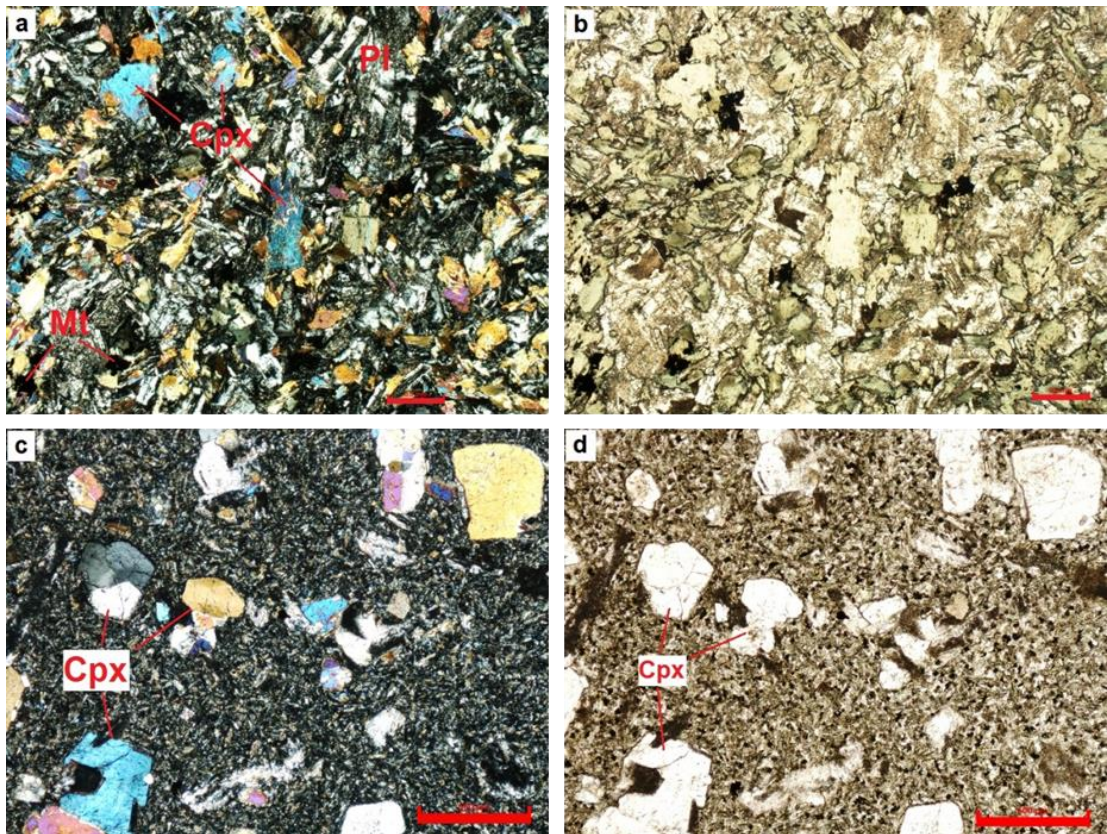


**Figure 4.3.** Photomicrographs (under crossed polars and in plane polarized light) of selected dolerite dyke samples from the Mersin ophiolite. (a and b) Doleritic dyke sample displaying intergranular texture and hydrothermal alteration. (c and d) Clinopyroxene-phyric dyke sample indicating a boninitic origin of the magma. Scale bar: 0.5 mm. (Mt = magnetite; Cpx = clinopyroxene; Pl = plagioclase).

In thin section, some samples showed porphyritic texture and consist mainly of clinopyroxene phenocrysts (approximately 0.05–0.5 mm in size) with fine-grained groundmass that is predominantly fine-grained pyroxene and also contains opaques (mostly magnetite), suggesting a boninitic magma origin (Gill, 2011) (Figure 4.3). This observation is in agreement with geochemical analyses, which are described in the following section. Large clinopyroxene grains also show concentric zoning under cross-polars (Figure 4.3c), indicative of changes in magma composition (Zhu and Ogasawara, 2001), with simple twinning in the upper-right corner.

## **4.2 Whole rock geochemistry**

### **4.2.1 Aims of the study**

In this section, geochemical analyses of the studied area were restricted to the cross-cutting basaltic veins (dyke-like veins; site MC10) and the host gabbros (adjacent to the basaltic veins), which have been described in Section 3.5.3.1; (Figure 3.14). This is because the geochemistry of all lithological units of the Mersin ophiolite have generally been reported comprehensively elsewhere (Parlak *et al.*, 1995; Parlak, 1996; Parlak *et al.*, 1996 b, c; Parlak and Robertson, 2004; Çelik, 2008). Thus, the aim of this chapter is primarily to determine the relationship of the dyke-like veins to the host gabbros, compare these with the geochemical characteristics of other dykes found elsewhere in the Mersin complex, and set these in the wider geochemical context of the ophiolite as a whole.

#### **4.2.2 General description and field relations of the basaltic veins**

The dyke-like veins observed at site MC10 are located at a distance of about 15 metres from site MC09, and extend about 20 metres long the section. The rocks at this site are dipping 52° to the south and contain a millimetre to centimetre scale, fine-grained basaltic material which clearly cross-cuts layering in the gabbro (Figure 4.4).

#### **4.2.3 Geochemical results**

Twenty five samples (whole rock and core samples) from both basaltic veins (14 samples) and host gabbros (11 samples) were collected (Figure 4.4), and then were analysed using X-ray fluorescence at the University of Southampton for oxides (SiO<sub>2</sub>, TiO<sub>2</sub>, Al<sub>2</sub>O<sub>3</sub>, Fe<sub>2</sub>O<sub>3</sub>, MnO, MgO, CaO, K<sub>2</sub>O, Na<sub>2</sub>O and P<sub>2</sub>O<sub>5</sub>) and trace elements (Cr, V, Ni, Sc, Cu, Zn, Pb, Ba, Rb, Sr, Y, Zr, Nb, Th, U, Hf, La, Ce and Ga). Details of the operating conditions and sample preparation methods are presented in Section 2.8.2.

The results of the geochemical analyses of the samples, including 14 basaltic vein samples and 11 gabbro samples, are presented in Tables 4.1 and 4.2 respectively. Where measured trace elements are below detection limit these are indicated by the symbol <. Both basaltic vein and gabbro samples showed low loss-on-ignition (LOI) values (most samples 0.05–0.7 wt %), suggesting that alteration of the minerals were negligible, as LOI > 2 wt% is generally considered to characterise altered rocks (e.g. Harrise et al., 2001; Burianek et al., 2008; Charkwu and Obiora, 2014).

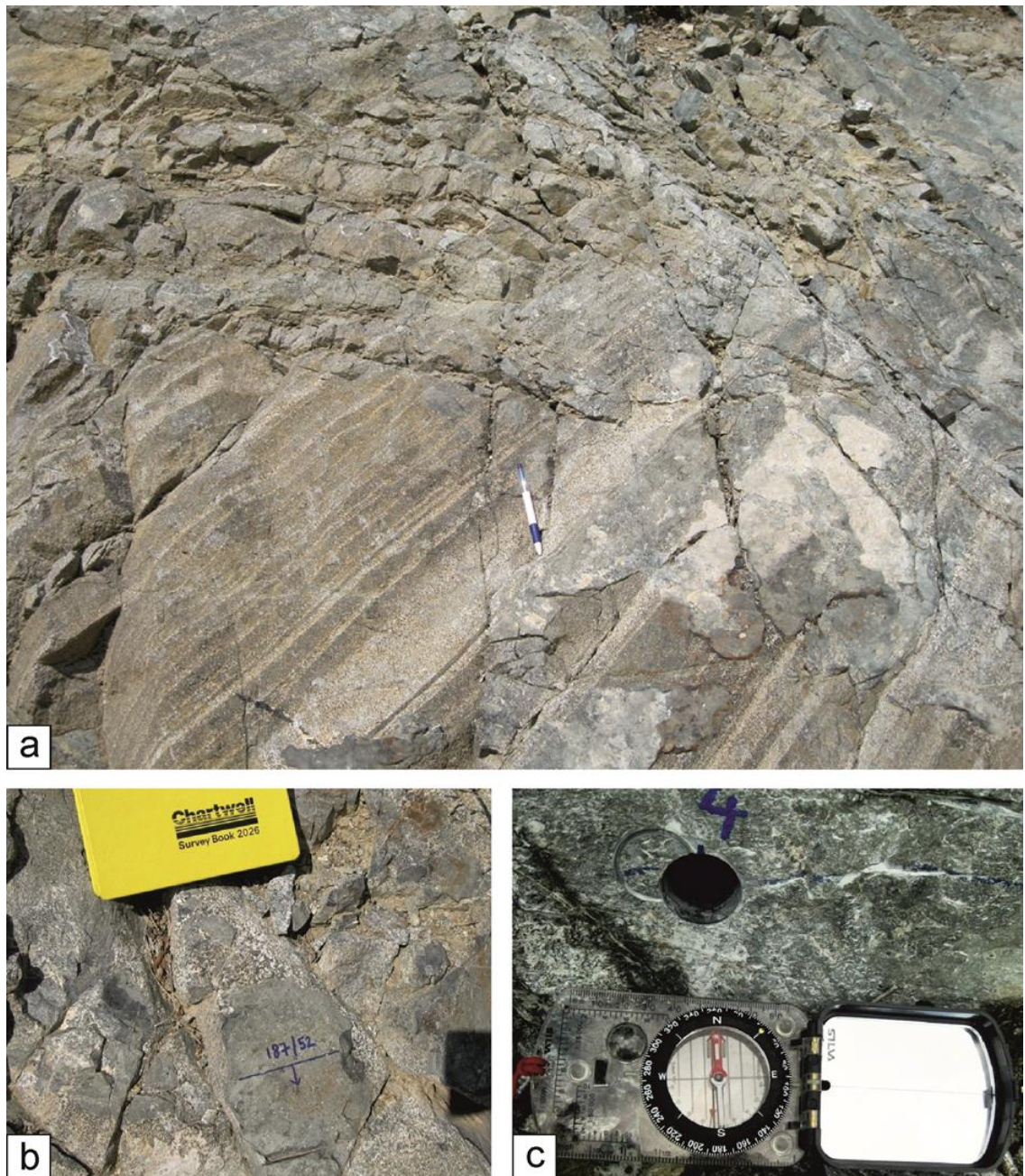


**Figure 4.4.** Field photographs of site MC10. (a) Cumulate layering, cross-cut by thin basaltic vein. (b) Oriented hand sample collected from the site. (c) Location of drilled core sample collected from the site.

**Table 4.1.** Whole rock major oxide (wt%) and trace element (ppm) data of basaltic veins analysed from the Mersin ophiolite.

Lithology	Basaltic vein samples													
Sample	MC1001	MC1002	MC1003	MC1004	MC1005	MC1006	MC1007	MC1008	MC10H1D	MC10H2D	MC10H3D	MC10H4D	MC10H5D	MC10H6D
(wt %)														
SiO <sub>2</sub>	49.52	47.50	48.55	48.96	48.44	48.08	47.62	48.17	47.45	47.50	47.36	49.07	47.11	48.74
TiO <sub>2</sub>	0.14	0.15	0.14	0.17	0.12	0.10	0.09	0.09	0.38	0.36	0.26	0.18	0.26	0.07
Al <sub>2</sub> O <sub>3</sub>	15.96	17.25	18.03	15.48	14.68	17.66	19.82	19.52	16.18	16.63	17.93	18.37	20.39	24.35
Fe <sub>2</sub> O <sub>3</sub>	7.24	7.03	6.95	7.86	8.13	7.83	6.61	6.35	11.46	11.04	9.82	7.65	8.57	5.12
MnO	0.11	0.11	0.11	0.13	0.15	0.14	0.12	0.12	0.16	0.17	0.14	0.14	0.13	0.09
MgO	11.25	10.26	10.25	11.15	12.59	11.22	9.94	9.84	10.26	10.09	9.61	9.47	8.55	6.72
CaO	14.97	14.69	15.01	15.53	15.10	14.11	15.11	15.20	12.77	12.75	13.95	14.18	13.94	16.57
K <sub>2</sub> O	0.010	0.005	0.01	0.007	0.002	<	<	0.002	0.078	0.087	0.028	0.05	0.041	0.01
Na <sub>2</sub> O	0.570	0.553	0.621	0.407	0.314	0.347	0.382	0.379	0.782	0.833	0.668	0.566	0.65	0.59
P <sub>2</sub> O <sub>5</sub>	0.001	0.002	0.002	0.001	0.001	0.001	0	0.002	0.001	0	0.002	0.001	0.001	0.001
S	0.007	0.01	0.008	0.009	0.008	0.008	0.01	0.012	0.008	0.008	0.012	0.007	0.008	0.007
Cl	<	<	<	<	<	<	<	<	<	<	<	<	<	<
LOI	0.2184	2.4783	0.3234	0.2993	0.4759	0.4904	0.3074	0.328	0.458	0.5225	0.2141	0.3252	0.3399	0.00
Total	100.00	100.02	100.00	100.00	99.99	100.00	100.00	100.00	99.99	99.99	100.01	100.00	100.00	102.27
Mg#	77.4	76.2	76.5	75.7	77.3	75.9	76.8	77.3	66.3	66.8	68.3	73.1	68.7	74.3

**Table 4.1. (Continued)**

(ppm)														
Cr	328	282	278	292	466	339	286	324	212	193	233	190	157	147
V	192	212	202	223	176	156	138	138	481	441	340	227	321	113
Ni	101	96	91	89	108	109	98	108	103	95	94	79	79	51
Sc	47	42	44	54	51	50	42	43	44	46	44	38	37	30
Cu	20	50	58	210	80	102	125	212	101	136	152	105	205	17
Zn	20	20	19	24	31	29	27	29	41	40	35	27	32	16
Pb	2	3	2	2	2	2	2	2	3	3	2	2	2	2
Ba	<	<	<	<	<	<	<	18	<	8	<	8	<	11
Rb	<	<	<	<	<	<	<	<	<	<	<	<	<	<
Sr	85	92	85	70	54	64	74	77	81	83	81	106	98	113
Y	3	2	3	3	3	3	2	2	3	2	3	2	2	<
Zr	11	11	12	12	12	12	12	12	12	12	12	11	11	11
Nb	<	<	<	<	<	<	<	<	<	<	<	<	<	<
Th	<	<	<	<	<	<	<	<	<	<	<	<	<	<
U	<	<	<	<	<	<	<	<	<	<	<	<	<	<
Hf	<	<	<	<	<	<	<	<	<	<	<	<	<	<
La	<	<	<	<	<	<	<	<	<	<	<	<	<	<
Ce	<	19	<	<	10	11	<	<	<	<	14	8	17	<
Ga	11	12	12	11	10	12	12	12	13	13	13	12	14	15

---

< = Below detection limit. LOI = Loss in ignition. Mg# = Mg/(Mg + Fe\*), Fe\* means total Fe as FeO.

**Table 4.2.** Whole rock major oxide (wt%) and trace element (ppm) data for gabbros of the Mersin ophiolite.

Lithology	Mafic gabbros										
Sample	MC10 H1G	MC10 H2G	MC10 H3G	MC10 H4G	MC10 H5G	MC09 H1G	MC09 H2G	MC09 H3G	MC09 H4G	MC09 H5G	MC09 H6G
(wt %)											
SiO <sub>2</sub>	48.20	47.07	48.44	48.83	47.97	48.11	48.20	47.48	48.44	48.75	47.30
TiO <sub>2</sub>	0.07	0.07	0.13	0.08	0.07	0.09	0.10	0.08	0.13	0.11	0.07
Al <sub>2</sub> O <sub>3</sub>	19.51	20.35	17.97	18.48	20.53	21.76	19.74	22.90	18.68	17.03	25.96
Fe <sub>2</sub> O <sub>3</sub>	7.26	7.67	7.56	7.57	7.13	5.99	7.29	5.27	6.48	8.50	4.28
MnO	0.14	0.13	0.13	0.14	0.13	0.11	0.14	0.09	0.13	0.16	0.08
MgO	9.69	10.33	9.99	10.49	9.27	6.97	8.29	6.75	8.08	10.18	4.63
CaO	13.97	13.08	14.99	13.89	13.88	16.20	15.60	16.46	17.24	14.72	16.82
K <sub>2</sub> O	0.038	0.063	0.006	0.022	0.08	0.007	0.001	0.01	0.005	0	0.008
Na <sub>2</sub> O	0.635	0.546	0.487	0.451	0.48	0.64	0.538	0.587	0.574	0.475	0.711
P <sub>2</sub> O <sub>5</sub>	0.001	0	0.001	0.001	0	<	0	0	0.002	0.003	0.003
S	0.007	0.007	0.015	0.007	0.01	0.007	0.007	0.007	0.007	0.007	0.007
Cl	<	<	<	<	<	<	<	<	<	<	<
LOI	0.461	0.669	0.288	0.049	0.47	0.118	0.107	0.371	0.24	0.07	0.152
Total	99.99	99.98	100.01	100.01	99.99	100.01	100.01	100.00	100.00	100.01	100.00
Mg#	74.6	74.8	74.4	75.3	74.1	71.9	71.5	73.8	73.3	72.5	70.4
(ppm)											
Cr	150	116	226	174	117	249	233	231	384	223	183
V	126	110	206	138	118	136	148	112	164	168	88
Ni	62	62	75	80	58	50	59	51	77	77	37
Sc	40	32	48	37	29	39	41	30	43	49	27
Cu	30	18	230	71	28	15	23	18	122	29	15
Zn	38	33	33	34	34	24	39	25	32	51	18
Pb	4	2	3	3	3	2	3	3	3	3	2
Ba	<	16	<	<	<	<	15	<	<	<	<
Rb	<	<	<	<	<	<	<	<	<	<	<
Sr	88	76	74	80	98	98	81	113	79	73	105
Y	<	<	3	<	<	3	3	2	4	3	2
Zr	11	11	12	11	11	11	12	10	12	12	11
Nb	<	<	<	<	<	<	<	<	<	<	<
Th	<	<	<	<	<	<	<	<	<	<	<
U	<	<	<	<	<	<	<	<	<	<	<
Hf	<	<	<	<	<	<	<	<	<	<	<
La	<	<	<	<	<	<	<	<	<	<	<
Ce	8	<	<	12	8	9	<	<	14	9	8
Ga	13	13	12	12	13	15	14	14	13	12	17

< = Below detection limit. LOI = Loss in ignition. Mg# = Mg/(Mg + Fe\*), Fe\* means total Fe as FeO.

According to Wilson (1989), primary magmas in equilibrium with upper mantle mineralogy usually have high values of Mg# (> 70.0), Cr (> 1000 ppm), Ni (> 400-500 ppm) and SiO<sub>2</sub> not exceeding 50%. In the current study, overall, the samples from dyke-like veins display high values of Mg# (66.3–77.4), moderate SiO<sub>2</sub> content (47.11–49.5%). Concentrations of Cr and Ni are 147-466 ppm and 51-109 ppm, respectively, with extreme depletion in incompatible elements (e.g. Y, Nb, Hf, Th, La and Rb). This indicates their cumulate origin and primitive magma signature (Barth and Gluhak, 2008), but suggests some changes of the magma by fractional crystallization which can be identified using variation diagrams (Hari *et al.*, 2011).

In general, all data from both basaltic vein and gabbros are consistent with the gabbro data reported by Parlak *et al.* (1996c), but they differ from the both the dyke data of Parlak *et al.* (1995) and Çelik (2008) and the ultramafic data values of Parlak *et al.* (1996c).

However, in this chapter, published data from Parlak *et al.* (1995, 1996c) and Çelik (2008) were used in order to compare with data obtained from the dyke-like veins, and to find the fractional crystallization trend of magma, as data from the current study are not sufficient to display fractional crystallization processes.

Selected major oxides and Sr content are plotted versus MgO (which is considered as an indicator of differentiation (e.g. Wright, 1971) for the different lithology units.

MgO contents revealed that there is a clear inverse correlation with the majority of these oxides and Sr content which is considered to be incompatible element (Wilson, 1989), indicating the fractional crystallization trend of the magma (Figures 4.5 and 4.6). This fractional crystallization trend has also been

confirmed by plotting major oxides against Zr contents of different lithological units (Figure 4.7). Zr is considered an incompatible element and remains unaffected in most secondary processes (Cann, 1989). Thus, these plots have revealed high correlations between Zr and many oxides. For example,  $\text{TiO}_2$  and  $\text{Na}_2\text{O}$  concentrations show a positive correlation with Zr values, whereas CaO and MgO concentrations show a negative (inverse) correlation with Zr values. All these variations in fractional crystallization trends reflect compositional changes with progressive crystallization processes within the magma chamber.

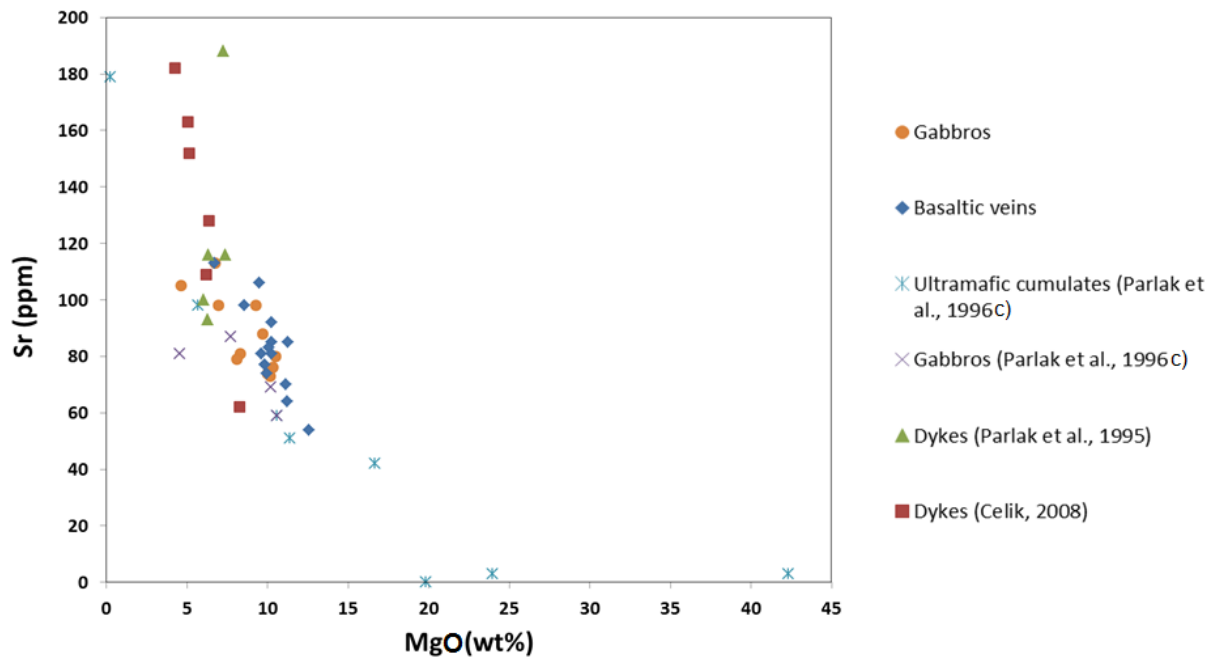


**Figure 4.5.** MgO vs Sr diagram for the basaltic veins and gabbroic rocks from the Mersin ophiolite (including the data from Parlak *et al.*, 1995, 1996c and Çelik, 2008), showing fractional crystallization processes.

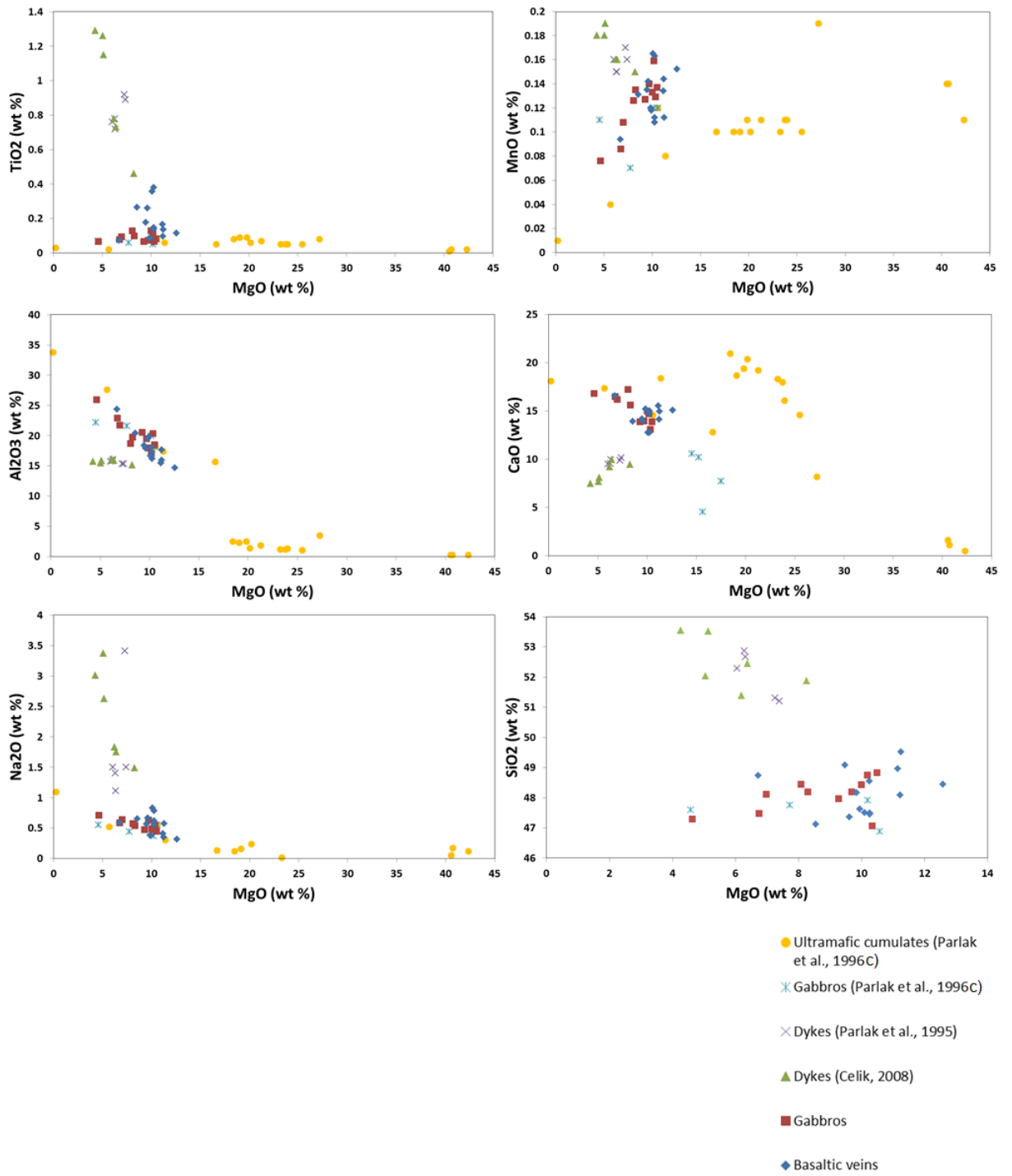


**Figure 4.6.** Selected major element variations for the basaltic veins and gabbroic rocks from the Mersin ophiolite (including the data from Parlak *et al.*, 1995, 1996c and Çelik, 2008), showing fractional crystallization processes.

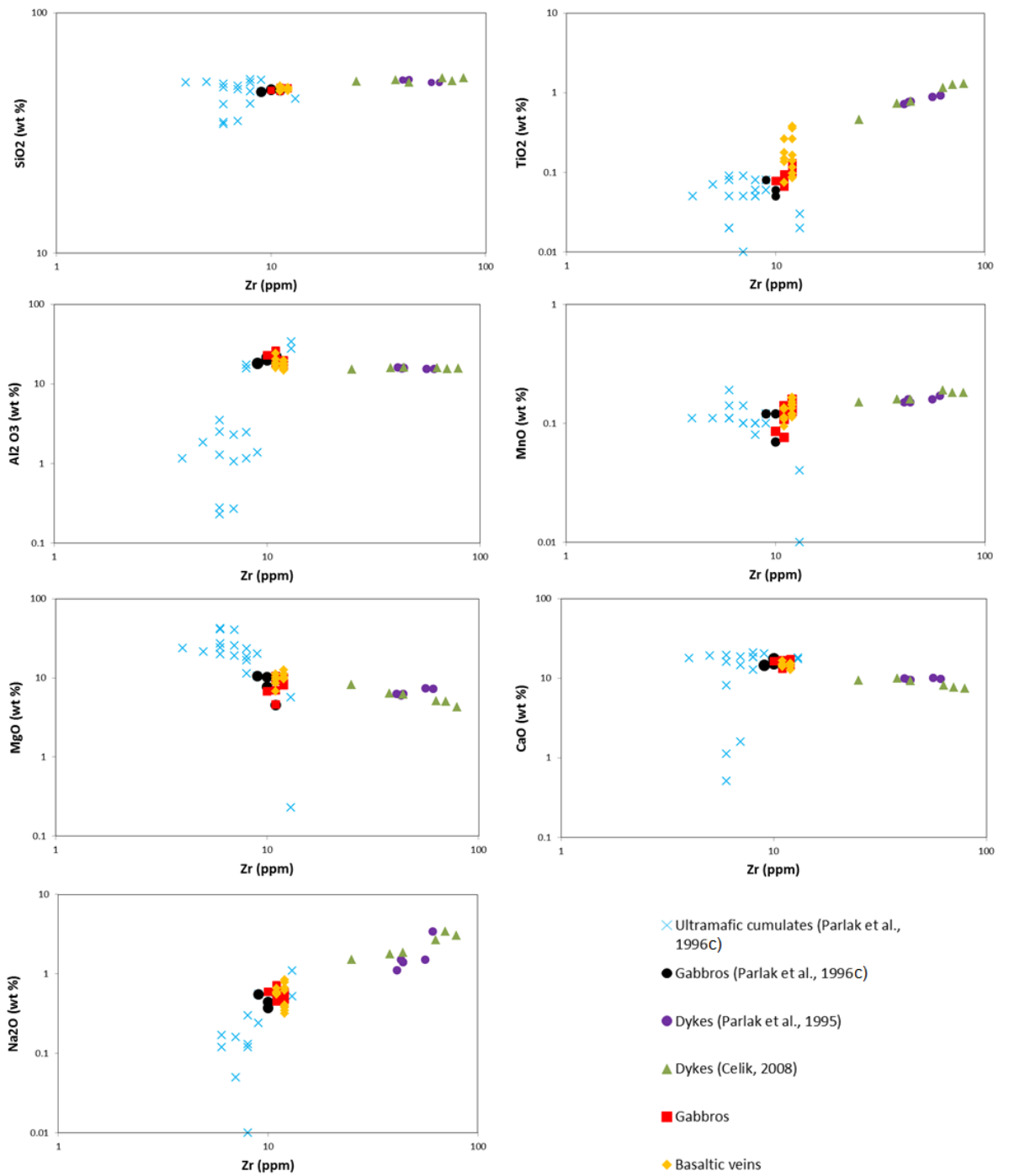


**Figure 4.7.** Variation of selected major oxides with Zr for the basaltic veins and gabbroic rocks from the Mersin ophiolite (including the data from Parlak *et al.*, 1995, 1996c and Çelik, 2008), showing fractional crystallization processes.

Both the MgO and Zr variation diagrams suggest a possible link between the samples analysed in this study and the published data of Parlak *et al.* (1995) and Çelik (2008). The plots suggest possible primary fractional crystallization trends from the ultramafics to the more evolved dykes. However, in all cases, results from samples of the basaltic veins sampled in this study are clustered with those from gabbro samples and with the gabbro analyses reported by Parlak *et al.* (1996c), rather than the dykes reported by Çelik (2008). It seems likely, therefore, that these veins reflect minor internal variations of melt within the gabbros rather than late stage fractionation products represented by dykes found elsewhere in the ophiolite. This is discussed further later in this chapter.

According to Le Maitre (2002), boninite type rocks have  $\text{SiO}_2 > 52\%$ ,  $\text{MgO} > 8\%$  and  $\text{TiO}_2 < 0.5$ . In the present study, the analyses showed that both basaltic vein and gabbro samples exhibit low  $\text{TiO}_2$  wt% (0.07- 0.4%), but their  $\text{SiO}_2$  wt% and  $\text{MgO}$  wt% values are 47.07- 49.5% and 4.63 – 12.6%, respectively, suggesting that their sources are closer to boninitic magma (Crawford *et al.*, 1981).

In the  $\text{TiO}_2$ - $\text{MnO}$ - $\text{P}_2\text{O}_5$  diagram of Mullen (1983), both basalt vein and gabbro samples from this study, together with gabbro and ultramafic cumulate samples from Parlak *et al.* (1996c), showed boninitic affinity, whereas, all the dykes from Parlak *et al.* (1995) and Çelik (2008) are clustered in the IAT field (Figure 4.8).

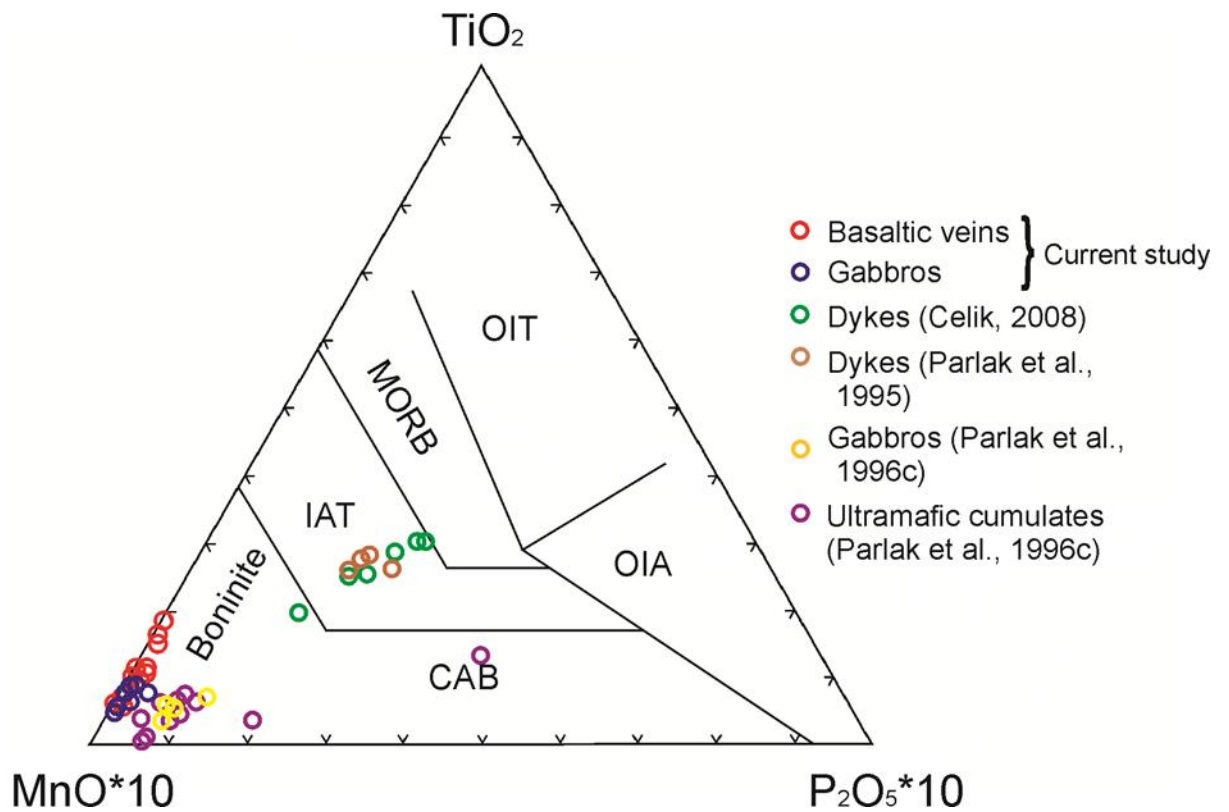


**Figure 4.8.**  $TiO_2$ - $MnO$ - $P_2O_5$  discrimination diagram (Mullen, 1983) for basaltic vein rocks and gabbros from the Mersin ophiolite, compared with data from Parlak *et al.*, 1995, 1996c; Çelik, 2008.

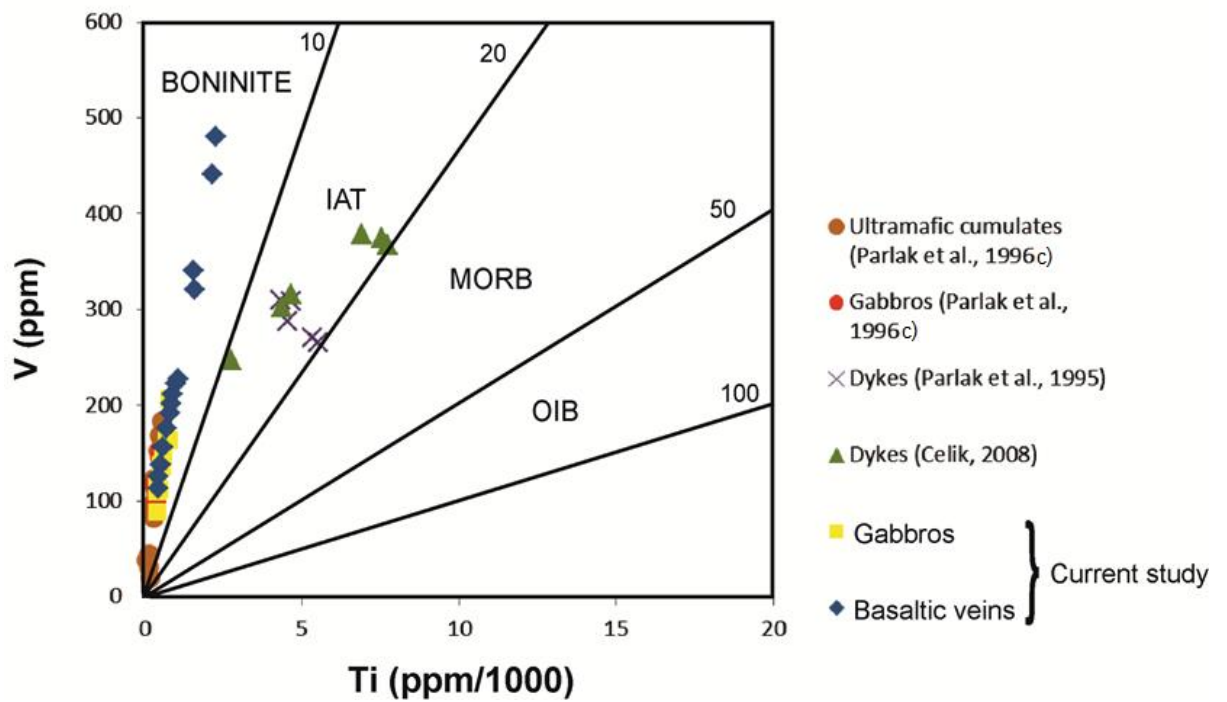


**Figure 4.9.** Ti vs V diagram (after Shervais, 1982) for basaltic vein rocks and gabbros from the Mersin ophiolite, compared with data from Parlak *et al.*, 1995, 1996c; Çelik, 2008.

The  $\text{TiO}_2$  vs V diagram (Figure 4.9; Shervais, 1982), confirms that all basaltic vein and gabbro rocks have depleted (possibly boninitic) character through the low Ti/V ratio  $< 10$  (Crawford *et al.*, 1981). These results are also consistent with petrographic observations of some samples, which were described in Section 4.1.1.

Thus, petrographic and geochemical results of the current study indicate for the first time that the Mersin ophiolite not only contain IAT magmas, but may also contain boninitic magmas, suggesting its formation at early stage of island arcs in a SSZ tectonic setting (Sarifakioğlu *et al.*, 2009; Dilek and Furnes, 2011). Therefore, the Mersin ophiolite displays a similar tectonic setting to nearby L. Cretaceous Ali Hoca ophiolite, which was also suggested to have formed in the inner Tauride Ocean (Sarifakioğlu *et al.*, 2012).

In the AFM diagram (Figure 4.10; Beard, 1986), all basaltic and gabbroic samples from the current study, together with gabbro samples from Parlak *et al.* (1996c), fall in the same area, within the arc related mafic field.

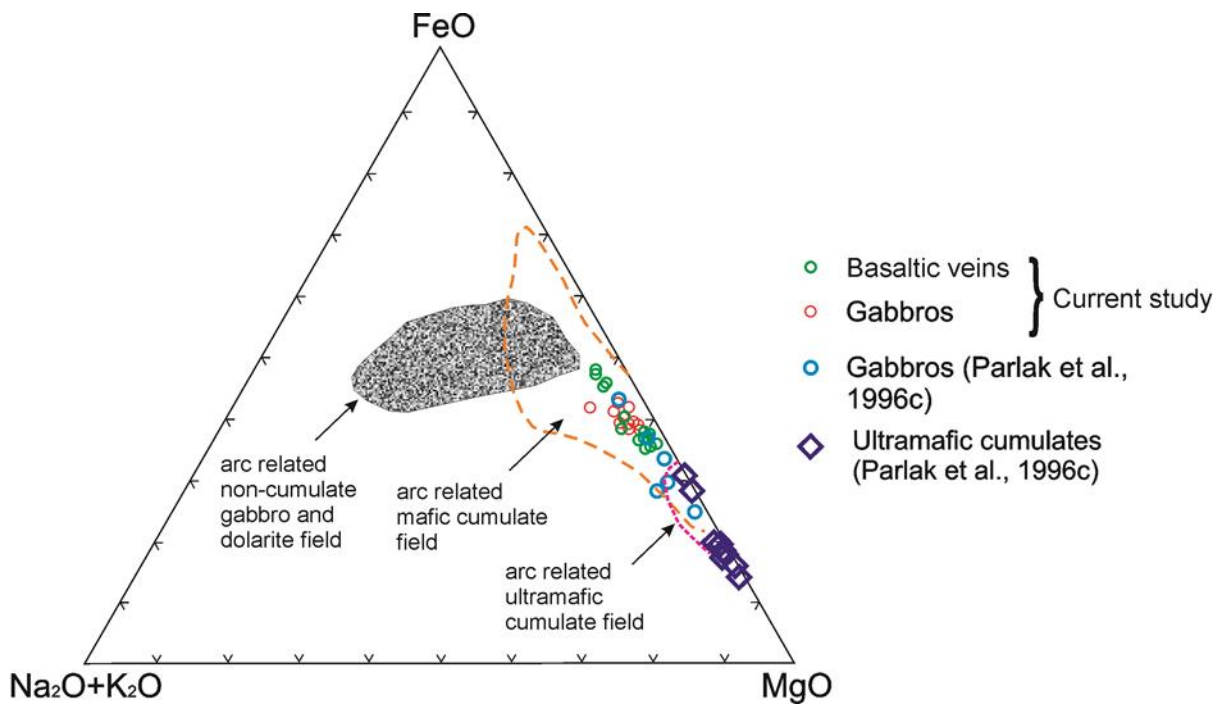


**Figure 4.10.** AFM composition of the samples of the current study (basaltic veins and gabbros) and gabbros with ultramafic cumulates from Parlak *et al.* (1996c). Fields of cumulate and non-cumulate rocks are from Beard (1986).

### 4.3 Discussion of the origin of the basaltic veins within the layered gabbros

Geochemical analysis of basaltic vein rocks reveals that these rocks have more affinity to the host gabbroic rocks than other late stage dykes reported elsewhere in the Mersin ophiolite. Nearly all the major oxides and trace elements values from the basaltic veins are in agreement with gabbro values from the current study and with gabbro data reported by Parlak *et al.* (1996c) (Table 4.3).

**Table 4.3.** Average values of the major oxides and trace elements of rock samples from the current study compared to the previous studies on the Mersin ophiolite.

Type of rocks	Basaltic vein	Gabbros (current study)	Gabbros (Parlak <i>et al.</i> , 1996)	Dykes (Çelik, 2008)	Dykes (Parlak <i>et al.</i> , 1995)
(wt %)					
SiO <sub>2</sub>	48.1	48.1	47.5	52.5	52.1
TiO <sub>2</sub>	0.2	0.1	0.1	0.9	0.8
Al <sub>2</sub> O <sub>3</sub>	18.0	20.3	20.5	15.7	15.7
Fe <sub>2</sub> O <sub>3</sub>	7.2	6.1	5.5	10.6	9.7
MnO	0.1	0.1	0.1	0.2	0.2
MgO	10.1	8.6	8.3	5.9	6.7
CaO	14.6	15.2	15.7	8.7	9.8
K <sub>2</sub> O	0.0	0.0	0.0	1.2	1.0
Na <sub>2</sub> O	0.5	0.6	0.5	2.3	1.8
P <sub>2</sub> O <sub>5</sub>	0.0	0.0	0.0	0.1	0.1
LOI	0.5	0.27	1.2	1.76	2.1
(ppm)					
Cr	266.2	207.8	129.3	92.3	151.8
V	240.0	137.6	119.3	331.2	288.0
Ni	92.9	62.5	52.5	48.3	52.6
Zn	27.9	32.8	—	78.8	—
Sr	83.1	87.7	74.0	132.7	122.6
Zr	11.6	11.3	10.0	53.2	49.0

Petrographic analyses have shown that these basaltic vein rocks consist mainly of plagioclase and pyroxene, similar to the host gabbros, but that the fine grain nature of the veins compared with the gabbros may be the result of extreme grain-size reduction during deformation (Figure 4.11a-d) rather than primary grain-size variation (Passchier and Trouw, 2005). This observation introduces the intriguing possibility that the veins in fact represent shear zones, which have partitioned strain within the gabbros. In thin section, the majority of the “phenocrysts” within the basaltic veins have distinguishable tails on each side of the host grain. Although masked by subsequent alteration, several of the host crystals display evidence of intracrystalline plasticity and are, most likely, porphyroclasts in a recrystallized matrix (Fig 4.12a-d). Asymmetry of the

porphyroclast system is consistent throughout the samples studied and is considered to be a reliable kinematic indicator for the shear zones (Simpson and Schmid, 1983; Hatcher, 1990; Twiss and Moores, 1992; Passchier and Trouw, 2005). Moreover, petrographic analyses reveals further shear sense indicators, such as fractured porphyroclasts (Figure 4.12e and f). These grains can be used together with the porphyroclast system to deduce the overall sense of movement (Simpson and Schmid, 1983; Twiss and Moores, 1992; Fossen, 2010) (Figure 4.12g and h and Figure 4.13). Detailed examination of porphyroclast tails under microscope has shown that the mineralogy is dominated by aggregates of fine-grained hydrated silicate phases such as chlorite and actinolite. The identified assemblage is indicative of growth under greenschist facies conditions, with temperatures below approximately 500°C and likely to be in the P-T range  $T = 350\text{-}500^{\circ}\text{C}$  and  $P = 2\text{-}8$  kbar as suggested by Hefferan & O'Brien (2010). It is interesting to note that coarse grained, relatively undeformed gabbro immediately adjacent to the veins is also extensively altered to a similar assemblage and that the crystals are increasingly deformed towards areas of intense grain size reduction and foliation development. Chlorite and actinolite crystals are commonly kinked and rotated into alignment sub-parallel to the localised shear zones. This suggests that hydration and alteration of the host gabbros occurred either before or was coeval with deformation. It seems possible, therefore, that the partitioning of deformation may alternatively be a function of focusing of volatiles within the gabbros after cooling below 500°C.

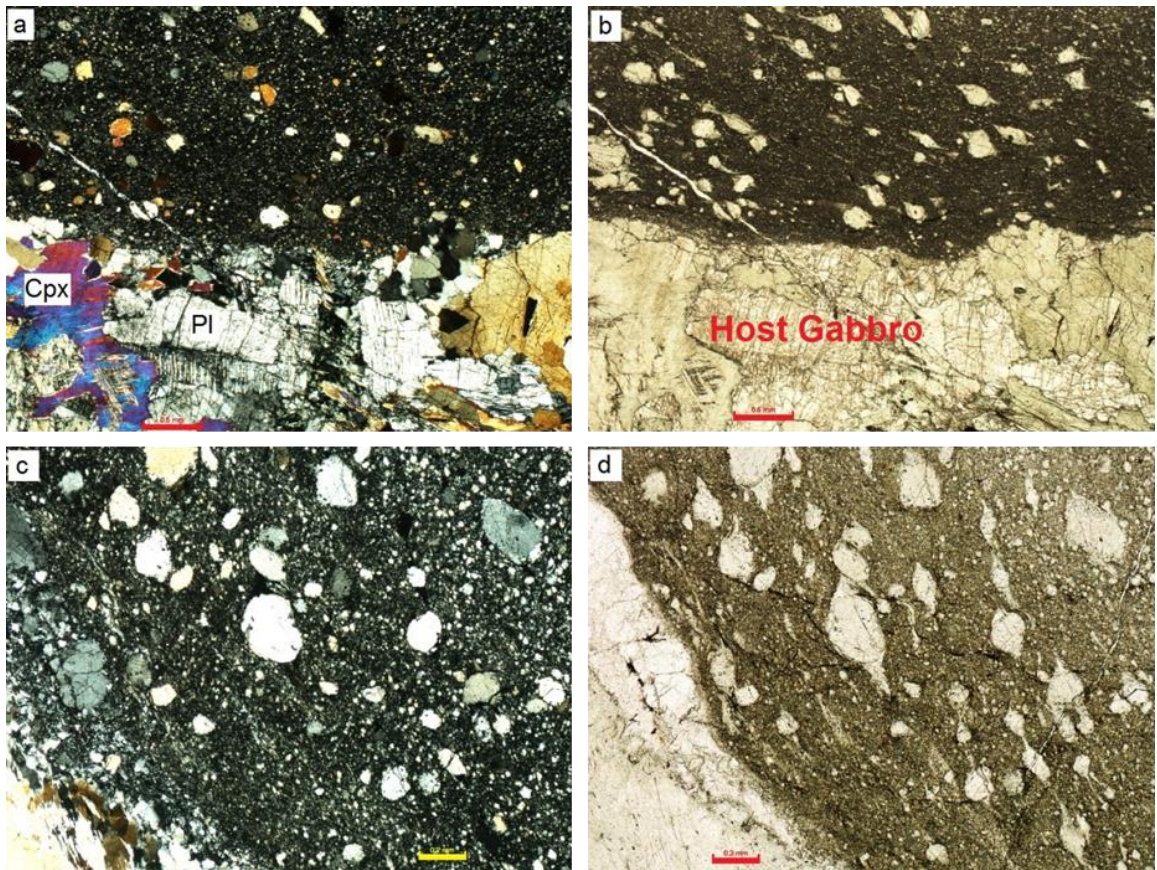


**Figure 4.11.** Photomicrographs (under crossed polars and in plane polarized light) of a cross-cutting basaltic vein within the host gabbro of the Mersin ophiolite showing the alteration of the clinopyroxene and plagioclase in the host gabbro with reduction of the grain sizes in the basaltic vein. Scale bar: 0.5 mm for Figure 4.11 (a,b) and 0.2 mm for Figure 4.11 (c,d). (Cpx = clinopyroxene; Pl = plagioclase).

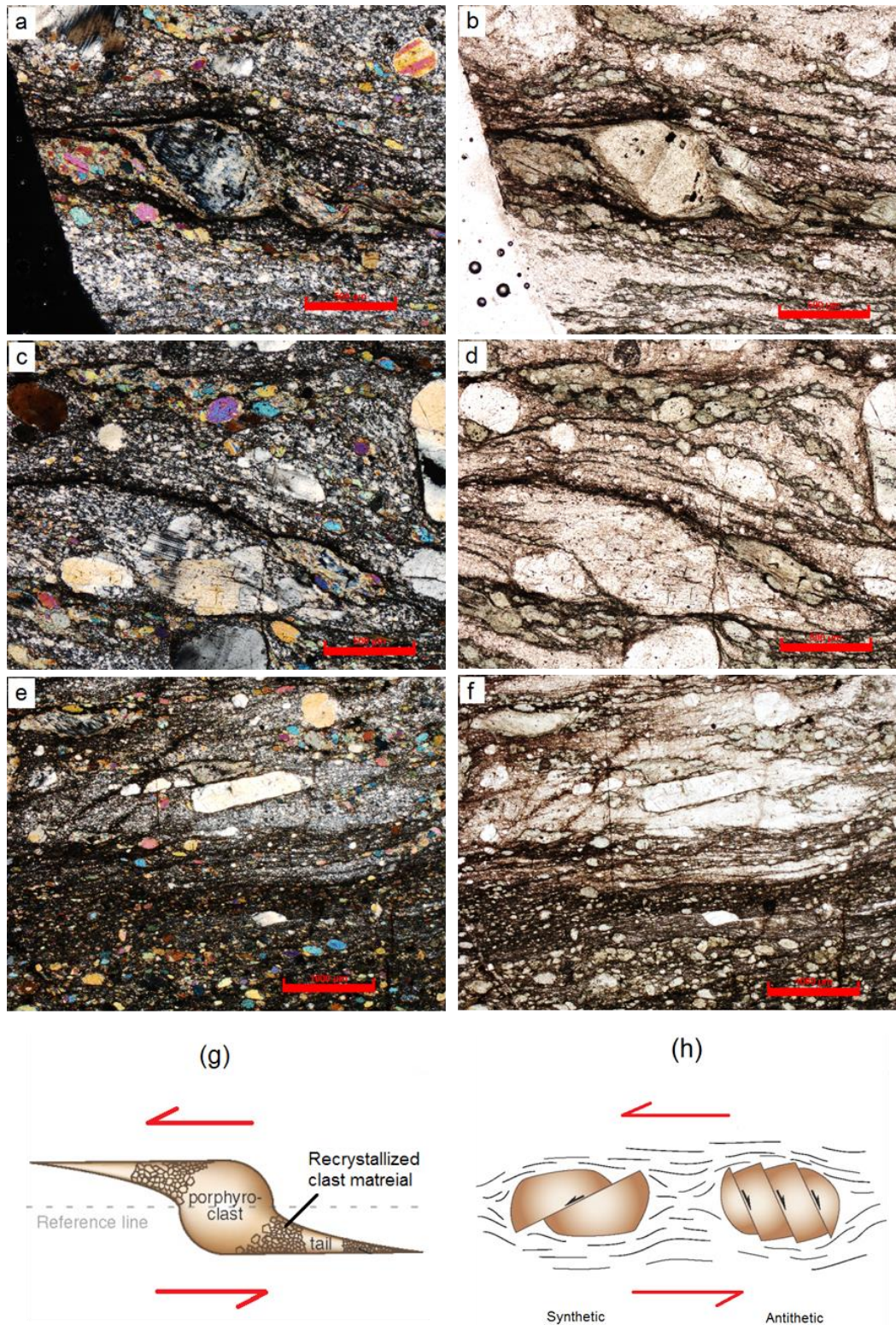


**Figure 4.12.** Microstructural shear sense indicators in cross-cutting vein samples from Mersin ophiolite. (a, b, c and d) Optical micrographs (under crossed polars and in plane polarized light) showing porphyroclasts with recrystallized tails. (e and f) Optical micrographs (under crossed polars and in plane polarized light) showing synthetic fractures in porphyroclasts within the basaltic vein. (g and h) Schematic diagrams illustrating the shear sense criteria in shear zones (modified from Fossen, 2010). Scale bar 0.5 mm for Figures (a-d), and 1 mm for Figures (e-f).

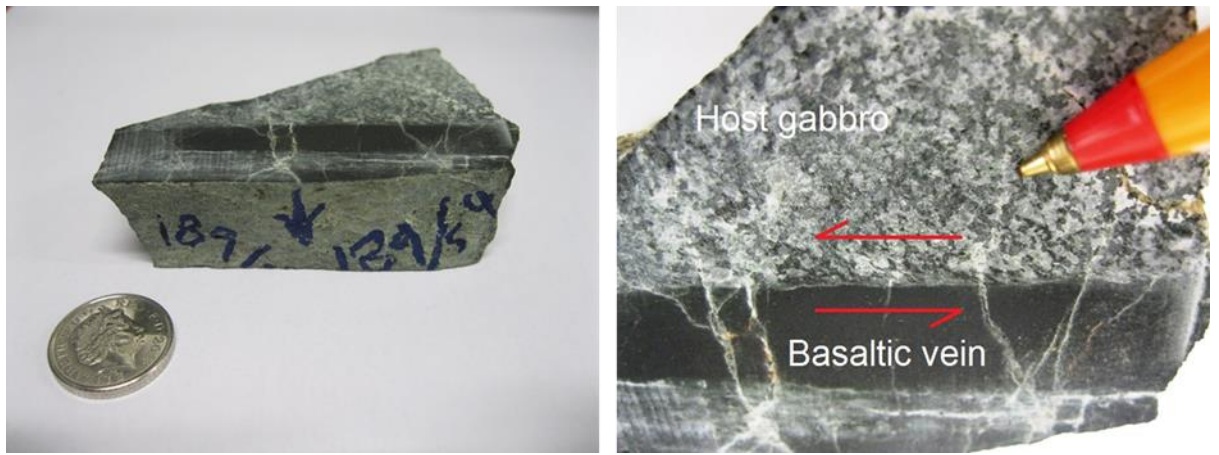


**Figure 4.13.** Hand specimen from the cross-cutting vein of Mersin ophiolite showing a sigmoidal fabric in the host gabbro.

The presence of all the evidence (i.e. reduction of the grain size, porphyroclasts and disrupted grains) gives an important indicator of shear zone processes (Passchier and Trouw, 2005), and gives evidence for solid state shearing that is not seen in the host gabbro, suggesting that the dyke-like veins have taken up strain in the section preferentially (strain partitioning) (Lee et al., 2012).

Kinematic indicators within these rocks (e.g. lineations), are not clearly visible in the field. However, analyses of thin sections cut parallel to strike show a component of sinistral movement for this vein. The shear sense determined from thin section analyses equates to shearing along the basaltic vein with a top to the west sense of displacement in present coordinates.

Samples from site MC10 have also been analysed for anisotropy of low field magnetic susceptibility. They have a prolate (elongate) magnetic fabric with an average Jelinek (1981) shape parameter,  $T = -0.474$ . For prolate anisotropies, the  $k_1$  principal susceptibility axis usually represents the preferred orientation of elongate grains. The mean  $k_1$  axis at site MC10 has an azimuth/plunge of  $263^\circ/10^\circ$  (see Table 5.2), which is sub-parallel to the strike of the sampled vein (which dips at  $52^\circ$  to  $183^\circ$ , striking  $273^\circ$ ), supporting an E-W displacement

along the basaltic shear zone and consistent with the top-to-W shear sense inferred from the thin section analysis. Both AMS and structural fabrics observed in the dyke-like veins are unrelated to magnetic anisotropy lineations in the host gabbros, which at site MC09 have  $k_1$  axes plunging  $14^\circ$  towards  $035^\circ$  (interpreted to reflect magmatic deformation/flow; see Chapter 5). Palaeomagnetic data from the site MC10 dyke-like veins and the host gabbros (site MC09) indicate that both units share the same remanence direction (Table 5.4). This suggests that deformation occurred above the magnetite Curie temperature ( $580^\circ\text{C}$ ), consistent with the mineral assemblages that have been observed through petrographic analyses. Back-stripping the overall net tectonic rotation determined for the cumulate section along the Sorgun Valley (axis =  $051^\circ/27^\circ$ , rotation =  $117^\circ$  clockwise; Chapter 5), results in a restored  $k_1$  axis with an orientation of  $005^\circ/06^\circ$  and an orientation for the dyke-like vein that strikes N-S, dipping to the W. However, this is not likely to be the original orientation at the time of shearing but instead the best estimate of the orientation of the shear zone at the time of blocking in of remanence (i.e. below  $580^\circ\text{C}$ ).

#### **4.4 Summary**

Based on the results of geochemical investigations and petrographic observations a new category of basaltic vein has been identified within the lower crustal section of the Mersin ophiolite. It is clear that these rocks do not have characteristics typical of other late stage dykes found within the ophiolite but rather represent shear zones where intense strain localisation has occurred within the layered gabbros (Passchier and Trouw, 2005). The kinematics of the shear zones discussed above suggests development of these structures oblique to the NNW-SSE orientation of the spreading axis inferred from the magnetic fabric data, suggesting a spreading related origin. Furthermore, the

very rapid transition from undeformed layered gabbro, to intensely recrystallized gabbros within the shear zones suggests that strain localisation may have been facilitated by primary variations within the crystallising gabbro body whilst it was still hot. Possible causes of strain localisation of this nature could be enhanced volatile content and/or local melt pockets within a crystal mush, although the secondary mineralogy associated with the deformation suggests that the gabbros had cooled below 500°C. High volatile content could also be indicated by the generally increased values for LOI within the vein samples compared to the host gabbros. Moreover, microstructural textures of both primary and secondary mineral assemblages in close proximity to the shear zones all support solid state deformation (Vernon, 2000; Passchier and Trouw, 2005).

## Chapter 5

### Palaeomagnetic study of the Mersin Ophiolite

#### 5.1 Introduction

In this chapter, palaeomagnetic and structural analyses are used to quantify and analyse the amount and style of tectonic rotation that has occurred during the evolution of the Mersin ophiolite of the central Taurides of Turkey, and a comparison made with rotations previously documented in ophiolites formed in the southern Neotethyan ocean basin (Troodos and Hatay/Baër-Bassit). The Mersin ophiolite has never been sampled for palaeomagnetic analyses, yet represents one of the best examples of Tethyan-type ophiolites, providing a 3 km long continuous lower oceanic crustal section, consisting predominantly of layered gabbros, that formed by supra-subduction zone spreading within the northern Neotethyan ocean basin during the Late Cretaceous (Parlak *et al.*, 1995; Chapter 3). To achieve the project aims, sampling was conducted mainly along the Sorgun Valley section, where layered gabbros are well exposed. In addition, samples were collected from discrete dykes cutting the mantle sequence and metamorphic sole within the Findikpinari valley area and also from the post-emplacement Miocene sedimentary cover.

#### 5.2 Recap of the context of previous palaeomagnetic results from ophiolites in this region

The Troodos, Hatay and Baer-Bassit ophiolites formed in the southern Neotethyan ocean basin at the same time that the Mersin ophiolite was being formed in the Intra-Tauride ocean basin to the north. Previous palaeomagnetic

analyses in these ophiolites have shown that a large area of southern Neotethyan oceanic lithosphere underwent up to 90° of anticlockwise rotation subsequent to its formation by seafloor spreading (Moores and Vine, 1971; Clube *et al.*, 1985; Clube and Robertson, 1986). The timing of this rotation has been constrained by palaeomagnetic analyses of the sedimentary cover of the Troodos ophiolite (Clube 1985; Clube and Robertson, 1986; Morris *et al.*, 1990) to have begun in the Late Cretaceous and ended by the Eocene. Subsequent palaeomagnetic investigations of the Hatay and Baer-Bassit ophiolites, located further to the east and emplaced onto the Arabian continental margin, showed that these units were also variably rotated in an anticlockwise sense (Morris *et al.*, 2002; Inwood *et al.*, 2009) (Figure 5.1). This suggests that the size of rotated unit is larger than the present day Troodos ophiolite. The data from these ophiolites are best explained by: (i) approximately 60° rotation of an intraoceanic microplate; (ii) subsequent emplacement of part of this microplate onto the Arabian margin, to form the Hatay and Baer-Bassit ophiolite while the Troodos section continued to rotate; and (iii) variable emplacement and post-emplacement-related tectonic rotations.

In addition to these broad, regional-scale results, detailed palaeomagnetic analysis of the Troodos ophiolite has documented tectonic rotations that took place during seafloor spreading, either as tilting of crustal blocks during extensional faulting (Allerton, 1989; Hurst *et al.*, 1992), or as vertical and inclined axis rotations associated with shearing along an oceanic transform fault zone (Allerton, 1989a, b; MacLeod *et al.*, 1990; Morris *et al.*, 1998).

Hence, previous palaeomagnetic research on the Late Cretaceous ophiolites of the Eastern Mediterranean region shows that they have experienced a diverse,

complex history of rotational deformation, including successive phases of spreading-related, emplacement-related and post-emplacement deformation. Until the present study, however, no comparable palaeomagnetic constraints on rotations in the Mersin ophiolite were available or indeed for any ophiolites formed in the northern Neotethyan ocean basin.

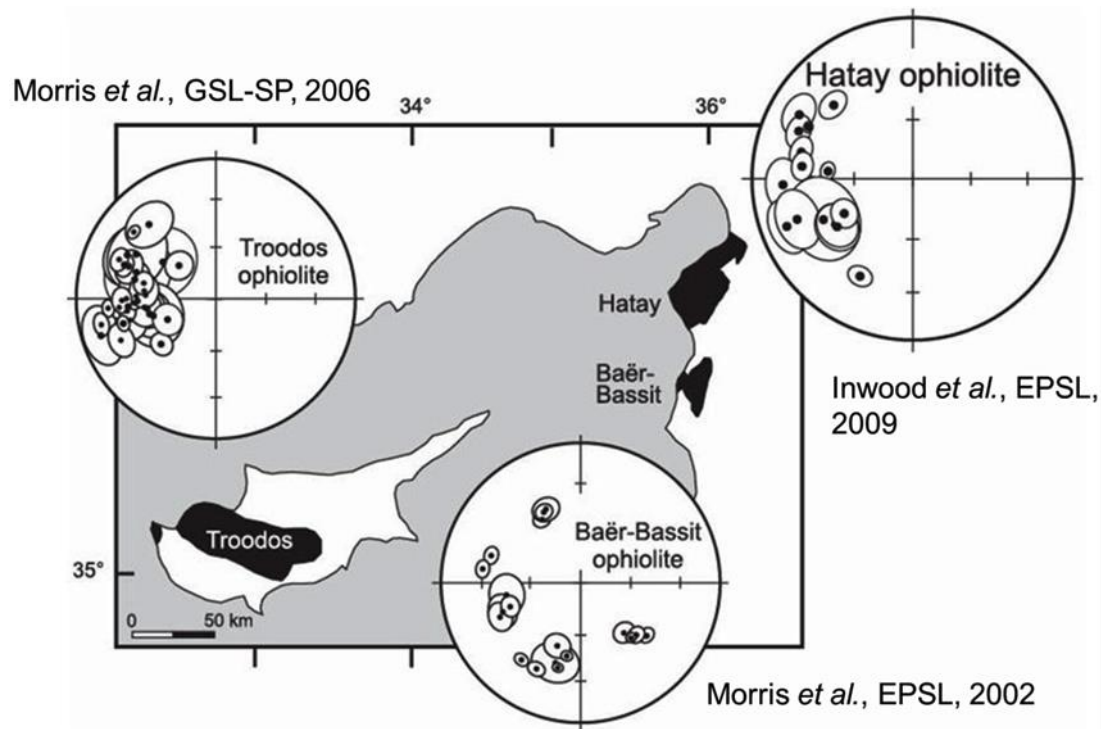


**Figure 5.1.** Stereographic projections of mean remanence directions from other Late Cretaceous ophiolites (Troodos and Hatay/Baër-Bassit ophiolites)

### 5.3 Fieldwork and palaeomagnetic sampling localities

Field sampling was conducted in the Mersin ophiolite during September 2011, mainly along the Sorgun Valley (in the area between the villages of Sorgun and Arslanlı) where layered gabbros and ultramafic cumulates are well-exposed (Figure 5.2 and 5.4). Sampling was carried out using a portable, hand-held rock drill using methods previously described in the section 2.7.1, in addition to block sampling. Fieldwork also included collection of structural data on the orientation

of cumulate layering and cross-cutting basaltic veins and dykes. The Sorgun Valley section was sampled at 18 sites; the first three sites sampled ultramafic rocks, whereas the rest sampled gabbroic rocks. In addition to the main cumulate gabbro sequence, samples were collected from discrete dykes cross-cutting both the metamorphic sole of the ophiolite and tectonized harzburgite, and from basaltic lavas which are located in the Fındıklıpınarı valley area approximately 20 km NE of the Sorgun valley (Figure 5.3), in addition to a single site in Miocene carbonate sediments to test for recent neotectonic rotation. Examples of general field photographs are given in Figures 5.5 and 5.6. Thirty one sites were sampled overall, yielding a total of 289 oriented samples, including hand samples (Table 5.1).

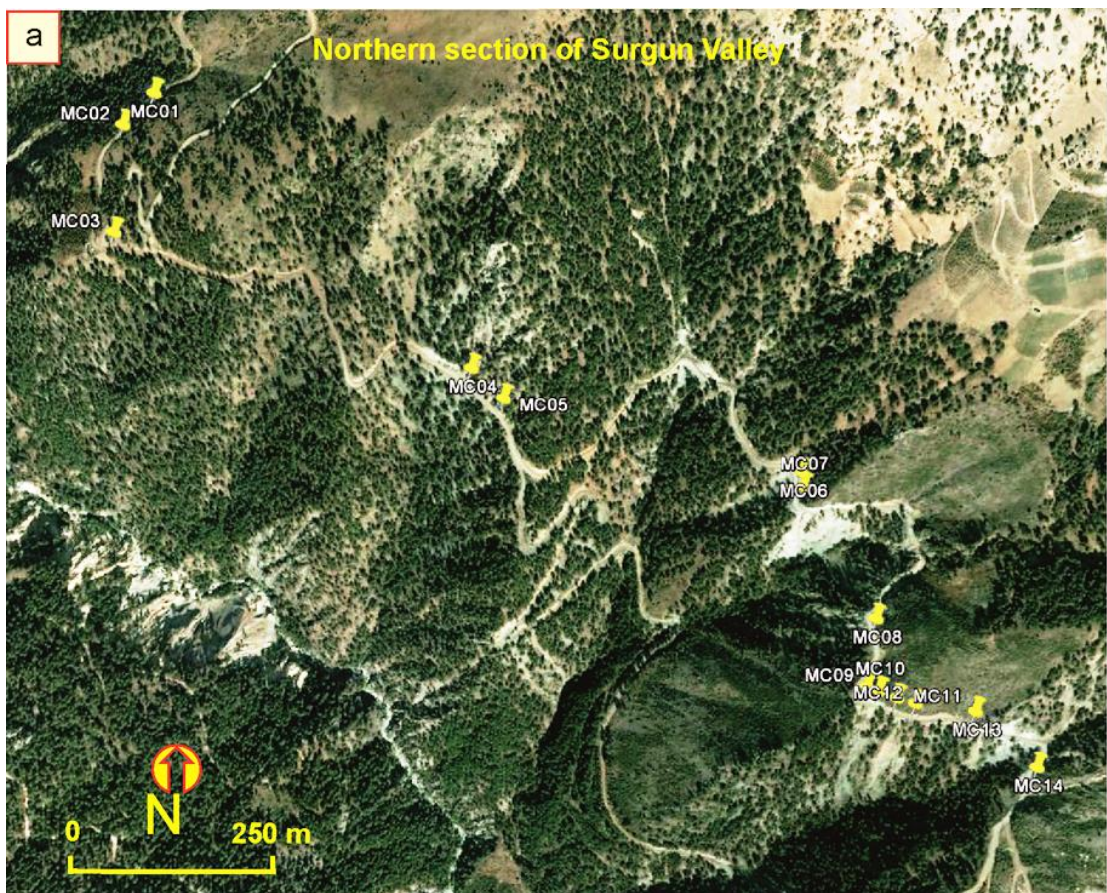


**Figure 5.2.** Google Earth images of studied area showing the sampling sites of the northern and southern sections of the Sorgun Valley. (a) Northern section of the Sorgun valley. (B) Southern section of the Sorgun Valley.

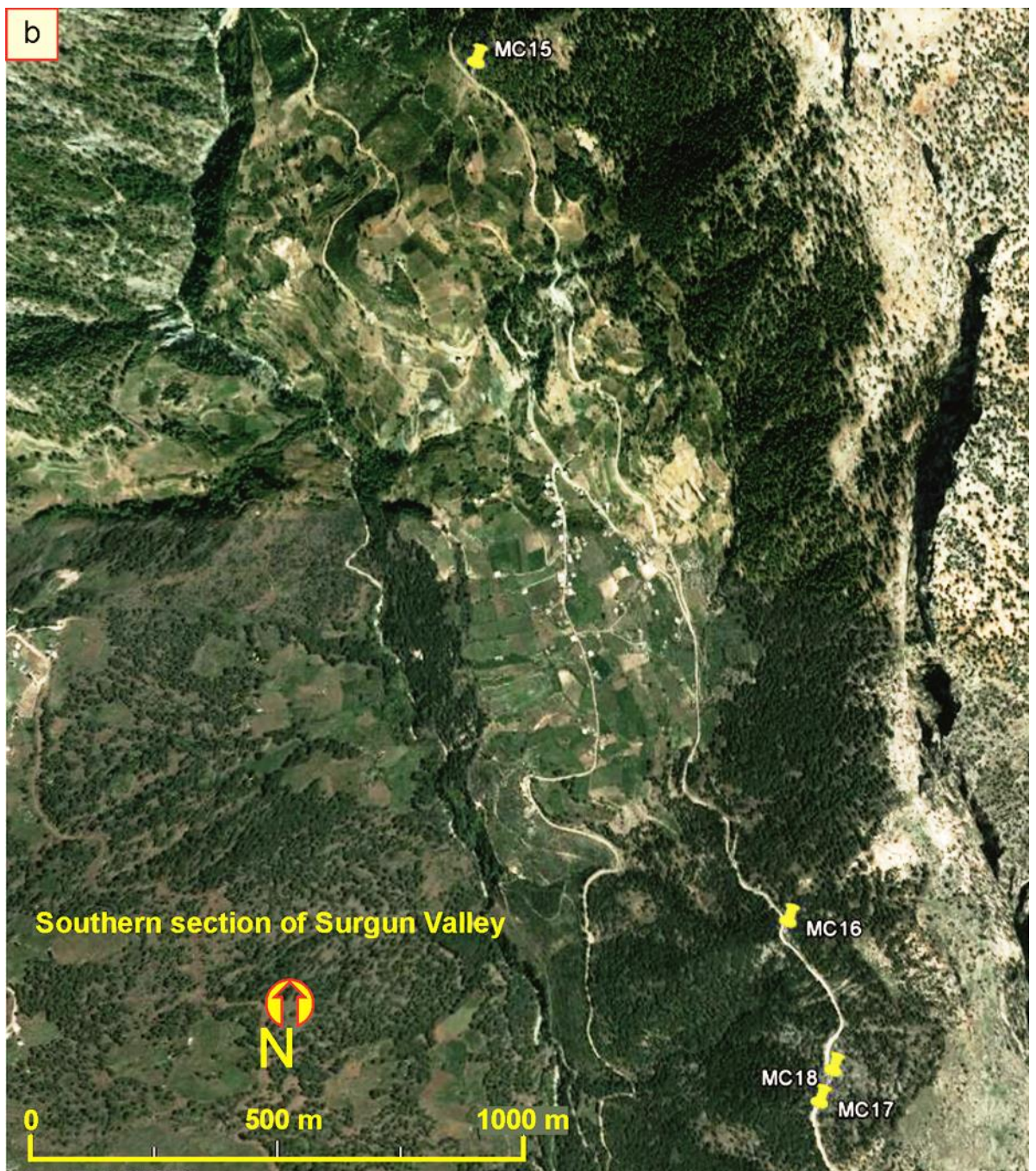
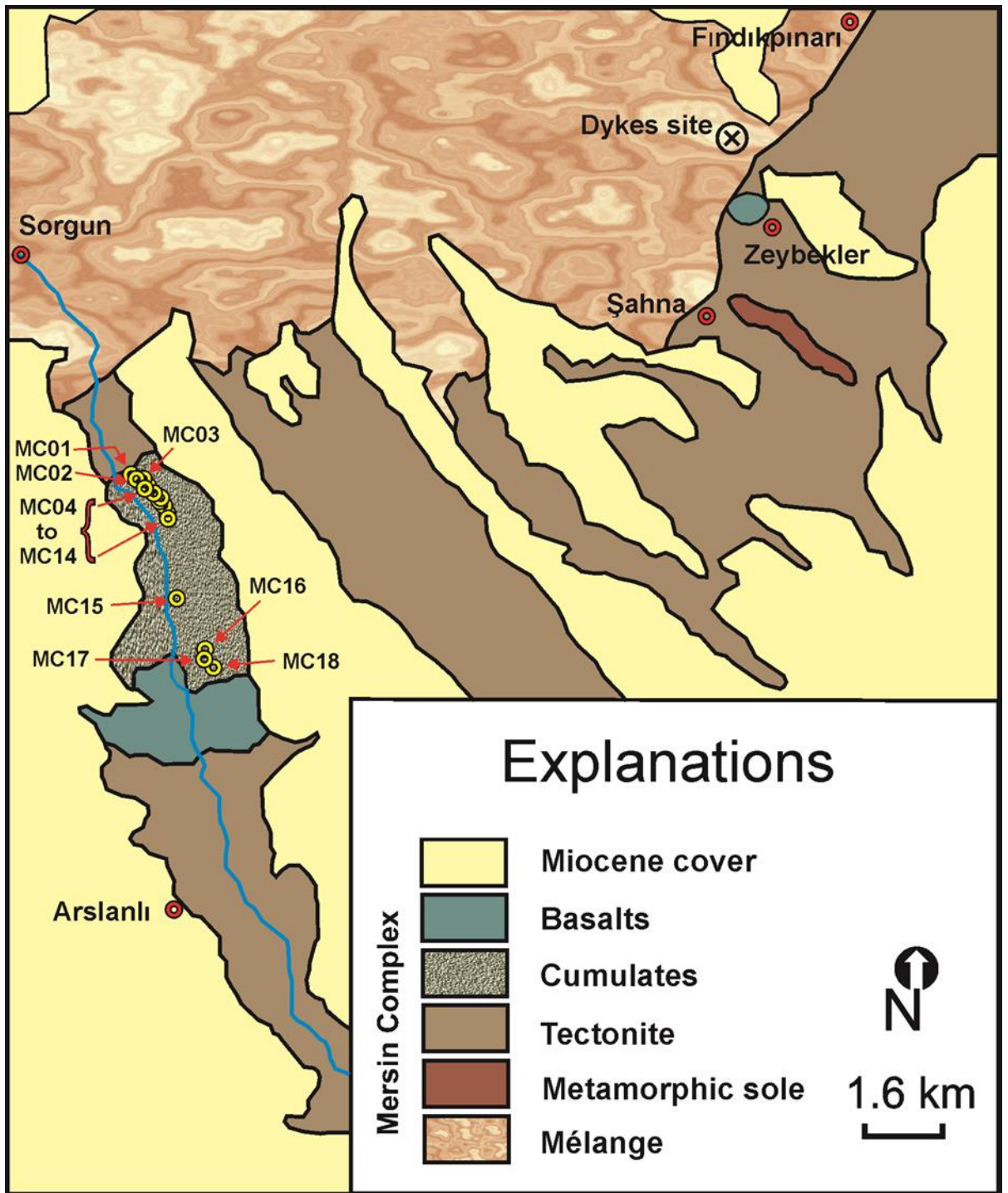


Figure 5.2. (Continued)



**Figure 5.3.** Google Earth image of the Fındıklı valley area showing the localities of the dykes.



**Figure 5.4.** Simplified geological map of the western part of Mersin ophiolite showing the studied area and cumulate and dyke sampling localities (modified from Parlak and Delaloye, 2001).

**Table 5.1.** Summary of the number of samples collected during fieldwork.

Geological unit	No. of Sites	No. of cores	No. of hand samples	No. of specimens
Ultramafic cumulates & Layered gabbros	18	168	12	405
Dykes	11	98	15	215
Basalt lavas	1	15	3	27
Carbonate sediments	1	8	—	16
Total	31	289	30	663



**Figure 5.5.** Fieldwork in the Sorgun valley. (a) Drilling into cumulate gabbro. (b) Taking structural measurements of cumulate layering.



**Figure 5.6.** (a) Massive lava flow sampled at Fındıkpınarı, with columnar jointing visible on the left hand side of the image; (b) sub-horizontally bedded Miocene carbonates exposed at Arslanlı.

## **5.4 Rock magnetic analyses and microscopy**

Quantitative rock magnetic investigations on samples of different lithologies from the study area were performed to find out the carriers of natural remanence.

In addition to the rock magnetic analyses, polished thin section analyses were performed on 28 representative samples from different lithologies of Mersin ophiolite in order to identify the magnetic minerals within these rocks and to determine the preferred alignment of the minerals which are responsible for carrying magnetic anisotropy and remanent magnetization. In addition, these thin sections have been used in petrographic studies, which are described in the sections below and in Chapter 4. All thin section analyses were performed at Plymouth University using an Alphaphot-2 YS2 Polarizing Microscope produced by Nikon, and a JEOL JSM-6610LV Scanning Electron Microscope.

Results of these studies are presented in the following sections.

### **5.4.1 Isothermal remanent magnetization (IRM) analyses**

The isothermal remanent magnetization (IRM) technique represents one of the easiest methods to obtain useful information about the magnetic mineralogy of rocks (see section 2.7.5), because each magnetic mineral has its own distinctive IRM curve when the acquired magnetization data are plotted versus the applied field.

In this study, IRM acquisition experiments were performed on samples from ultramafic and gabbroic cumulates, dykes, basaltic lavas and Miocene carbonates.

All IRM acquisition curves from the various lithologies are shown in Figure 5.7. In general, all samples from all lithologies showed a sharp increase in magnetization in fields less than 200 mT, reaching saturation of remanence at fields mainly below 400 mT. Backfield demagnetization of IRM for all samples yielded coercivity of remanence values that ranged from 24 to 53 mT. Together, these data suggest that low to medium coercivity fine-grained magnetic carriers are dominant in these rocks, most likely single-domain (SD) or pseudo-single domain (PSD) magnetite and/ or titanomagnetite, with no indication of haematite or goethite. These results are entirely compatible with those obtained in other Neotethyan ophiolites (e.g. Troodos, Hatay and Baer-Bassit; Morris et al., 1998, 2002; Inwood, 2005), which also show a dominance of low coercivity magnetite.

#### **5.4.2 Thermomagnetic analysis**

High-temperature susceptibility experiments were performed on 20 representative samples from different lithologies and all the measurements were carried out using argon gas to reduce the oxidation of the samples during heating. Results from representative samples are shown in Figure 5.8. The majority of samples showed a clear decrease in susceptibility upon heating to around 580°C, suggesting the presence of magnetite as a dominant magnetic mineral in these rocks (Butler, 1998). Numerous samples showed a good correlation between heating and cooling curves and are reversible, indicating that no new magnetic minerals have been created during the heating (e.g. MC0103; Figure 5.8). A few samples (e.g. MC1804; Figure 5.8) show a bump in the heating curve between 150 °C and 400 °C. The increasing limb of this bump is reversible until 300°C, but the curve becomes irreversible after further

heating, suggesting the presence of titanomagnetite/titanomaghemite (Morris *et al.*, 2002). This observation is supported by SEM analyses described below. In the heating curve of sample MD0708 (Figure 5.8), a distinct decrease in susceptibility is observed up to c. 400°C that suggests that the initial susceptibility in this sample is predominantly carried by paramagnetic minerals. This is followed by a rapid increase of susceptibility after 400°C and subsequent decrease to reach a Curie temperature at 580°C. This suggests the production of significant fine-grained magnetite during heating to high temperatures, leading to higher susceptibility during the cooling cycle. A few samples (e.g. MD4H301) showed relatively low susceptibilities and parabolic heating curves, indicating that these rocks are dominated by paramagnetic minerals. Sample MS0106 (from Miocene sediment) showed a very low susceptibility and a noisy signal, suggesting very low concentrations of magnetite in these carbonate rocks.

#### **5.4.3 Petrographic and SEM analyses**

The rock magnetic observations suggesting a dominance of magnetite in most sampled lithologies are in agreement with petrographic and SEM analyses, where nearly all the samples from gabbroic cumulates and dykes again were seen to have magnetite and titanomagnetite as the dominant opaque constituents. Optical and SEM analyses show that opaque minerals in the ultramafic rocks are mostly in the form of secondary magnetite, probably produced by serpentinization of the olivine in these rocks (Figures 5.9 and 5.10).

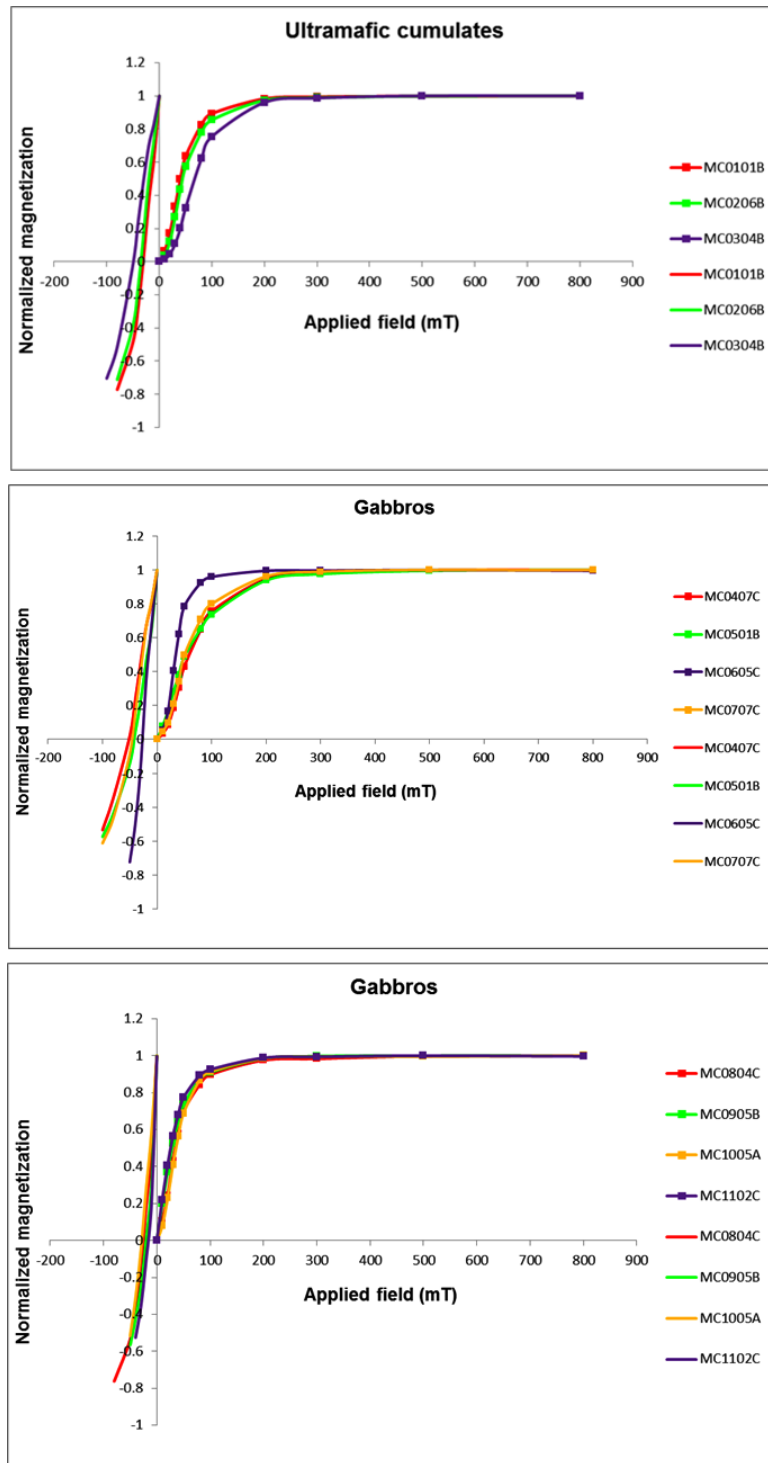


**Figure 5.7.** Isothermal remanent magnetization (IRM) curves and backfield demagnetization curves for representative samples of the Mersin Ophiolite Complex and Miocen sedimentary cover.

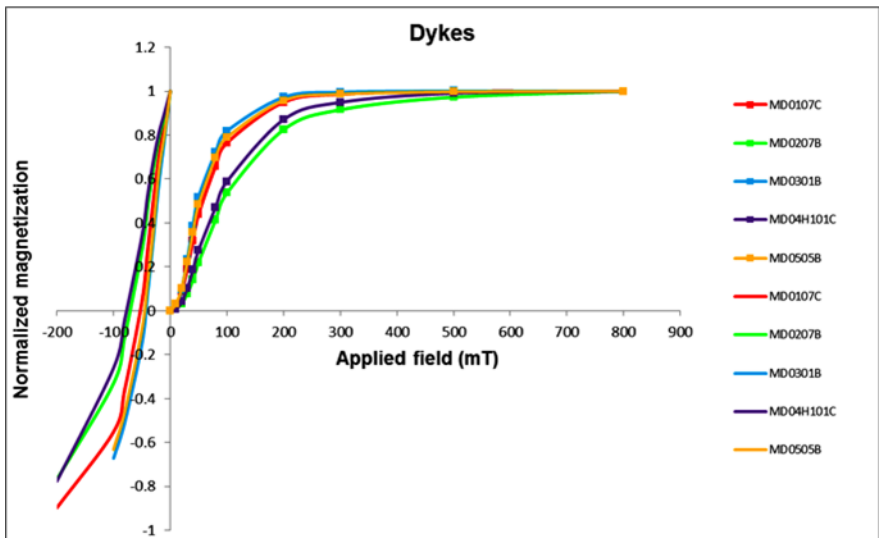
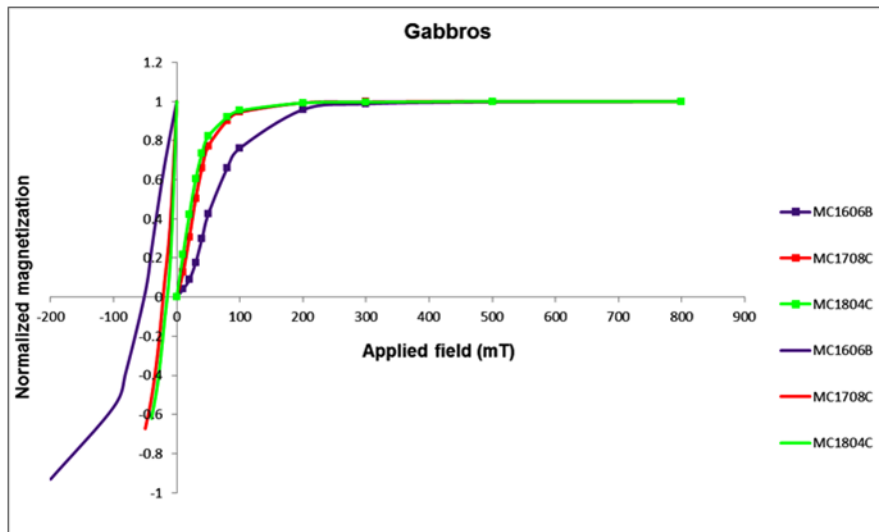
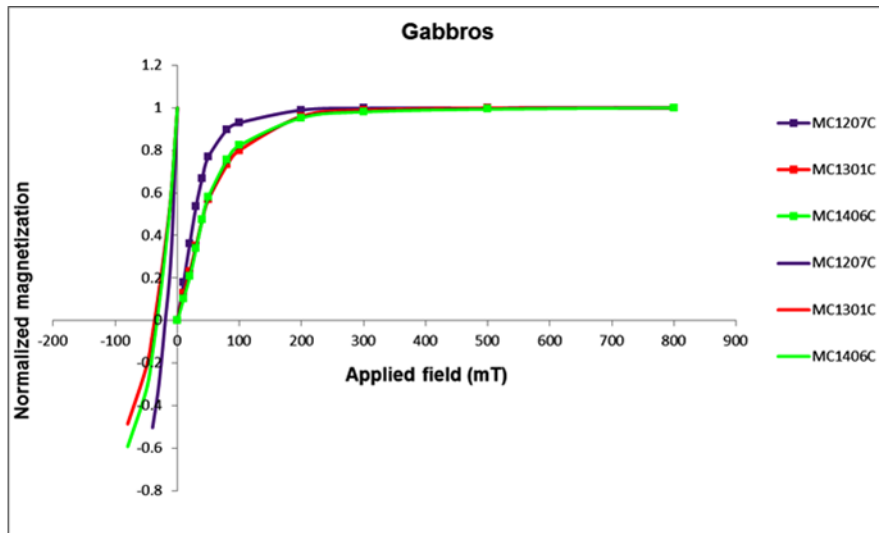


Figure 5.7. (Continued)

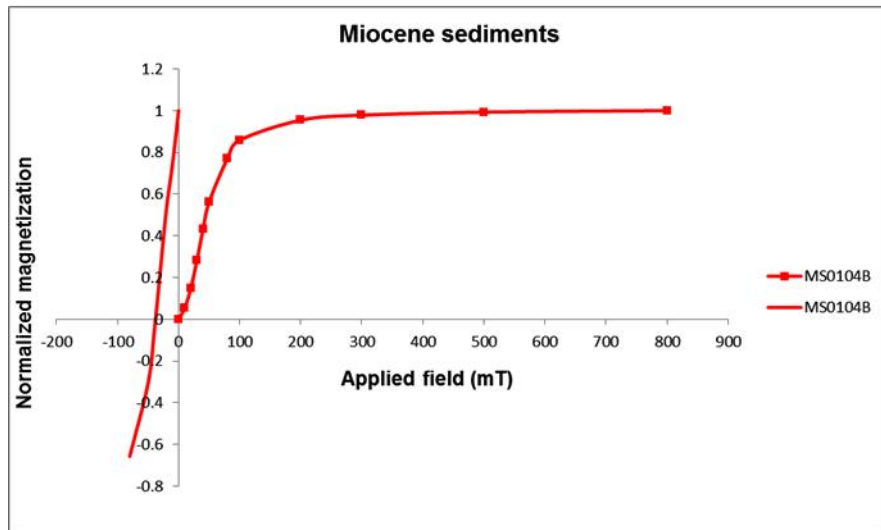
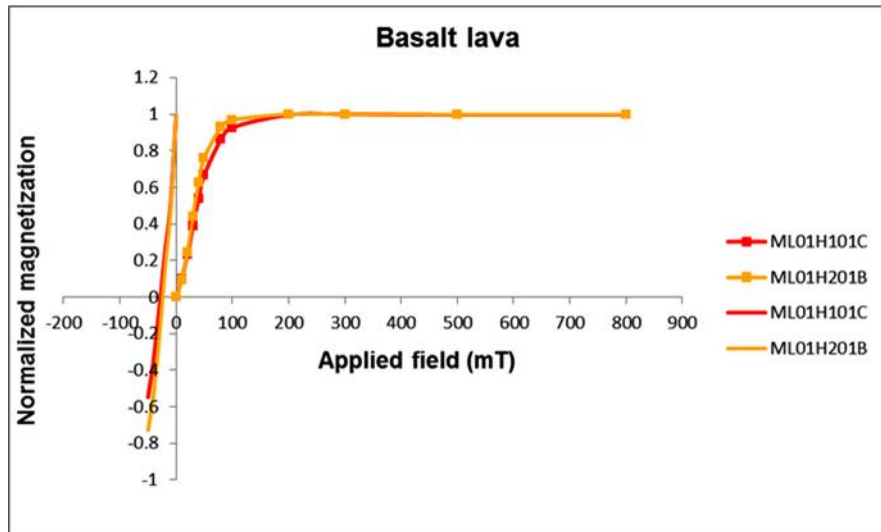
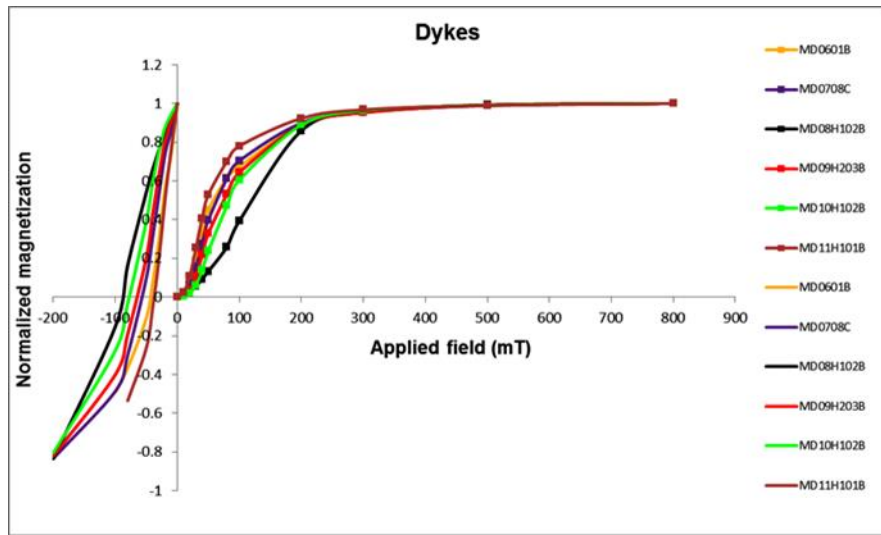
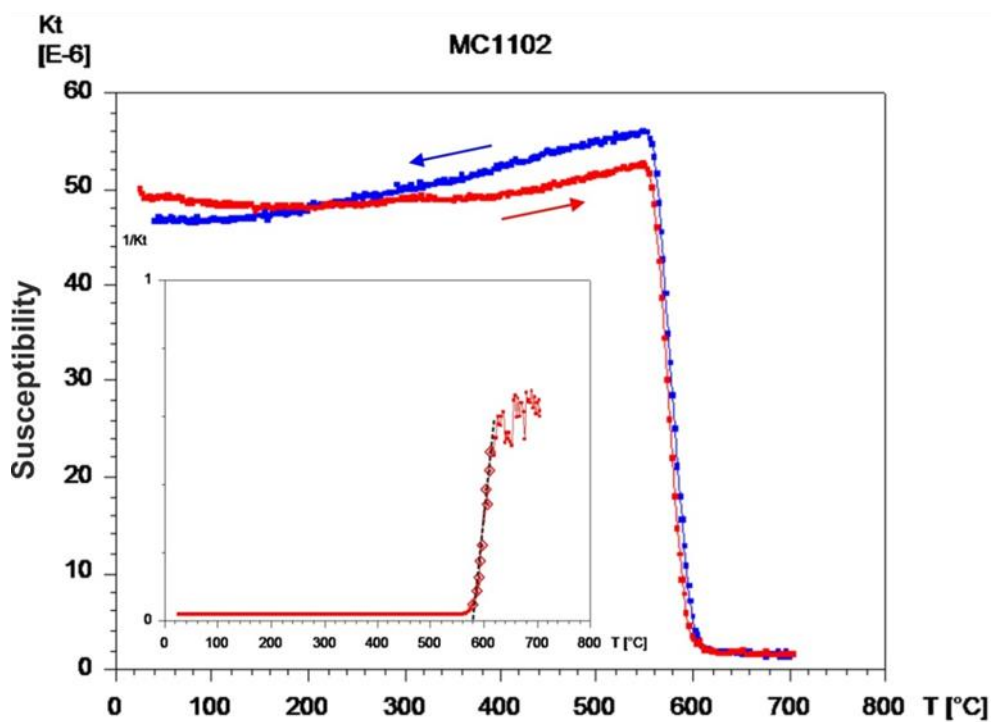
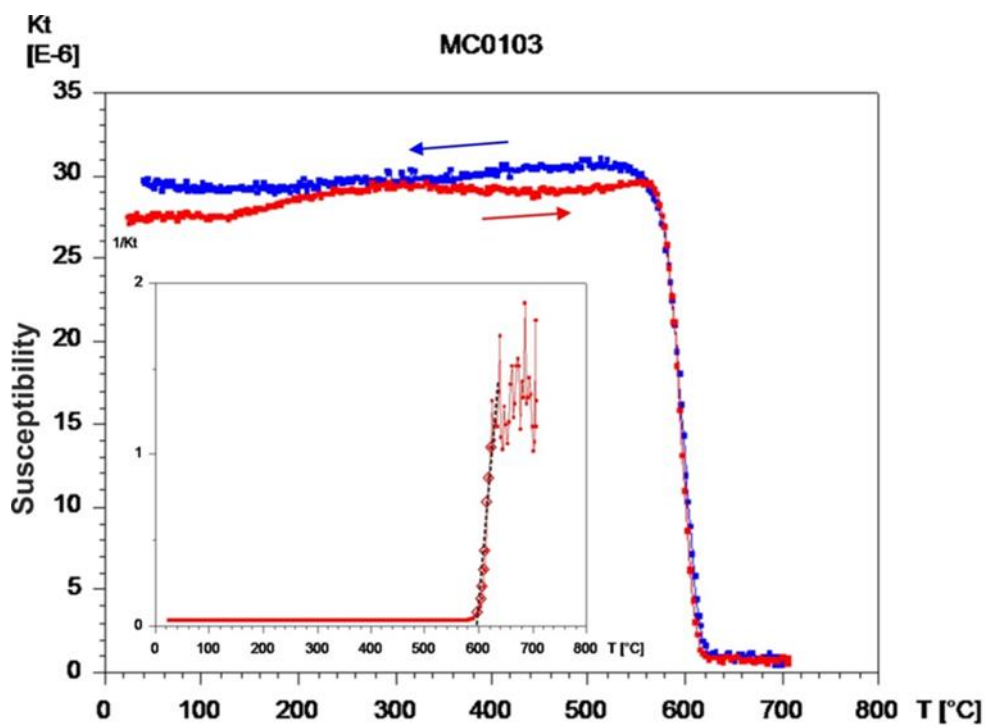


Figure 5.7. (Continued)



**Figure 5.8.** Curie temperature results from representative samples of Mersin Ophiolite Complex and its Miocene sedimentary cover. Note: the red curve illustrates the heating from room temperature to 700°C, and the blue curve illustrates the cooling from 700°C to room temperature.

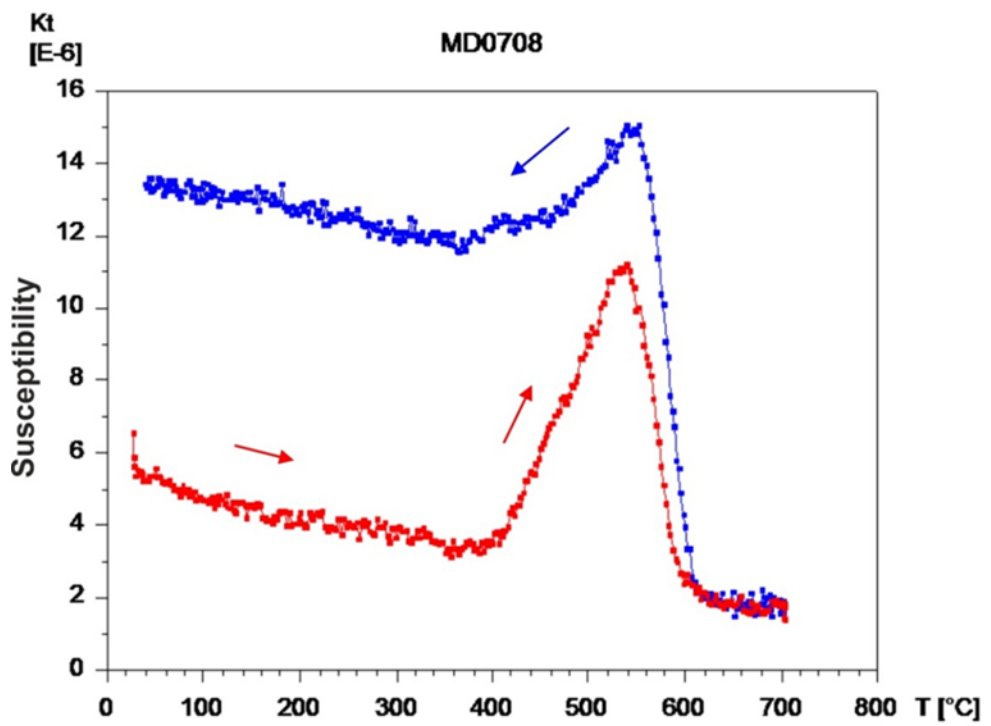
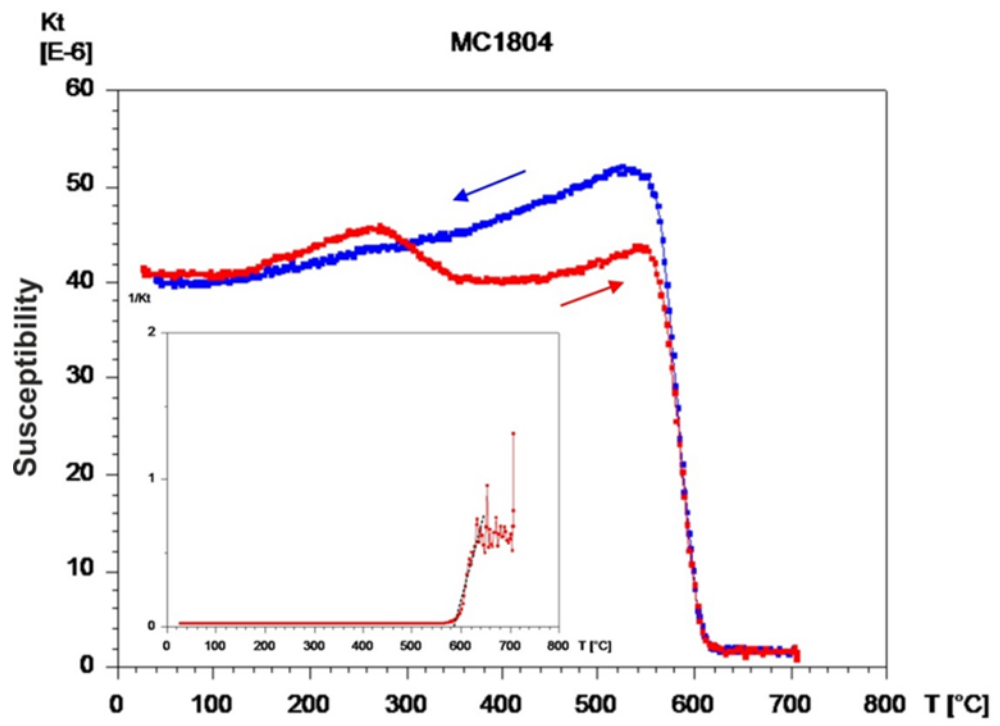


Figure 5.8. (Continued)

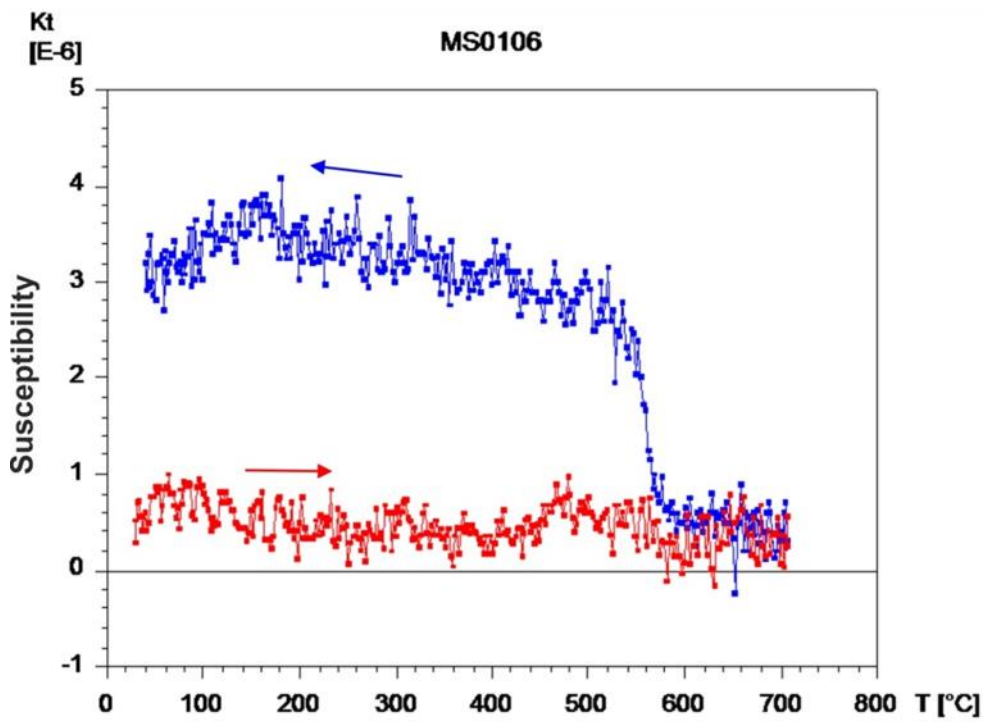
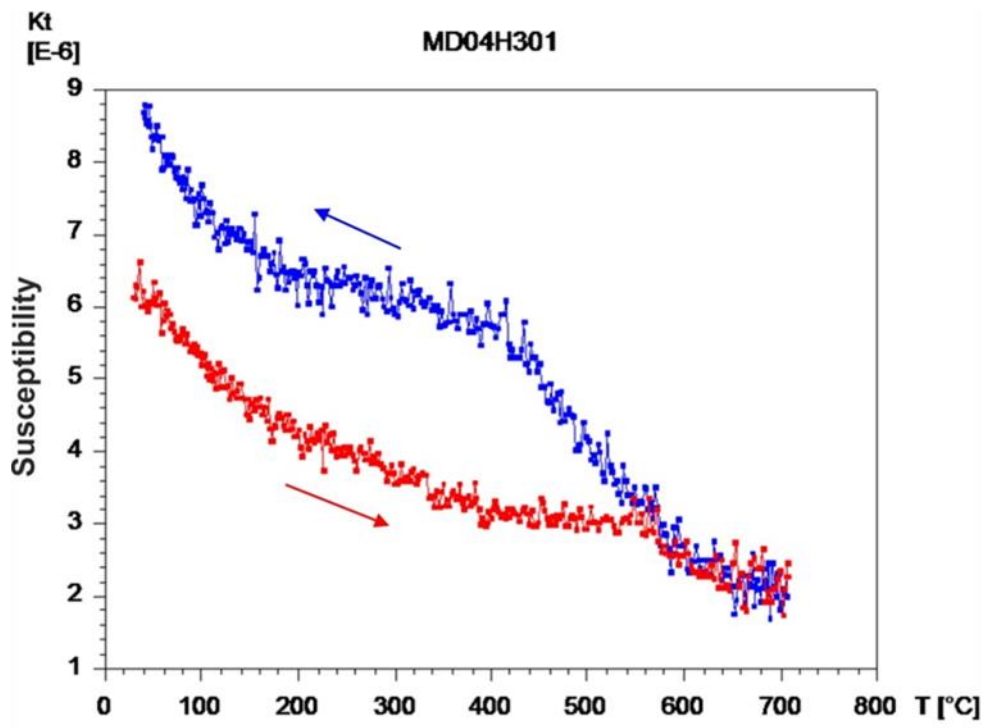
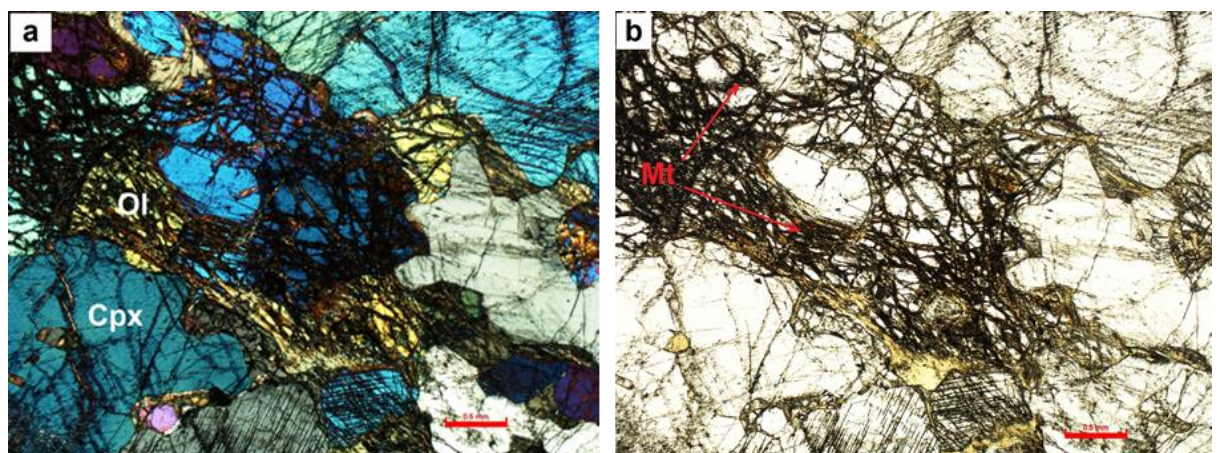


Figure 5.8. (Continued)

SEM observations of polished thin sections for some samples from gabbros showed numerous Fe-Ti oxide crystals with a few crystals of iron sulphide (i.e. pyrrhotite) as the important types of ferromagnetic minerals present. These are considered to be the important remanence carriers in these rocks (Butler, 1998). In some samples, these Fe-Ti oxide crystals appear in the form of a large number of coarse-grained opaque minerals ( $\geq 1$  mm), generally with little alteration (Figures 5.11, to 5.13). This observation is consistent with the thermomagnetic analyses described above. Primary Fe-Ti oxides are often common constituents in mafic rocks which form during magmatic differentiation processes at nearly 1300°C. However, Ti-poor titanomagnetite usually exsolves from plagioclase or pyroxene within plutonic rocks (Butler, 1998).

Dykes generally displayed a range of paramagnetic/diamagnetic minerals (e.g. pyroxene, amphibole and plagioclase) and opaque minerals, where magnetite and titanomagnetite are the dominant ferromagnetic minerals. Occasionally, some samples showed pyrrhotite (e.g. Figures 5.14 and 5.15), which has been also observed through thermal demagnetization analysis (Figure 5.34).



**Figure 5.9.** Photomicrographs of an ultramafic cumulate sample (MC0203B) from the Mersin ophiolite showing secondary magnetite produced by serpentinization of olivine. (a) Under crossed polars. (b) Under plane-polarized light. Scale bar: 0.5 mm. (Cpx = clinopyroxene; Ol = olivine; Mt = magnetite).

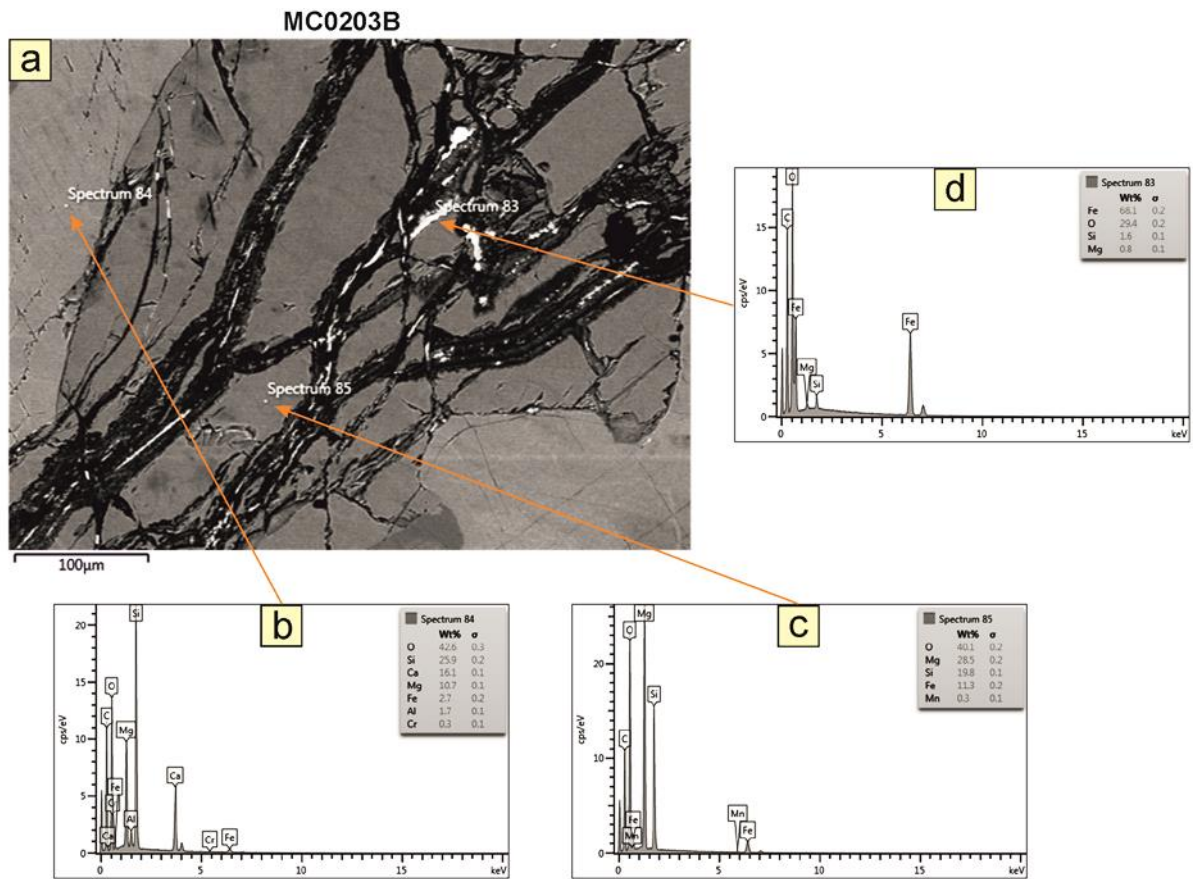


**Figure 5.10.** SEM photograph and energy-dispersive X-ray (EDX) spectral analysis of sample MC0203B, confirming presence of secondary magnetite within olivine grains.

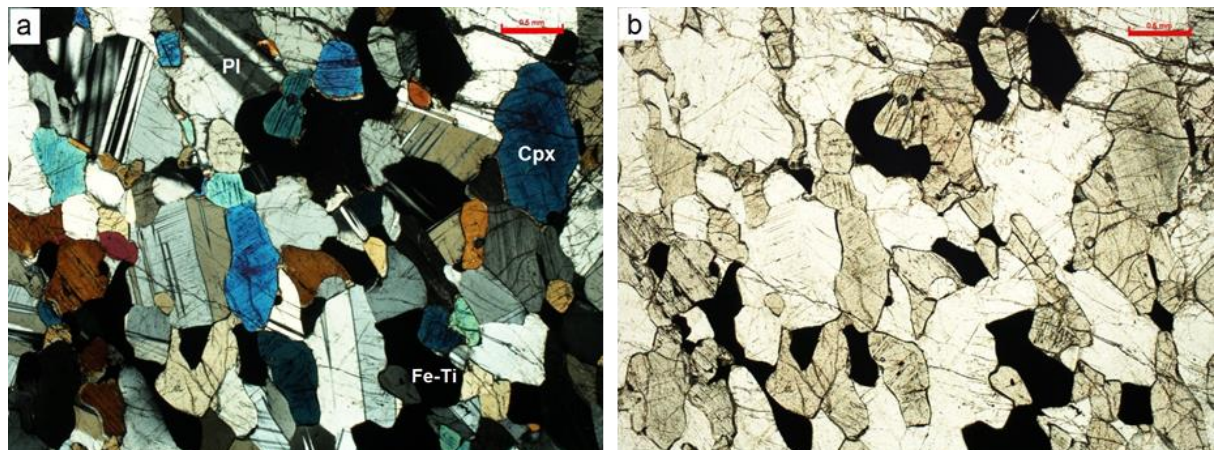


**Figure 5.11.** Optical photomicrographs of a gabbro sample (MC1505C) from the Mersin ophiolite showing the Fe-Ti oxide minerals along with clinopyroxene and plagioclase. (a) Under crossed polars. (b) Under plane-polarized light. Scale bar: 0.5 mm. (Cpx = clinopyroxene; Pl = plagioclase; Fe-Ti = Fe-Ti Oxide).

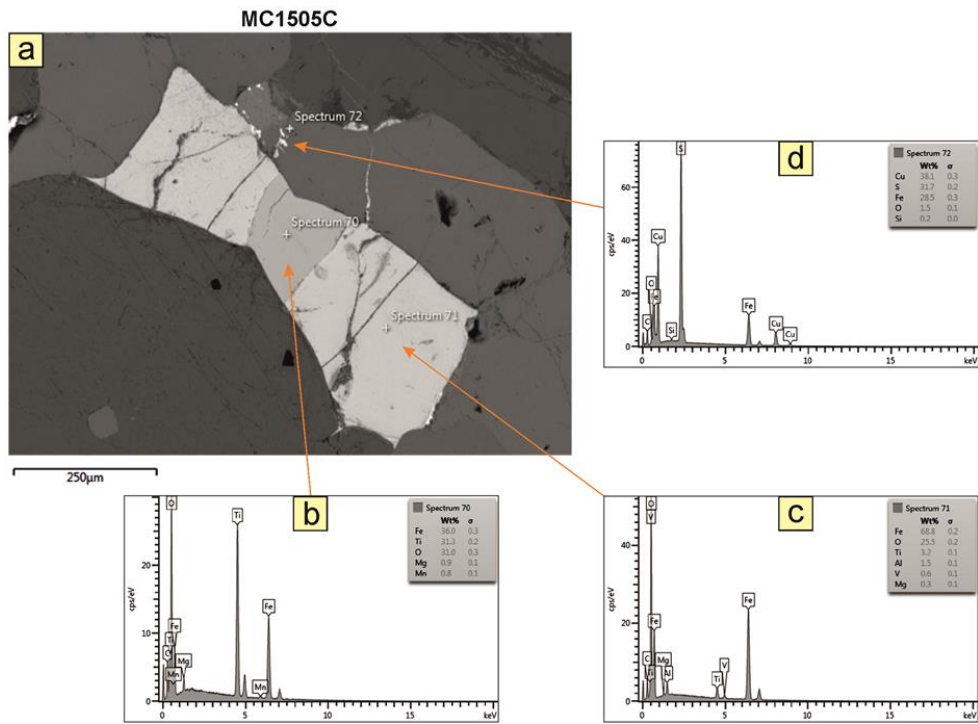


**Figure 5.12.** SEM photograph and EDX spectral analysis of gabbro sample MC1505C, showing variations in Ti content within a titanomagnetite grain.

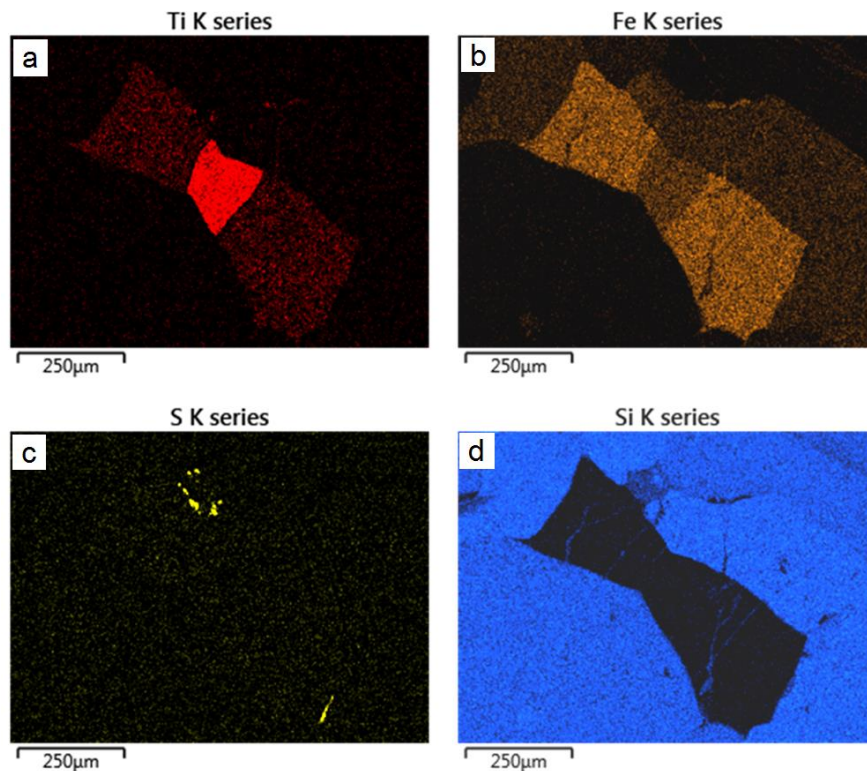
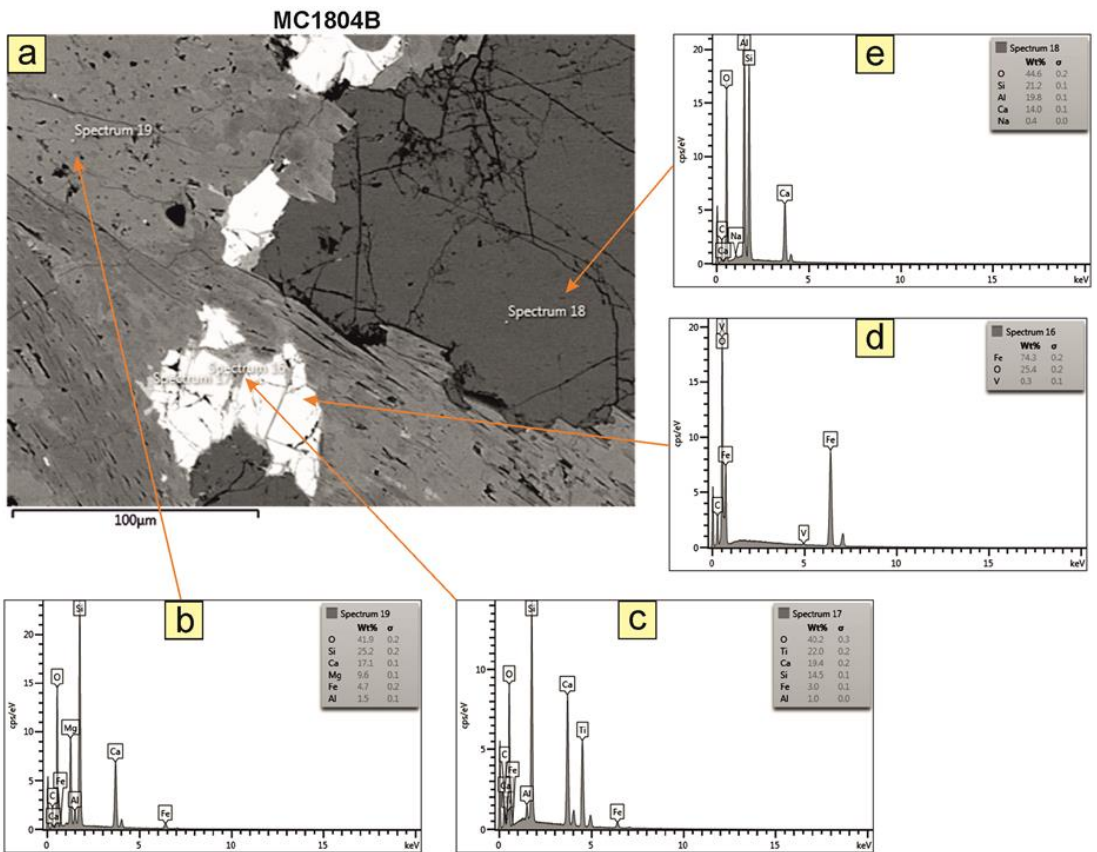
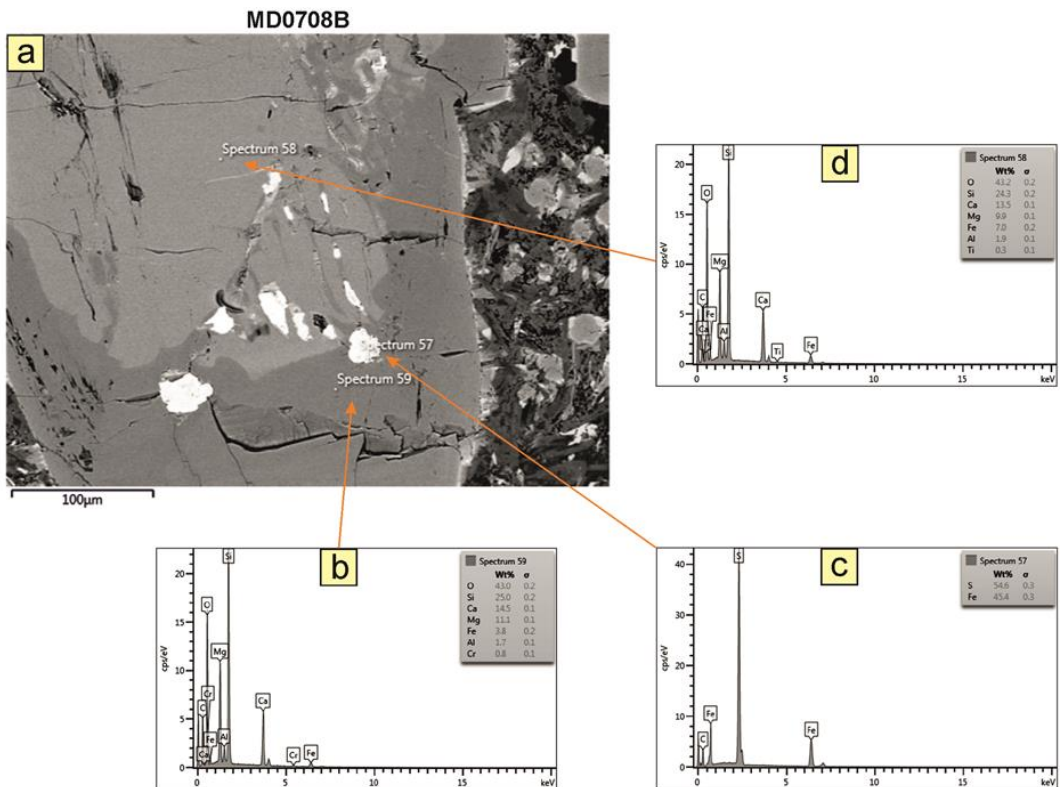


**Figure 5.13.** SEM images of a gabbro sample (MC1505C) from the Mersin ophiolite showing the concentrations of the Fe, Ti, S and Si. (a) Concentration of the titanium (Ti) in red colour. (b) Concentration of the iron (Fe) in brown colour. (c) Concentration of the Sulfur (S) in yellow colour. (d) Concentration of the silicon (Si) in blue colour.



**Figures 5.14 (above) and 5.15 (below).** SEM photograph and EDX spectral analysis of gabbro sample MC1804B and dyke sample MD0708B, showing presence of magnetite and subordinate pyrrhotite.



## 5.5 Magnetic fabric analyses and petrofabric observations

### 5.5.1 Anisotropy of magnetic susceptibility results

The anisotropy of low-field magnetic susceptibility (AMS) technique was used to identify the orientation and degree of development of magnetic fabrics of Fe-bearing grains in the sampled rocks. AMS of 663 specimens from 31 sites of ultramafic and gabbroic cumulates, dykes and Miocene carbonate sediments were determined using a KLY-3 Kappabridge (AGICO, Brno, Czech Republic) at Plymouth University (Figure 2.18a). All AMS measurements were carried out before the specimens were subjected to demagnetization during palaeomagnetic analysis. Many anisotropy factors are conventionally used to describe the AMS fabric of rocks. In this study the Jelinek Pj and T parameters are used to describe the degree of magnetic anisotropy and the shape of the AMS ellipsoid, respectively (Tarling and Hrouda, 1993). These parameters are normally plotted against each other in the form of a Jelinek plot. Values of T range from +1 to -1, where positive values refer to oblate magnetic fabric shapes (disks) and negative values refer to prolate magnetic fabric shape (rods or cigars) (Tarling and Hrouda, 1993).

#### *5.5.1.1 Bulk susceptibility and anisotropy parameters*

All samples from the ultramafic and gabbroic cumulates show intermediate to high bulk susceptibilities, ranging from  $4 \times 10^{-4}$  to  $5.6 \times 10^{-3}$  SI and  $1.8 \times 10^{-4}$  to  $2.5 \times 10^{-2}$  SI respectively, indicative of a ferrimagnetic mineralogy (e.g. magnetite). These observations are consistent with results of rock magnetic analyses that demonstrate the presence of magnetite. Dyke and lava samples also show intermediate to high bulk susceptibility, ranging  $4.9 \times 10^{-4}$  to  $1.3 \times 10^{-2}$  SI and  $3.9 \times 10^{-2}$  to  $9.1 \times 10^{-2}$  SI respectively, indicative of a ferrimagnetic

mineralogy, and again these observations are consistent with presence of magnetite inferred from rock magnetic data. In contrast, results from Miocene carbonates have low bulk susceptibilities, ranging from  $2.6 \times 10^{-6}$  to  $1.4 \times 10^{-5}$  SI, indicative of a mixture of diamagnetic and paramagnetic minerals in these rocks.

Both gabbros and dykes showed a mixture of oblate and prolate magnetic fabric shapes, and the corrected anisotropy degree,  $P_j$ , at all gabbro and dyke sites ranges from 1.003 – 1.431 and 1.004 – 1.109 respectively. Both basaltic lavas and Miocene carbonates showed only oblate magnetic fabric shapes, with corrected anisotropy degrees of 1.011 – 1.061 and 1.023 – 1.141 respectively (Figure 5.16 and Tables 5.2 and 5.3).

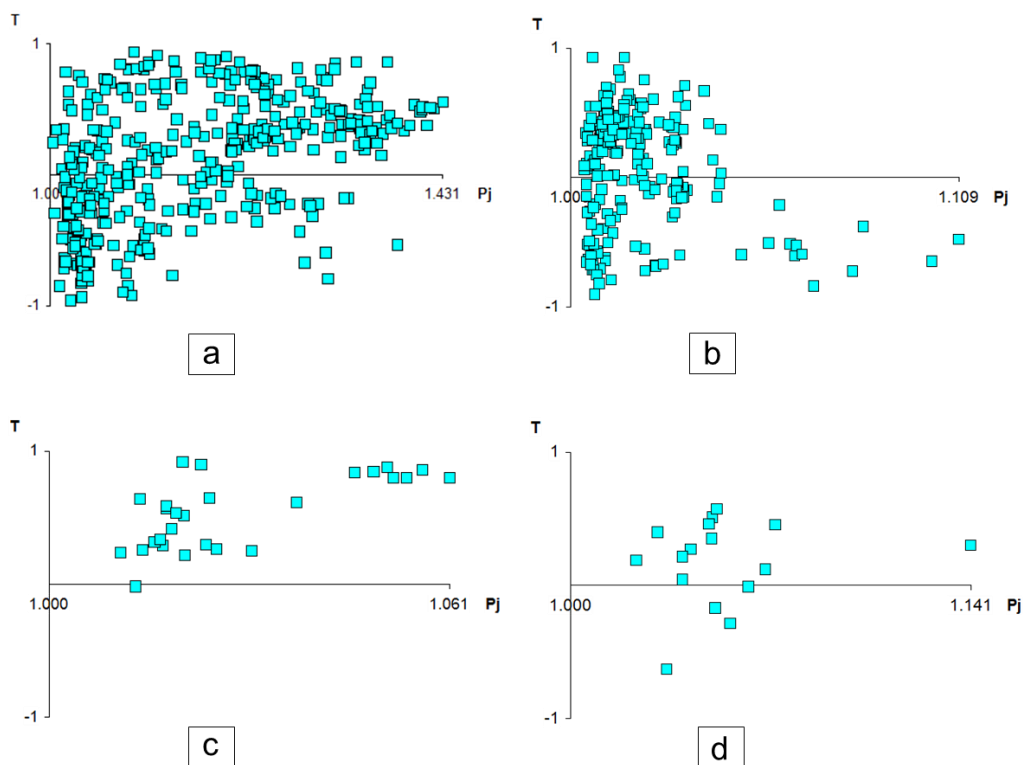


**Figure 5.16.** Degree of anisotropy  $P_j$ , versus shape parameter  $T$  diagram (Jelinek, 1981) for rocks from the Mersin ophiolite. (a) Ultramafic and gabbroic cumulates. (b) Discrete dykes. (c) Lava flow samples. (d) Miocene sediments.

**Table 5.2.** Magnetic fabric results for ultramafic and gabbroic cumulates of the Mersin ophiolite.

		Mean orientation of the axis															
Site	Unit	n	K1				K2				K3				Pj	T	
			Susceptibility	Dec	Inc	Conf. angles	Susceptibility	Dec	Inc	Conf. angles	Susceptibility	Dec	Inc	Conf. angles			
<b>Sorgun Valley section</b>																	
MC01	Ultramafic cumulate	16	3.72E-03	262.4	36.3	23.3/14.4	3.58E-03	148	29.3	78.3/15.7	3.56E-03	30.1	39.7	78.3/18.7	1.048	-0.824	
MC02	Ultramafic cumulate	16	3.43E-03	71	19.4	8.4/3.3	3.24E-03	268.2	69.7	16.8/7.8	2.94E-03	163	5.5	16.8/4.1	1.168	0.258	
MC03	Ultramafic cumulate	16	1.12E-03	107.9	51	57/16.4	1.12E-03	257.8	35	57.4/24.3	1.09E-03	358.6	15	29.9/12	1.036	0.776	
MC04	Gabbro	19	3.65E-04	279.9	23	12.5/7.2	3.59E-04	19.4	21.3	27.7/9.4	3.57E-04	147.6	57.8	27/6.4	1.024	-0.554	
MC05	Gabbro	19	1.13E-03	51.9	5.2	15.6/3.3	1.10E-03	146	38.6	15.2/3.9	1.03E-03	315.4	51	4.9/3.8	1.101	0.452	
MC06	Gabbro	36	5.93E-04	242.9	1.1	16.8/5.6	5.70E-04	333	6.2	54.2/4.4	5.61E-04	143	83.7	54.3/10	1.059	-0.407	
MC07	Gabbro	24	5.26E-04	249.4	39.7	4.9/1.3	5.12E-04	358.1	21.1	5.2/4.3	5.10E-04	109.1	42.9	4.7/1.3	1.036	-0.714	
MC08	Gabbro	23	4.40E-03	55.3	9.6	8.3/4.4	4.10E-03	153.4	39.7	8.3/6.3	3.67E-03	314.3	48.7	6.8/3.7	1.197	0.195	
MC09	Gabbro	22	1.80E-03	35.3	14.1	16.6/3.8	1.69E-03	136.4	37.5	17.9/6.3	1.52E-03	288.5	49.1	11.1/4.2	1.185	0.295	
MC10	Gabbro	23	9.91E-04	263	10	24.4/17.5	9.51E-04	155.2	60	40.1/17.5	9.38E-04	358.4	27.9	42.3/16.1	1.058	-0.474	
MC11	Gabbro	44	1.83E-02	219.1	9.4	5.2/2.7	1.63E-02	122.4	35.2	12.4/3.9	1.51E-02	321.8	53.2	12.4/3	1.214	-0.182	
MC12	Gabbro	23	1.73E-02	217.1	18	5.6/2.5	1.61E-02	105	49.2	5.6/1.6	1.37E-02	320.4	35.1	2.6/1.5	1.273	0.373	
MC13	Gabbro	19	1.69E-03	80.8	16.1	12.4/3.3	1.63E-03	171.2	1.4	16/4.8	1.42E-03	265.9	73.9	11.6/3.5	1.198	0.566	
MC14	Gabbro	22	1.43E-03	79.4	8.9	11.2/3.3	1.40E-03	169.4	0.1	11.2/4	1.23E-03	259.9	81.1	4.4/2.8	1.18	0.67	
MC15	Gabbro	23	2.10E-01	295.8	26.2	6.5/3.4	1.88E-01	200.6	10.4	6.4/2.4	1.55E-01	90.8	61.5	4.0/2.0	1.332	0.371	
MC16	Gabbro	17	6.38E-04	63.6	7.6	36.9/5.7	6.33E-04	331.2	17.1	40.2/24.5	6.21E-04	176.6	71.2	31.2/3.4	1.029	0.41	
MC17	Gabbro	19	7.38E-03	123.4	7.3	14.3/6.9	7.27E-03	25.6	46.7	14.4	6.42E-03	220.1	42.4	8.0/3.3	1.164	0.782	
MC18	Gabbro	24	5.64E-03	277.7	11	40.4/16.4	5.50E-03	38.9	69.4	38.2/15	5.29E-03	184.3	17.2	34.7/15.6	1.067	0.185	

**n** = number of specimens; **Pj** = corrected anisotropy degree; **T** = shape parameter; **Dec** = declination; **Inc** = inclination.

**Table 5.3.** Magnetic fabric results for dykes of the Mersin ophiolite.

**Mean orientation of the axis**

Site	Unit	n	K1				K2				K3				Pj	T
			Susceptibility	Dec	Inc	Conf. angles	Susceptibility	Dec	Inc	Conf. angles	Susceptibility	Dec	Inc	Conf. angles		
<b>Fındıklı Valley section</b>																
MD01	Dykes hosted by Mantle	21	7.86E-04	55	15.3	8.1/6.9	7.80E-04	230.7	74.6	13.4/6.2	7.75E-04	324.7	1.1	14/5.9	1.015	-0.078
MD02		16	1.64E-03	320.2	22.3	15.7/7.3	1.59E-03	137	67.7	49.2/7.7	1.58E-03	229.7	1.1	49.4/8	1.038	-0.681
MD03		17	6.67E-04	109.6	29.2	12.9/4.0	6.64E-04	216.6	27.6	13.0/4.7	6.58E-04	314.7	47.7	5.2/4.2	1.014	0.526
MD04		19	6.83E-04	117	44.9	28.1/6.6	6.82E-04	26.2	0.9	27.9/5.7	6.75E-04	295.3	45.1	8.9/3.4	1.014	0.664
MD05		22	7.47E-04	206.4	0.2	4.2/2.3	7.37E-04	116.3	23.3	9.2/3.7	7.27E-04	296.9	66.7	9.1/2.7	1.028	0.034
MD10		18	6.28E-04	64.3	28.4	20.1/9.7	6.27E-04	196.4	51.1	19.9/12.0	6.23E-04	320.3	24.2	15.1/3.8	1.008	0.489
MD11		20	9.04E-04	78	73.9	20.0/9.7	8.96E-04	347	0.3	25.0/11.7	8.91E-04	256.9	16.1	26.3/12.8	1.015	-0.199
MD06	Dykes hosted by Metamorphic rocks	18	4.35E-03	212.6	36.9	65.3/14.5	4.34E-03	109.1	17.2	65.3/19.8	4.30E-03	359	48	23.0/12.0	1.012	0.516
MD07		20	5.34E-04	276.9	14.9	9.5/5.7	5.32E-04	186.1	3	42.1/5.3	5.31E-04	85.1	74.8	41.8/5.6	1.005	-0.395
MD08		20	1.40E-03	259.4	15	12.7/6.4	1.39E-03	158.4	35.6	21.8/10.5	1.38E-03	8.4	50.4	21.5/6.1	1.018	-0.284
MD09		24	6.98E-04	252.5	18.1	5.3/4.5	6.95E-04	147.2	38.8	77.6/4.8	6.95E-04	2	45.6	77.6/5.0	1.006	-0.915
<b>Lava flow</b>																
MS01	Basalt	27	6.39E-02	215.2	63.7	19.5/5.8	6.34E-02	40.3	26.2	37.1/8.7	6.26E-02	309.3	2	35.9/9.1	1.021	0.326
<b>Miocene cover</b>																
ML01	Carbonates	16	9.14E-06	317.8	2	32.8/10.5	9.03E-06	47.9	3.9	34.5/12.1	8.76E-06	200.2	85.6	18.2/9.6	1.045	0.44

n = number of specimens; Pj = corrected anisotropy degree; T = shape parameter; Dec = declination; Inc = inclination.

### 5.5.1.2 Distribution of AMS principal axes in the Mersin cumulate sequence

In general, ultramafic cumulates (sites MC01-03) showed scattering in AMS principal axes with no clear relationship to the orientation of cumulate layering (Figure 5.17). This probably reflects the very coarse crystal size of these rocks, such that the fabric of each specimen is dominated by the crystallographic orientation of just a few crystals. Within the gabbroic cumulate section, significant variations in fabrics defined on the basis of the orientation distributions of AMS principal axes are seen. Excluding one gabbroic site (MC16) where generally scattered AMS axes are observed, these can be classified into three fabric types:

(i) Triaxial fabrics: these are marked by presence of three distinct clusters of principal axes. At some sites, two of these clusters lie within or close to the measured plane of cumulate layering (sites MC02, 05, 08 and 14). At others (sites MC07, 12 and 15), only the cluster of  $k_1$  axes is within or close to the plane of cumulate layering, or all three axes lie off of this plane.

(ii) Clustered  $k_1$  axes with a girdle distribution of  $k_2$  and  $k_3$  axes (sites MC04, 06, 09-11 and 13): in these cases,  $k_1$  axes lie within or close to the plane of cumulate layering, but  $k_2$  and  $k_3$  axes form a girdle distribution that is discordant to the layering.

(iii) Clustered  $k_3$  axes with a girdle distribution of  $k_1$  and  $k_2$  axes (sites MC17 and 18): at these sites,  $k_3$  axes lie within or close to the plane of cumulate layering with  $k_1$  and  $k_2$  axes forming a girdle distribution that is discordant to the layering.

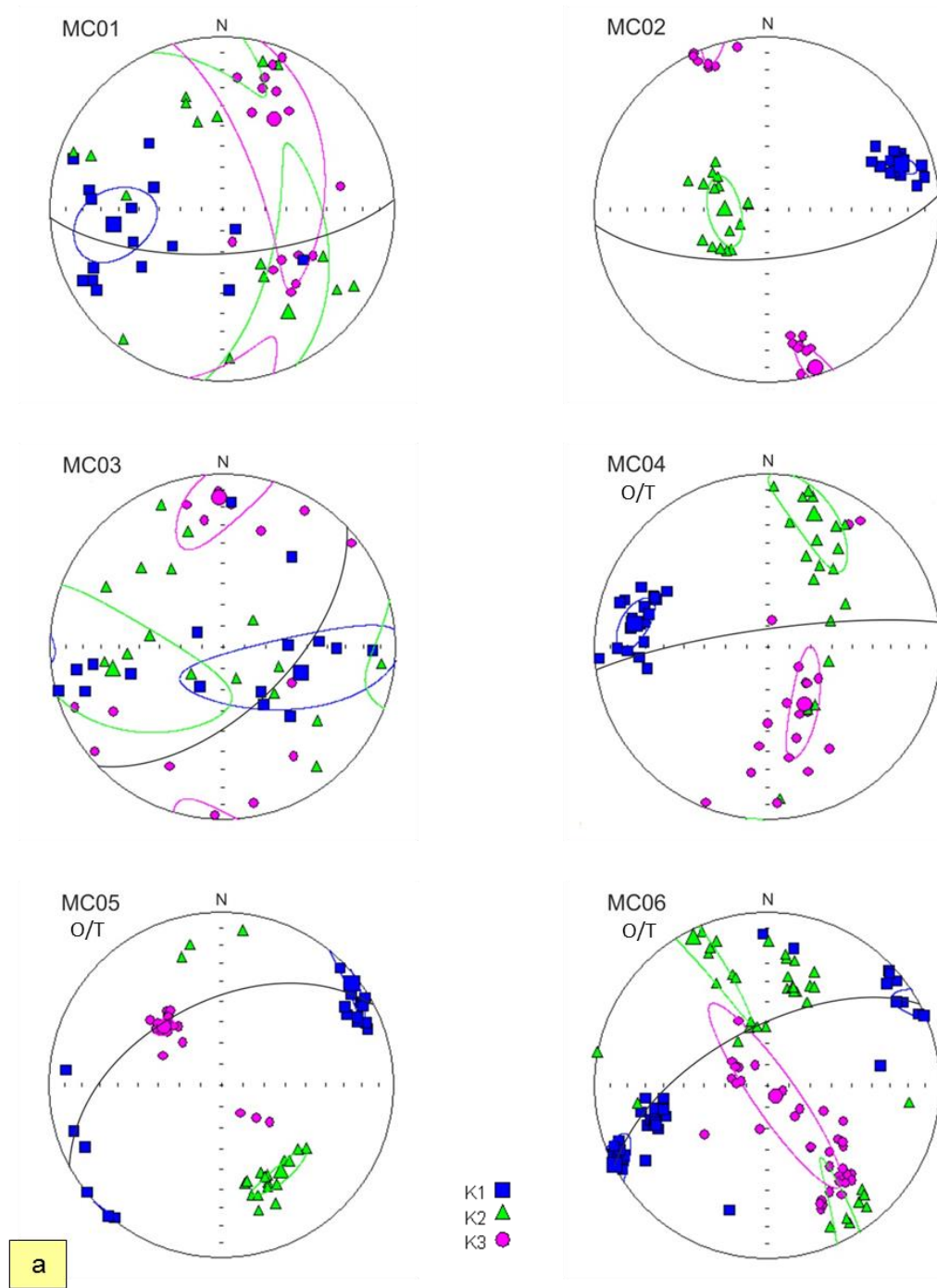


**Figure 5.17.** (a) Stereoplots of AMS ellipsoid principal axes, together with planes of the layering of ultramafic and gabbroic cumulates from the Mersin ophiolite; (b) diagrammatic cross-section showing the status and the dip direction of the layering for the sites within the Sorgun Valley.

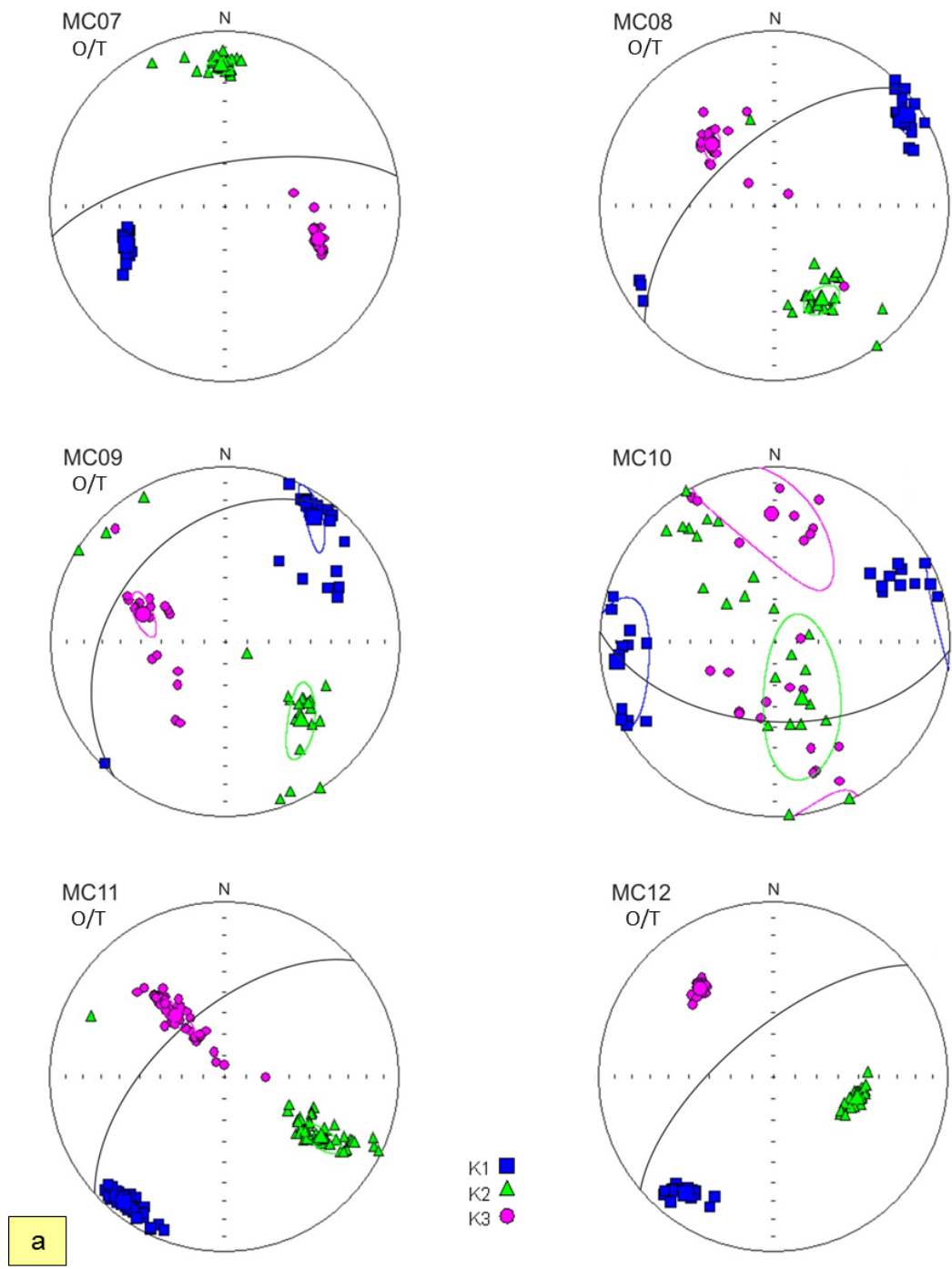


Figure 5.17. (Continued)

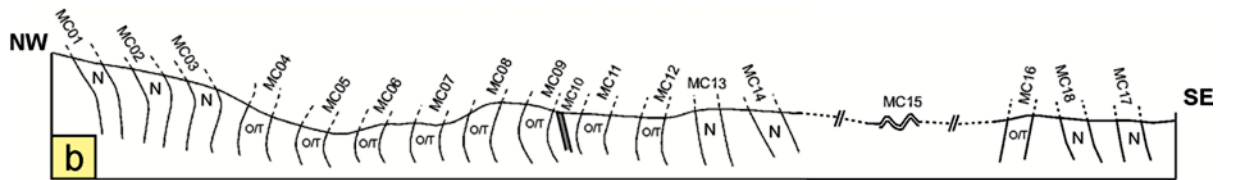
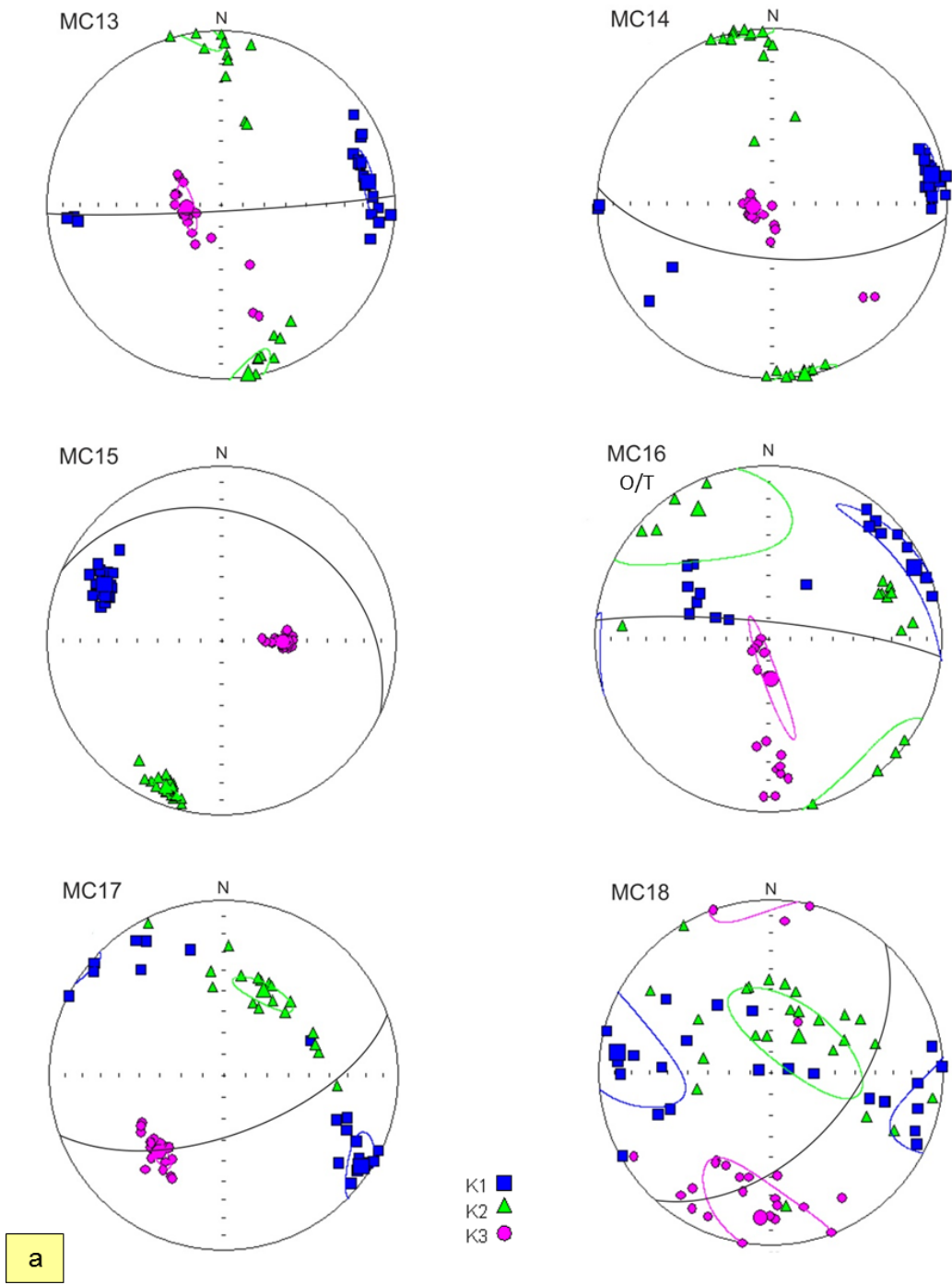


Figure 5.17. (Continued)

However, in all three types of fabrics,  $k_1$  axes generally have shallow plunges with azimuths on or close to the strike of the cumulate layering and trending generally ENE-WSW. This consistency across the majority of sites is inconsistent with simple models for the development of cumulate layering via crystal settling in a magma chamber, which should result in a dominance of oblate fabrics where  $k_3$  axes cluster around the pole to the layering. Instead, these data suggest that some other geological process has resulted in a preferred orientation of  $k_1$  axes within or close to the plane of cumulate layering with a broadly similar azimuth between different sites. Three potential scenarios capable of generating this preferred orientation are: (a) consistent direction of magmatic flow during the formation of the cumulates; (b) shearing of the cumulate crystal mush, for example due to mantle drag; or (c) development of a post-magmatic tectonic fabric, for example via superposition of magmatic and structural fabrics to produce an intersection magnetic lineation. The origin and potential significance of this consistency in AMS  $k_1$  axes is discussed further below (Section 5.8.1).

#### *5.5.1.3 Distribution of AMS principal axes in discrete dykes*

In general, AMS principal axes in dykes are generally found to lie within or close to the dyke plane in the majority of cases reported in the literature (e.g. Borradaile and Gauthier, 2006). This is because magma-flow alignment of accessory magnetite dominates the magnetic fabric, with a subordinate contribution from paramagnetic silicate minerals that also preferentially align with the flow. Under certain circumstances, the direction of magma flow may be determined from AMS data (e.g. Staudigel *et al.*, 1992), but this requires collection of multiple samples from opposing dykes margins that was not possible in the case of the Mersin discrete dykes.

Various forms of relationship were found in the Mersin dykes between AMS fabrics and dyke margin orientations, ranging from very good to poor agreement with dyke orientations determined in the field, suggesting that the controls of AMS may vary between dykes (Figure 5.18).

In the eastern area (sites MD01-05, MD10 and 11), thick dykes hosted by the mantle sequence have magnetic fabrics broadly consistent with measured dyke margins. For example, sites MD04 and MD10 showed a very good relationship between AMS fabrics and dyke orientations. In these cases, maximum and intermediate principal axes of AMS ( $k_1$  and  $k_2$ ) form a girdle distribution that broadly corresponds to the measured plane of the dykes, with minimum axes ( $k_3$ ) forming clusters corresponding to the poles to the dykes. This suggests a normal magnetic fabric. A similar arrangement of AMS principal axes is observed at site MD03, but with a mismatch with the overall dyke orientation. In this case there is likely a fabric developed that is related to the local dyke orientation at the point of sampling that is different to the overall average orientation of the dyke. Sites MD01 and MD05 exhibit generally triaxial magnetic fabrics, i.e. with distinct clustering of each of the principal axes, but again have  $k_3$  axes close to the corresponding dyke poles.

Dykes cutting the metamorphic sole of the ophiolite show well-defined magnetic fabrics at three sites (MD07-09), with girdle distributions of  $k_2$  and  $k_3$  axes that dip steeply to the E or ENE and clustered  $k_1$  axes plunging shallowly to the W or WSW (with fabric at the remaining site (MD06) being poorly defined). In each case,  $k_1$  axes are close to lying within the measured planes of the sampled dykes, but the girdle distributions of  $k_2$  and  $k_3$  axes are discordant to the dyke planes.

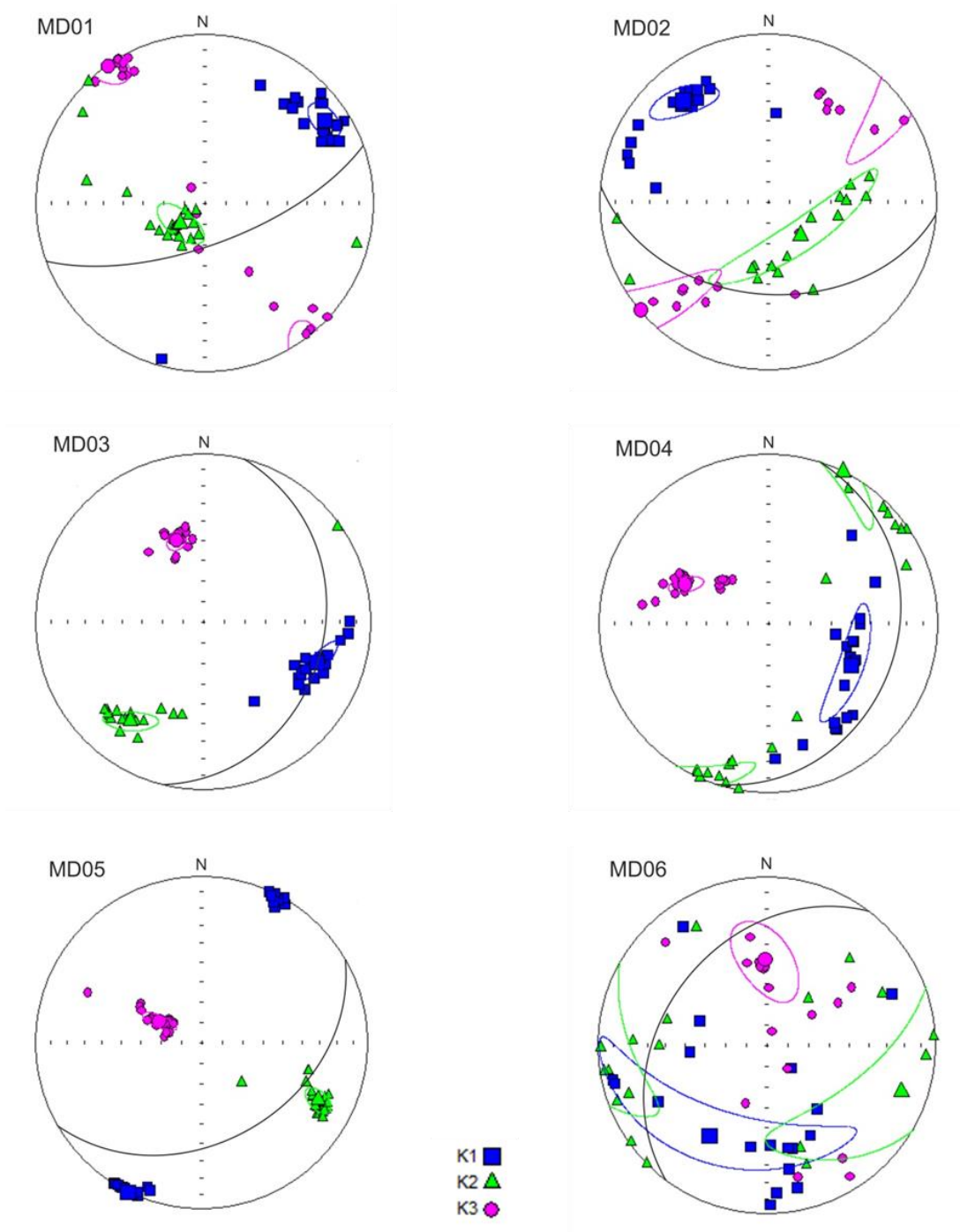


**Figure 5.18.** Stereoplots of AMS ellipsoid principal axes together with dyke orientations from the Mersin ophiolite.

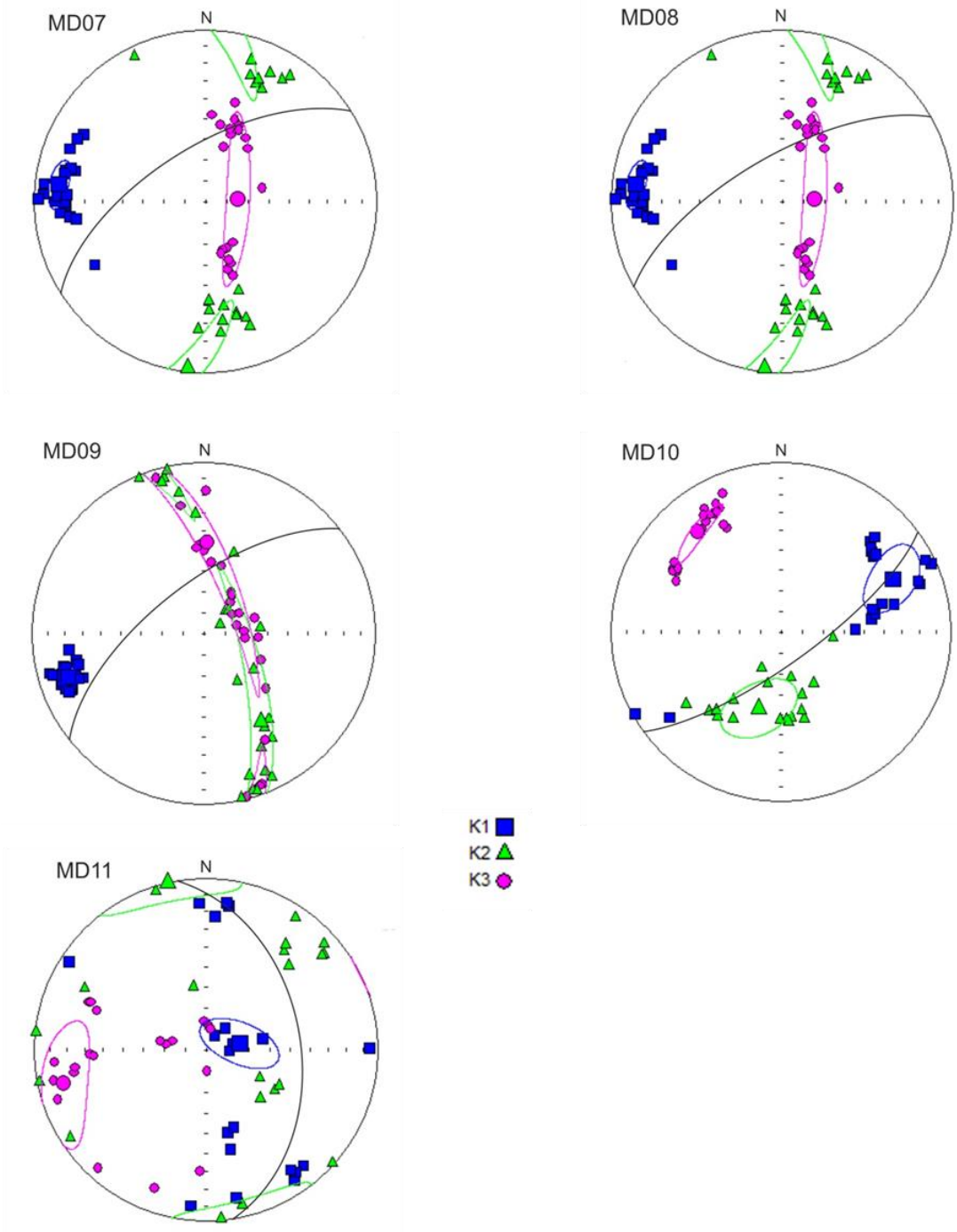


Figure 5.18. (Continued)

#### 5.5.1.4 Distribution of AMS principal axes in lavas

The limited number of samples available from the site in the lava flow showed a complex fabric with no obvious relationship to the orientation of the flow inferred from the orientation of well-developed columnar jointing (Figure 5.19a).

#### 5.5.1.5 Distribution of AMS principal axes in Miocene sediments

The results from Miocene sediments show a well-defined magnetic fabric that is consistent with measured bedding, where maximum and intermediate principal axes of AMS ( $k_1$  and  $k_2$ ) form a girdle distribution that corresponds to the measured bedding plane (which is close to the primitive circle because it represents a sub-horizontal layer), and minimum axes ( $k_3$ ) form a cluster corresponding to the pole to the bedding. This suggests a normal, deposition-related fabric unaffected by tectonism (Figure 5.19b).

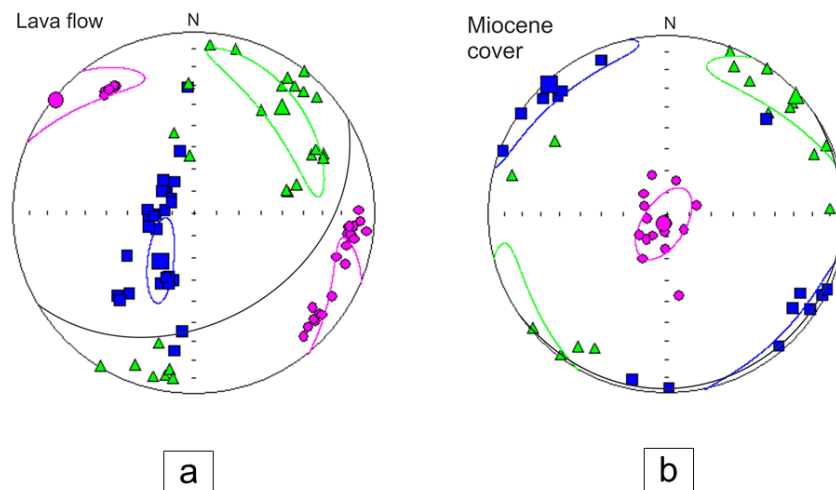


**Figure 5.19.** Stereoplots of AMS ellipsoid principal axes from: (a) lava flow samples from site ML01, together with plane perpendicular to columnar jointing (that provides the best estimate of the orientation of the flow). (b) Miocene sediments, together with subhorizontal bedding plane.

### 5.5.2 Thin section observations of petrofabrics

Optical microscope analyses of the rock samples revealed that both paramagnetic and ferromagnetic minerals contribute to the AMS, and the amount of these minerals varies between different rock types. In ultramafic samples, olivine is highly serpentinized, resulting in production of secondary magnetite. Opaque grains are distributed along fractures within the serpentinized olivine and are clearly observable both with the naked eye and under the microscope in the form of greenish colour banding that shows a strong correspondence with  $k_1$  (Figure 5.20). In most of the gabbroic cumulate samples, both opaque and paramagnetic minerals within the rock show a good agreement of alignment with  $k_1$  axes, which is clearly observed both with the naked eye and under the microscope (Figure 5.21 and Figure 5.22). One sample (MC1206C; Figure 5.23) in particular showed distinctive oriented inclusions of magnetite in clinopyroxene phenocrysts which are thought to be of exsolution origin, together with intergrowths of composite lamellae of orthopyroxene (Fleet *et al.*, 1980; Butler, 1998; Rajesh *et al.*, 1998; Renne *et al.*, 2002). Similar observations have been reported in many studies, as early as that of Judd (1885). In the current study, such inclusions of magnetite with a preferred orientation are frequently observed, and in a number of samples (such as MC1206C) show a good agreement with  $k_1$  axes (Figure 5.23). In addition, such inclusions may be an important source of stable remanent magnetization (Renne *et al.*, 2002; Gee and Kent, 2007). SEM analyses (Figure 5.24) indicated that magnetite is only ferromagnetic mineral in this sample (in agreement with rock magnetic analyses), and the presence of oriented exsolution lamellae of low-Ca orthopyroxene within high-Ca clinopyroxene. Exsolution usually occurs by the growth of lamellae within the host mineral in a

slow manner. Thus this provides evidence for slow cooling of these plutonic rocks (Butler, 1998).

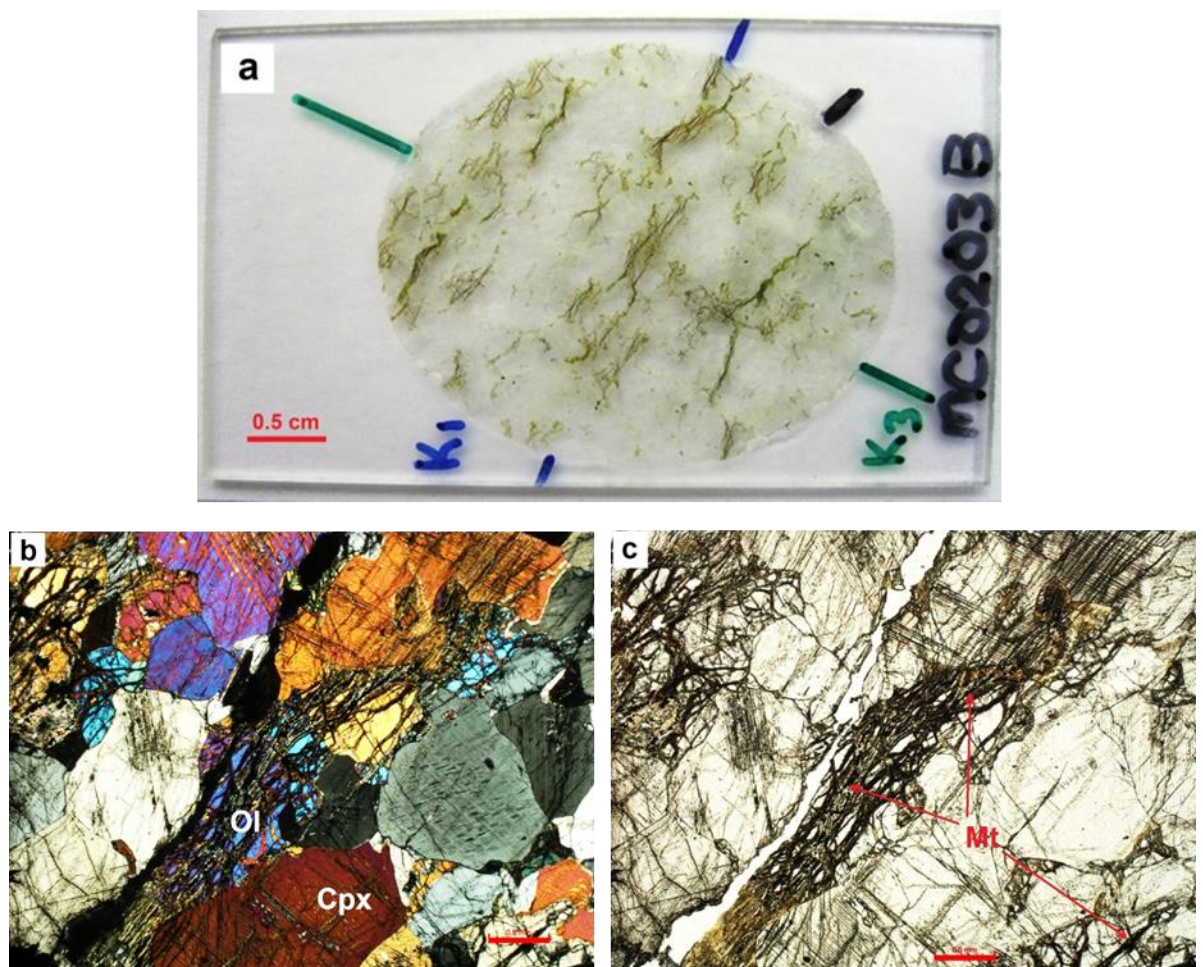


**Figure 5.20.** Images of ultramafic cumulate sample MC0203B showing a banding caused by serpentinization. (a) Direct image of the slide under normal light. (b) Under crossed polars. (c) Under plane-polarized light. Scale bar: 0.5 cm for Figure 5.20(a) and 0.5 mm for Figure 5.20(b,c). (Cpx = clinopyroxene; Ol = olivine; Mt = magnetite).

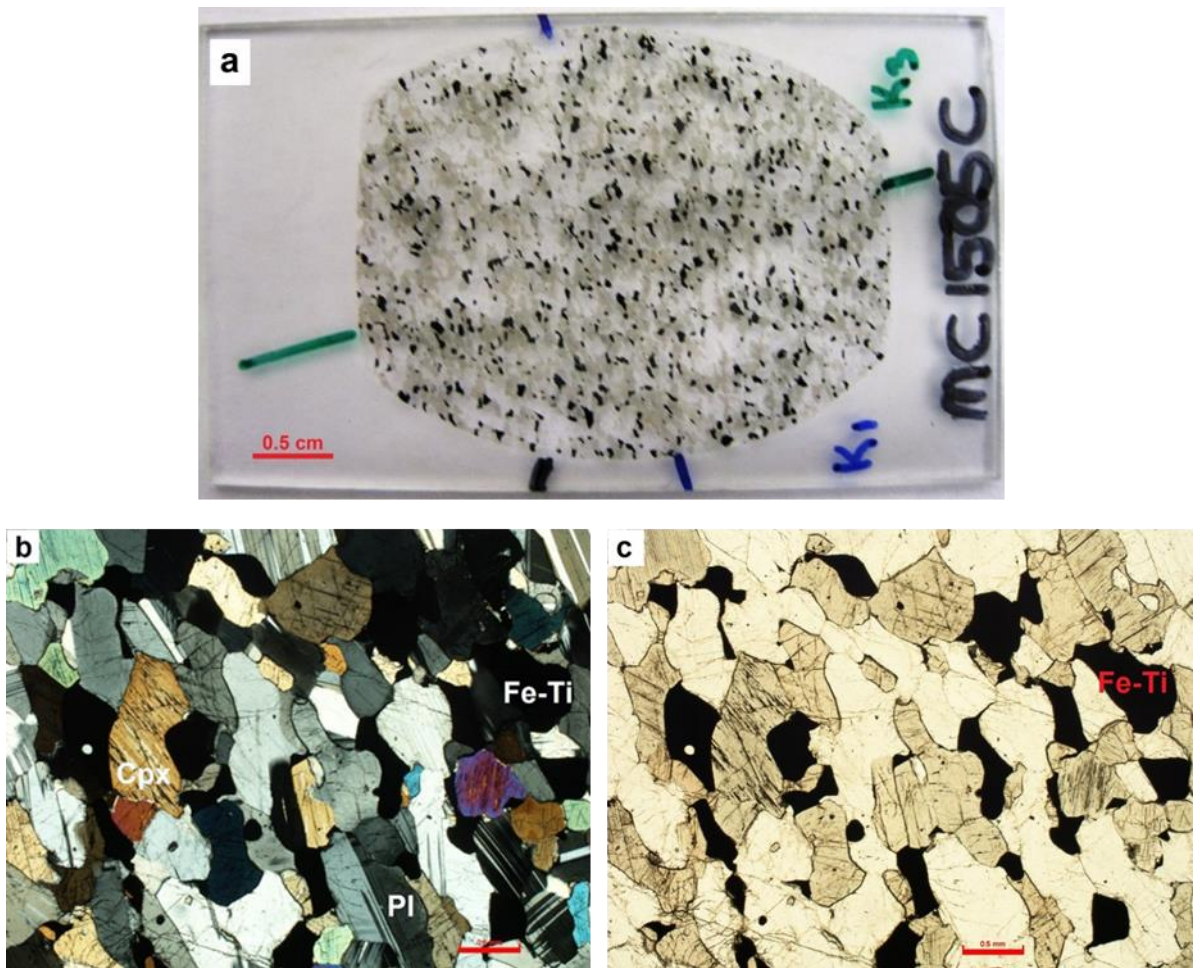


**Figure 5.21.** Images of cumulate gabbro sample MC1505C showing a good agreement of both magnetite and plagioclase crystal alignments with k1. (a) Direct image of the slide under normal light. (b) Under crossed polars. (c) Under plane-polarized light. Scale bar: 0.5 cm for Figure 5.21(a) and 0.5 mm for Figure 5.21(b,c). (Cpx = clinopyroxene; Pl = plagioclase; Fe-Ti = Fe-Ti Oxide).

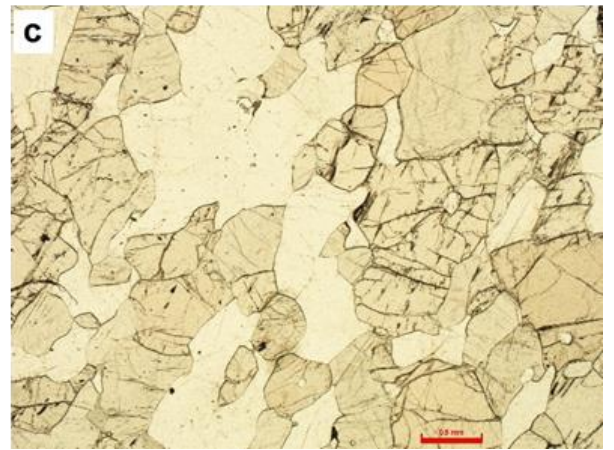
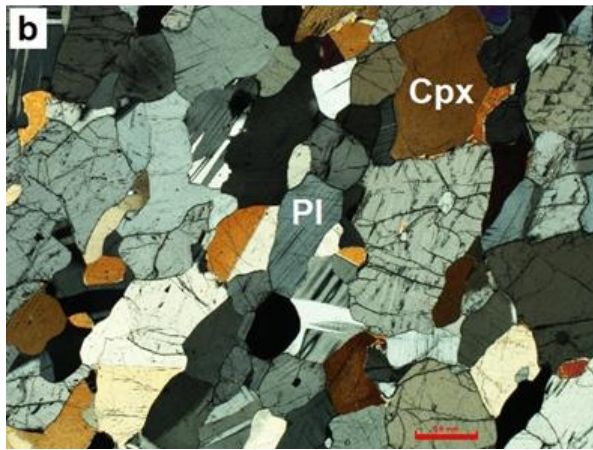
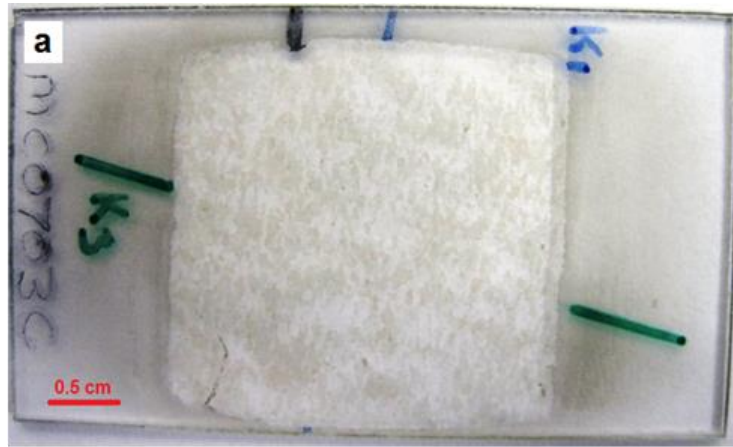


**Figure 5.22.** Images of gabbroic cumulate sample MC0703C showing a good agreement of both pyroxene and plagioclase crystal alignments with k1. (a) Direct image of the slide under normal light. (b) Under crossed polars. (c) Under plane-polarized light. Scale bar: 0.5 cm for Figure 5.22(a) and 0.5 mm for Figure 5.22(b,c). (Cpx = clinopyroxene; Pl = plagioclase).

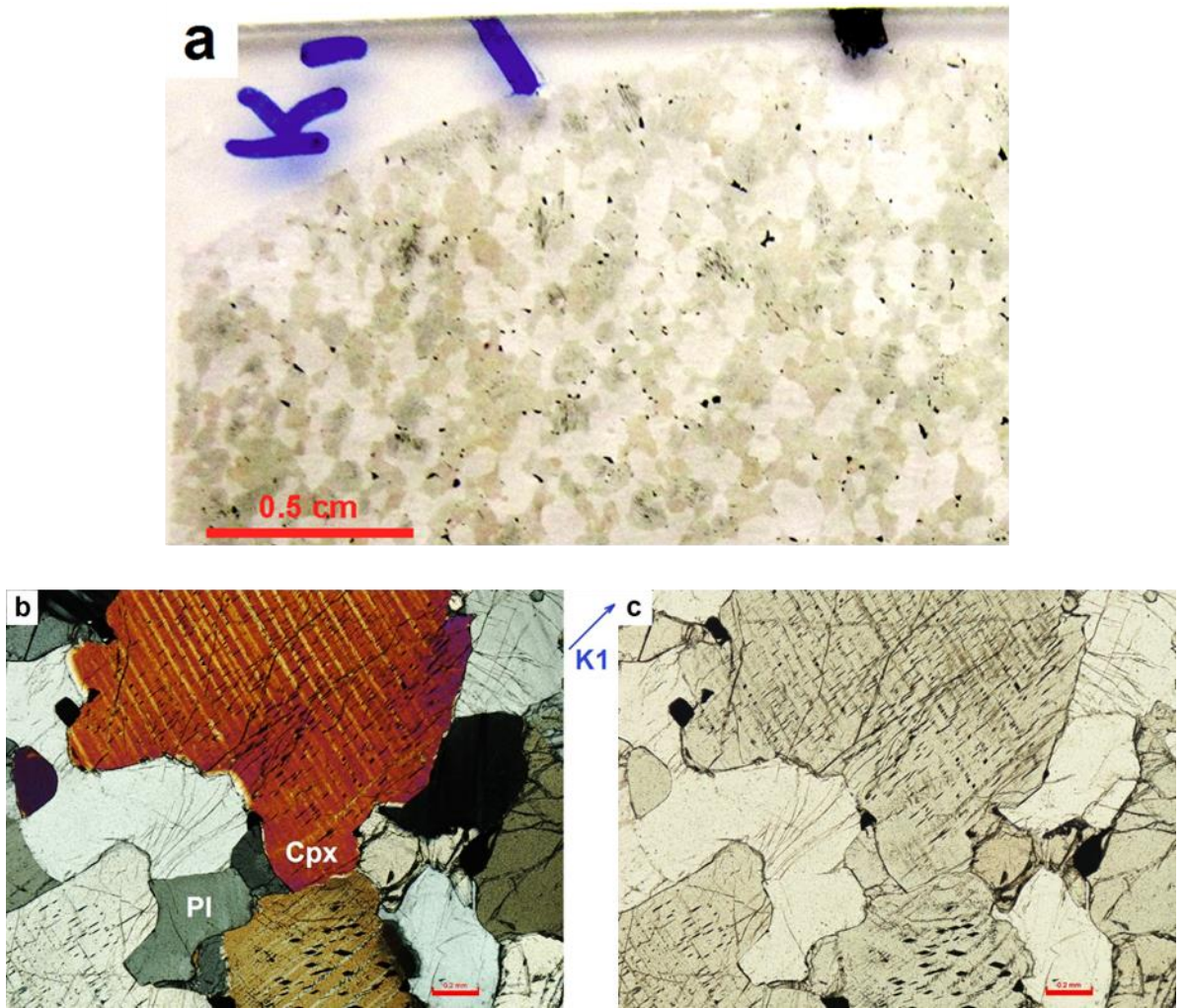


**Figure 5.23.** Images of gabbroic cumulate sample MC1206C illustrating both exsolved inclusions of oriented magnetite and intergrowths of composite lamellae of orthopyroxene in clinopyroxene phenocrysts. (a) Direct image of the slide under normal light. (b) Under crossed polars. (c) Under plane-polarized light. Scale bar: 0.5 cm for Figure 5.23(a) and 0.2 mm for Figure 5.23(b,c). (Cpx = clinopyroxene; Pl = plagioclase).

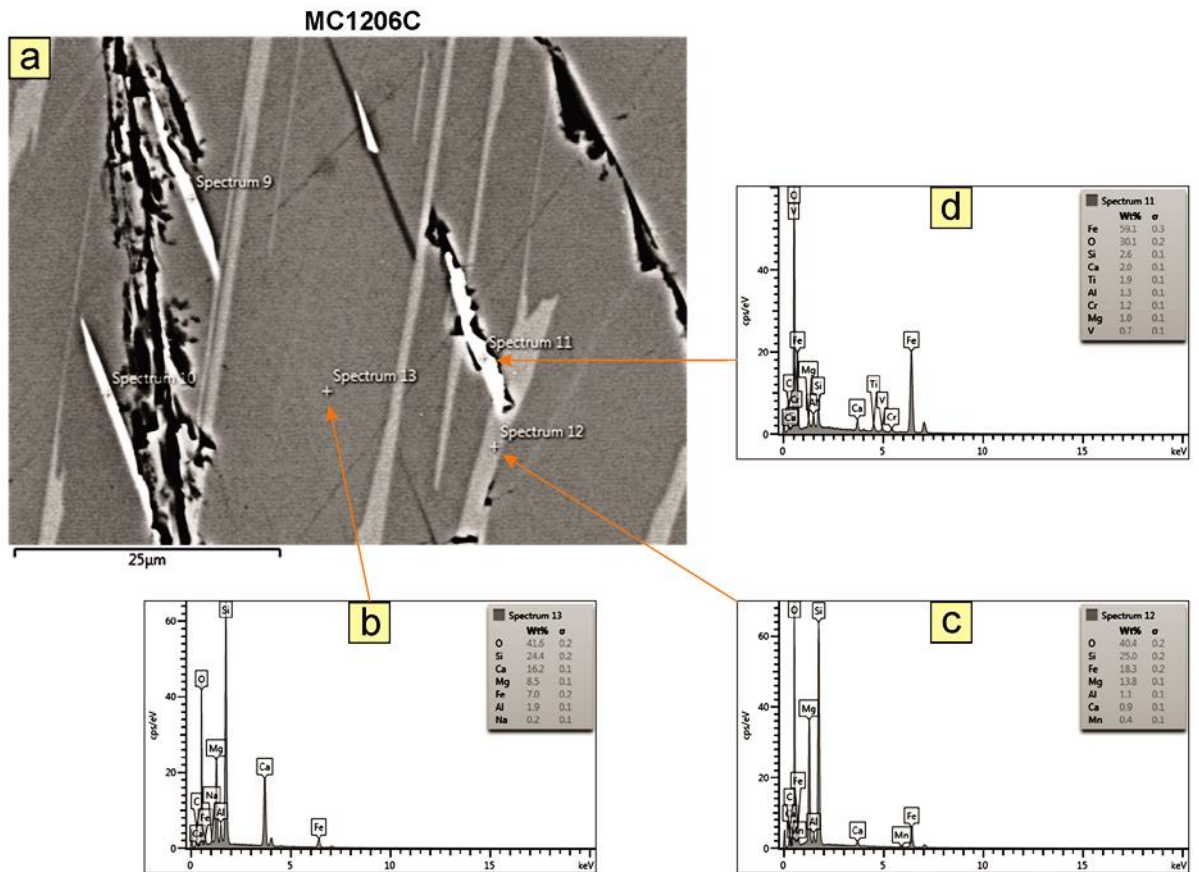


**Figure 5.24.** SEM photograph and EDX spectral analysis of sample MC1206C, indicating the presence of exsolved magnetite.

### 5.5.3 Anisotropy of anhysteretic remanent magnetization (AARM) results

Anisotropy of anhysteretic remanent magnetization (AARM) measurements were performed on a limited number of representative samples to allow comparison with AMS results from the same samples in order to check for presence of inverse or intermediate magnetic fabrics. In this study, one specimen from each site in the ultramafic and gabbroic cumulate section was analysed after specimens were subjected to a demagnetizing field of 100 mT to remove any natural remanence present.

Four diverse relationships between AMS and AARM fabrics were found in the selected samples. The first set of the fabric relationships is a normal case where all three principal axes of the AMS coincide with the AARM axes and

generally showed oblate fabric in both AMS and AARM ellipsoids (Figure 5.25a and Fig 5.26a). The second set showed coincidence of  $k_1$  with  $AARM_1$  axes in both fabrics, but with an interchanging of the  $k_2$  and  $k_3$  axes of the AMS fabrics with the  $AARM_2$  and  $AARM_3$  axes, and generally showed prolate fabric in both AMS and AARM ellipsoids (Figure 5.25b and Figure 5.26b). The third kind of relationship is the case in which the  $k_3$  axis of the AMS fabric coincides with the  $AARM_3$  axis, but there is an interchange of the  $k_1$  and  $k_2$  axes of the AMS fabrics with the  $AARM_1$  and  $AARM_2$  axes. This kind of relationship was observed only in one sample, and it showed triaxial and oblate magnetic shapes in the AMS and AARM fabrics respectively (Figure 5.25c and Figure 5.26c). The fourth set of samples showed no obvious relationship between AMS and AARM fabrics. The first fabric relationship type is interpreted as a normal fabric, while the second and third kinds of relationship may be classified as intermediate fabrics, that along with reverse fabrics represent types of abnormal fabrics (Rochette *et al.*, 1992). These abnormal fabrics might be of primary and secondary origin (Borradaile and Gauthier, 2003; Raposo *et al.*, 2007).

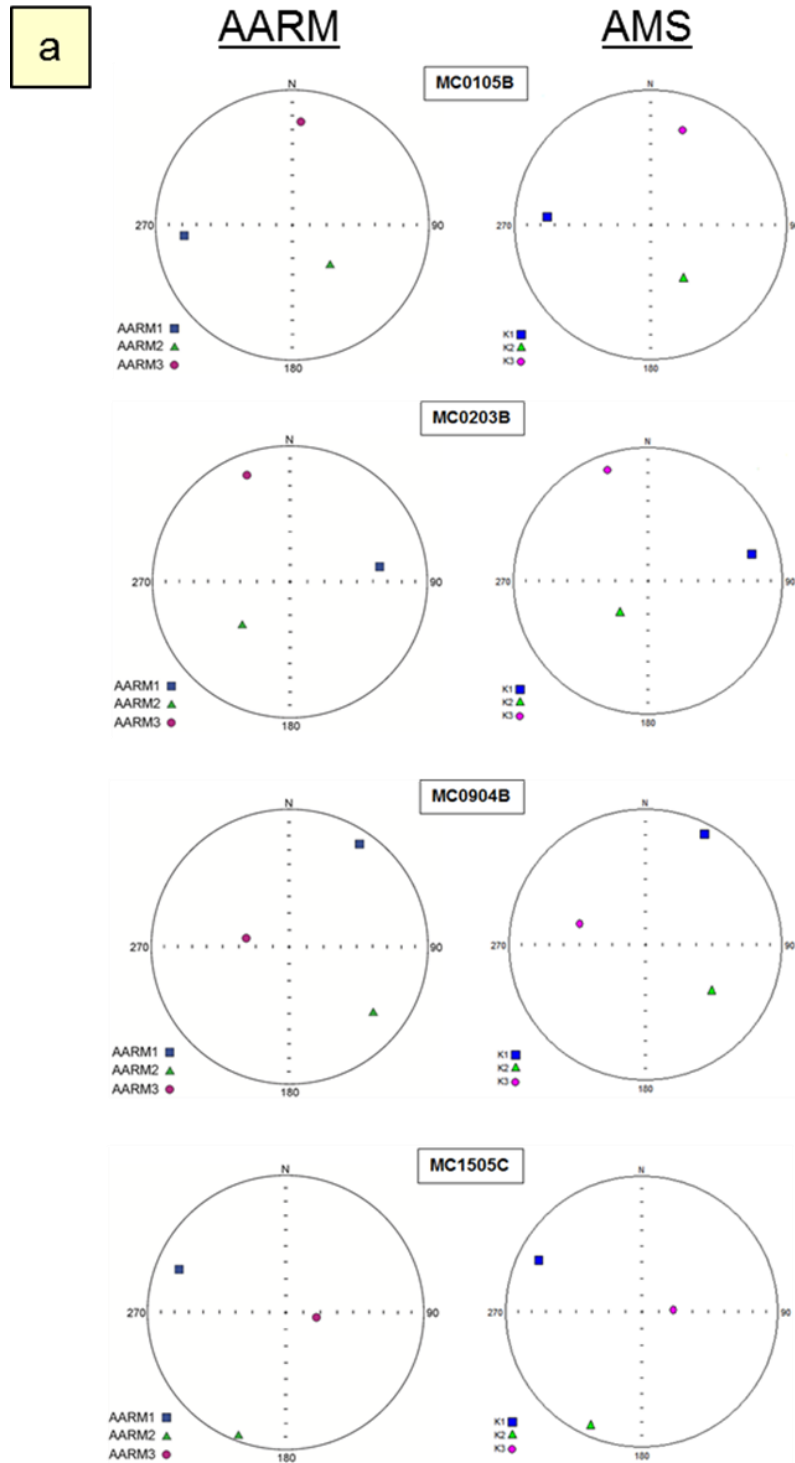
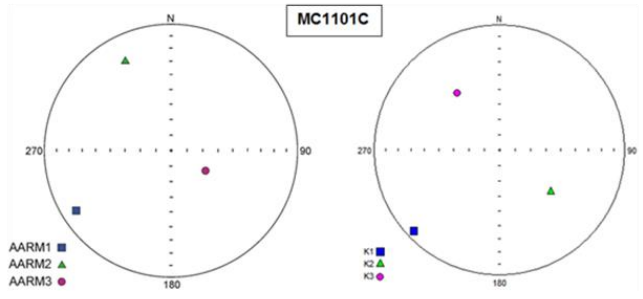
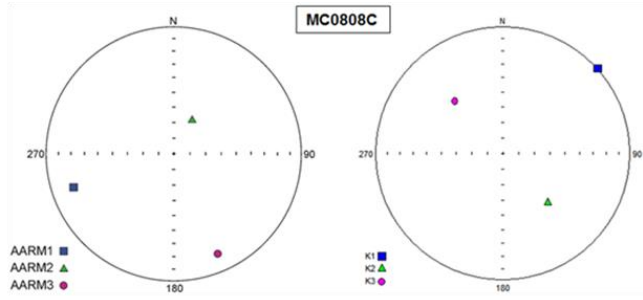
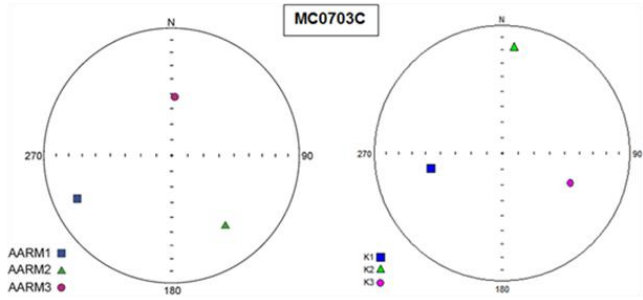
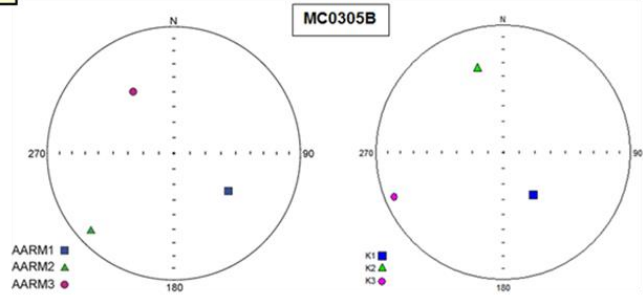


**Figure 5.25.** Comparison of AMS and AARM results for ultramafic and mafic cumulates from Mersin ophiolite. (a) All three principal axes of the AMS coincide with the AARM axes in these samples. (b) The samples show a coincidence of  $k_1$  with  $AARM_1$  axes in both fabrics, but there is an interchanging of the axes  $k_2$  and  $k_3$  of the AMS fabrics with the  $AARM_2$  and  $AARM_3$  axes of the AARM fabrics. (c) This sample shows a coincidence between the  $k_3$  axis of the AMS fabric and the  $AARM_3$  axis, but there is an interchange of the  $k_1$  and  $k_2$  axes of the AMS fabric with the  $AARM_1$  and  $AARM_2$  axes of the AARM fabrics.

b

AARM

AMS



c

AARM

AMS

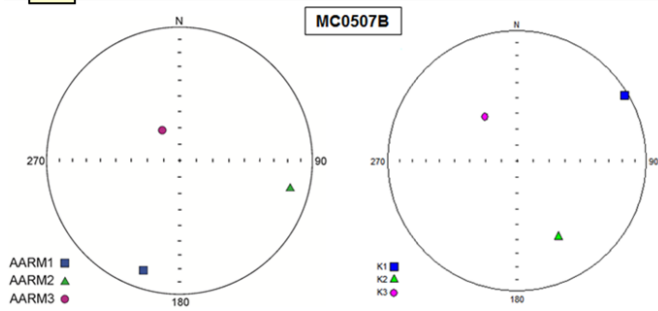
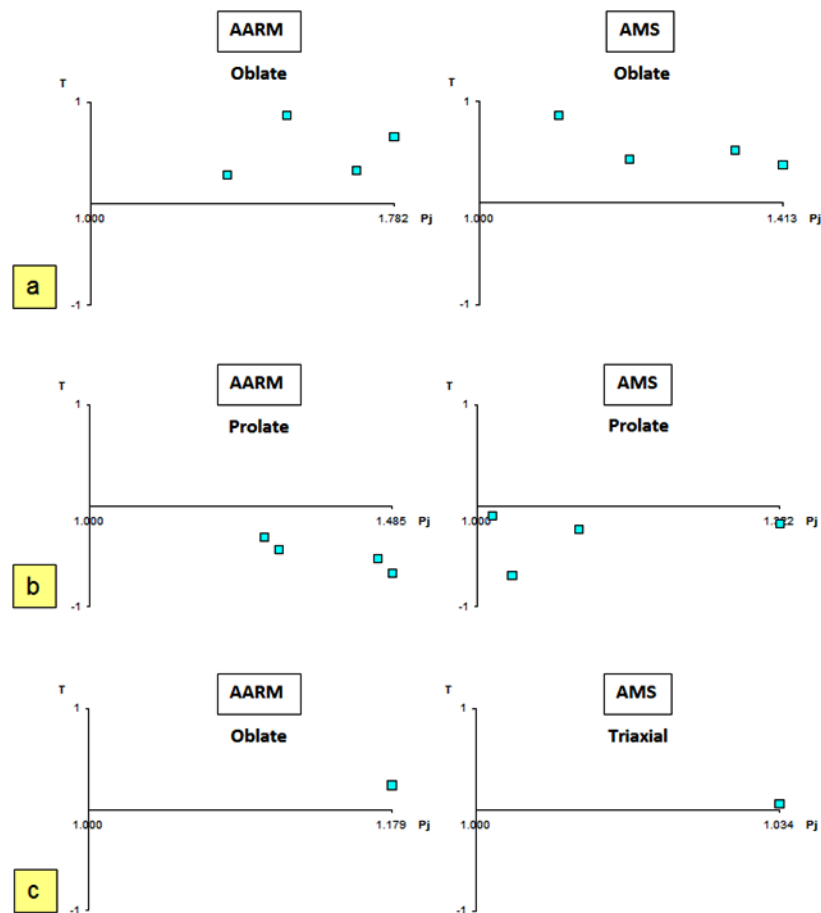


Figure 5.25. (Continued)



**Figure 5.26.** Degree of anisotropy  $P_j$ , versus shape parameter  $T$  diagrams (Jelinek, 1981) of AARM and AMS ellipsoids for ultramafic and mafic cumulates from Mersin ophiolite. (a) Samples display oblate fabric in both AMS and AARM ellipsoids. (b) Samples display prolate fabric in both AMS and AARM ellipsoids. (c) Sample shows triaxial and oblate magnetic shapes in the AMS and AARM fabrics respectively.

## 5.6 Remanent magnetizations and demagnetization

### characteristics

#### 5.6.1 Demagnetization of NRM

The natural remanent magnetization (NRM) of a rock is usually the vector sum of a mixture of magnetization components acquired at a range of times during its geologic history. Each rock acquires a “primary” magnetization component during its formation. Igneous rocks formed by crystallization from magma acquire a stable NRM called thermoremanent magnetization (TRM) during solidification and cooling in the Earth’s magnetic field. Subsequent exposure to

alteration or weathering may lead to the acquisition of several secondary components.

To examine the nature of the remanent magnetization from all the sites, selected specimens were progressively AF or thermally demagnetized and all remanences measured as described in Section 2.7.4. Progressive demagnetization isolates various remanence components on the basis of different coercivities of the ferromagnetic mineral grains or on the basis of different unblocking temperatures of the mineral grains (Butler, 1992). Usually, the grain size of ferromagnetic minerals controls the ability of a rock to acquire and retain an ancient remanence. Small particles occur as single domain or pseudo single domain (SD/PSD) grains which can hold remanence more efficiently than larger multi-domain (MD) grains, which are more likely to acquire unwanted secondary remanences (Butler, 1992).

Prior to the application of stepwise demagnetization techniques, the natural remanent magnetization (NRM) intensities were measured for all specimens. The measurements showed a clear difference in the intensities between the various types of the lithologies ranging between  $2.12 \times 10^{-5}$  A/m to 8 A/m. The average NRM intensities of all lithologies are listed in Table 5.4.

The palaeomagnetic results from both alternating field and thermal demagnetization techniques on all samples show that both techniques are equally effective in determining the characteristic remanent magnetization (ChRM). The maximum angular deviation (MAD) for identifying acceptable ChRM directions was set to  $10^\circ$ , and data from individual samples with  $MAD > 10^\circ$  were excluded from subsequent palaeomagnetic analyses. All palaeomagnetic sampling sites (except site MC15) have mean directions with

$\alpha_{95}$  cones of confidence less than  $9^\circ$ , whereas the Fisher precision parameter ( $kappa$ ) values for all sites (except site MC15), are greater than 30, and more than a half of sites yielded  $kappa$  values more than 100. These results indicate that the demagnetization data obtained from all samples of the different lithologies are highly reliable. Typical examples of demagnetization behavior from various lithologies are shown in Figures 5.33 to 5.36, and site level data from all lithologies are listed in Tables 5.5 and 5.6.

**Table 5.4.** Average intensities of natural remanent magnetization (NRM) for sampled lithologies.

Lithology	Number of specimens	Average NRM intensity (A/m)
Ultramafic cumulates	36	0.132
Gabbroic cumulates	180	1.116
Dykes	132	0.08
Basaltic lava	12	2.085
Carbonate sediments	16	$3.30 \times 10^{-5}$

### 5.6.2 Demagnetization characteristics

Both AF and thermal demagnetization curves were collated for all the samples of the lithologies of Mersin ophiolite in order to determine dominant coercivities (Figures 5.28, 5.30, 5.32) and unblocking temperatures (Figures 5.29, 5.31). AF demagnetization curves for samples with high coercivities are marked by high median destructive fields (MDF; the alternating field required to reduce the intensity to 50% of its initial NRM value), which in turn reflect finer magnetite

grain sizes. The average grain size can be inferred indirectly by comparing curves with those obtained from sized magnetite grains provided by Argyle *et al.* (1994) (Figure 5.27).

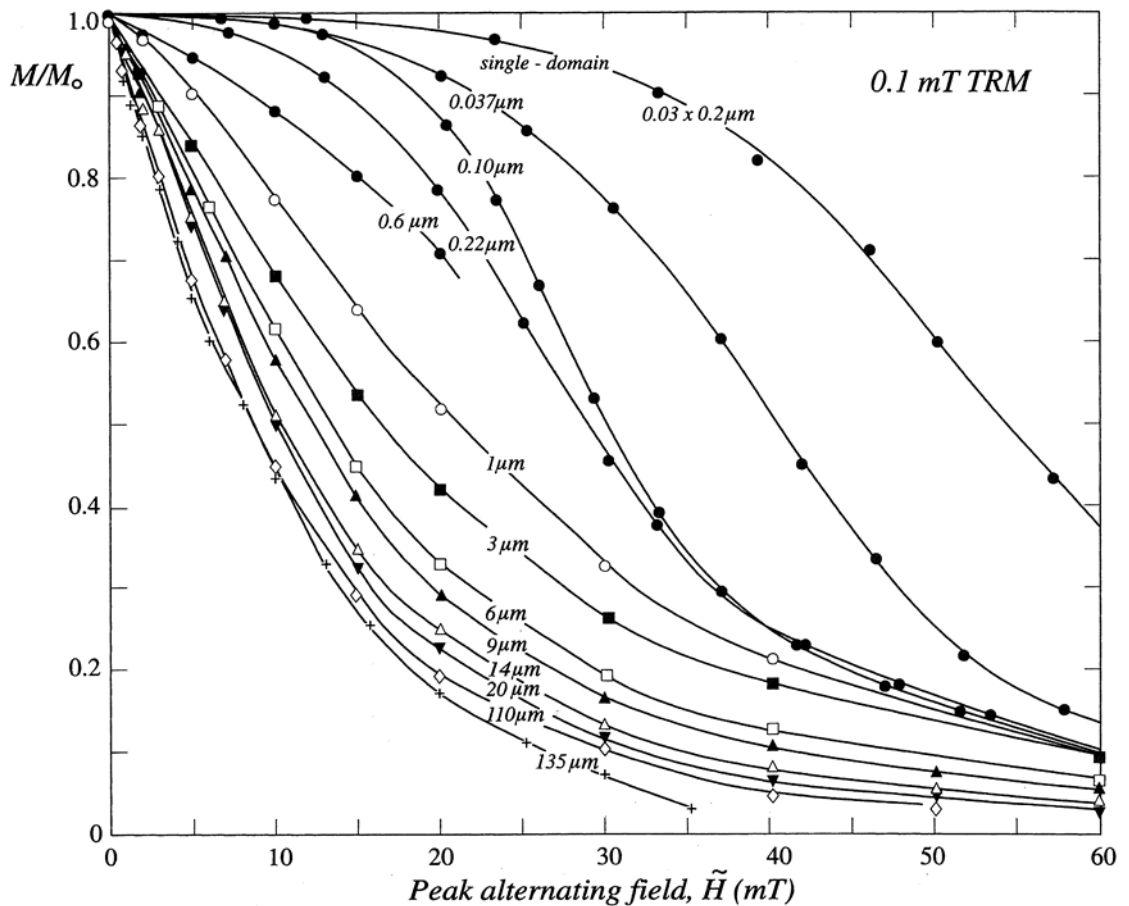


**Figure 5.27.** Shapes of AF demagnetization curves of a 0.1 mT TRM in magnetite over a broad range of grain sizes, extending from SD to large MD (from Dunlop and Özdemir, 1997, after Argyle *et al.*, 1994).

By comparison with the standard curves of Argyle *et al.* (1994), ultramafic samples of sites MC01 and MC02 have MDFs of c. 23 mT (Figure 5.28a) and are dominated by magnetite of approximately 1  $\mu\text{m}$  in size, i.e. at the approximate upper size limit for elongate SD grains (Morris, 2003). Samples from site MC03 have MDFs of c. 48 mT (Figure 5.28b) and are characterized by very fine SD magnetite grains ( $\sim 0.03 \mu\text{m}$ ). Thermal demagnetization of the ultramafic rocks yields curves with maximum unblocking temperatures of 580°C

(close to the magnetite Curie temperature), and the demagnetization trends show distributed unblocking temperature spectra (Figure 5.29a), probably reflecting a range\* of grain sizes of magnetite within these rocks possibly formed as a result of serpentinization, as described in Section 5.5.2 (Figure 5.20). [\*note that unblocking temperature is *highly* sensitive to very small variations in grain size, varying by several 100's °C across changes in grain size of tenths of microns; Tarling, 1983].

Overall, AF demagnetization also identifies two types of curves in gabbroic samples. The first type, which includes sites MC06, MC08-12 and MC17-18, has MDFs of c. 25 mT indicative of SD grain sizes of < 1 µm (Figure 5.28c), while the second type includes sites MC04-05, MC07, MC13-14 and MC16, has MDFs of c. 60 mT, characteristic of very fine (< 0.03 µm) SD grains (Figure 5.28d). Thermal demagnetization of the gabbroic samples shows very discrete unblocking just below 580°C, suggesting presence of a limited range of grain sizes of magnetite in these rocks (Figure 5.29b). Unblocking spectra with these characteristics are often taken as evidence of thermoremanent magnetizations in intrusive igneous rocks (e.g. Gee and Kent, 2007; Morris *et al.*, 2009).

AF demagnetization of the samples from discrete dykes has shown three types of characteristic curves. The first type, which includes sites MD02, MD04, MD08 and MD10, is dominated by a very fine (< 0.03 µm) SD magnetite with MDFs of c. 70 mT (Figure 5.30a). The second type, which includes sites MD01, MD03, MD05, MD07, MD09 and MD11, is also dominated by fine SD grains (~0.03 µm), but with MDFs of c. 45 mT (Figure 5.30b). The third type only includes samples from site MD06, and is dominated by MD magnetite with MDFs of c. 8 mT (Figure 5.30c).

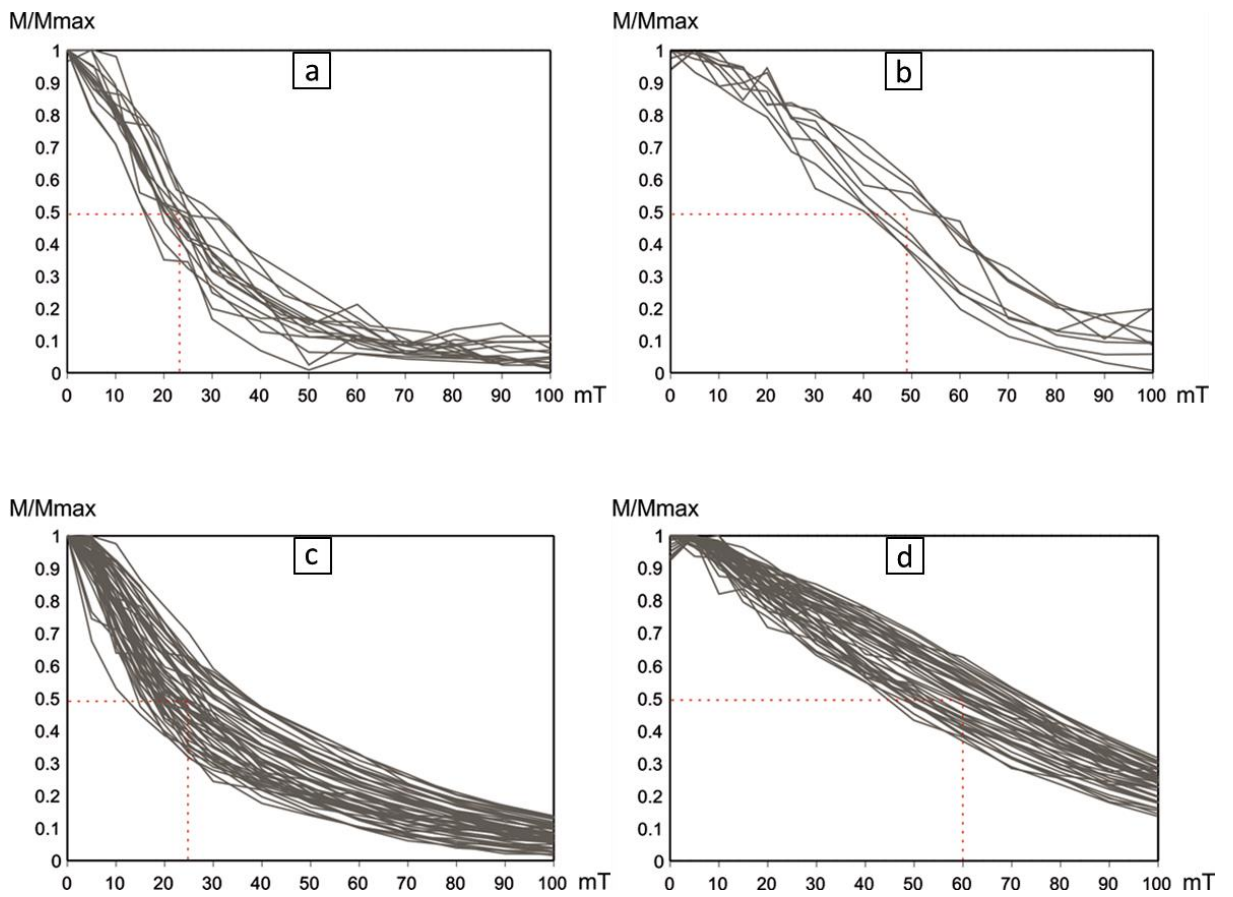


**Figure 5.28.** Normalized intensity against applied field diagrams illustrating the different types of magnetic behavior obtained during AF demagnetization of the samples. (a and b) ultramafic cumulate samples of the Mersin ophiolite. (c and d) gabbroic samples of the Mersin ophiolite. Red dashed lines indicate approximate average values of median destructive fields.

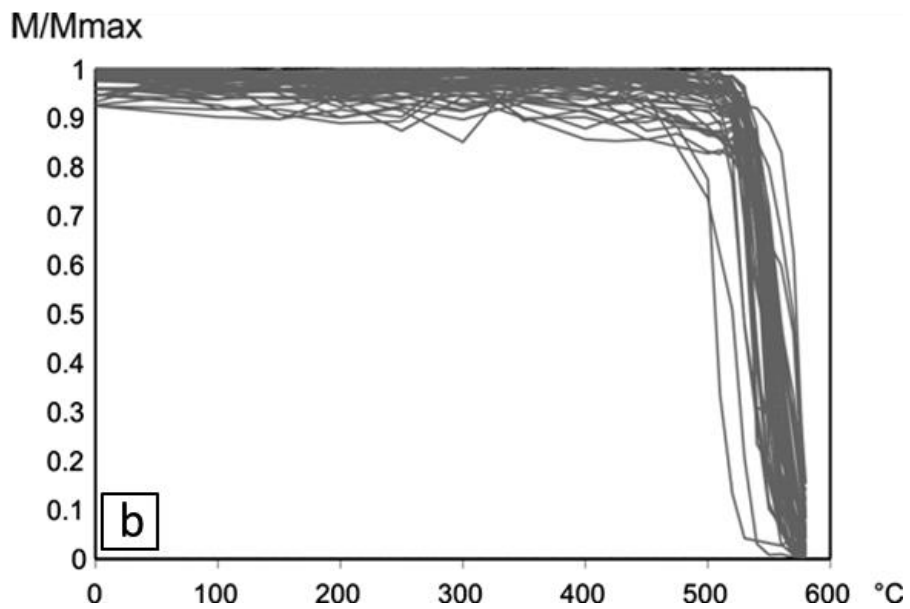
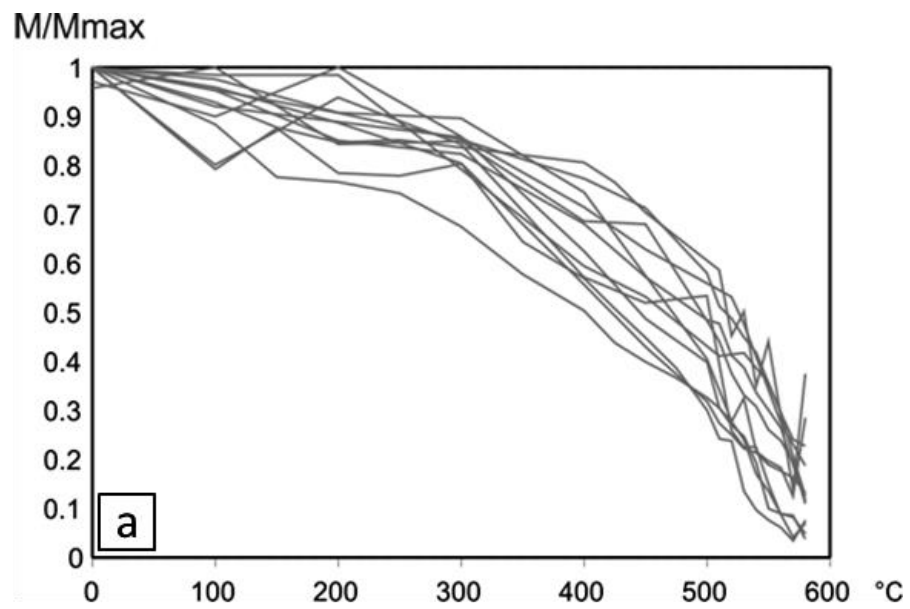


**Figure 5.29.** Normalized intensity against temperature diagrams illustrating the different types of magnetic behavior obtained during thermal demagnetization of the samples. (a) ultramafic cumulate samples of the Mersin ophiolite. (b) gabbroic samples of the Mersin ophiolite.

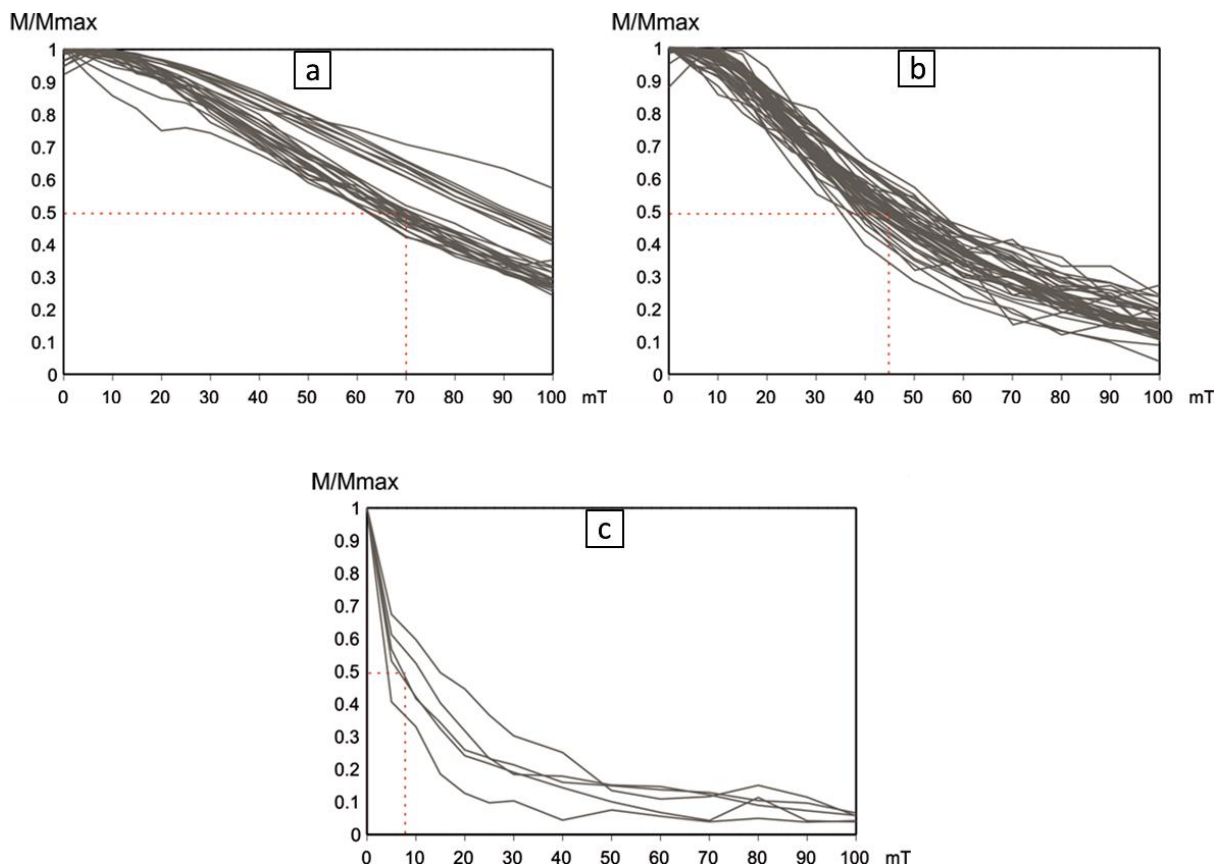


**Figure 5.30.** Normalized intensity against applied field diagrams illustrating the different types of magnetic behavior obtained during AF demagnetization of dyke samples from the Mersin ophiolite. Red dashed lines indicate approximate average values of median destructive fields.

Thermal demagnetization of the dyke samples has identified three types of characteristic curves. The first type, including sites MD01-05 and MD11, demonstrates very discrete unblocking close to the magnetite Curie temperature of 580°C, again suggesting a very limited range of grain sizes of magnetite in these rocks (Figure 5.31a). The second type only includes site MD10, and shows a maximum unblocking temperature of 580°C with demagnetization characterized by distributed unblocking above temperatures of 300°C (Figure 5. 31b). By contrast, the third type which includes the metamorphic sole hosted dykes (sites MD06-09), shows more complex unblocking, suggesting that there are two different magnetic minerals with Curie temperatures of c. 320°C and c. 580°C, indicating the presence of ferromagnetic pyrrhotite and magnetite respectively (Figure 5.31c).

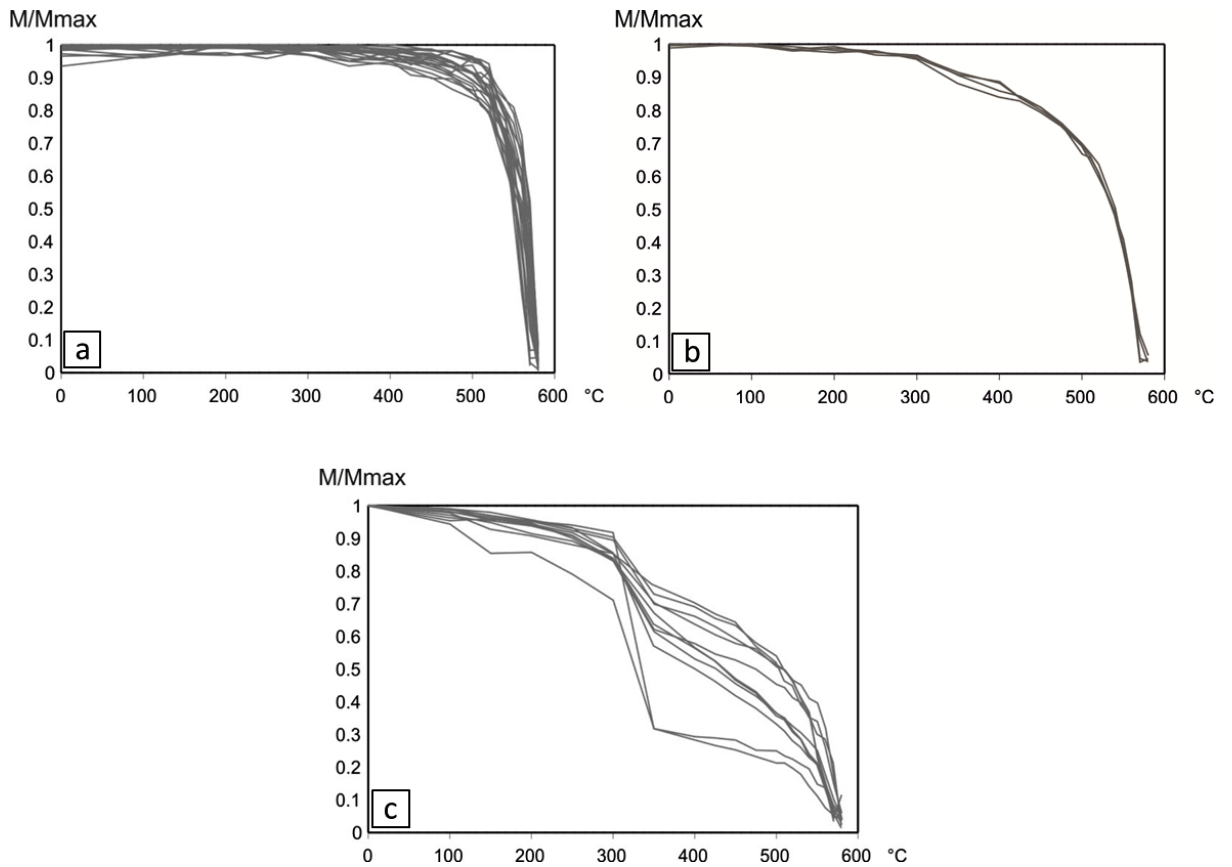


**Figure 5.31.** Normalized intensity against temperature diagrams illustrating the different types of magnetic behavior obtained during thermal demagnetization of the dyke samples from the Mersin ophiolite.

AF demagnetization curves from lava flow samples have MDFs of c. 7 mT, suggesting a dominance of MD grain sizes (Figure 5.32a), whereas thermal demagnetization of these samples has yielded characteristic curves which have distributed unblocking temperatures, indicative of a range of magnetite grain sizes in these samples (Figure 5.32b).

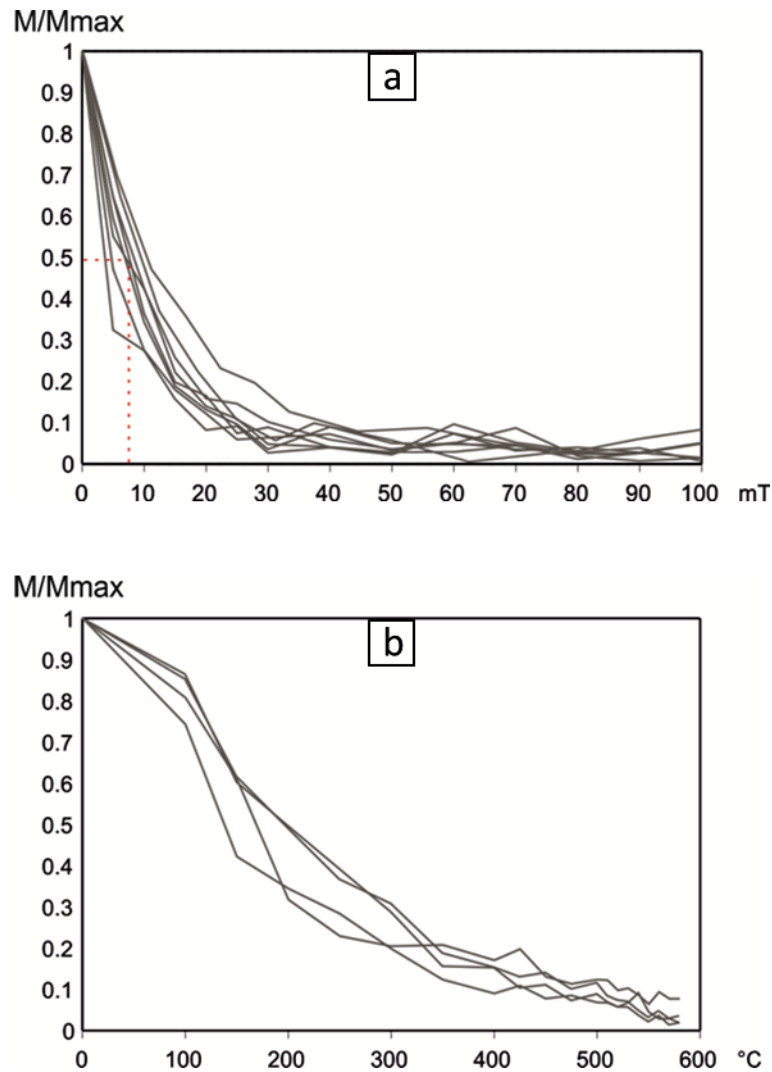


**Figure 5.32.** Normalized intensity against demagnetization level diagrams illustrating the magnetic behavior obtained during AF and thermal demagnetization of the lava flow samples from the Mersin ophiolite.

### 5.6.3 Stepwise demagnetization and palaeomagnetic directions

Stepwise thermal and alternating field demagnetization of ultramafic and gabbroic cumulates mostly identified single components of remanent magnetization characterized by ENE directed, moderately upwards inclined directions in *in situ* (geographic) coordinates with high coercivities/high unblocking temperatures (Figure 5.33). These components become directed downwards (positive inclinations) when a simple tilt correction is applied based on the orientation of the cumulate layering, although it is shown below that these surfaces do not represent perfect palaeohorizontal markers. The simple

nature of the remanences and discrete, high unblocking temperatures are consistent with a thermoremanent origin. The gabbroic rocks are exceptionally fresh with little or no significant alteration, which also supports the inference that remanences in these rocks are primary thermoremanent magnetizations. Positive inclinations after removing the present day tilt of the cumulate layering together with formation of these rocks in the northern hemisphere are consistent with normal polarity remanences acquired close to the time of formation of the cumulates by seafloor spreading in the Late Cretaceous during the Cretaceous long normal polarity interval (chron C34N; Cande and Kent, 1992, 1995).

As mentioned before in Section 3.5.3, the dykes at Fındıklı area are divided into two groups; the first group which is hosted by the mantle sequence includes sites MD01, MD02, MD03, MD04, MD05, MD10 and MD11, and the second group is hosted by the metamorphic sole and includes sites MD06, MD07 MD08 and MD09. During AF and thermal demagnetization of the dyke samples, these groups are revealed to have significantly different *in situ* directions of magnetization. Dykes in the mantle sequence generally show ENE directions with moderate negative inclinations, whereas dykes in the metamorphic sole show ENE directed components with positive inclinations. Examples of demagnetization behavior from both groups are shown in Fig 5.34.

For both AF and thermal demagnetization techniques, the majority of dyke samples show single components of magnetization. For the majority of the samples, a relatively stable component was isolated by fields up to 100 mT or by thermal demagnetization to 580°C. Some individual samples show evidence for having two remanence carriers with unblocking temperatures of c. 320°C and c. 580°C, indicative of pyrrhotite and magnetite respectively (e.g., samples MD0708A and MD0801A; Figure 5.34). All of these observations are consistent

with results of the magnetic mineralogy experiments, described in Section 5.4. Viscous overprints were only occasionally observed, but these could easily be removed at demagnetization steps up to 200° and 30 mT (see Figure 5.35).

AF and thermal demagnetization of basalt samples from the lava flow, also identified single components of magnetization characterized by intermediate coercivity/unblocking temperature components, with a mean *in situ* direction of Dec = 351.5°, Inc = 50.5°, ( $k = 37$  and  $\alpha_{95} = 7.6^\circ$ ).

In contrast to the igneous samples, Miocene sediments subjected to both demagnetization techniques generally became noisy at high treatment steps (Figure 5.36), due to the very weak remanences in these rocks. Despite this, almost all samples from the Miocene carbonate sediments have interpretable components of remanent magnetization, characterized by WNW-directed, low to intermediate coercivity/unblocking temperature components with a mean *in situ* direction of Dec = 349.6°, Inc = 58.1°, ( $k = 48$ ;  $\alpha_{95} = 8.1^\circ$ ). A tilt correction is not required for these rocks due to the almost horizontal (<5°) dip of the carbonates.

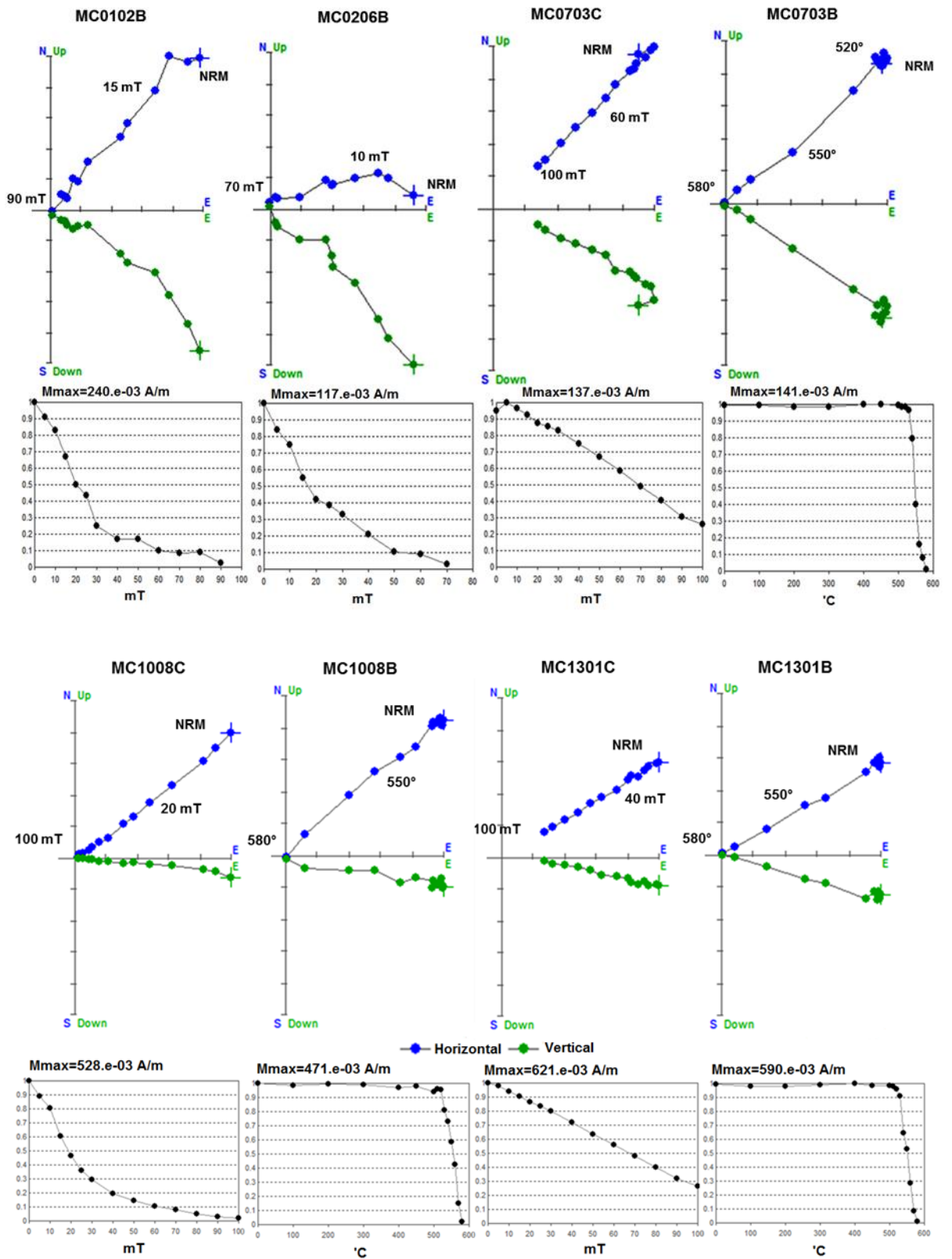


**Figure 5.33.** Zijderveld and intensity decay plots of AF and thermal demagnetization data from gabbroic and ultramafic samples of the Mersin ophiolite.

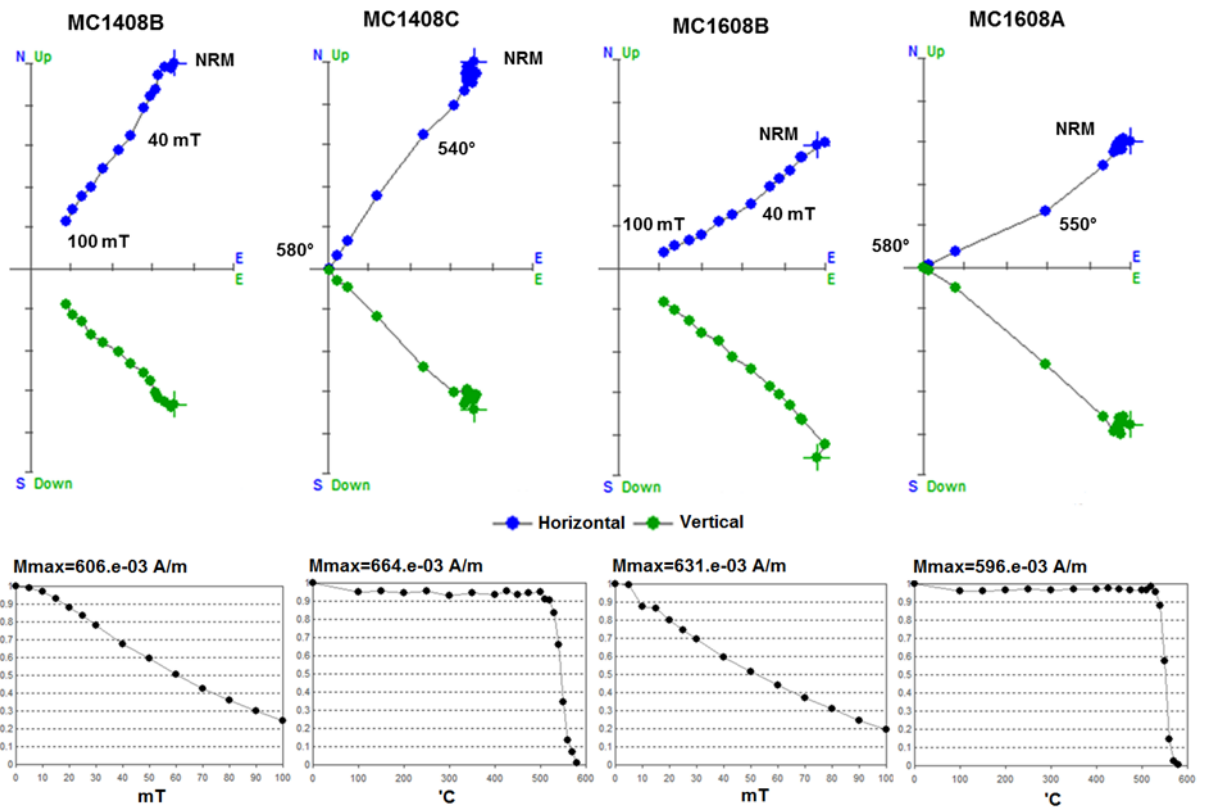
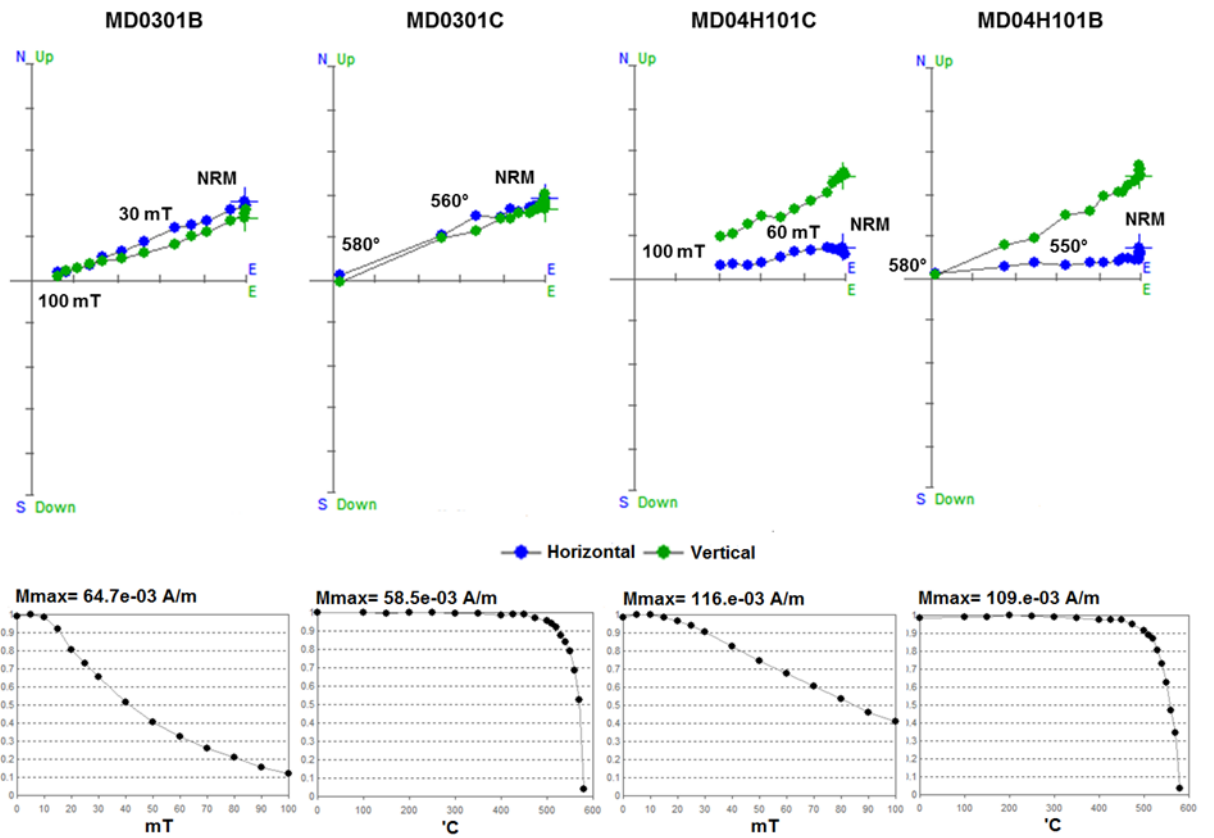


Figure 5.33. (Continued)



**Figure 5.34.** Zijderveld and intensity decay plots of AF and thermal demagnetization data from dyke samples of the Mersin ophiolite.

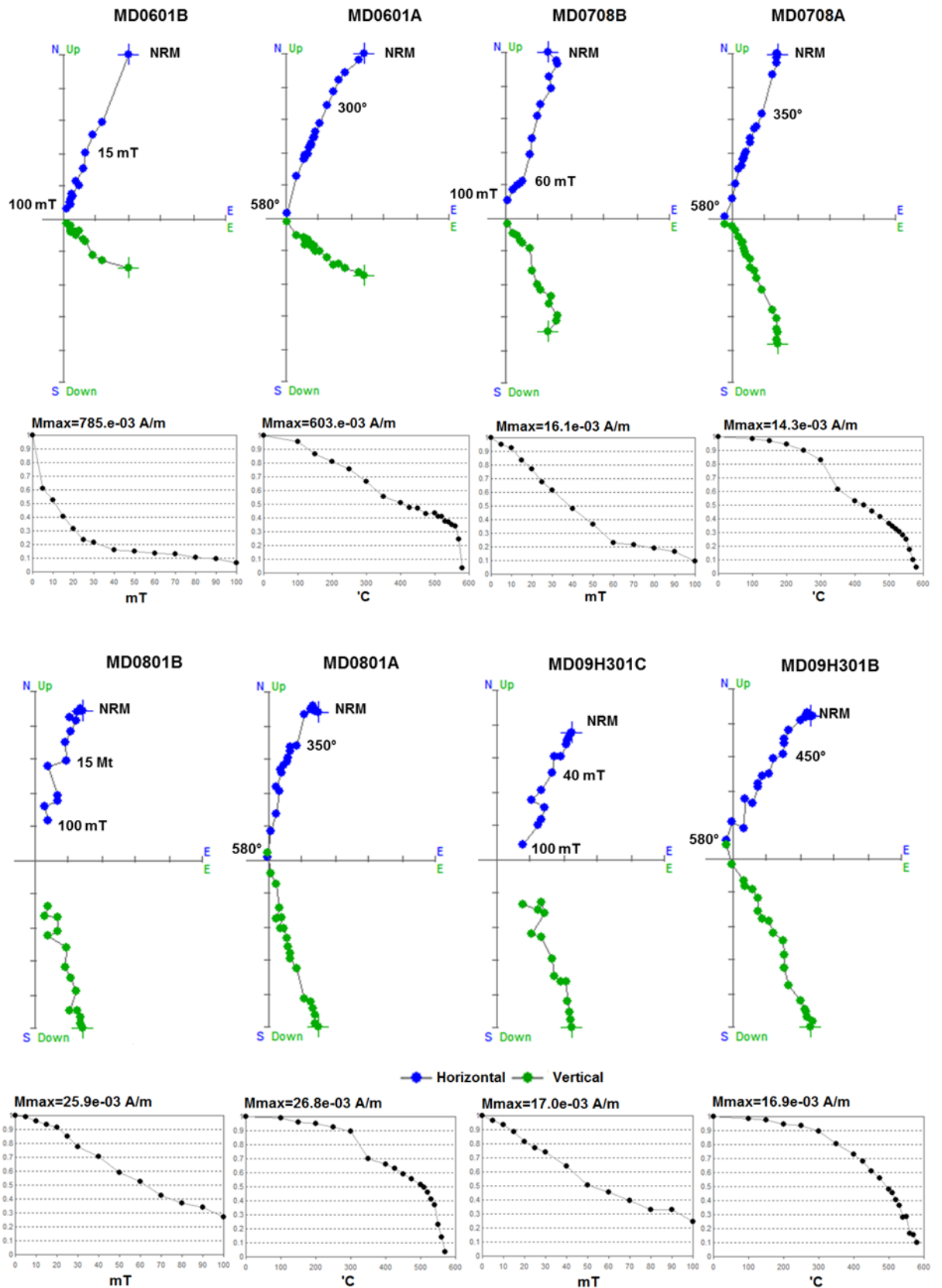
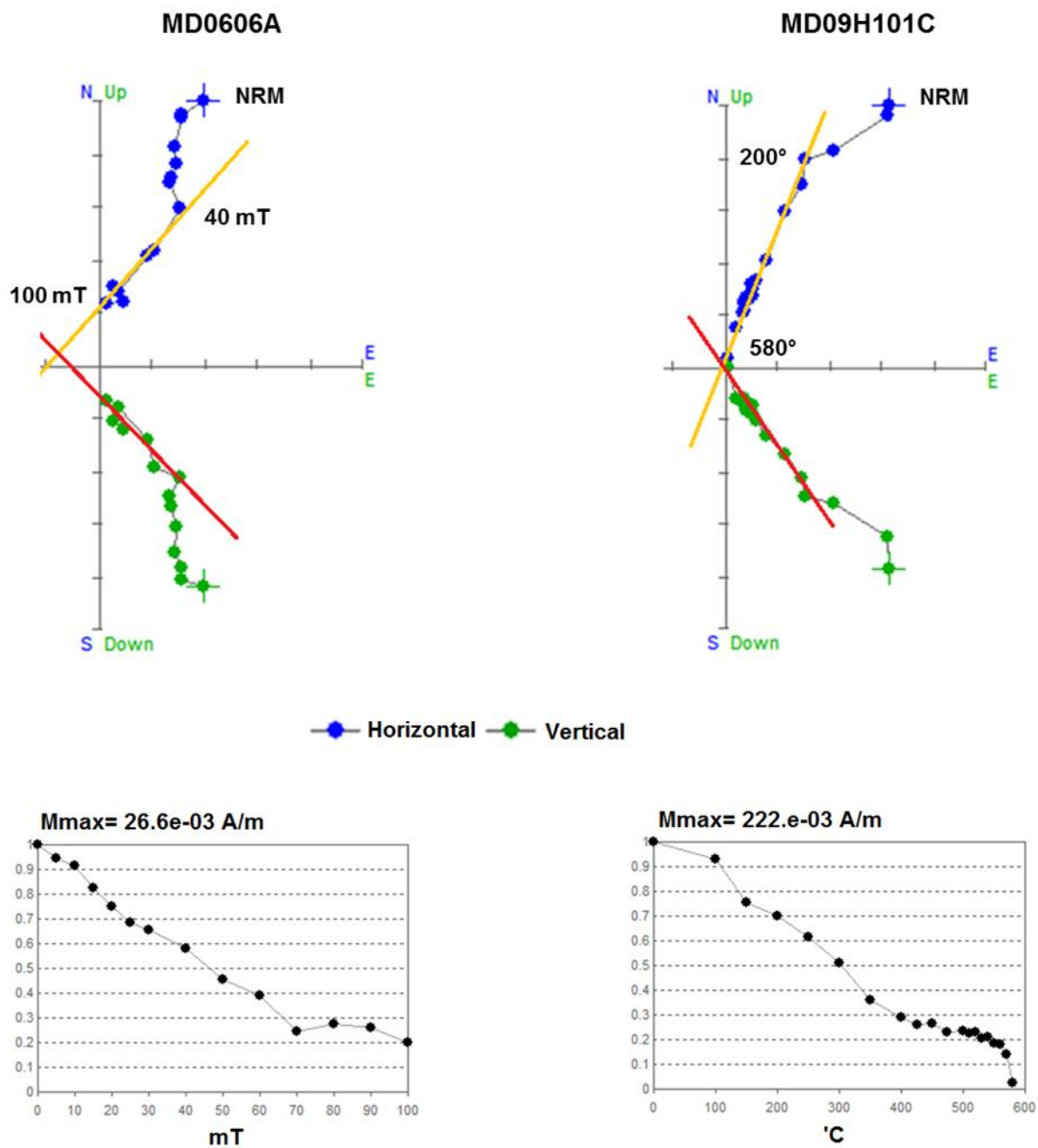
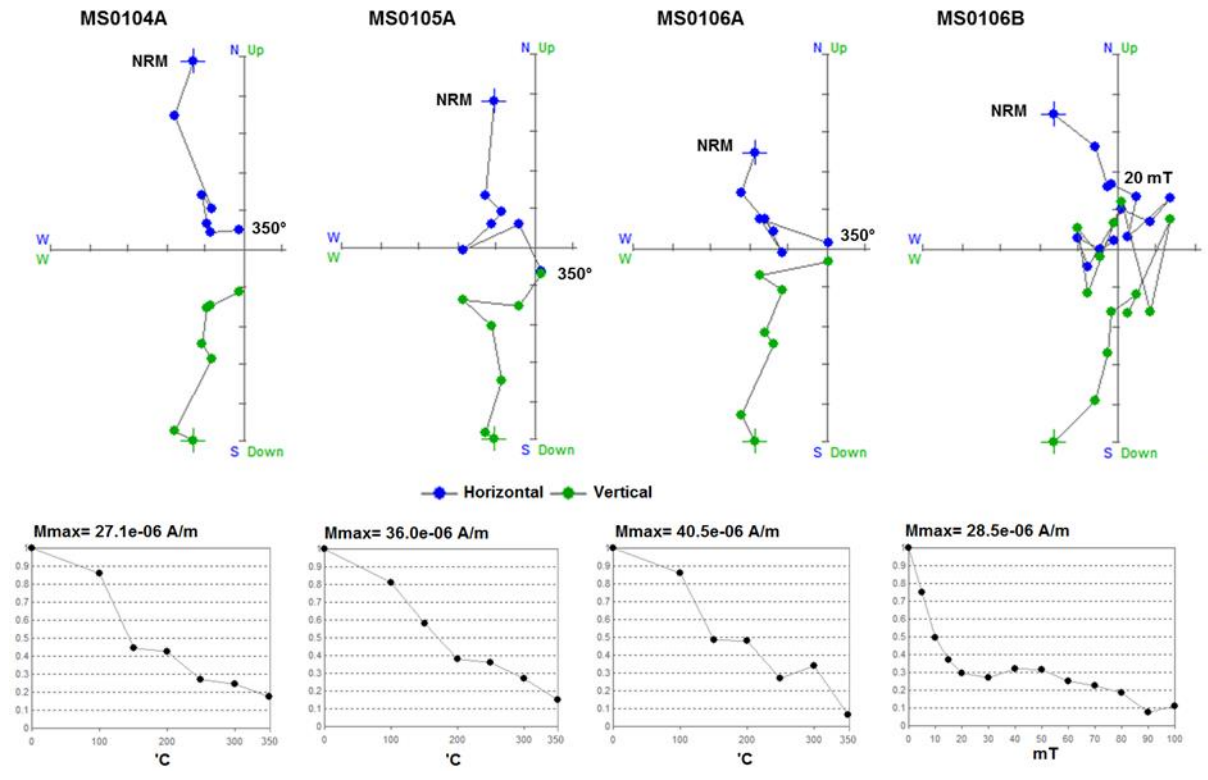


Figure 5.34. (Continued)



**Figure 5.35.** Zijderveld and intensity decay plots of AF and thermal demagnetization data for selected samples showing viscous overprints.



**Figure 5.36.** Zijderveld and intensity decay plots of AF and thermal demagnetization data from Miocene sediments.

**Table 5.5.** Palaeomagnetic data from the ultramafic and gabbroic cumulates of the Mersin ophiolite.

Site	Lithology	Location		DD/D	n	Mean remanence							
		Northing	Easting			<i>In situ</i>				Tilt corrected			
						Dec	Inc	$\alpha 95$	<i>k</i>	Dec	Inc	$\alpha 95$	<i>k</i>
		36 S											
MC01	Ultra mafic cumulates	4074624	604410	177/69	10	50.7	-21.6	8.8	31.3	51.2	22.5	8.8	31.4
MC02	Ultra mafic cumulates	4074571	604356	175/67	12	44.7	2.5	4.9	80.7	69.4	37.7	4.9	80.7
MC03	Ultra mafic cumulates	4074388	604343	136/59	10	44.3	-22.5	7.2	46.4	25.6	-10	7.2	46.2
MC04	Layered gabbro	4074168	604955	352/82	12	61.8	-34.3	4.4	98.5	48.2	21.1	4.4	98.4
MC05	Layered gabbro	4074117	605012	332/50	12	56	-34	5	75.7	37.7	25.2	5	75.5
MC06	Layered gabbro	4073994	605531	332/63	12	63.7	-26.1	3.4	168	37.9	10.1	3.4	168
MC07	Layered gabbro	4073970	605536	350/70	12	62.5	-37.9	1.8	596.2	46.6	25.7	1.8	595.3
MC08	Layered gabbro	4073746	605656	318/60	12	63.3	-20.9	3.1	202.2	22.3	-2	3.1	202.7
MC09	Layered gabbro	4073626	605650	318/60	12	60.8	-25.9	4.4	99.2	19.4	2.6	4.4	99.5
MC10	Fine grained gabbro	4073618	605670	183/52	12	53.7	-27	3.9	124.6	47.4	9.5	3.9	124.1
MC11	Layered gabbro	4073606	605701	318/60	12	52.4	-26.6	3.4	167.3	22.7	9.5	3.4	166.6
MC12	Layered gabbro	4073597	605735	320/68	12	60.8	-24.7	2.5	291	23.2	-0.1	2.5	290.9
MC13	Layered gabbro	4073587	605833	177/87	12	76.2	-23	2.5	297	63.1	8.7	2.5	297.8
MC14	Layered gabbro	4073490	605945	185/64	12	37.7	-32.4	4.3	104	34.9	23.8	4.3	104.5
MC15	Folded layered gabbro	4071026	606078	024/28	8	53.3	-16.5	20.4	8.3	61.9	-40	20.4	8.3
MC16	Layered gabbro	4068859	606861	006/82	12	67.4	-43.7	4	120.5	51	26	4	120.5
MC17	Layered gabbro	4068489	606992	160/62	12	13	-10	7.7	33	24.8	40.3	7.7	33
MC18	Layered gabbro	4068403	606955	132/52	12	48	-11.6	3.7	125.8	36.3	-11.8	3.7	125.9
<b>The mean of sites excluding the sites MC10 &amp; MC15</b>													
						<i>In situ</i>				Tilt corrected			
<b>N</b>						<b>Dec</b>	<b>Inc</b>	<b><math>\alpha 95</math></b>	<b><i>k</i></b>	<b>Dec</b>	<b>Inc</b>	<b><math>\alpha 95</math></b>	<b><i>k</i></b>
16						53.7	-25.4	8.1	21.7	37.9	14.7	10.1	14.3

**N**=number of sites; **n**=number of specimens; **Dec**=declination; **Inc**=inclination;  **$\alpha 95$** =semi-angle of 95% cone of confidence; **K**=Fisher precision parameter; **DD/D**=dip direction and dip. . Sites MC10 and MC15 are excluded from the overall locality mean calculation as MC10 is a fine-grained vein cutting the cumulate sequence and gabbros at MC15 exhibited small-scale local folding.

**Table 5.6** Palaeomagnetic data from the dykes of the Mersin ophiolite.

Site	Location		DD/D	n	Mean remanence				Tilt corrected			
	Northing	Easting			<i>In situ</i>							
					Dec	Inc	$\alpha_{95}$	<i>k</i>	Dec	Inc	$\alpha_{95}$	<i>k</i>
36 S												
<b><i>Mantle-hosted dykes</i></b>												
MD01	4084068	621261	160/70	12	330.8	34.0	7.2	36.9	332.2	14.2	7.2	36.9
MD02	4083961	621215	185/44	12	3.2	-73.9	3.7	141.7	186.0	-60.1	3.7	141.7
MD03	4083928	621212	104/28	12	24.7	-55.4	2.6	282.0	68.3	-17.1	2.6	282.4
MD04	4083916	621217	108/24	12	14.3	-64.6	3.0	210.3	80.2	-23.1	3.0	209.8
MD05	4083859	621272	152/40	12	34.9	-48.5	2.8	247.0	94.8	-45.5	2.8	248.3
MD10	4083373	619291	144/75	12	354.2	-3.9	3.7	139.9	355.6	-16.8	3.7	140.4
MD11	4083127	620091	081/44	12	14.6	-50.0	3.0	210.6	15.8	14.0	3.0	211.2
<b><i>Metamorphic sole-hosted dykes</i></b>												
MD06	4083739	618843	307/38	12	6.0	12.2	7.1	37.8	27.3	31.7	7.2	37.8
MD07	4083766	618832	328/64	12	9.8	16.1	2.7	263.3	18.8	34.3	2.7	263.6
MD08	4083788	618824	330/50	12	1.6	13.6	4.2	105.9	16.6	45.4	4.2	105.7
MD09	4083809	618829	322/66	12	9.4	28.7	3.0	209.4	23.8	42.8	3.0	208.1

**n**=number of specimens; **Dec** = declination; **Inc** = inclination;  **$\alpha_{95}$**  = semi-angle of 95% cone of confidence; **K** = Fisher precision parameter; **DD/D** = dip direction and dip.

## 5.7 Tectonic analysis of palaeomagnetic data

### 5.7.1 Expected palaeomagnetic reference direction

An expected reference direction for the Late Cretaceous igneous rocks sampled in this study was obtained using the 80 Ma African palaeomagnetic pole of Besse and Courtillot (2002), since the ophiolite is dated at  $82.8 \pm 4.0$  Ma (Parlak *et al.*, 2013). This pole (latitude =  $70.3^\circ\text{N}$ , longitude =  $241.6^\circ\text{E}$ ) yields a reference direction of Dec/Inc =  $350.6/34.4$  for sampling sites at the present day location of the Mersin ophiolite (latitude =  $36.8^\circ\text{N}$ , longitude =  $34.2^\circ\text{E}$ ). This direction is then used to quantify tectonic rotations that have affected the sampled units. Use of alternative apparent polar wander paths leads to insignificant differences in inferred rotation angles, as does use of Eurasian poles.

### 5.7.2 Discussion of structural corrections and timing of magnetization

The classical method to identify the timing of magnetization is by applying the fold test (or bedding-tilt test). In this test, relative timing of remanence acquisition and tilting can be identified (Butler, 1998). The fold test involves comparing magnetization directions before and after removing tilting by rotating sampled units around a structural line of strike back to the horizontal. Directions and palaeomagnetic statistics are then compared in *in situ* (or geographic) and tilt corrected (or stratigraphic) coordinates. If directions are clustered better in tilt corrected coordinates, this means the magnetization was acquired prior to folding; in contrast, increased scattering of directions after a tilt correction indicates that remanence acquisition was after tilting (Figure 5.37).

In the current study, the cumulate sites showed an overall mean *in situ* direction of Dec = 53.7, Inc = -25.4, ( $\alpha_{95} = 8.1^\circ$ ,  $k = 21.7$ ;  $N = 16$ ; Table 5.5). Application of individual site-level tilt corrections to these sites yields an overall mean tilt corrected direction of Dec = 37.9, Inc = 14.7, ( $\alpha_{95} = 10.1^\circ$ ;  $k = 14.3$ ). This slight increase in scattering in remanence directions after tilt correction might be taken at face value to indicate that the section was magnetized after tectonic disruption of the cumulate layering, in contrast to the rock magnetic, palaeomagnetic and petrographic data that support presence of a primary thermoremanence. However, unlike sedimentary bedding, cumulate layering in a magma chamber may have significant local variations in orientation. In addition, slow-cooled lower crustal cumulates might have acquired remanences some time after more rapidly cooled upper crustal units, with potential for seafloor spreading-related tilting of a section before remanence is blocked in (e.g. see Johnson *et al.*, 1987; Gee and Kent, 2007). This is supported by a more sophisticated net tectonic rotation approach to the structural correction of the palaeomagnetic data (applied below; Allerton and Vine, 1987; Morris *et al.*, 1998) that shows that the cumulates may have had several 10's of degrees of dip at the time of remanence blocking. Unfortunately, this means that the remanence inclination data from the cumulate section cannot be used to calculate the palaeolatitude of the Mersin spreading axis, and so this study cannot provide constraints that might inform regional palaeogeographical reconstructions. In addition, the simple tilt correction approach, as mentioned in Section 2.7.6, may introduce significant declination errors if the actual rotation history of a site was not strictly around a strike-parallel horizontal axis (MacDonald, 1980). Hence: (i) the slight increase in dispersion of site-level data after standard tilt correction is not considered to be significant; (ii)

remanences are assumed to represent primary magnetizations acquired during cooling of the cumulates below the blocking temperature of the remanence carriers; and (iii) the net tectonic rotation approach is considered to be the best way of quantifying and analyzing rotations in this case, for both the cumulates and dykes.

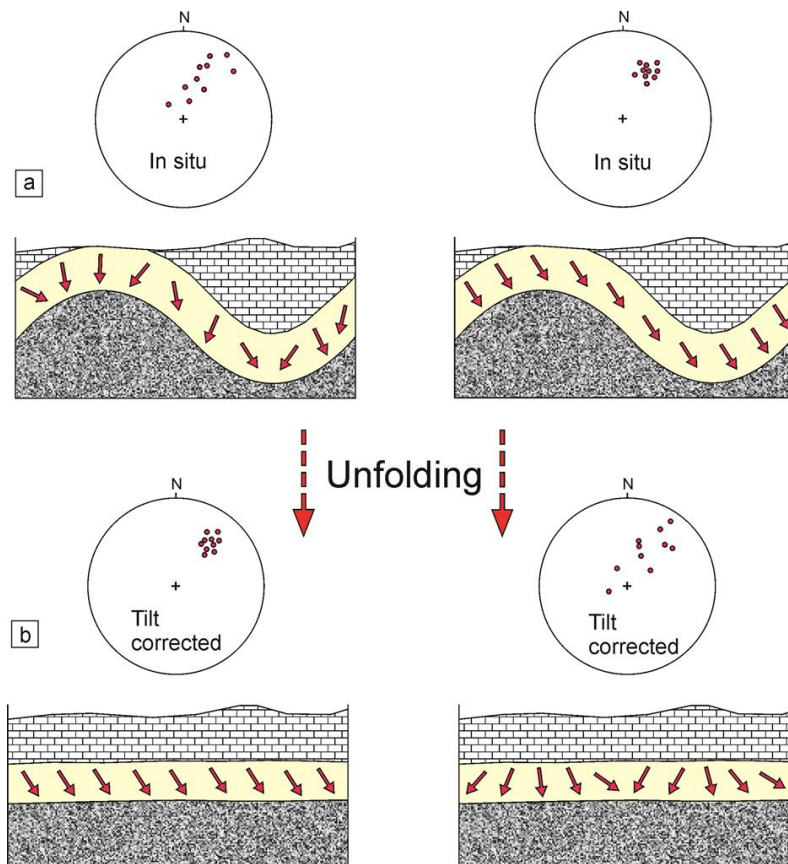


**Figure 5.37.** Schematic diagrams with stereoplots illustrating the classical palaeomagnetic fold test. (a) Before tilt correction. (b) After tilt correction. In the lower left stereoplot, the remanence directions are more clustered after tilt correction, indicating that the remanence was acquired prior to folding. In the lower right stereoplot, the remanence directions are more scattered after tilt correction, indicating that the remanence was acquired after folding.

### 5.7.3 Net Tectonic Rotation Analysis

The fundamentals of net tectonic analysis have been described in Chapter Two. It involves determining the pole(s) of rotation which allow restoration of both the site magnetization vector (SMV) back to the appropriate palaeomagnetic reference direction and the present day pole to a dyke or layering to as close to

its initial orientation (vertical for layering and horizontal for dykes) as possible. A net tectonic rotation is described by three parameters, i.e. the azimuth and plunge of the pole of rotation and the angle of rotation, where a positive angle represents an anticlockwise net rotation (Allerton and Vine, 1987).

In this study, a modification to the original net tectonic rotation algorithm of Allerton and Vine (1987) has been used, as proposed by Morris *et al.* (1998), which allows the confidence region associated with the calculated rotation axis to be assessed. This modification applies the Allerton and Vine (1987) technique to all combinations of each of five orientations for the three vectors input into the analysis (i.e. reference direction, site magnetization vector and pole to dyke or layering). These orientations are distributed around the  $\alpha_{95}$  circles for each vector (n.b. an  $\alpha_{95}$  of  $5^\circ$  was assigned to the structural data as a best estimate of uncertainties in measuring structures in the field). Thus, this provides 125 combinations of input vectors, and an output that contains either 125 or 250 determinations of the net tectonic rotation pole and rotation angle for each site (depending on whether two solutions are found in dyke cases). The envelope on a stereonet that surrounds the set of permissible rotation axes provides a first-order approximation of the associated 95% confidence region, and the associated permissible rotation angles are displayed on histograms. The net tectonic rotation results from both cumulates and dykes are given in Tables 5.7 and 5.8, whereas Figures 5.38 and 5.39 illustrate stereonets with envelopes of potential rotation poles and histograms of rotation angles for each of the sampled sites.

In each case, the results of this analysis indicate that the cumulate sites have been tectonically rotated in a clockwise sense around NE plunging axes by approximately  $100\text{-}140^\circ$ . Results also show that it is impossible to restore both

the remanence to the expected direction and the pole to cumulate layering to the vertical, indicating that the cumulate layering was not horizontal at the time that remanences became blocked in (Table 5.7). As noted previously, this means that the remanence data cannot be used to provide palaeolatitudinal constraints on the N-S position of the Mersin spreading axis within Neotethys.

An alternative approach to applying the net tectonic rotation method to individual sites in the cumulate section is to use the overall mean *in situ* direction calculated from these sites together with the mean orientation of cumulate layering to calculate net tectonic rotation parameters at the locality-level. The overall *in situ* mean direction of magnetization of the section is Dec = 53.7°, Inc = -25.4°, and the mean orientation of the cumulate layering has a strike = 68.8° and dip = 90.8° (slightly overturned). These input parameters yield a net tectonic rotation solution (Table 5.7) indicating a 117° clockwise rotation of the section around a pole plunging at 27° towards 051° (Figure 5.39).

**Table 5.7.** Net tectonic rotation parameters for ultramafic and gabbroic cumulates of the Mersin ophiolite.

Site	Status	Net Tectonic Rotation Parameters										
		Reference direction		<i>In situ</i> magnetization		Cumulate layering		Rotation axis		Angle of rotation	Beta	Residual initial dip
Dec	Inc	Dec	Inc	Strike	Dip	Azimuth	Plunge					
MC01	N	350.6	34.4	50.7	-21.6	87	69	63.1	35.3	98.3 CW	67.5	11.8
MC02	N	350.6	34.4	44.7	2.5	85	67	43.1	43.6	97.8 CW	52.3	3.4
MC03	N	350.6	34.4	44.3	-22.5	46	59	56.8	31.0	98.2 CW	100	44.3
MC04	O/T	350.6	34.4	61.8	-34.3	82	98	57.7	24.0	120.7 CW	68.8	13.1
MC05	O/T	350.6	34.4	56.0	-34.0	62	130	40.4	13.3	141.1 CW	64.8	9.1
MC06	O/T	350.6	34.4	63.7	-26.1	62	117	44.9	20.1	140.7 CW	79.9	24.2
MC07	O/T	350.6	34.4	62.5	-37.9	80	110	54.5	19.5	126.4 CW	64.3	8.6
MC08	O/T	350.6	34.4	63.3	-20.9	48	120	41.1	20.2	147.7 CW	92.0	36.3
MC09	O/T	350.6	34.4	60.8	-25.9	48	120	41.2	17.9	144.5 CW	87.4	31.7
MC11	O/T	350.6	34.4	52.4	-26.6	48	120	38.2	17.0	139.6 CW	80.5	24.8
MC12	O/T	350.6	34.4	60.8	-24.7	50	112	43.4	20.5	139.6 CW	90.1	34.4
MC13	N	350.6	34.4	76.2	-23.0	87	87	62.0	33.4	128.1 CW	81.3	25.6
MC14	N	350.6	34.4	37.7	-32.4	95	64	76.6	28.6	85.5 CW	66.2	10.5
MC16	O/T	350.6	34.4	67.4	-43.7	96	98	68.3	23.5	118.3 CW	64.0	8.3
MC17	N	350.6	34.4	13.0	-10.0	70	62	49.1	26.3	65.2 CW	49.6	6.1
MC18	N	350.6	34.4	48.0	-11.6	42	52	57.8	40.1	94.3 CW	101.8	46.1
Mean (all)		350.6	34.4	53.7	-25.4	68.8	90.75	51.2	26.6	117.2	76.1	20.5

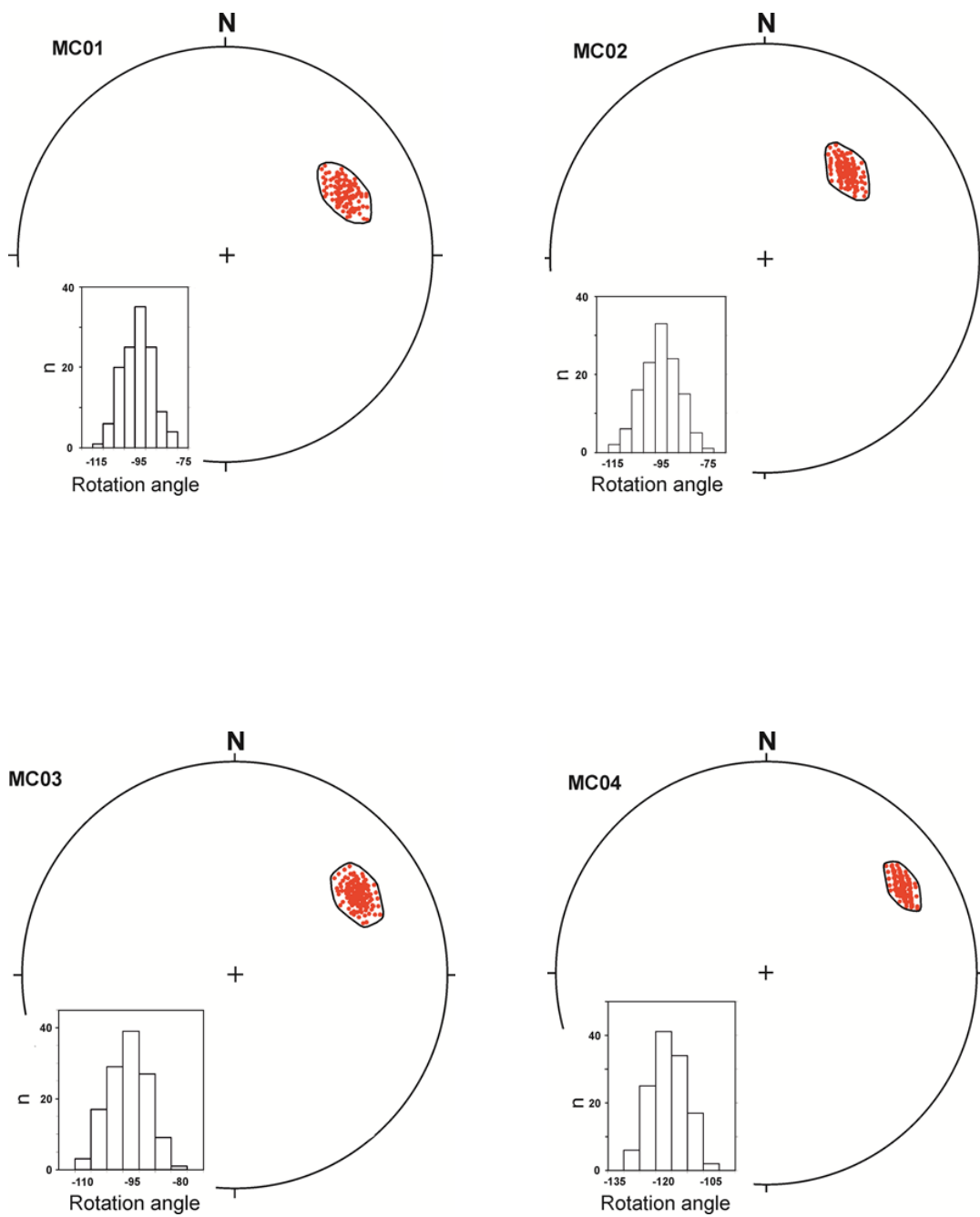


**Figure 5.38.** Results of the net tectonic analysis at each site in the gabbroic and ultramafic cumulate section of the Mersin ophiolite (continued on next two pages)

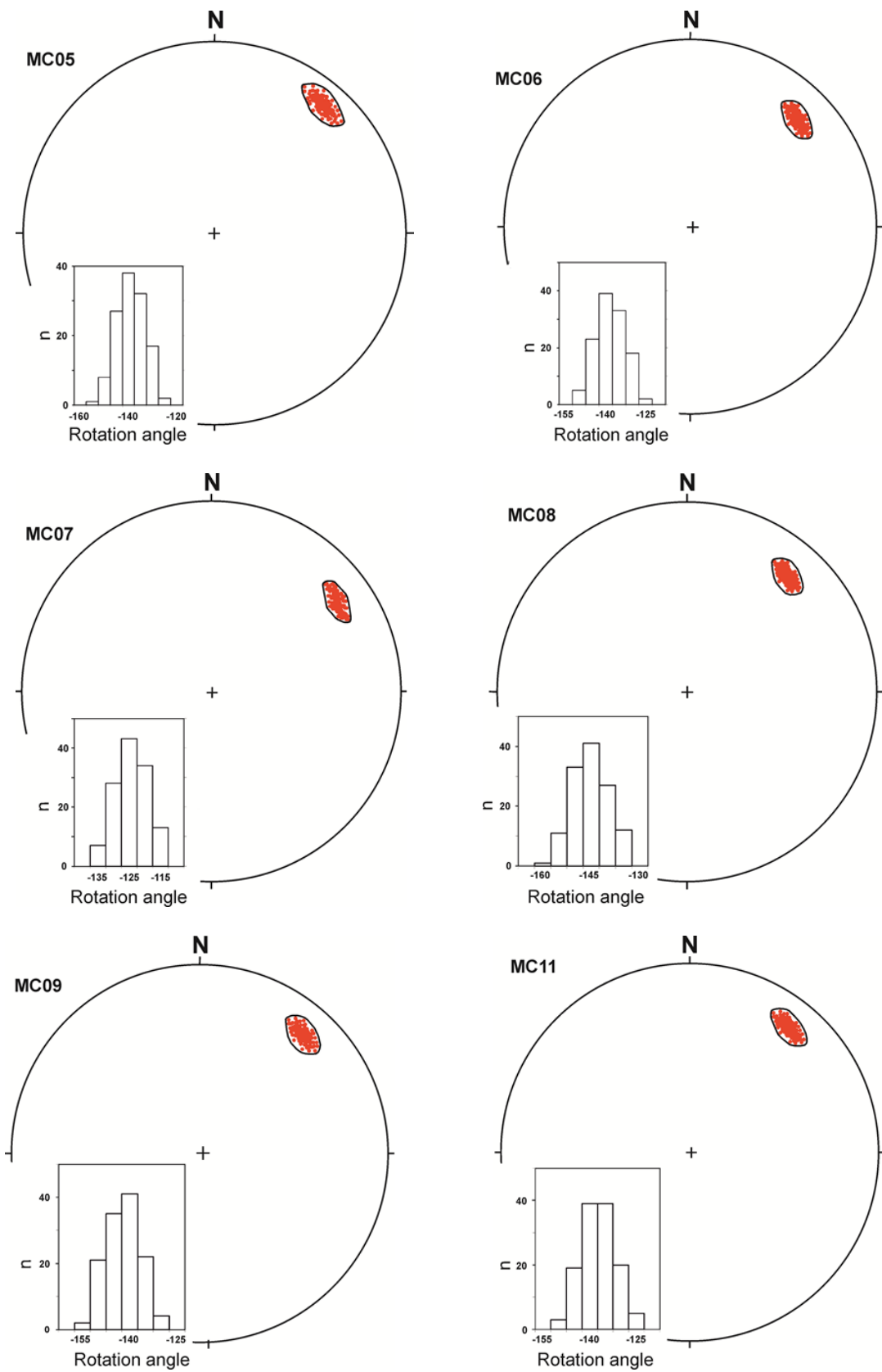


Figure 5.38. (Continued)

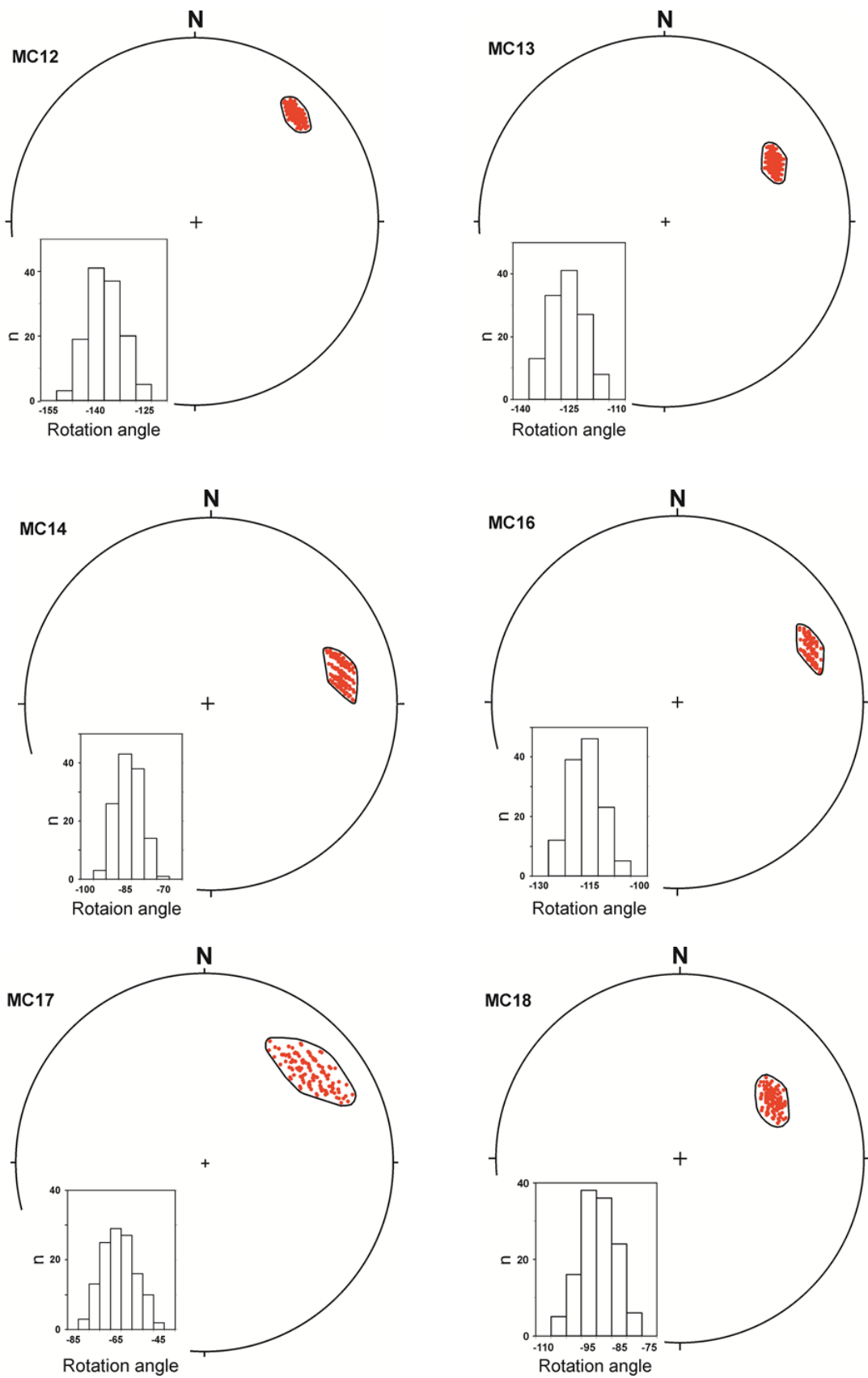
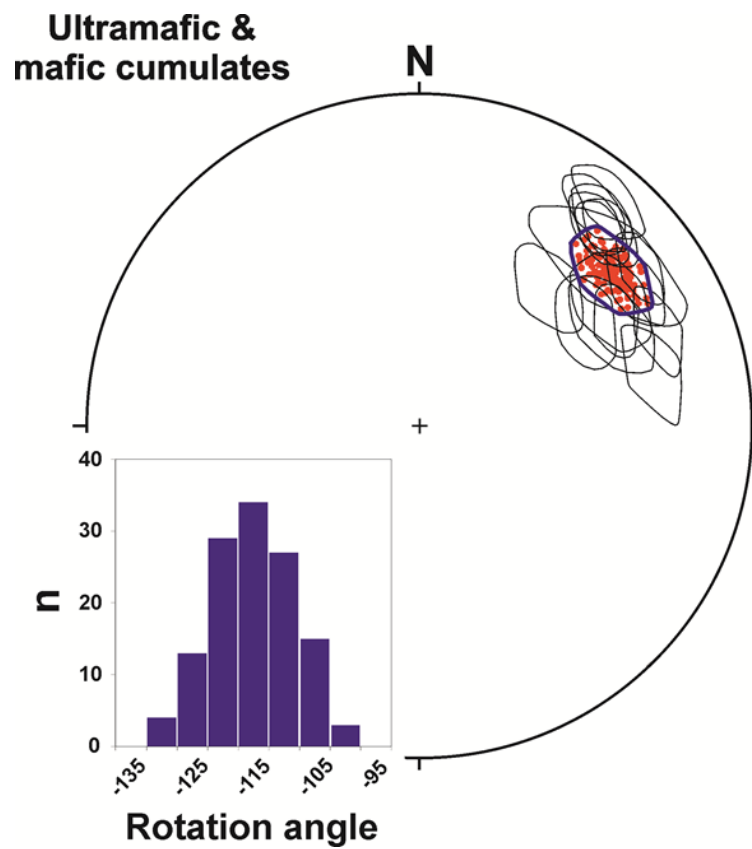


Figure 5.38. (Continued)



**Figure 5.39.** Overall net tectonic analysis for the ultramafic and gabbroic cumulate section in the Sorgun Valley section of Mersin ophiolite, using the mean magnetization vector of the section and the mean orientation of cumulate layering. Red symbols and surrounding envelope show the 125 solutions found using this approach, with permissible rotation angles shown in the inset histogram. Other envelopes on the stereonet show the results of applying the net tectonic rotation method to individual sampling sites (i.e. the results shown in Figure 5.38).

**Table 5.8.** Net tectonic rotation parameters for dykes of the Mersin ophiolite.

Site	Unit	Net Tectonic Rotation Parameters													
		Reference direction		<i>In situ</i> magnetization		Dyke margin		Rotation axis				Initial dyke orientation			
		Dec	Inc	Dec	Inc	Strike	Dip	Alternative	Preferred	Angle of rotation	Beta	Strike	Dip		
MD01		350.6	34.4	330.8	34	70	70	Single		161.5	2.4	26.9 CCW	16.2	80.6	71.8
MD02		350.6	34.4	3.0	-73.9	95	44	Alternative		125.1	15.8	125.1 CW	60.1	133.4	90
								Preferred		230.2	8.5	118.7 CCW	60.1	27.8	90
MD03	Dykes hosted by Mantle	350.6	34.4	24.7	-55.4	14	28	Alternative		87.6	14.5	94.5 CW	39.1	100.4	90
								Preferred		48.4	3.3	112.6 CW	39.1	60.8	90
MD04		350.6	34.4	14.3	-64.6	18	24	Alternative		74.9	5.0	101.9 CW	35.5	90.0	90
								Preferred		235.8	1.0	109.7 CCW	35.5	71.2	90
MD05		350.6	34.4	34.9	-48.5	62	40	Alternative		128.4	23.5	99.3 CW	67.7	143.2	90
								Preferred		37	4.1	129.4 CW	67.7	18.0	90
MD10		350.6	34.4	354	-4.0	54	75	Alternative		345	14.5	139.8 CCW	35.4	89.5	90
								Preferred		338.4	13.6	111.2 CCW	35.4	71.7	90
MD11		350.6	34.4	15.0	-50	351	44	Alternative		74.1	9.9	89.1 CW	43.1	108.4	90
								Preferred		207.3	1.5	129 CCW	43.1	52.8	90
MD06	Dykes hosted by Metamorphic Sole	350.6	34.4	6.0	12.2	217	38	Alternative		350.9	18.5	112.4 CCW	81.8	160.6	90
								Preferred		21.5	33.5	63.5 CW	81.8	0.6	90
MD07		350.6	34.4	10.0	16.1	238	64	Alternative		353.2	18.5	103.7 CCW	58.5	131.3	90
								Preferred		44.3	46.5	38.2 CW	58.5	29.9	90
MD08		350.6	34.4	2.0	13.6	240	50	Alternative		345.9	18.9	92.8 CCW	61.1	134.8	90
								Preferred		24.3	32.5	50.4 CW	61.1	26.4	90
MD09		350.6	34.4	9.0	28.7	232	66	Alternative		358.1	26.4	112.1 CCW	69.7	145.7	90
								Preferred		12.5	52.5	42.8 CW	69.7	15.5	90

The results of net tectonic analyses for each dyke (excluding site MD01) yielded two solutions. Dykes hosted by the mantle sequence (sites MD02, MD03, MD04, MD05 and MD11) give preferred solutions (Figure 5.40) with sub-horizontal, NE-SW-directed rotation poles and clockwise rotations (when looking towards the NE along the rotation axis) ranging from 110°-130°. The alternative solution in each case is characterised by shallowly-plunging rotation axes with widely variable NE-SW-directed azimuths and clockwise rotations of 95°-125° (when looking towards the NE along the rotation axis). These alternative solutions are discounted because of the lack of consistency of the orientation of rotation axes between different sites, compared to the very consistent orientations of the preferred solutions. Results from site MD01 are discounted as they yield only single solutions that have a very broad scatter of permissible rotation axes when uncertainties in input vectors are incorporated. Site MD10 is also discounted as this has a very different orientation to the suite of other dykes cutting the mantle and gives therefore only a single result that may not be representative of the whole section.

The dykes hosted by the metamorphic sole (sites MD06, M07, MD08 and MD09) also yielded two solutions. The preferred solutions (Figure 5.41) show moderately plunging, NE-directed rotation axes and 40°-60° clockwise rotation. The alternative solutions yield shallowly plunging, N-to-NW-directed rotation poles, with large anticlockwise rotations of 90°-110°. These solutions are rejected on the basis of lack of consistency of sense of rotation compared to all other results (from both dykes in the mantle sequence and the cumulate section). Examples of these inconsistent alternative solutions are provided in Figure 5.42.

A summary of all preferred solutions for the sampled dykes is shown in Figure 5.43.

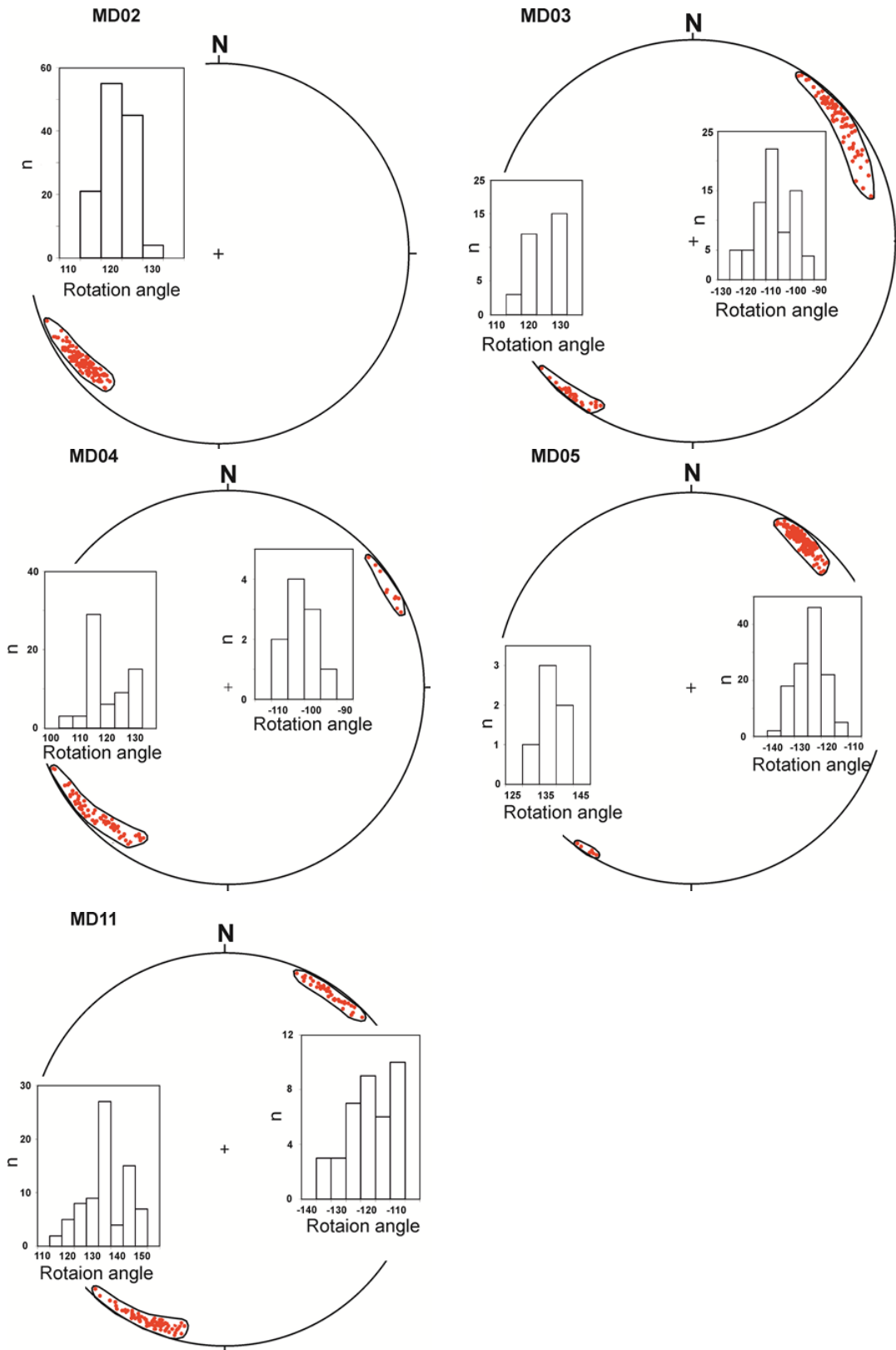


**Figure 5.40.** Results of net tectonic analyses for each site within the discrete dykes cutting the mantle sequence of the Mersin ophiolite (preferred solutions only).

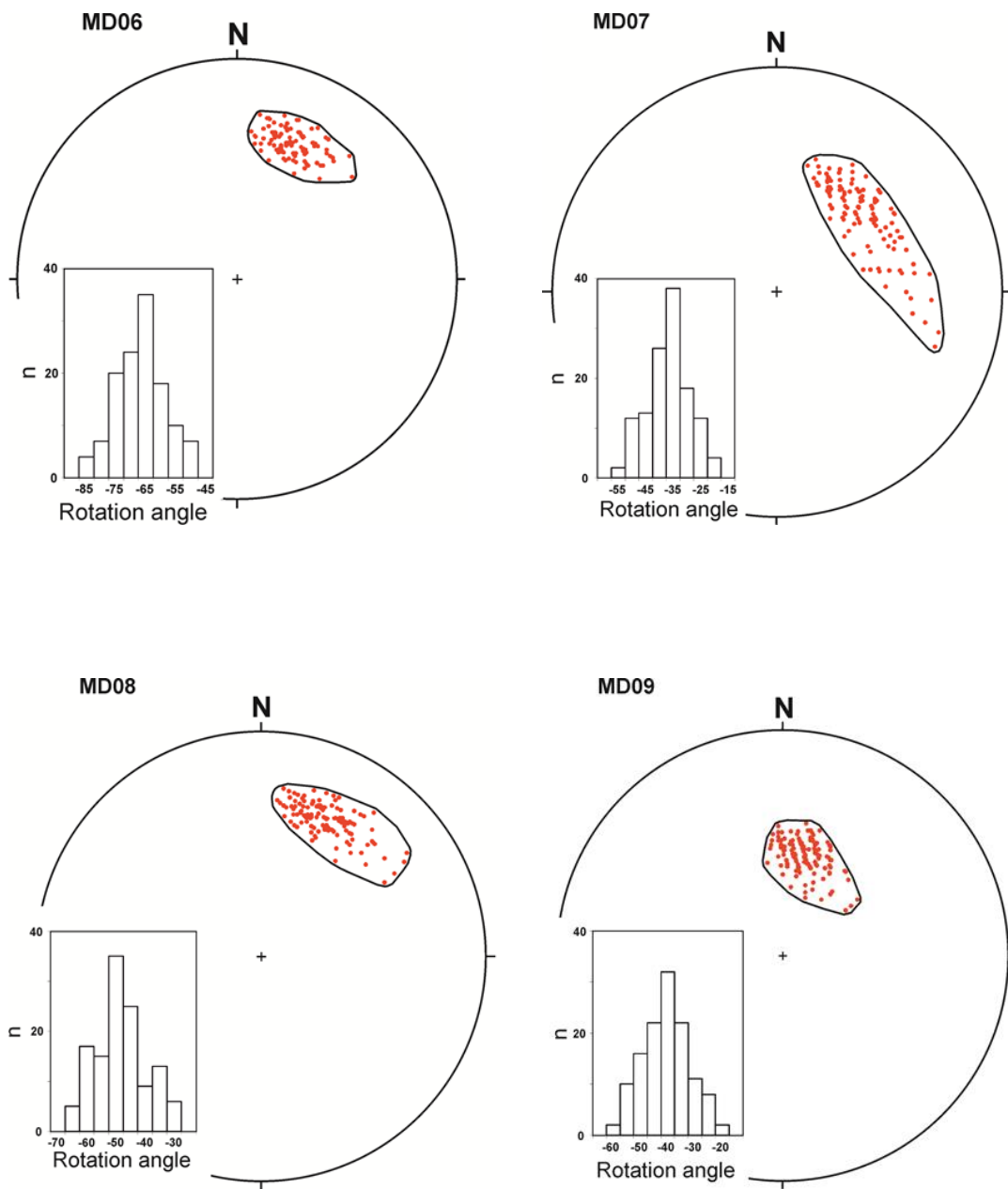


**Figure 5.41.** Results of net tectonic analyses for each site within the discrete dykes cutting the metamorphic sole of the Mersin ophiolite (preferred solutions only).

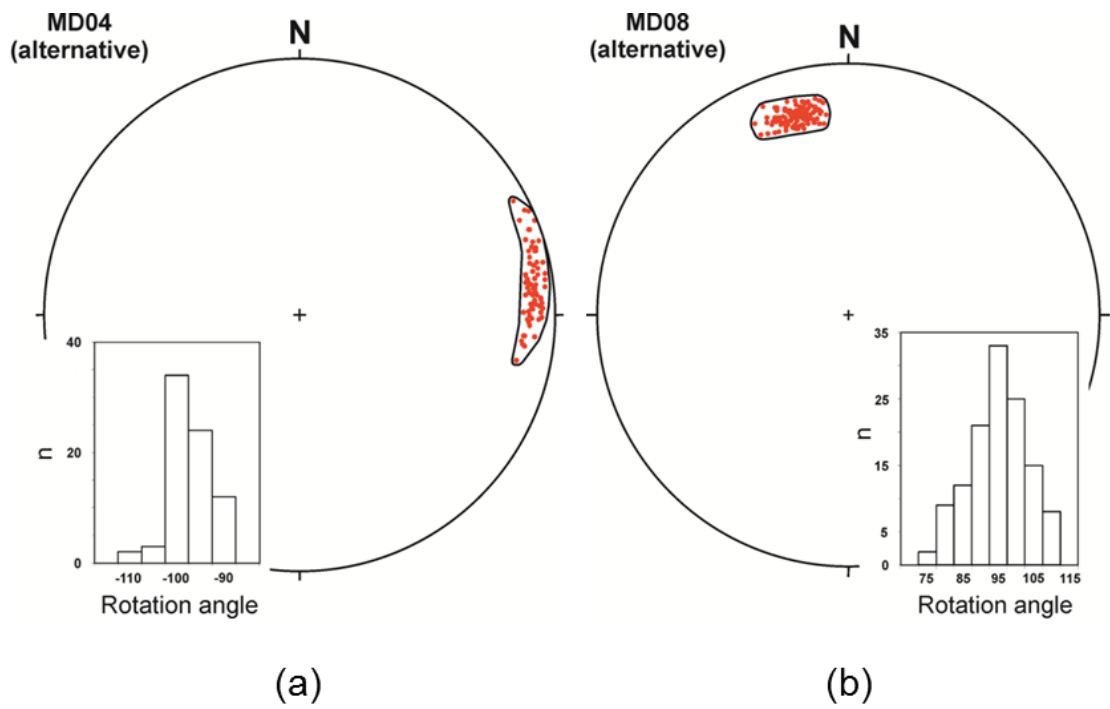


**Figure 5.42.** Examples of alternative net tectonic rotation solutions from dykes of the Mersin ophiolite. (a) Site MD04 (hosted by mantle). (b) Site MD08 (hosted by metamorphic sole).

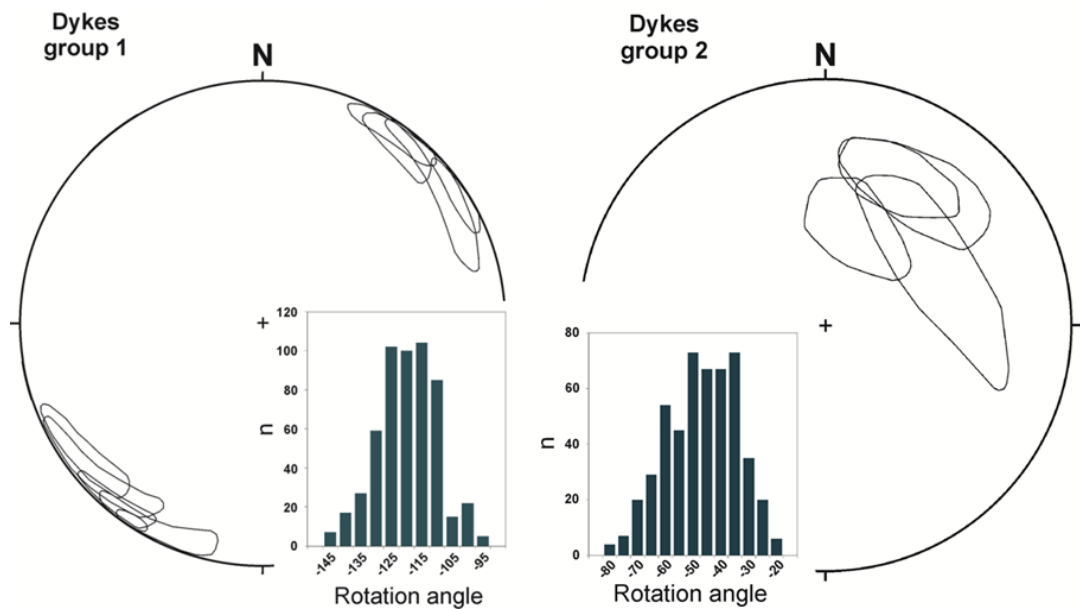


**Figure 5.43.** Summary of net tectonic analysis results for both groups of dykes from Fındıklı section of Mersin ophiolite, combining all preferred solutions. Group 1 = dykes in the mantle sequence; Group 2 = dykes in the metamorphic sole.

## 5.8 Discussion

### 5.8.1 Significance of the magnetic fabric data

Although AMS fabrics vary significantly between sampling sites in the Mersin cumulate section in terms of the distribution of  $k_2$  (intermediate) and  $k_3$  (minimum) principal axes, there is a marked consistency in the orientation of  $k_1$  (maximum) principal anisotropy axes, which tend to lie on or close to the plane of cumulate layering at each site and share a broad ENE-WSW trend between sites. As noted in Section 5.5.1.2 above, such a consistency in  $k_1$  axes may result from either magmatic or tectonic processes.

In thin section, the majority of the samples from these sites show no obvious evidence for crystal plastic deformation that might be indicative of shearing or tectonism. Any strain in the gabbroic sequence appears to be partitioned into minor, very thin mylonitic zones (see Chapter 4). These observations suggest, therefore, that the preferred orientation of  $k_1$  axes is related to magmatic flow or deformation in the magmatic state during the formation of the lower crustal cumulates.

Mineral lineations of magmatic origin have been reported previously in ophiolitic gabbros (e.g. Thayer, 1963; Jackson *et al.*, 1975; Girardeau and Nicolas, 1981; Benn and Allard, 1989; Yaouancq and MacLeod, 2000; Morales *et al.*, 2011) and have been inferred from AMS data in Ocean Drilling Program drill core samples of *in situ* lower crustal gabbros recovered at Hess Deep in the Pacific (MacLeod *et al.*, 1996). In the Oman ophiolite, Nicolas *et al.* (1988) have described magmatic mineral foliations and lineations within lower crustal gabbros, and interpreted these as resulting from large-scale viscous

deformation within unconsolidated magma chambers. Subsequently, Benn and Allard (1989) used data on shape and lattice preferred orientations in Oman gabbros to suggest that large-scale laminar magmatic flow had occurred, resulting in strong preferred orientations of minerals. They suggested that the azimuth, and in some cases the shear sense, of magmatic flow could be inferred from the lineation data (Benn and Allard, 1989), providing insights into the structure and dynamics of magmatic bodies at oceanic spreading centres.

In the case of the magnetic lineation ( $k_1$  axes) documented in this study in the Mersin gabbros, thin section analyses demonstrate that this reflects a preferred orientation of opaque magnetite grains that is itself controlled by a preferred orientation of silicate crystals. At the simplest level, if these preferred orientations are considered to result from magmatic flow/deformation away from the Mersin spreading axis (as is inferred in the case of some fabrics observed in Oman; e.g. Benn and Allard, 1989), then the E-W to NE-SW oriented  $k_1$  axes (mean orientation: azimuth = 249.1, plunge = 0.5°; Figure 5.44) must be corrected for net tectonic rotation in order to estimate the orientation of the Mersin spreading axis. This is best achieved by back-stripping the net tectonic rotation calculated using data from the whole cumulate section. This rotation is around an axis of azimuth = 051.2°, plunge = 26.6° (Section 5.7.3 above), with a clockwise rotation of 117.2°, requiring an anticlockwise rotation of this magnitude around the same axis to restore  $k_1$  axes to their pre-rotation orientation. This yields a restored  $k_1$  mean orientation of azimuth = 017.6°, plunge = 18.2°, implying a WNW-ESE oriented spreading Mersin spreading axis (Figure 5.44).

This estimate is compatible with reconstructions of the eastern Mediterranean in the Late Cretaceous that indicate a broad E-W orientation of both the northern and southern strands of the Neotethyan Ocean (e.g. Robertson *et al.*, 2013b; Figure 5.45). It is also consistent with previous palaeomagnetic research in the Troodos ophiolite (Moores and Vine, 1971; Clube and Robertson, 1986; Allerton and Vine, 1987, 1991) that indicates that the Troodos Sheeted Dyke Complex formed at a WSW-ENE oriented spreading axis (once the effects of Troodos microplate rotation are removed).

As a corollary, this broad agreement between the orientation of spreading axes inferred from palaeomagnetically corrected  $k_1$  axes in lower crustal cumulates of the Mersin ophiolite and those inferred from regional geological evidence and from restored orientations of sheeted dykes suggests that magnetic fabric analysis may form a useful tool in reconstructing spreading directions when direct determinations from sheeted dyke complexes are not possible. However, it must be noted that at slow-spreading axes there may be significant ridge-parallel migration of melt away from discontinuous zones of magma supply, e.g. from spreading segment centres towards transforms at segment ends (e.g. Dunn *et al.*, 2005). Such along axis melt migration has been documented in both the upper crustal Sheeted Dyke Complex (Staudigel *et al.*, 1992) and lower crustal gabbros (Granot *et al.*, 2011) in the Troodos ophiolite using AMS data. In detail, Granot *et al.* (2011) used AMS to establish presence of two major domains of fabrics associated with the Solea spreading axis in the Troodos ophiolite. The first domain, found at the inferred spreading segment edge, was marked by vertical magnetic lineations that are inferred to result from uniform mantle upwelling and melt supply (blue data in Figure 5.46). In contrast subhorizontal, N-S oriented magnetic lineations in an adjacent domain (red data

in Figure 5.46) are consistent with focused mantle upwelling and melting near the segment midpoint with lateral magma flow in the lower crust towards the sampled region at the fossil segment-edge.

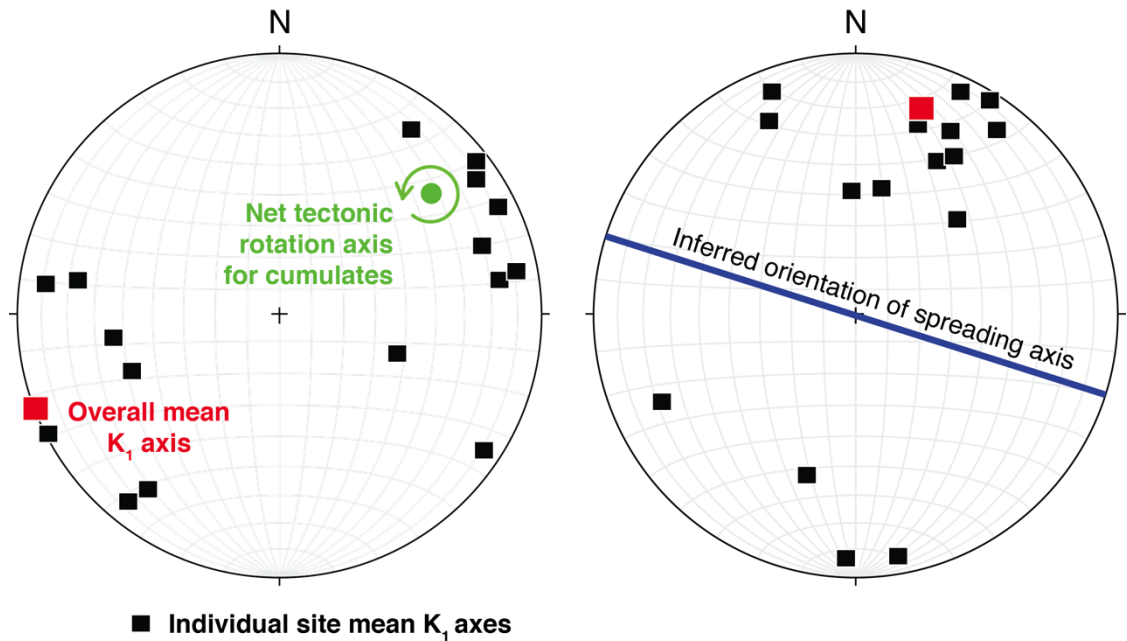


**Figure 5.44.** Restoration of anisotropy of magnetic susceptibility (AMS)  $k_1$  axes using the overall net tectonic rotation determined for lower crustal cumulates of the Sorgun Valley, Mersin ophiolite. Left: Stereonet showing the distribution of site mean  $k_1$  axes (black squares), the overall mean  $k_1$  axis (red square), and the axis of net tectonic rotation (green circle). Right: Back-rotating the AMS data by  $117.2^\circ$  in an anticlockwise sense (green arrow in left-hand stereonet) around the net tectonic rotation axis restores the  $k_1$  data to a NNE-SSW orientation, implying a WNW-ESE-oriented spreading axis (assuming that magmatic flow was on average parallel to the spreading direction during crustal accretion).

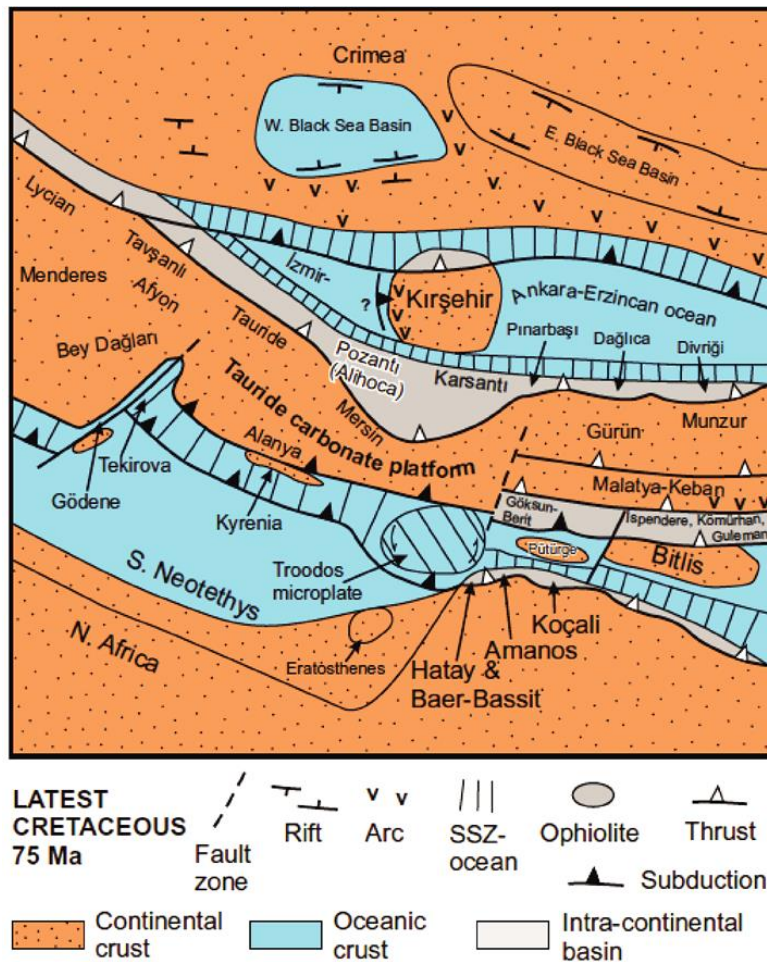


**Figure 5.45.** Palaeogeographic reconstruction of the eastern Mediterranean region in the latest Cretaceous (from Robertson *et al.*, 2013b). Note that the WNW-ESE orientation of the Mersin spreading axis inferred from net tectonic rotation restoration of AMS data is consistent with the broad orientation of the Neotethyan ocean basins.

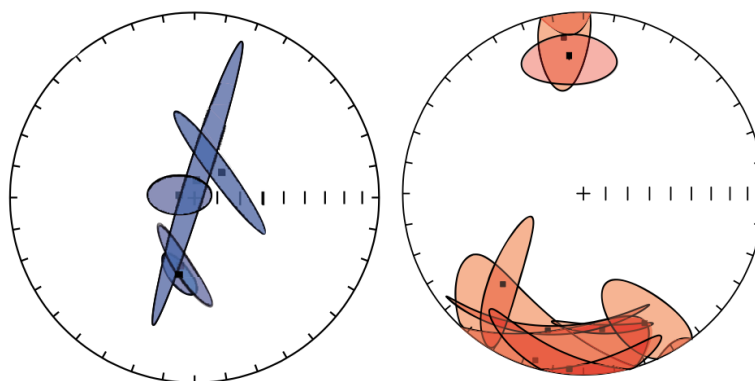


**Figure 5.46.** AMS data from the gabbros of the Troodos ophiolite, from Granot *et al.* (2011), showing presence of two contrasting fabric domains. Left: Subvertical maximum AMS axes in one domain indicate focused upwards flow during a period of plentiful magma supply; Right: Subhorizontal N-S oriented maximum axes in an adjacent domain indicate lateral lower crustal magma flow towards the segment end (represented by the intersection of the Solea spreading axis and the South Troodos Transform Fault Zone).

## 5.8.2 Tectonic interpretation of the palaeomagnetic data and net tectonic rotation analyses

The net tectonic rotation analyses demonstrate that all levels of the Mersin ophiolite (lower crustal cumulates; mantle sequence; metamorphic sole) have experienced large clockwise rotations around NE-trending moderately plunging to sub-horizontal axes. These net rotations could be potentially decomposed into components of tilting and vertical axis rotation. Evidence of the effects of a major component of rotation around a shallowly-plunging or horizontal axis may be seen directly in the field, as cumulate layering is presently sub-vertical to overturned along the Sorgun Valley. Subtraction of this tilt from the net tectonic rotation results leaves a residual component of moderate clockwise rotation around a steeply-plunging or vertical axis in order to explain the palaeomagnetic data. However, geologically meaningful decomposition of the net rotation would require independent structural constraints on the orientation and kinematics of faults that potentially accommodated the rotation components, as well as information on the precise sequence of rotations. Hence, it is more appropriate and informative to interpret the net tectonic rotation parameters directly, but remembering that this assigns all rotation to a single deformation event.

Palaeomagnetic data collected in this study from Miocene carbonates that form part of the post-emplacement, unconformable sedimentary cover of the Mersin ophiolite, give a direction of Dec = 349.6°, Inc = 58.1° ( $k = 48$ ;  $\alpha_{95} = 8.1^\circ$ ). This indicates a small, anticlockwise rotation that, although based on limited sampling at a single site, is consistent with the regional pattern of palaeodeclinations and rotations that has been established by many workers

who have analysed Neogene and younger rocks in the broad Anatolian region.

The available “neotectonic” palaeomagnetic data were

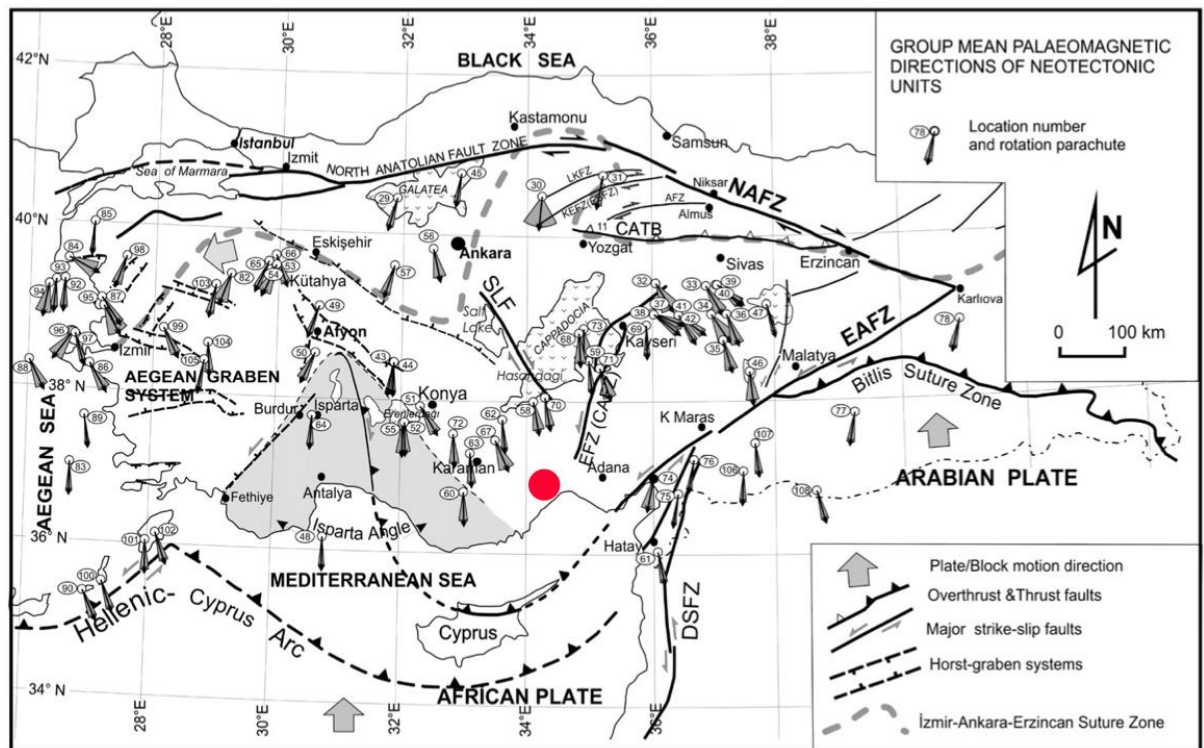


**Figure 5.47.** Schematic tectonic map of Turkey and adjoining region (from Piper *et al.*, 2010) showing the pattern of declinations of mean palaeomagnetic vectors affected by Neotectonic rotations (with arcs embracing 95% confidence limits and converted to a common reversed polarity). The red circle marks the position of the Mersin ophiolite. Note that only very minor anticlockwise rotation of the Anatolian microplate is documented by palaeomagnetic data closest to Mersin.

recently collated and analysed by Piper *et al.* (2010; Figure 5.47). This compilation, and the single site mean direction from carbonates reported here, demonstrate that only a small (c.  $10^\circ$ ) regional anticlockwise rotation of Anatolia has affected the Mersin area since the Miocene. Hence the large, clockwise rotations documented in the ophiolite are demonstrably not of neotectonic origin. Strictly speaking, the small, regional Anatolian anticlockwise rotation should be back-stripped from the ophiolite palaeomagnetic data prior to subsequent tectonic analysis. However, given the small magnitude of this rotation compared to inherent uncertainties in the net tectonic rotation parameters (propagating

through from the statistics of the palaeomagnetic and structural data), and the lack of adequate Neogene data directly from the Mersin area, it was not deemed necessary to incorporate neotectonic rotation into the analysis.

Figure 5.48 provides a graphical summary of the net tectonic rotation parameters for each of the main ophiolitic units sampled (the single site in a basaltic lava flow is not considered further as it is located in an isolated exposure). Results for the cumulate sequence and the dykes in the mantle sequence are remarkably similar, considering that they are geographically separated by c. 20 km and their structural relationship cannot be determined directly in the field. Both have experienced c. 115° clockwise rotation. This implies that little or no significant relative rotation of these units occurred between crustal accretion and emplacement of dykes into the underlying lithospheric mantle (although the order of these magmatic events cannot be

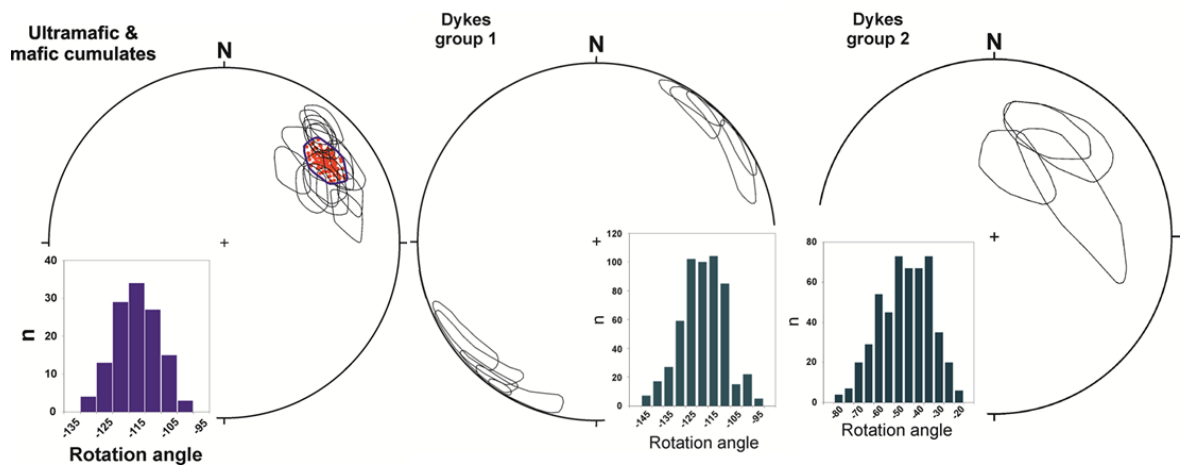


**Figure 5.48.** Comparison of net tectonic rotation parameters for the Mersin cumulate section (left), dykes cutting the mantle sequence (middle) and dykes cutting the metamorphic sole (right). In all cases, rotation is around NE-trending axes and is clockwise in sense. The cumulates and mantle-hosted dykes have experienced similar rotation magnitudes (see inset histograms), whereas the dykes in the metamorphic sole have experienced c. 70° less rotation. See captions of Figures 5.39 and 5.42 for further explanation.

determined). The possibility that these different sections represent different ophiolite thrust slices that coincidentally experienced similar rotations around similar axes cannot be discounted, but it seems more likely that the cumulates and mantle sequence are part of a single coherent unit that has experienced a consistent rotation history. In contrast, dykes in the metamorphic sole have experienced c. 45° of clockwise rotation, again around NE-trending axes, i.e. c. 70° less rotation than the structurally higher mantle and cumulate sections.

There is a possibility that this differential rotation of the lowermost and uppermost parts of the Mersin ophiolite pseudostratigraphy occurred during tectonic emplacement on to the Taurides. Such relative rotation could result from pinning of the metamorphic sole during thrust emplacement, but this would likely result in significantly different orientations of rotation axes between lower and upper sheets. Instead, it is more probable that this differential rotation occurred in an intraoceanic setting, prior to final emplacement, and is more likely to result from progressive rotation of a coherent section of the ophiolite during initial oceanic detachment, with emplacement of dykes into the metamorphic sole occurring synchronously with tectonic rotation.

It must be noted that the large net tectonic rotations documented here in the Mersin ophiolite are very different in style from those documented in the southern Neotethyan, Troodos, Hatay and Baer-Bassit ophiolites (Morris et al., 1998, 2002; Inwood, 2005; Inwood et al., 2008). In these ophiolites, net rotations occurred around steeply plunging axes. These may be associated with regional microplate rotation within the southern Neotethys (driven by convergence of the Arabian promontory with a subduction zone to the south of the supra-subduction zone crust now represented by these ophiolites), and also

(on a more local scale) to shear associated with earlier phases of intraoceanic transform fault tectonism. In contrast, the Mersin net tectonic rotations are dominated by a major component of rotation (tilt) around sub-horizontal axes (Figure 5.48), with a residual moderate clockwise rotation required once tilting is accounted for. Hence there is no need to infer major regional scale intraoceanic microplate rotation within the northern Neotethys in order to account for the large net rotations documented in this thesis. At present no palaeomagnetic data exist for other northern Neotethyan ophiolites in Turkey (e.g. the Pozantı–Karsantı units) that would potentially allow testing of whether large-scale intraoceanic microplate rotation had occurred in this ocean.

The preferred interpretation of the palaeomagnetic data and net tectonic rotation analyses is therefore as follows (as illustrated in Figure 5.49):

1. Convergence between the Afro-Arabian and Eurasia plates in the Late Cretaceous led to the development of a northward-dipping subduction zone in the northern branch of the Neotethyan ocean (Intra-Tauride ocean). This in turn led to supra-subduction zone spreading and formation of the oceanic lithosphere of the future Mersin ophiolite (Figure 5.49a).
2. Seafloor spreading-related magmatism led to formation of ultramafic and gabbroic cumulates in the lower oceanic crust (Figure 5.49a), which crystallized and acquired a normal polarity thermoremanence as they cooled through the blocking temperatures of magnetite grains. Cumulate layering in the lower crust may have been tilted by up to 20-30° prior to blocking in of remanences as the net tectonic rotation analysis cannot restore the layering to a palaeohorizontal while simultaneously restoring remanences to the expected reference direction.

3. Effectively coeval with acquisition of thermoremanence by the cumulate section, basaltic dykes were emplaced into the lithospheric mantle (Figure 5.49a), which also acquired normal polarity thermoremanent magnetizations.
4. As a result of continued regional contraction, shortly after the development of the oceanic lithosphere, initial intra-oceanic detachment by thrusting occurred (Parlak and Delaloye, 1999), due to the weakness of the spreading axis (e.g. Hacker, 1991).
5. Initial intra-oceanic detachment led to rotation of the over-riding plate (Figure 5.49b) and formation of the Mersin metamorphic sole (Parlak and Delaloye, 1999) from an ocean island or seamount-type protolith.
6. Further magmatism above the subduction zone led to emplacement of dykes that cross-cut the metamorphic sole and acquired normal polarity remanences (Figure 5.49c). According to Parlak et al. (1995), Parlak (1996), Parlak et al. (1996a), Dilek *et al.* (1999), Çelilk and Delaloye (2003) and Çelik (2008), the intrusion of these dykes occurred in an oceanic environment after ductile deformation of the metamorphic sole, but before the final obduction of the ophiolite onto the Tauride carbonate platform.
7. Continued intra-oceanic thrusting of the detached oceanic lithospheric sheet and the under-plated metamorphic sole led to further clockwise rotation (Figure 5.49d), affecting the lower crust, mantle sequence and metamorphic sole. Note, however, that there is also the potential for final emplacement of the ophiolite onto the continental margin to contribute to the phase of net rotation that post-dates intrusion of dykes into the metamorphic sole.

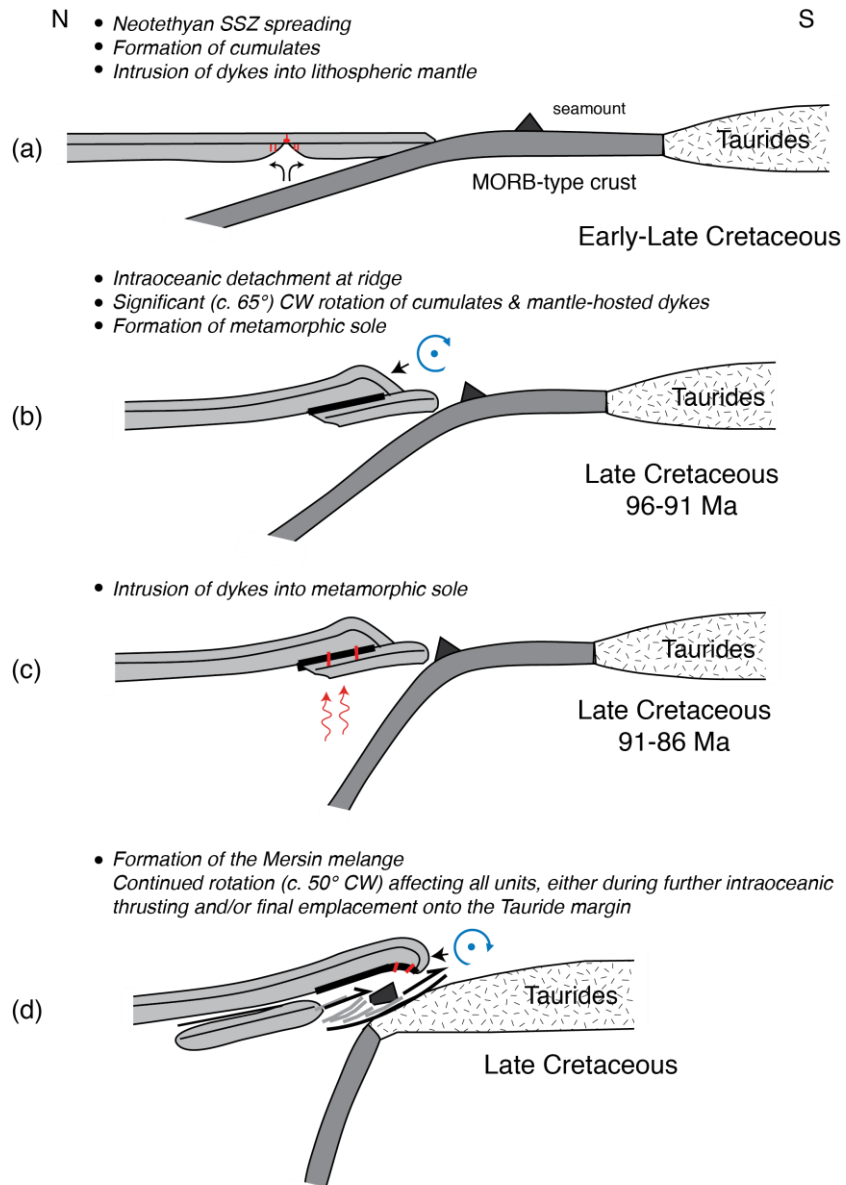


**Figure 5.49.** Schematic tectonic model illustrating the net tectonic rotation of the Mersin ophiolite. (a) Formation of the crust and intrusion of dykes into the lithospheric mantle during supra-subduction zone seafloor spreading. (b) Initial detachment led to intra-oceanic rotation of the first group of dykes (hosted by mantle) and the lower crustal cumulates, and triggered formation of the metamorphic sole by under-thrusting. (c) Further magmatism led to emplacement of dykes into the metamorphic sole, which (d) then experienced intra-oceanic rotation along with the overlying mantle and crustal sequences.

In terms of the key geological events inferred from the data presented in this study, this rotational history is also consistent with alternative plate tectonic models involving development of two subduction zones (e.g. Çelik, 2008).

# Chapter 6

## Conclusions

### 6.1 Summary

The Mersin ophiolite of Turkey represents one of the best examples of Tethyan-type ophiolites formed by supra-subduction zone spreading within the northern Neotethyan Ocean basin during the Late Cretaceous (e.g. Parlak and Delaloye, 1996), but has not been analysed palaeomagnetically prior to this study. Such analyses in other ophiolites of the region (e.g. Allerton and Vine, 1987; Morris et al., 1998, 2002, 2006; Inwood et al., 2009) have shown that tectonic rotations of a variety of styles have occurred during their evolution, but it was unknown whether the Mersin ophiolite has been rotated or, indeed, shared a common rotation history with ophiolites to the south, as predicted by some regional scale models (e.g. Ricou et al., 1984).

In this study 663 samples were collected from lower crustal ultramafic and gabbroic cumulates in the ophiolite, from dykes intruded into the underlying mantle sequence and metamorphic sole, and from overlying Miocene sedimentary rocks. These samples allow the amount and style of tectonic rotation during the evolution of the Mersin ophiolite to be quantified for the first time, and facilitate comparison with rotations previously documented in ophiolites which formed in the southern Neotethyan ocean basin (Troodos and Hatay/Baër-Bassit).

Anisotropy of low field magnetic susceptibility was measured on all samples. Data from the single site in the sedimentary cover have a standard depositional magnetic fabric, but more complex fabrics are seen in the igneous units.

Although fabrics in the cumulate section are variable at the site level, they show a reasonably consistent orientation of maximum susceptibility axes that is shown by thin section analysis to reflect a magmatic fabric arising from alignment of silicate and oxide grains. These fabric data can therefore provide useful information on magmatic accretion if corrected for the effects of later tectonic rotation using associated palaeomagnetic data. Magnetic fabrics in the sampled dykes are not as consistent, but in many cases principal susceptibility axes lie within the planes of the dykes, again suggesting a magmatic control.

Palaeomagnetic data from the single site in the Miocene sedimentary cover show a small anticlockwise rotation that is entirely consistent with the far more numerous data reported in the literature (e.g. Piper et al., 2010), that suggest minor anticlockwise neotectonic rotation of the Anatolian block. Data from the underlying igneous rocks of the ophiolite, in contrast, have NE-directed declinations, suggesting major clockwise rotation of these units occurred prior to the neotectonic period. Within the cumulates, applying a standard palaeomagnetic tilt correction about the present day line of strike of the cumulate layering produces a slight increase in dispersion after tilt correction. This is not considered significant, as variations in the primary orientation of cumulate layering might be present on a local scale. Rock magnetic and remanence characteristics, especially very discrete unblocking of remanence during thermal demagnetization just below the magnetite Curie temperature, and a lack of alteration in the gabbros support the assumption that the magnetization of these rocks represent thermoremanences acquired during crustal accretion. The directions of magnetization may therefore be used as markers to determine the rotation history, or at least the amount of rotation since the crust cooled through the Curie temperature.

Since there is potential for significant declination errors to be introduced by using a standard tilt correction (MacDonald, 1980; Tarling, 1983), especially when palaeohorizontal surfaces have steep present day dips, a more sophisticated net tectonic rotation approach (Allerton and Vine, 1987; Morris et al., 1998) has been applied to the ophiolite palaeomagnetic data. This approach has the advantage of being able to cope with analysis of dykes, whereas standard tilt corrections cannot resolve components of rotation around dyke-normal axes (Morris and Anderson, 2002). In the case of inferred palaeohorizontal markers like cumulate layering, this technique also does not force the observed layering to horizontal like standard structural corrections but restores layering to as close to horizontal as geometry of the rotation allows. This avoids over-correcting the data and can give an indication of the dip of the layering at the time that magnetization was locked in.

The net tectonic analyses show that all lithologies of the Mersin ophiolite (i.e. cumulates, dykes in the mantle sequence and the dykes in the metamorphic sole) underwent large clockwise rotations about NE-trending, moderately plunging to sub-horizontal axes. Dykes hosted by the metamorphic sole have experienced c. 45° clockwise rotation, whereas a consistent larger clockwise rotation of c. 115° is documented for dykes cutting the overlying mantle sequence and for the cumulate section. This difference, and the similarity of rotation parameters between the mantle and lower crust, suggests that rotation of the ophiolitic thrust sheets occurred in at least two phases. The first stage (c. 70°) occurred after initial detachment of the ophiolite at the Mersin spreading axis but prior to intrusion of dykes into the metamorphic sole. The second stage of rotation (affecting all units) occurred as a result of further intra-oceanic rotation (preferred interpretation) or potentially during final emplacement of the

ophiolite onto the Tauride carbonate platform. Note that these are not vertical axis rotations, but rather reflect the net rotation of the sampled units around inclined axes that also describe the significant tilting that these rocks have experienced. Applying these net tectonic rotation parameters to the anisotropy of magnetic susceptibility data provides a first-order estimate of the orientation of magmatic flow/deformation during accretion of the cumulate sequence. This restores maximum principal susceptibility axes to a NNE azimuth. If magmatic flow is assumed to result from simple spreading, then this suggests that the Mersin spreading axis had an original WNW-ESE orientation. Although this can only be considered as a tentative reconstruction, this would be consistent with the orientation of the spreading axis inferred from regional geological considerations. However, a caveat to this interpretation is that magmatic flow inferred using similar magnetic fabric data in the Troodos ophiolite (in both sheeted dykes and gabbros; Staudigel et al., 1992; Granot et al., 2011) has been shown to be directed along the spreading axis.

Finally, this study highlights that the Mersin ophiolite experienced a completely different rotation history to the ophiolites that formed in the southern Neotethys ocean. The clockwise intraoceanic rotations quantified here contrast completely with the dominant anticlockwise rotations previously documented in Troodos, Hatay and Baër-Bassit. This should be considered as definitive proof that these ophiolites did not originate as part of a single emplaced thrust sheet, as envisaged in early models (e.g. Ricou *et al.*, 1984).

## 6.2 Recommendations for further work

There is very limited scope for any further palaeomagnetic analysis in the Mersin ophiolite, beyond possible additional sampling of the sedimentary cover sequences, as all ophiolitic units suitable for such analyses have been sampled for this study. However, a number of additional investigations could be undertaken to add value to the data and analyses presented here, to allow additional or tighter constraints on the tectonic evolution of the ophiolite to be obtained.

Only limited structural data have been collected from the metamorphic sole of the ophiolite and reported in the literature (Parlak et al., 1995; Parlak and Robertson, 2004). As a result, the kinematics of structures in the sole rocks remain unclear. Further detailed structural analyses, both in the field and using thin sections, would allow a more robust interpretation of the emplacement direction of the ophiolite. Since high quality palaeomagnetic data have been acquired in this study from dykes that cut the metamorphic sole, these data could be used to restore such kinematic constraints into their origin palaeotectonic reference frame, as noted by Parlak and Robertson (2004). In addition, precise age constraints on the mafic dykes in both mantle sequence and in the metamorphic sole of Mersin ophiolite would clarify the timing of the stages of rotation documented in this study.

Only a provisional structural analysis of the “dyke-like veins” (site MC10) that cut the cumulate sequence (at site MC09) has been possible here, as the main focus of the project was the palaeomagnetic analyses. However, the tentative results of combining microstructural, magnetic fabric and palaeomagnetic data from these rocks suggests that a better understanding of these enigmatic

features might be possible to achieve by a more detailed study of this road section. This could also include electron back-scatter diffraction analysis to more fully understand the deformation mechanism in these sheared rocks.

Finally, there is now clear scope for extending integrated palaeomagnetic studies into other well-exposed ophiolites of the eastern Mediterranean area. For example, the Alihoca ophiolite located about 35 km NE of Mersin ophiolite, on the eastern side of Ecemis fault, provides good exposures of sheeted dykes. Palaeomagnetic data from these units would provide additional evidence about the geometry of Neotethyan spreading systems.

## **Appendix A**

### **A pilot palaeomagnetic study of the Lizard ophiolite**

#### **A1. Introduction**

This appendix presents results of a preliminary palaeomagnetic investigation of dykes and gabbros within the Lizard ophiolite of Cornwall. It reviews the geological history of the Lizard ophiolite and its relation with the tectonic evolution of the Rheic Ocean, and provides a general overview of geology of the ophiolite. The aim of the palaeomagnetic study was to evaluate the original orientation of various dykes within the gabbro sequence, and to compare the new palaeomagnetic results with previous studies. To achieve this aim, sampling was conducted along the east-coast section of the Lizard Complex (Coverack village - Godrevy cove), where the dykes and gabbroic rocks are well exposed.

#### **A2. Overview of the tectonic evolution of the Rheic Ocean**

The Rheic ocean, which developed between the major continents of Gondwana and Laurasia (Laurentia, Baltica, Avalonia) following closure of Iapetus ocean, was one of the main oceans of the Palaeozoic Era. The Rheic Ocean expanded at the expense of Iapetus making both Avalonia and Carolina move northward toward Baltica and Laurentia (Figure A1). Subsequent closure of the Rheic Ocean resulted in a 10,000 km long suture and formation of the major section of Pangea (Nance and Linnemann, 2008; Nance et al., 2012).

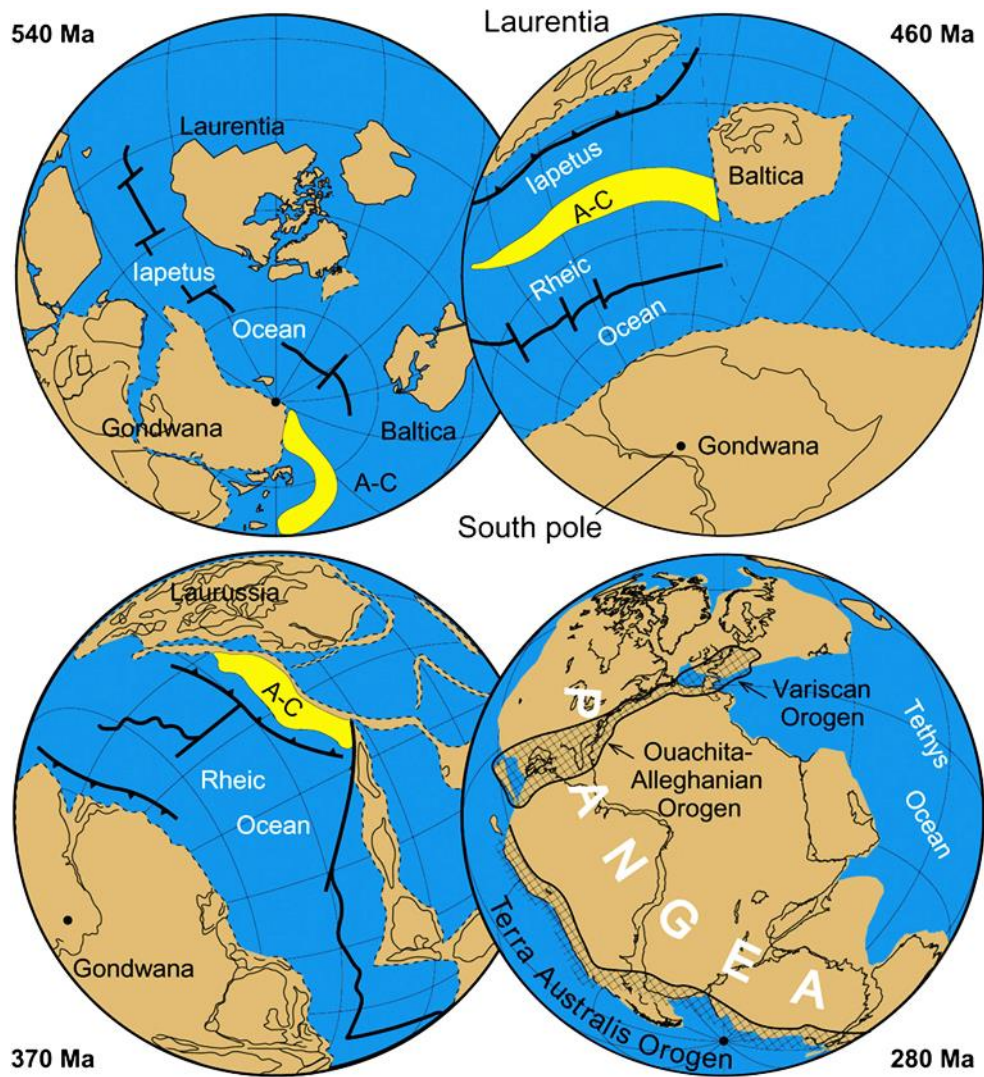


**Figure A1.** Palaeozoic reconstruction showing the evolution of the Iapetus and Rheic Oceans and location of Laurentia - Baltica - Avalonia–Carolinia, and their detachment from Gondwana with the development of the Rheic Ocean at the ages 540 Ma, 460 Ma, 370 Ma and 280 Ma (from Nance *et al.*, 2012).

### A2.1 Initial Rifting and Ocean Opening

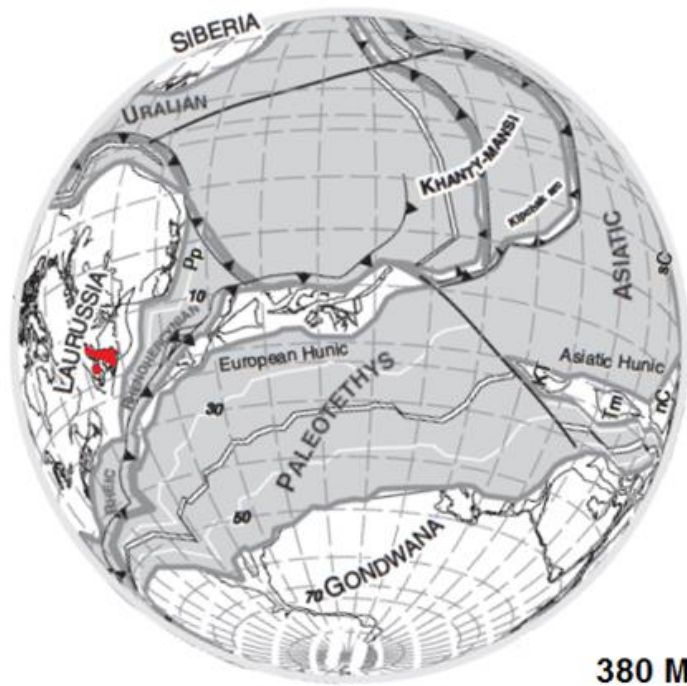
The primary opening of the Rheic Ocean began in the mid to Late Cambrian by rifting along the northern (African - South American) margin of Gondwana (Nance and Linnemann, 2008; Nance *et al.*, 2012) (Figure A1). In Late Cambrian - Early Ordovician times, after a long period of rifting, the Rheic Ocean began to open along the southern flank of Iapetus causing drift of

several peri-Gondwanan micro-continental terranes (e.g., Avalonia and Carolina) away from the northern margin of Gondwana (Nance *et al.*, 2012). Thus, the Rheic Ocean originated along the northern edge of Gondwana (mainly Amazonia and West Africa) (Cocks and Torsvik, 2002; Stampfi and Borel, 2002). During closure of the Iapetus Ocean, the micro-continent of Avalonia including the southern part of British Isles progressively moved northwards and approached Laurentia (Hunter and Easterbrook, 2004).

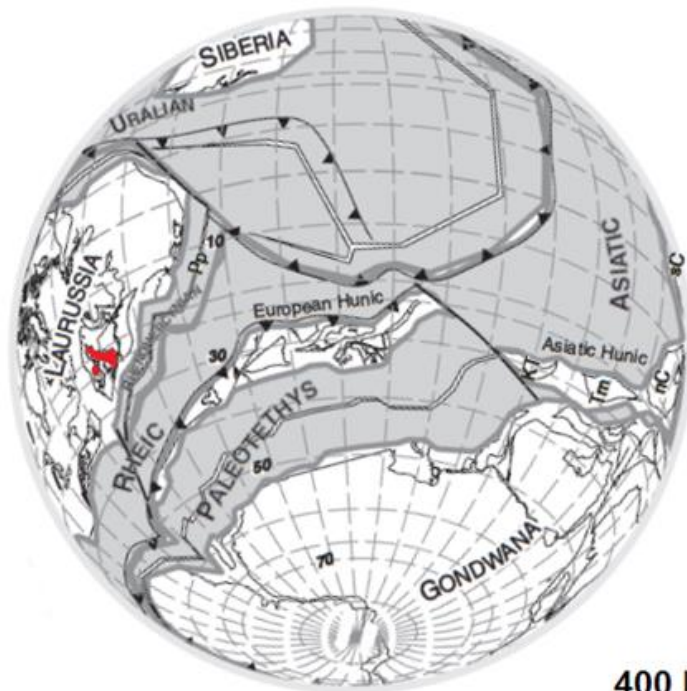
The Rheic Ocean reached its maximum width (ca. 4000 km) after the demise of the sea that existed between Avalonia and Baltica in the Late Ordovician and after closure of Iapetus Ocean in the Silurian (Figure A1) (Nance *et al.*, 2012).

## **A2.2 Collision and Ocean Closure**

Closure of the Rheic Ocean started in the Devonian and was mostly complete by the Early Carboniferous (Mississippian) as Pangea formed by suturing of Gondwana and Laurussia. During this process in the Devonian-Carboniferous (ca. 370 – 330 Ma), collision occurred between North Africa and southern Europe, leading to the Variscan orogeny (Figure A1 and Figure A2). The suture that formed by this closure runs westward from the Mid - German Crystalline zone and the Lizard ophiolite in southern Britain to the Pulo do Lobo unit of southern Iberia (Figure A.3). During the Carboniferous, Britain drifted northwards across the equator, into a location within subtropical latitudes (Hunter and Easterbrook, 2004). Suturing of West Africa and South America with North America in the Permo-Carboniferous formed the Alleghanian and Ouachita Orogens, respectively (Nance and Linnemann, 2008).



380 Ma



400 Ma

**Figure A2.** Palaeogeographic maps showing the position of the UK in the southern hemisphere during the Devonian (380 Ma – 400 Ma) (from Stampfli *et al.*, 2002).

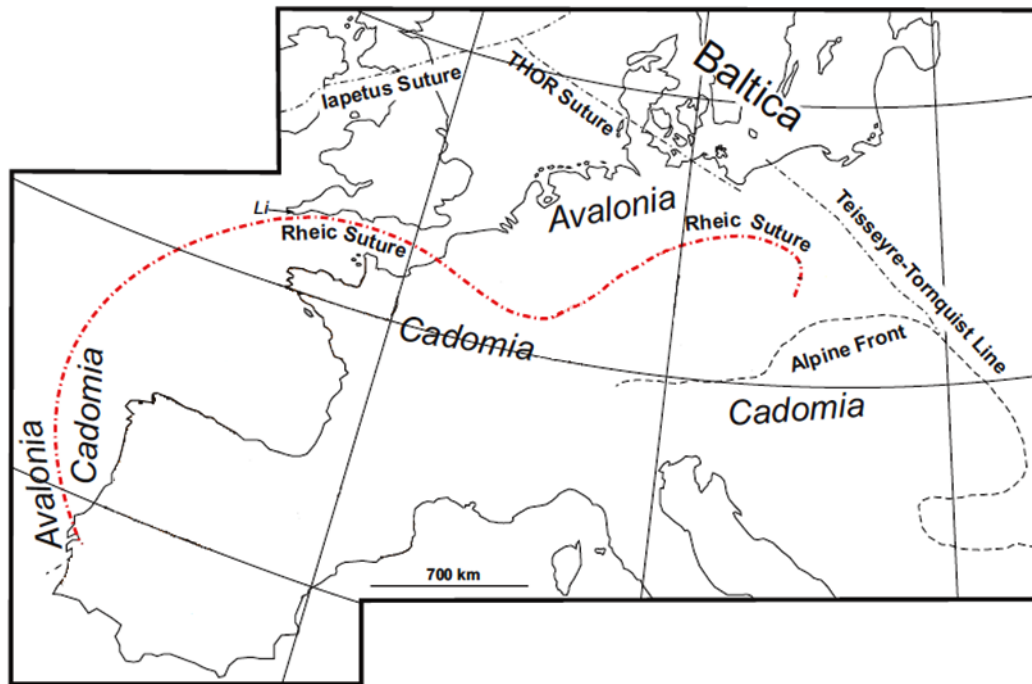


**Figure A3.** Simplified map showing the location of Rheic suture (dashed red line) in western and central Europe, and Lizard ophiolite in the south west of Britain (modified from Nance and Linnemann, 2008).

Closure of the Rheic Ocean was facilitated by two intra-oceanic subduction zones: (1) In the Variscan belt, where subduction happened northward beneath the southern margin of Baltica and was accompanied by occurrence of magmatism on the Avalonian terranes that formed previously by accretion (Kroner *et al.*, 2007); (2) In the Appalachian-Ouachita belt, where subduction happened southward beneath the northwestern margin of Gondwana.

In the final stage of the Rheic lifetime, the Rheic basin was trapped and compressed between two continents, leading to development of fold structures of the Variscan Orogen. This belt comprises a number of structural zones separated by main thrusts. These zones, starting from the northern margin, are: Rhenohercynian Zone, Saxothuringian Zone, Moldanubian Zone, Central Iberian Zone, Ossa-Morena Zone and South Portuguese South Europe Zone.

SW England represents part of the Rhenohercynian Zone (Leveridge and Hartley, 2006; Floyd *et al.*, 1993) (Figure A4).

### A2.3 Models for initial rifting

According to Floyd *et al.*, (1993), four different models have been proposed for the plate tectonic setting of initial rifting in the Rhenohercynian zone (including South Cornwall in England). These models are:

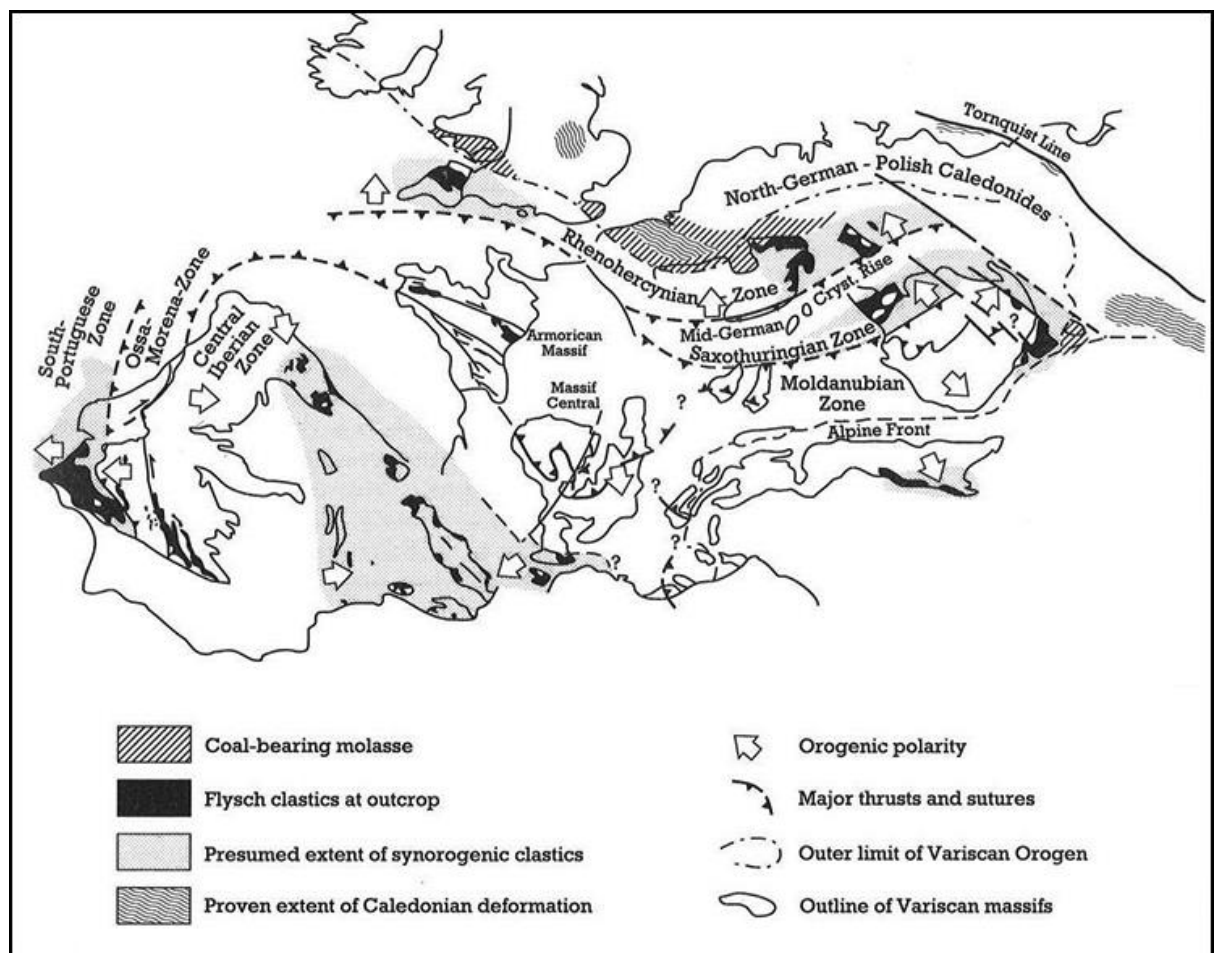


**Figure A4.** A map of the major tectonic zones of the Variscan Orogen in Europe (after Floyd *et al.*, 1993).

(1) Back arc basin: This model proposes that the oceanic basin formed in a back-arc setting associated with northerly directed subduction of oceanic crust to the south of Armorica.

(2) Intracontinental dextral transform system (Barnes and Andrews, 1986): This model suggests that the oceanic crust of the Lizard ophiolite formed within a pull-apart basin caused by lithospheric extension.

(3) A small ocean basin generated as a result of southerly directed subduction under an active arc located at the north of Armorica.

(4) A small ocean basin developed as continental crust was forced to override an initial Caledonian spreading centre.

In any case, the closure of the Rheic Ocean was recorded at ca. 395 - 370 Ma by the emplacement of ophiolites in southern Britain (i.e. Lizard ophiolite, Figure A5) and in the northwestern and southern Iberia (Murphy *et al.*, 2010; Nance *et al.*, 2010).

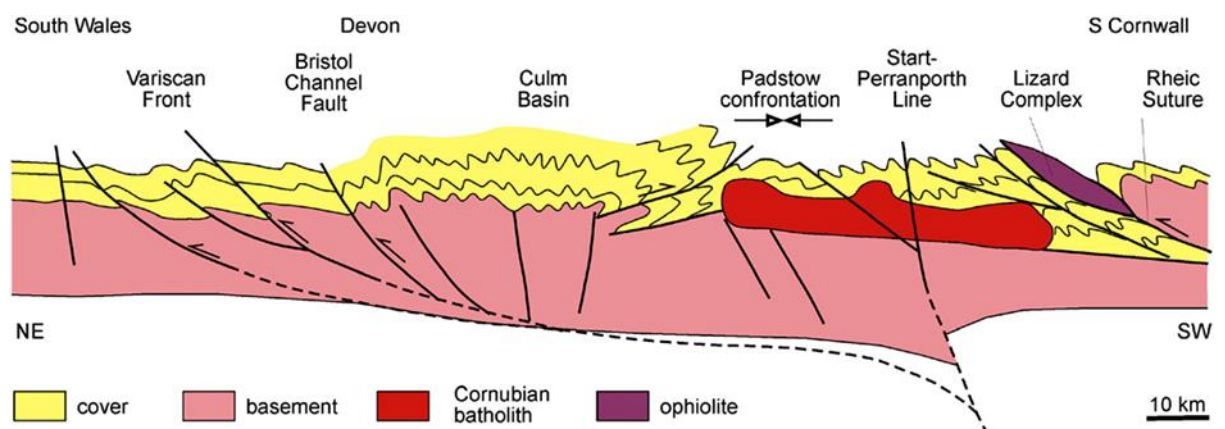


**Figure A5.** Cross section illustrating the main structures from South Wales to South Cornwall, and the locations of the Lizard ophiolite and Rheic Suture (after Nance *et al.*, 2010).

## A3. Geology of the Lizard Ophiolite

### A3.1 General Overview

The Lizard ophiolite complex at the present day occupies a peninsula about 15 km wide and 10 km deep that is bounded to the west, south and east by the sea, and is almost separated from the rest of Cornwall by the Helford River (Figure A6).

The Lizard Complex is of Palaeozoic (Late Devonian) age and represents a sliver of oceanic lithosphere that was overthrust (obducted) northwards onto continental crust during the Variscan orogeny and during closure of the Gramscatho Basin (Barnes and Andrews, 1986; Holder and Leveridge, 1986; Alexander and Shail, 1995; Brenchley and Rawson, 2006; Leveridge and Shail, 2011).

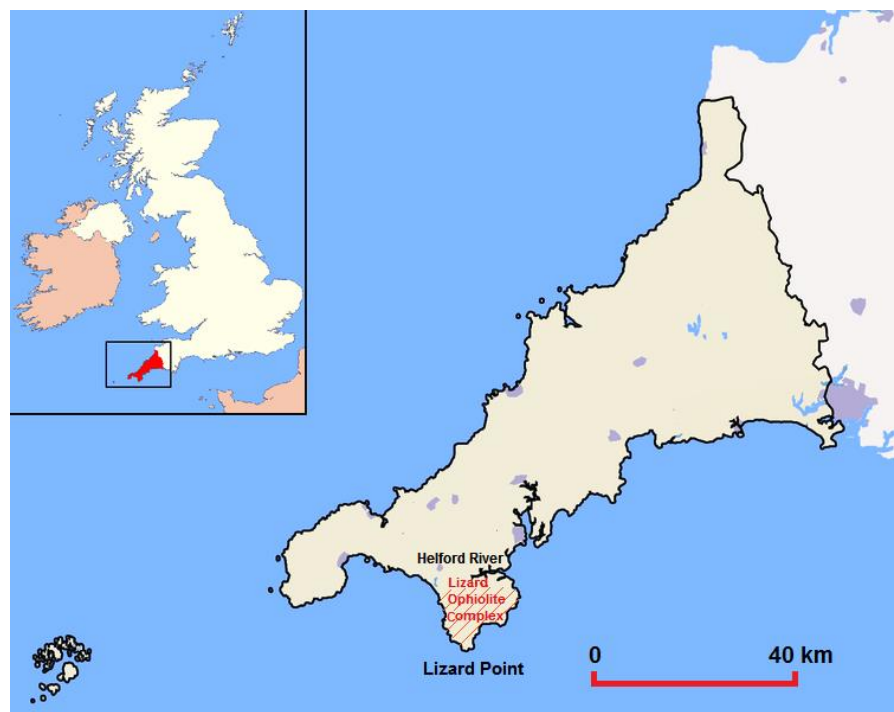


**Figure A6.** Simplified map showing the location of the Lizard ophiolite complex, Cornwall.

### **A3.2 Age and formation of the Lizard ophiolite**

Davies (1984) provided a Sm-Nd mineral isochron age for olivine gabbro with the Lizard Complex of  $375 \pm 34$  Ma, which they inferred to represent the formation age of the crust by seafloor spreading. In contrast, Cook *et al.* (2002) suggested that the ophiolite formed at c. 400-390 Ma within the Gramscatho pull-apart basin (Figure A7). This interpretation was based on the presence of pre-emplacment structural features such as foliations with NNW-SSE strikes and down-dip stretching lineations in mylonitic peridotites, Landewednack amphibolites and deformed Trabone cumulates. Furthermore, Barnes and Andrews (1986) have described the Lizard ophiolite as oceanic crust that formed by extensional processes in the Gramscatho basin that started in the upper part of the lower Devonian, at a point when crustal thinning was enough to allow dyke intrusion and the generation of new oceanic crust. In this model, the orientation of basaltic dykes exposed at, for example, Coverack, could indicate a ENE-WSW extension direction within the Gramscatho basin (Barnes and Andrews, 1986; Roberts *et al.*, 1993). This implies that the original spreading axis had a NNW-SSE trend (Cook *et al.*, 2002).

### **A3.3 Obduction of the ophiolite**

In general, the generation and emplacement of ophiolites includes two stages. The first stage involves pre-obduction processes within an intra-oceanic environment, such as generation of the ophiolite by seafloor-spreading and its initial detachment, whereas the second stage involves emplacement of oceanic lithosphere onto the continental crust (Jones, 1997). In this context, Cook *et al.* (2002) suggested that the Lizard Complex experienced a two stage emplacement (Figure A8): (a) Hot emplacement, which occurred at c. 390-375

Ma through stacking of mantle segments, oceanic crust and highly dismembered continental crust which represent the floor of the Gramscatho basin; (b) Cold emplacement, which occurred during the earliest Carboniferous c. 365 Ma, and represents the obduction of Lizard Complex onto Gramscatho sedimentary basin.

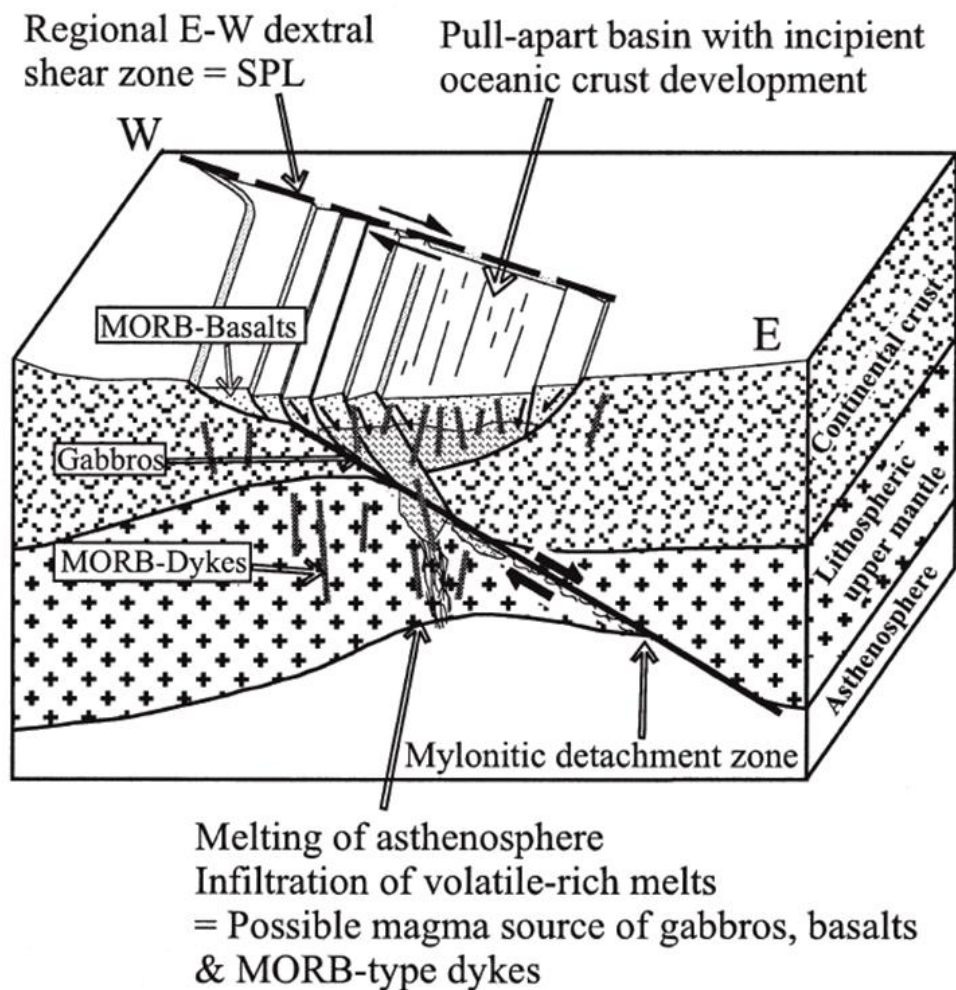


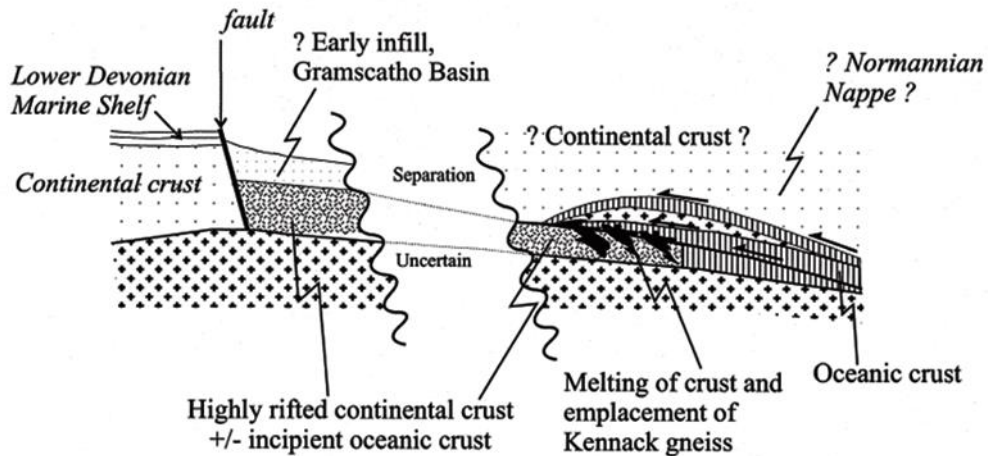
**Figure A7.** Schematic block diagram illustrating formation of the Lizard Complex-Gramscatho pull-part basin during the Emisian-Eifelian period (from Cook, *et al.*, 2002).

a) **“HOT” EMPLACEMENT (c. 390-375 Ma)**

NNW

[NOT TO SCALE]

SSE



b) **“COLD” EMPLACEMENT (c. 365 Ma)**

NNW

[NOT TO SCALE]

SSE

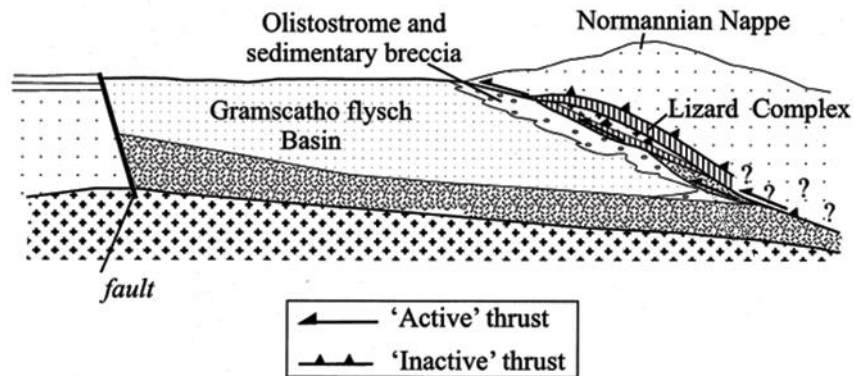


**Figure A8.** Schematic cross-sections illustrating emplacement steps of the Lizard complex. (a) Hot emplacement: occurred during the Eifeian-Famennian. (b) Cold emplacement: occurred during the early Carboniferous (Cook *et al.*, 2002).

Overall, the main tectonic events can be summarized as follows (Edmonds *et al.*, 1975; Jones, 1997; Hunter and Easterbrook, 2004) (Figure A9): (1) Thrusting started at ~ 375 Ma, after a primary stage of folding and shearing, with northerly thrusting of slivers of oceanic crust during oceanic basin closure; (2) continued closing of the ocean basin led to the formation of new thrusts at the back of the primary thrust, which also experienced inversion in same direction; (3) deformation and closure of the ocean basin occurred by ~ 370 Ma, refolding the primary thrust and piling up subsequent thrusts upon the

continental margin; (4) Initiation of small-scale partial melting due to progressive overthrusting with late stage failure of the thrust stack, and finally emplacement onto the continental margin. According to Barnes and Andrews (1984), the emplacement of the Lizard ophiolite complex occurred via cool thrusting at a regional temperature of 250-350 °C and at pressures of a few kilobars, which yielded very low grade metamorphism.

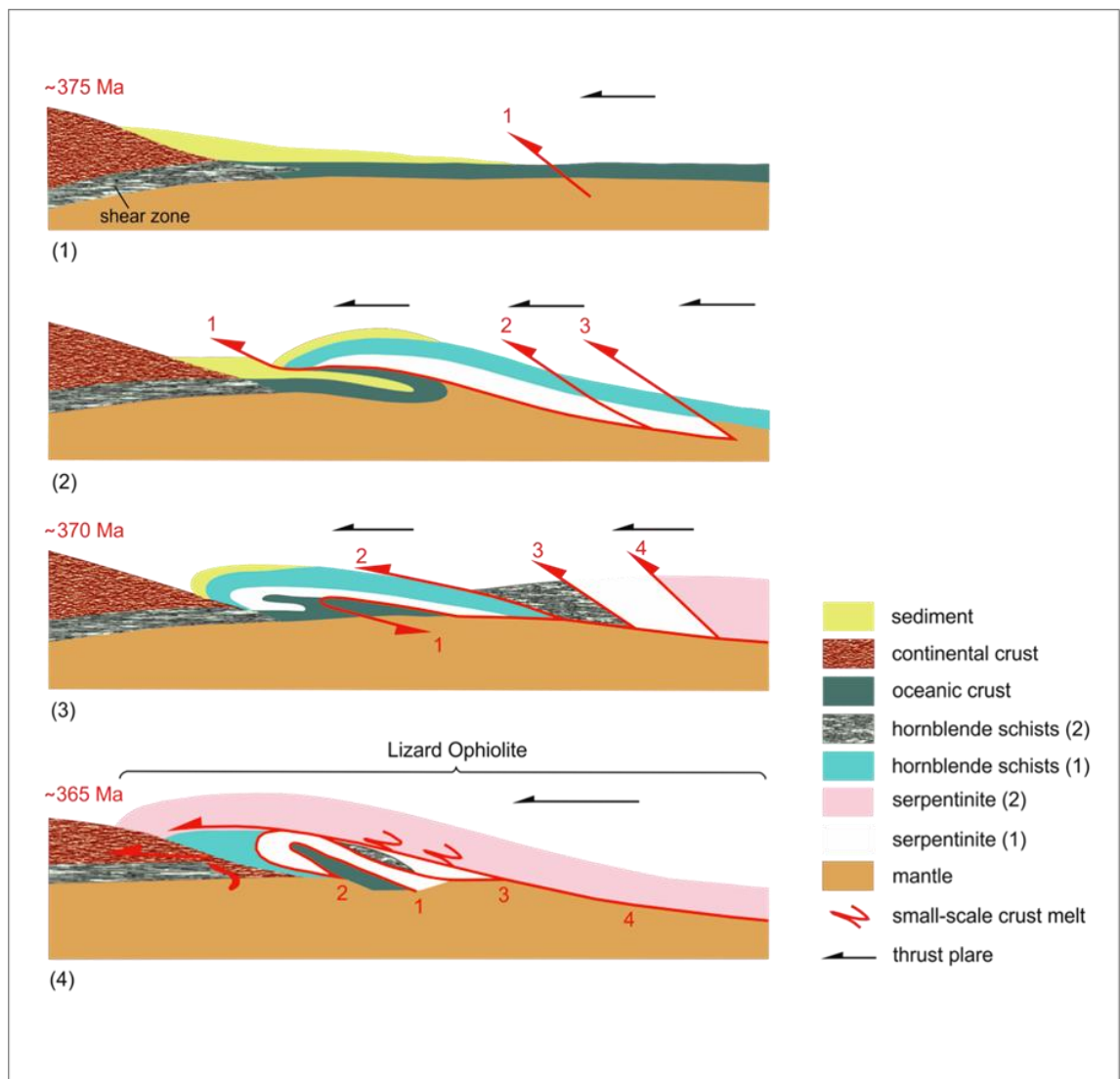


**Figure A9.** Deformation and emplacement history of the Lizard ophiolite (modified from Hunter and Easterbrook, 2004).

### A3.4 Description of lithologies

The Lizard ophiolite consists of three groups of igneous rocks (Flett and Hill, 1946; Floyd *et al.*, 1993; Selwood *et al.*, 1998) (Figure A10): mantle units (i.e. serpentinized peridotites), which comprises more than half (78 km<sup>2</sup>) of the complex (Edmonds *et al.*, 1975; Ealey and James, 2011); crustal units (i.e. cumulate complex, gabbros, MORB-type dykes and amphibolites); and later, thrust emplacement-related intrusions concentrated along the tectonic contact between the metamorphic basement (i.e. gneisses) and overlying Lizard peridotites.

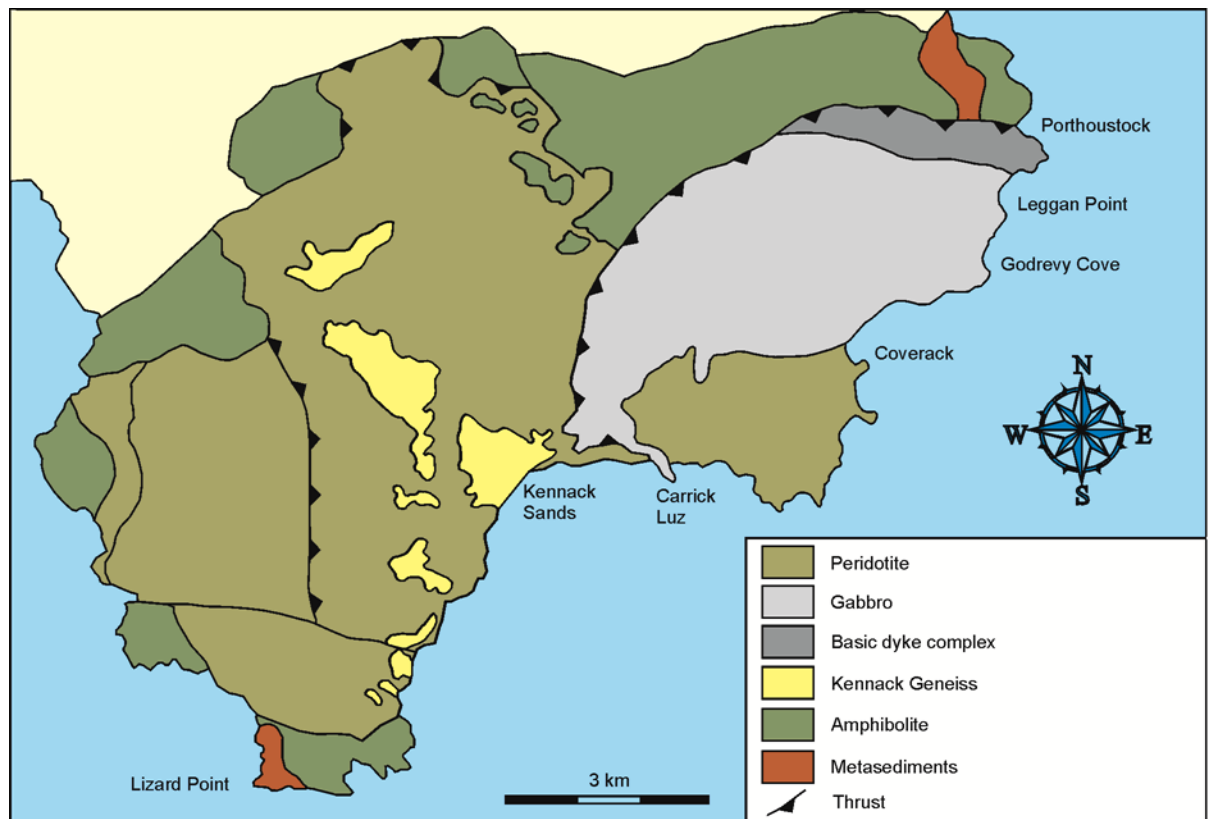


**Figure A10.** Simplified geological map of the Lizard complex, Cornwall (modified from Roberts *et al.*, 1993).

### A3.4.1 Peridotite

The dominant type of serpentinized peridotite, interpreted as upper mantle rocks (Cook *et al.*, 1998), is a coarse-grained, porphyroclastic spinel-lherzolite (Cook *et al.*, 2002; Ealey and James, 2011). These pass into regions of mylonitic plagioclase and amphibole-bearing peridotites through increasing recrystallization and grain-size reduction (Cook *et al.*, 2002). Alteration to serpentine and talc is common and is caused by low-temperature hydration which probably happened by seawater percolation along fractures within the rocks during cooling. The boundary between the peridotite unit and overlying gabbroic rock is exposed at Coverack (Figure A10 and A11), and is characterized by an interdigitating zone boundary (Flett and Hill, 1946) which represents the petrological Moho (Roberts *et al.*, 1993). Therefore, the Coverack area provides a transition section from the upper mantle to lower oceanic crust.

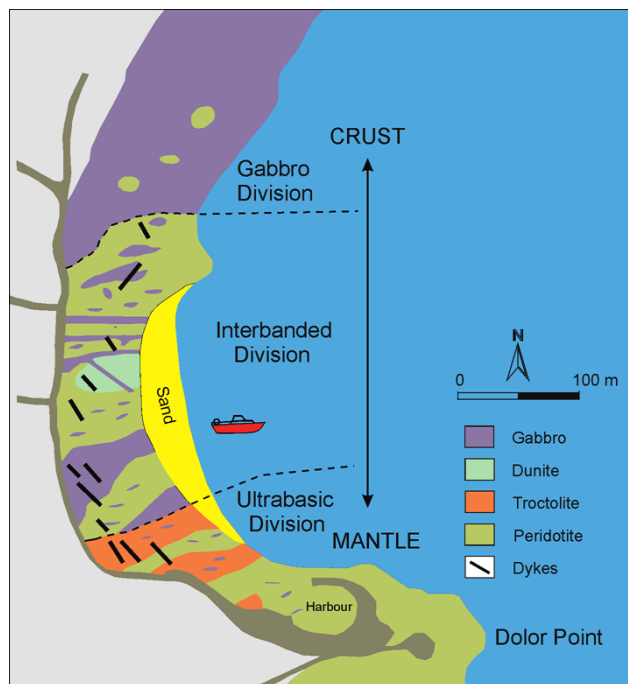


**Figure A11.** Geological map of the Coverack area, showing the interdigitation of gabbro and peridotite, and NW-SE trending dykes (modified from Floyd *et al.*, 1993).

There are also some distinctive rocks exposed at the north section of the peridotite, about 50 m north of the harbour (Figure A11); these are troctolites, which can be distinguished in the field through the mineral content (white plagioclase and red serpentinized olivine; Floyd *et al.*, 1993).

#### **A3.4.2 Gabbros**

The gabbros represent the lower oceanic crust overlying the mantle peridotites, and make up an important portion (18 km<sup>2</sup>) of the eastern complex with coastal exposure extending from Porthoustock 6 km southwards to Coverack (Ealey and James, 2011; Figure A10).

The gabbroic section at Coverack, especially in the lower part, is characterized by intrusion of a series of randomly oriented gabbro sheets into the peridotite over a wide range of scales. These gabbro sheets can be seen at Lankidden Cove and are characterized by coarse grains of chiefly plagioclase and augite with brown hornblende and a little ilmenite and magnetite. Olivine can be observed only in the southern part of this section (Floyd *et al.*, 1993). Generally the rocks of this section appear dark in colour especially when fresh, resulting in confusion between fresh gabbro and the ultrabasic rocks. In the numerous places, the gabbros have undergone different rates of hydrothermal alteration with replacement of clinopyroxene and plagioclase with amphibole and sericite (Floyd *et al.*, 1993; Selwood *et al.*, 1998).

#### **A3.4.3 Dykes**

The section between Dean Point and Porthoustock (i.e. around the Godrevy area) provides a rare opportunity to examine sheeted basic dykes, where the ratio of dyke to gabbro rises to a maximum of 50 - 70% along the coast, and swarms of sheeted dykes intrude into gabbro, sometimes showing chilled

margins (Roberts *et al.*, 1993; Selwood *et al.*, 1998). Therefore, this coastal location represents a remnant of the feeder dykes section of a spreading sea-floor centre and provides important geological evidence concerning the building of the Lizard ophiolite sequence. According to Roberts *et al.* (1993) there are three sets of dolerite dykes with distinctive orientations that cut the gabbros and they are geochemically well-defined with variable dip which increases with decreasing age. These three sets are:

Set 1: This represents the earliest set that cuts the gabbro, and consists of a small number of thin, metamorphosed, flat-lying dolerite bodies trending NE-SW, with gentle dips to the northwest. This set is exposed north of Coverack, and has an absence of chilled margins and are mostly comprised of plagioclase, amphibole and abundant opaque minerals (Roberts *et al.*, 1993). The lack of chilled margins, and complicated intrusive relationships with the gabbros, indicates that intrusion happened soon after the host gabbroic rocks had crystallized (Roberts *et al.*, 1993; Selwood *et al.*, 1998).

Set 2: The second set consists of plagioclase-phyric dolerite dykes, and are mostly observed in the direction of Porthoustock. These dykes trend NW-SE and dip moderately to steeply to the northeast, with thickness ranging from 0.1 - 2 m. Although the strikes of these dykes are parallel to shear zones, they dip more steeply and they are deformed within the shear zones. Geochemically the dykes are tholeiites with MORB properties (Roberts *et al.*, 1993; Selwood *et al.*, 1998).

Set 3: This set comprises a sequence of NW - SE trending, nearly-vertical, mostly aphyric dolerite dykes. These dykes are 0.1 - 1.5 m thick, variably altered, showing chilled margins and they cross-cut the peridotite, gabbros, flat-

lying dolerites (set 1) and the plagioclase-phyric dykes (set 2) (Figure A12). The dykes are also tholeiites, but geochemically they have more primitive MORB characteristics than the set 2 dykes (Kirby, 1984; Roberts *et al.*, 1993; Selwood *et al.*, 1998).

Kirby (1984) concludes that, all the dykes from Lizard complex have basaltic and tholeiitic characteristics, and have affinities with mid-oceanic ridge basalts (MORB).

The aim of this palaeomagnetic study was therefore to determine whether magnetic remanence data may be used to support the tectonomagmatic model of cross-cutting dykes intruded during extension, proposed by Roberts *et al.* (1993) (Figure A12). In practice, the majority of rocks are shown to be remagnetized, but results from one locality yield tentative constraints on the initial strike of dykes that may be of regional significance.

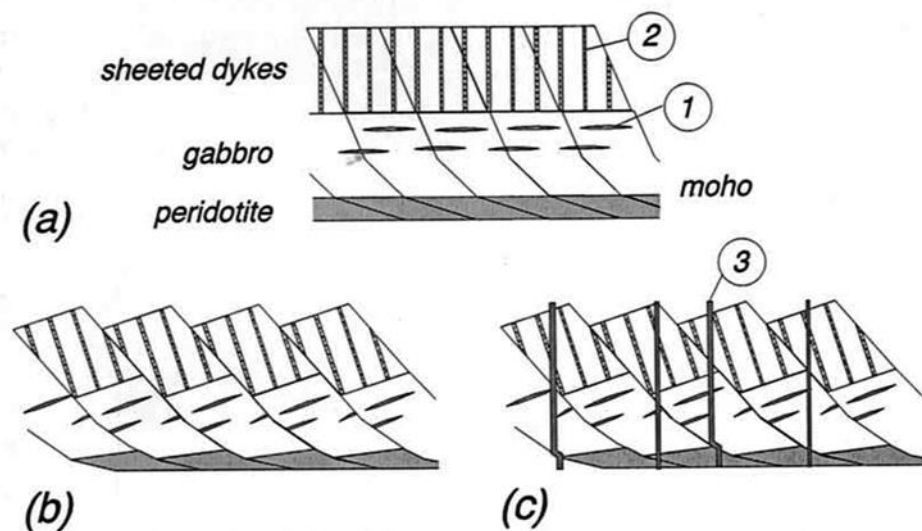


**Figure A12.** Schematic cross-section from Coverack to Porthoustock, showing the formation stages (a), (b) and (c) of the three sets of dolerite dykes (set 1, 2 and 3) during the tectonomagmatic evolution of the east-coast of the Lizard ophiolite (after Roberts *et al.*, 1993).

#### **A4. Previous Palaeomagnetic Studies**

The geology of the Lizard ophiolite has been widely studied for more than 100 years by many researchers, especially related to the petrology, structural geology, geochemistry, etc. However, there is only one palaeomagnetic study on the Lizard ophiolite. Hailwood *et al.* (1984) sampled rocks from the east coast section of the Lizard ophiolite complex, focusing on metadoleritic dykes, gabbros and peridotites. Laboratory demagnetization of these samples gave components with SSW declinations and shallow to intermediate negative inclinations. This direction of magnetization is similar to the Permian geomagnetic field for SW England, possibly suggesting remagnetization in the early Permian (Hailwood *et al.*, 1984). However, Hailwood *et al.* (1984) concluded that these SW-directed magnetizations are primary in origin and were acquired during formation of the ophiolite during seafloor spreading.

#### **A5. Fieldwork in the Lizard ophiolite**

In this study, sampling was restricted to the east-coast section of the Lizard complex (northern coast of Coverack village - Leggan cove), where dykes and gabbroic rocks are well-exposed (Figures A13 and A14).

Sampling of both dykes and gabbros was performed over four stages in different localities. At all localities, sampling was carried out using a gasoline-powered portable drill, with some extra oriented block samples collected and drilled in the laboratory.

The first stage of the fieldwork was conducted on 5<sup>th</sup> July 2010 for the south section of Godrevy Cove area. In this locality 23 core samples were collected from four sites, including dykes and gabbros. The second stage was on 14<sup>th</sup>

April 2011 for the Coverack coastal area. At this locality 23 core samples were collected from three sites, mostly from dykes with some samples from gabbros. The third stage of sampling was on 4<sup>th</sup> July 2011 for the north section of Godrevy Cove area. At this locality 19 core samples were collected from four sites, including dykes and gabbros. The fourth stage of sampling was on 23<sup>rd</sup> August 2012 in the Leggan Cove area (to the north of Godrevy Cove). At this locality 10 block samples were collected from five sites including dykes and gabbros (Figure A15).

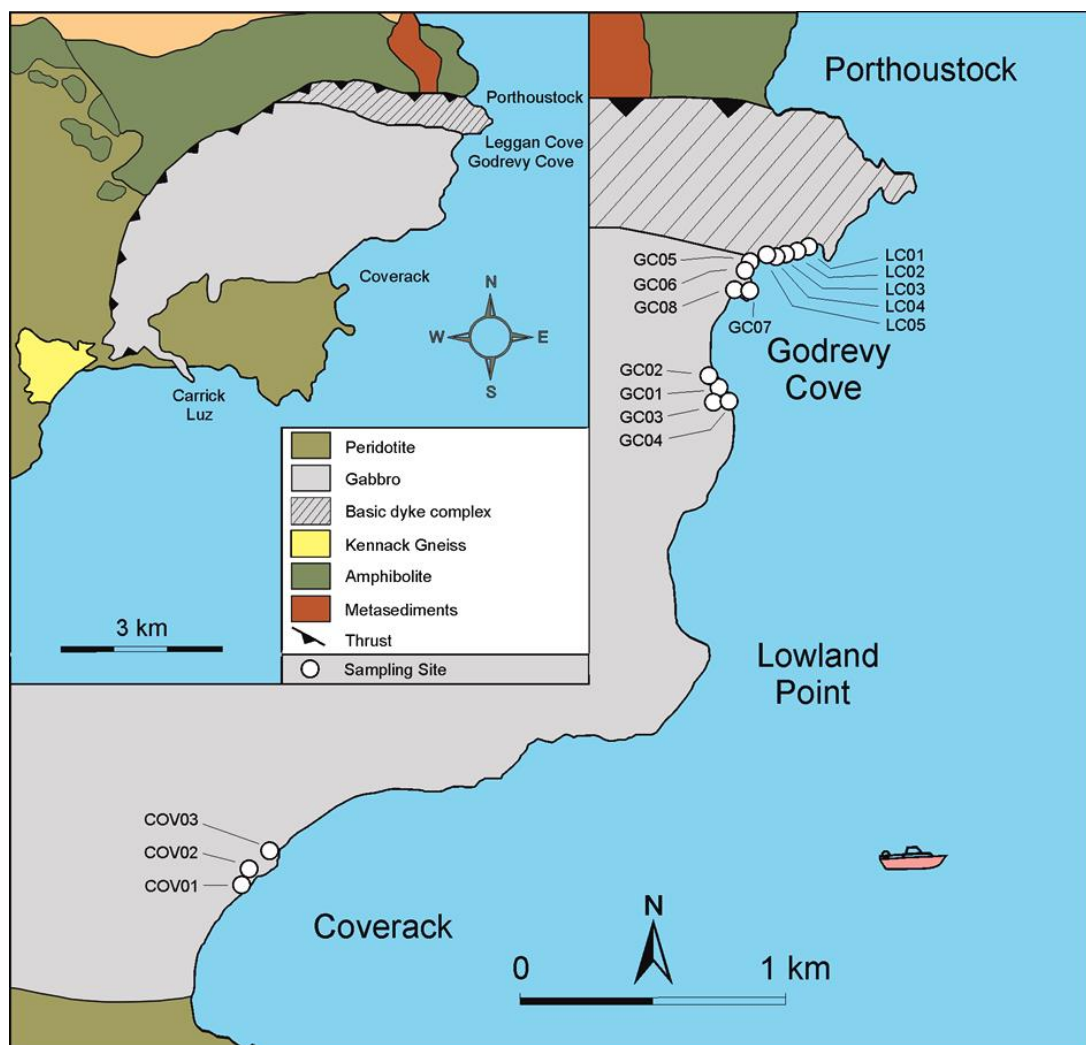


**Figure A13.** Geological map showing the studied area with indication of sampled dykes and gabbros localities. Inset is a simplified geological map of the Lizard peninsula (modified after Roberts *et al.*, 1993).

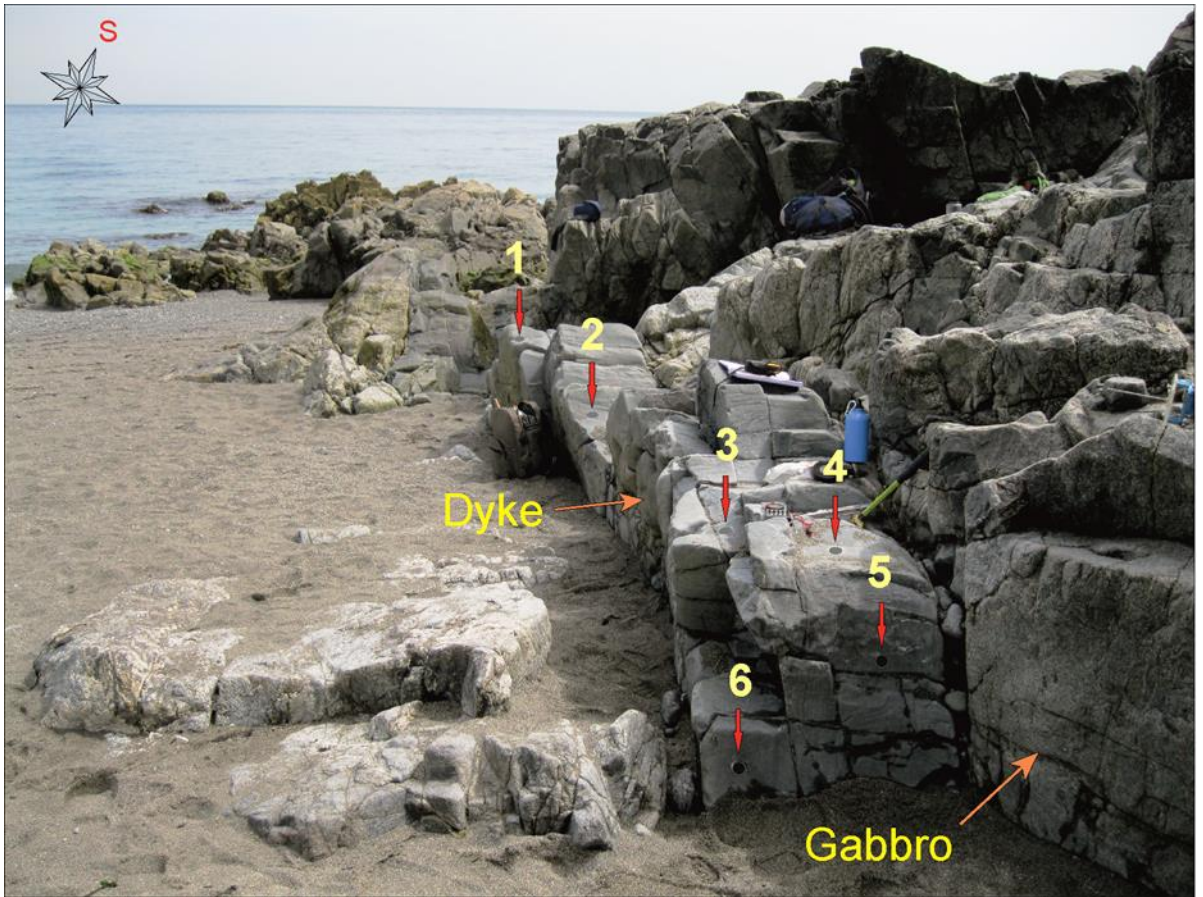


**Figure A14.** Outcrop photograph of site GC05 with location of drilled samples labelled.



**Figure A15.** Photographs of studied localities. (a) Leggan Cove. (b) Coverack Cove. (c) Godrevy–north section. (d) Godrevy-south section.

## A6. Results

### A6.1 Petrography

As described above, petrographic characteristics of rocks in the studied area are extensively reported elsewhere (e.g. Kirby, 1984; Roberts *et al.*, 1993; Floyd *et al.*, 1993; Selwood *et al.*, 1998). However this study attempted to examine the mineralogy of the limited samples from both dykes and gabbros using optical microscopy to determine if there is any alteration of these rocks.

Gabbroic rocks in the study area are mainly composed of plagioclase and clinopyroxene with some opaque minerals (i.e. magnetite and hematite) but with no olivine, and generally display ophitic to subophitic textures (Figure A16). In

some places, the gabbro showed some hydrothermal alteration, in which pyroxene is replaced by amphibole.

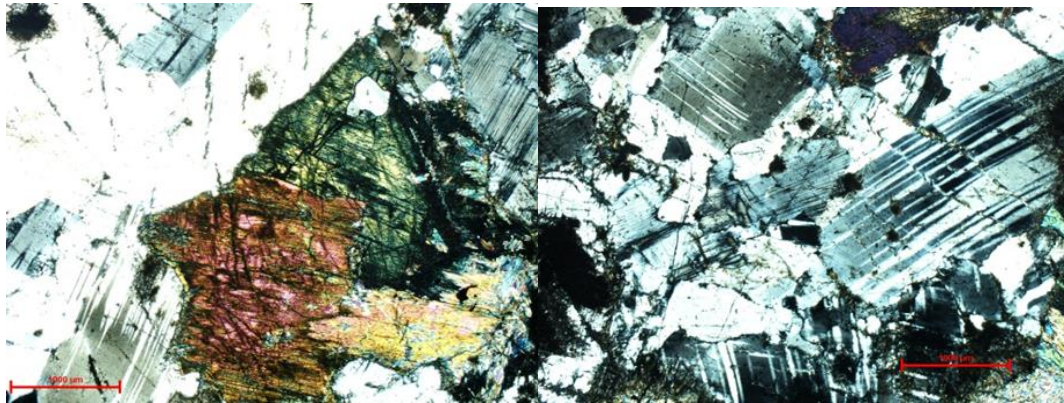


**Figure A16.** Photomicrographs (cross-polars) of the gabbro samples from the Lizard ophiolite showing clinopyroxene and plagioclase. Scale bar: 1 mm.

Dolerite dykes mostly consist of subhedral crystals of plagioclase and fine grained pyroxene with abundant opaque minerals and exhibit a granular texture (Figure A17). However, these dolerite dykes are generally highly hydrothermally altered, with clinopyroxene altered to chlorite.

In some samples, plagioclase phenocrysts occur with subhedral texture, and they exhibit distinctive crystal alignments, which indicate the magma flow direction (Figure A18).

## **A6.2 Rock magnetic results**

Rock magnetic analyses were performed on samples of gabbros and dykes of Lizard ophiolite in order to find out the type of ferromagnetic minerals in these rocks that are responsible for carrying the natural remanence.

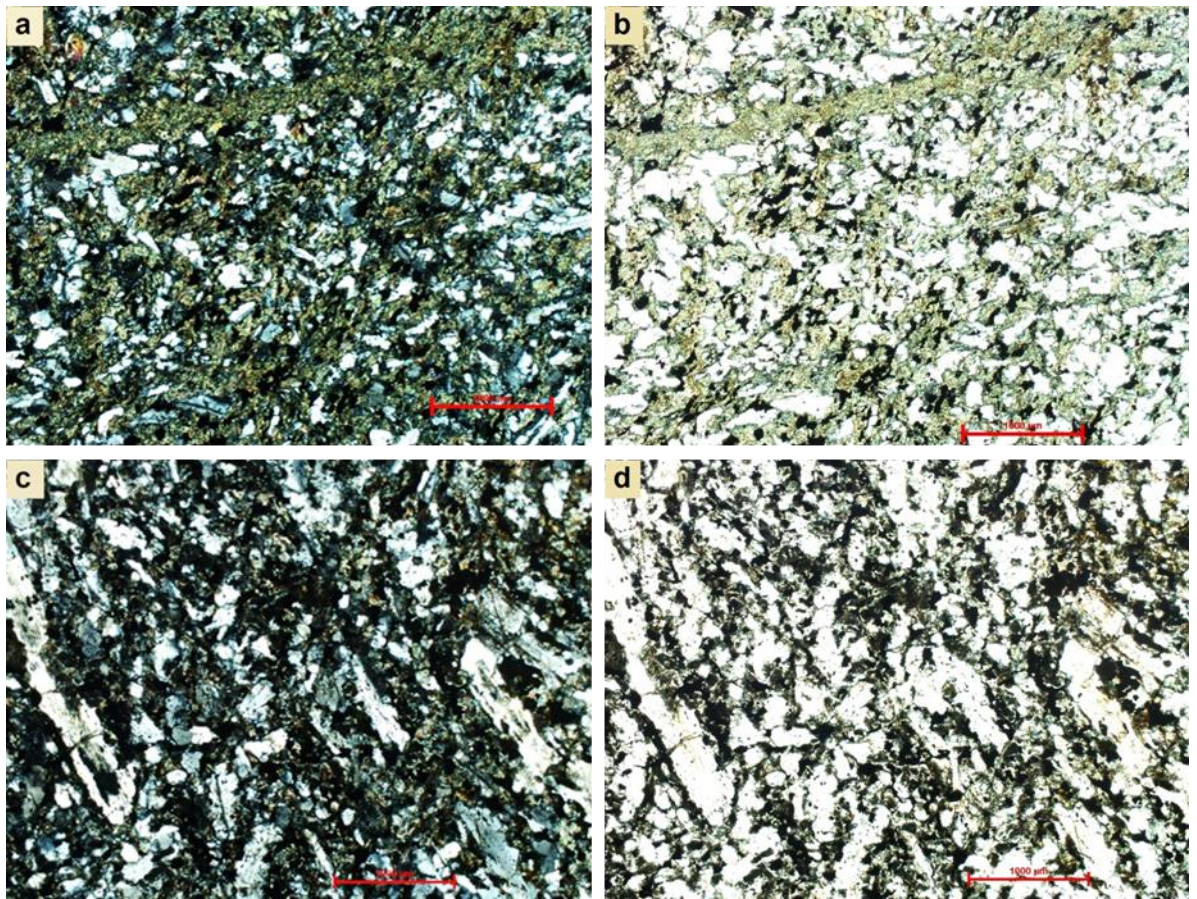


**Figure A17.** Photomicrographs of the dolerite dyke samples from the Lizard ophiolite showing plagioclase phenocrysts in a groundmass of mostly clinopyroxene, chlorite and opaque minerals and displaying alteration of the clinopyroxene to chlorite (a and b) Cross-polars. (c and d) Plane-polarized light. Scale bar: 1 mm.

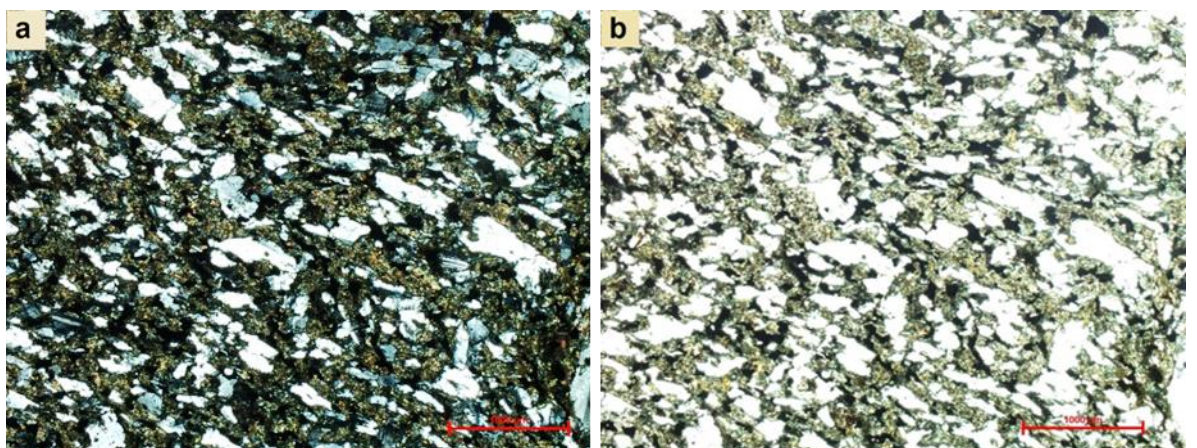


**Figure A18.** Photomicrographs of the dolerite dyke samples from the Lizard ophiolite showing alteration of the clinopyroxene to chlorite and alignments of plagioclase phenocrysts with the flow direction. (a) Cross-polars. (b) Plane-polarized light. Scale bar: 1 mm.

### **A6.2.1 Isothermal remanent magnetization (IRM) analyses**

IRM acquisition experiments were performed on 15 representative samples of gabbros and dykes from the sites of Coverack Cove, North and South section of Codrevy Cove and Leggan Cove, using the same technique and equipment which have been described in the section 2.7.5.1. All IRM acquisition curves from both gabbro and dyke samples are shown in Figure A19.

In general, all IRM acquisition curves for gabbro samples showed a rapid increase in magnetization in fields less than 200 mT, and nearly all samples displayed saturation below 400 mT. Backfield demagnetization of IRM of these samples yielded coercivity of remanence values ranging between 38 and 53 mT. These results suggest low to medium coercivity fine-grained magnetic minerals are dominant in these rocks (e.g. single-domain (SD) or pseudo-single domain (PSD) magnetite), with no indication of the presence of haematite or goethite.

The majority of dyke samples also showed a sharp increase in magnetization in fields less 200 mT and reached saturation below 400 mT, suggesting that these rocks are dominated by fine-grained low to medium coercivity minerals. Backfield demagnetization IRM of these samples yielded coercivity of remanence values of 36 to 72 mT. These data demonstrate that the majority of remanence carriers were single-domain (SD) or pseudo-single domain (PSD) (e.g. magnetite). However, some dyke samples showed continued increase in magnetization up to 800 mT. For example, the sample LC04H204 showed a more gentle rise in magnetization up to the maximum applied field of 800 mT. Backfield demagnetization of IRM of this sample yielded a coercivity of remanence of 400 mT, thus indicating the presence of only high coercivity minerals in this sample (i.e. haematite). Sample GC03H11B showed a rapid

increase in IRM acquisition up to 100 mT followed by a continuous and gentle increase in magnetization up to the maximum applied field of 800 mT, suggesting the presence of both low and high coercivity minerals in this sample, i.e magnetite and haematite respectively.

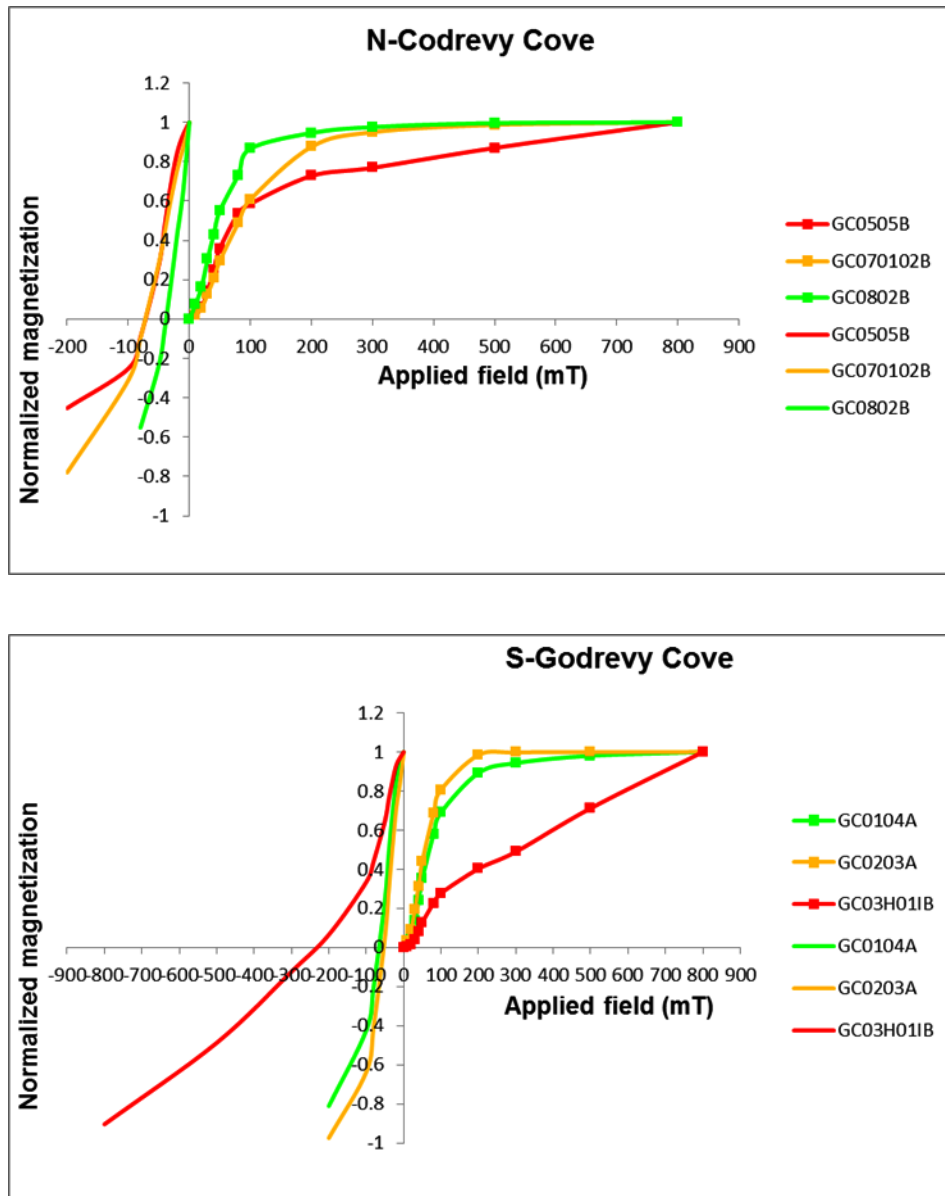


**Figure A19.** Isothermal remanent magnetization (IRM) curves and backfield demagnetization curves for representative samples of the Lizard ophiolite.

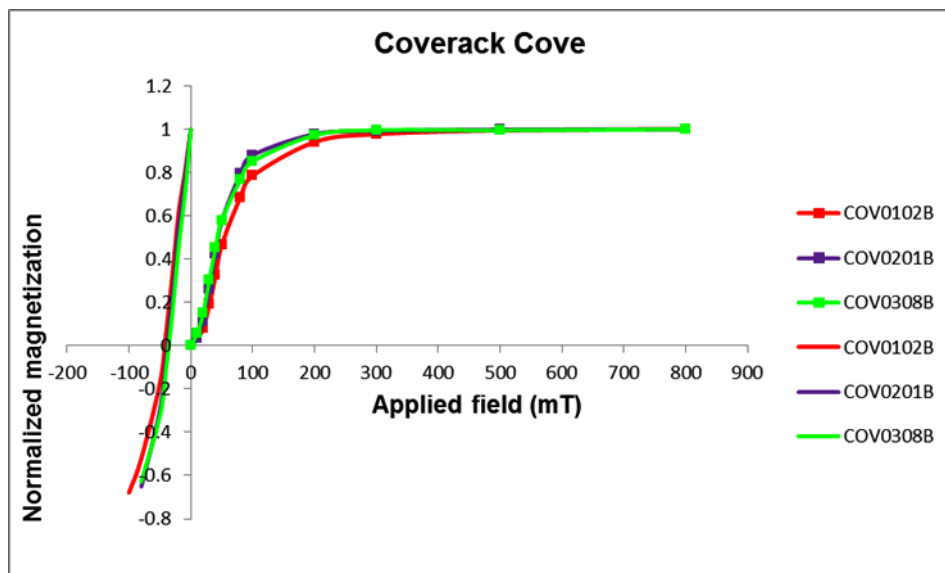
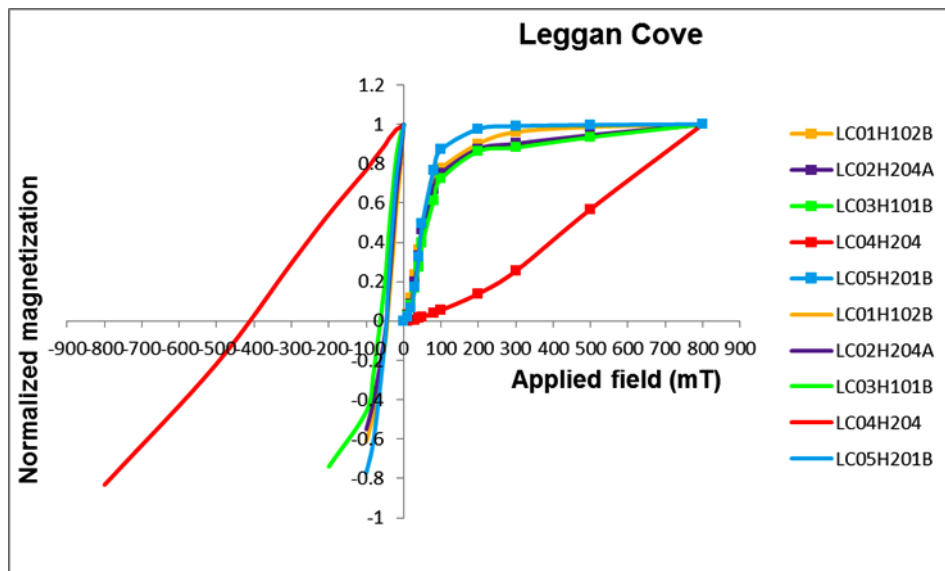
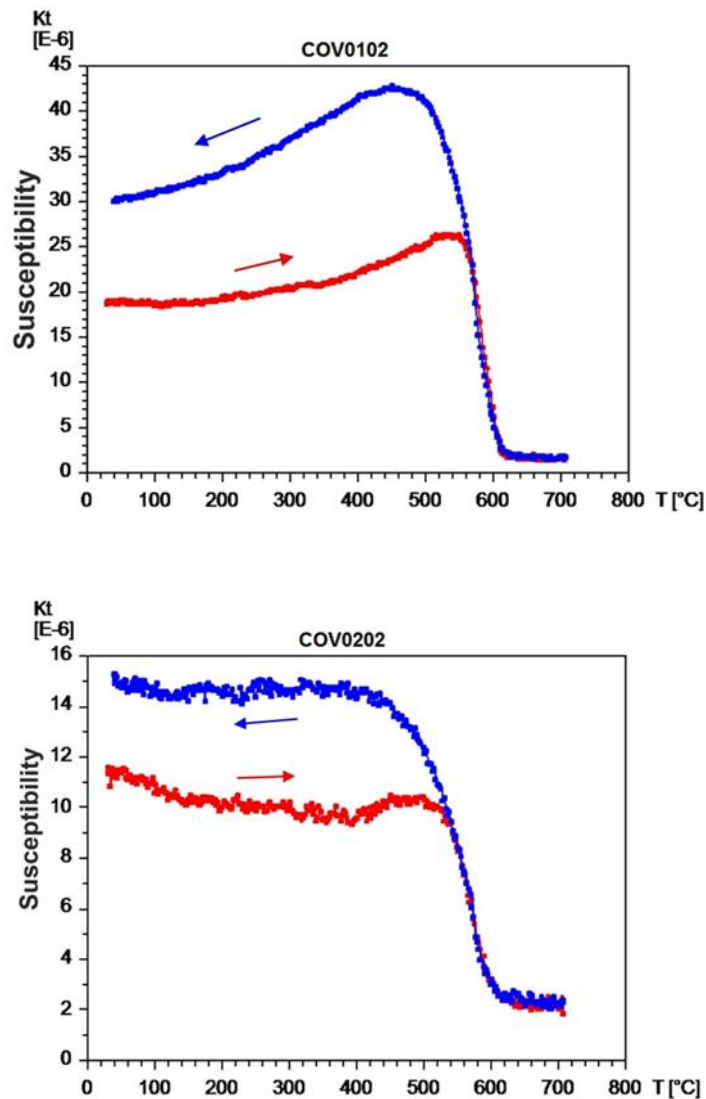


Figure A19. (Continued)

### A6.2.2 Thermomagnetic analysis

High-temperature susceptibility experiments were measured for representative samples from both gabbros and dykes, using the same techniques and equipment which have been described in section 2.7.5.2 of the main thesis. Results are shown in Figure A20. In general, all the samples showed a clear decrease of susceptibility upon heating to around 580 °C, suggesting the

presence of magnetite as a dominant magnetic mineral in these rocks, which is consistent with IRM acquisition experiments. Heating and cooling curves are irreversible, indicating that some new magnetic minerals have been created during the heating cycle. Sample GC0802 is observed to have a small bump in the heating curve between 150 °C and 400 °C, probably indicating the presence of subsidiary maghemite. Sample LC01H02 showed a noisy susceptibility curve with a shape suggesting that this sample is dominated by paramagnetic minerals.



**Figure A20.** Curie temperature experiments on representative samples from the Lizard ophiolite. Note: the red curve illustrates the heating from room temperature to 700°C, and the blue curve illustrates the cooling from 700°C to room temperature.

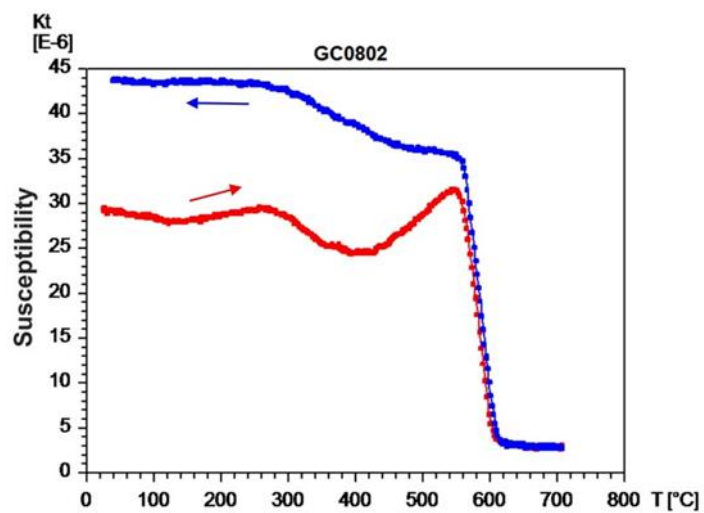
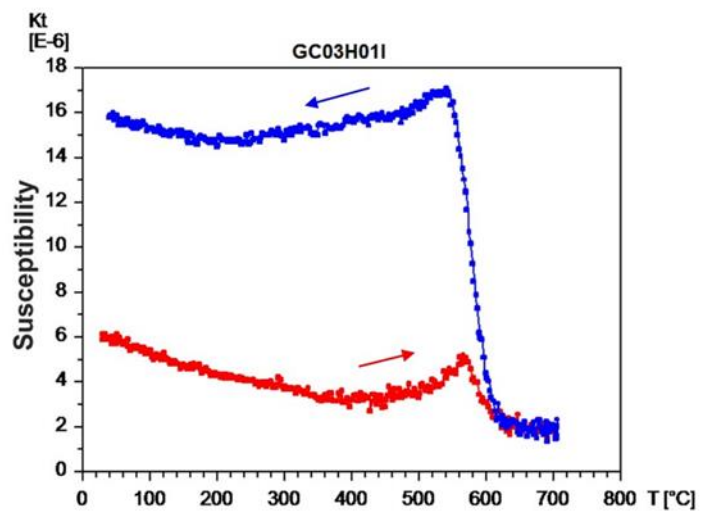
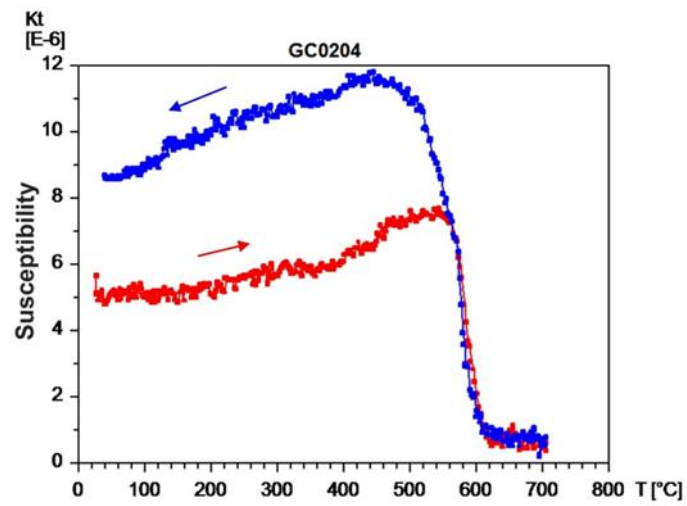


Figure A20. (Continued)

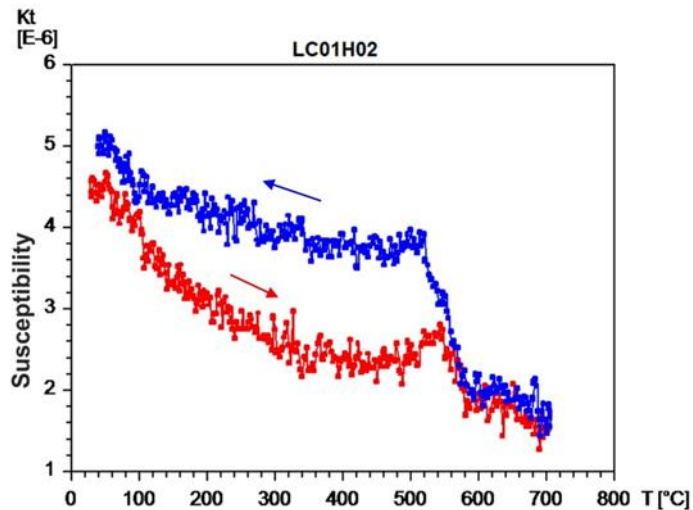


Figure A20. (Continued)

### A6.3 Anisotropy of magnetic susceptibility (AMS)

All samples from the dykes have intermediate to high bulk susceptibility, ranging from  $4.4 \times 10^{-4}$  SI to  $5.3 \times 10^{-3}$  SI, indicative of a ferromagnetic mineralogy (e.g. magnetite) which is consistent with rock magnetic analyses of these samples. Various fabric relationships were found in the dykes. Sites GC07 and LC03H1 showed a very good relationship between AMS fabric and dyke orientation, i.e. the magnetic foliation ( $K_1$  and  $K_2$ ) and the mean dyke wall are in good agreement with the mean orientation of the  $K_3$  axes perpendicular to the dyke wall, suggesting a normal magnetic fabric (Figure A21i-ii). Other dyke sites showed various forms of relationships between magnetic fabrics and dyke orientations, ranging from good to poor, suggesting that the controls of AMS may vary between dykes. For example, site COV3 (Figure A21iii) showed a reasonable AMS fabric relationship with dyke orientation but some scatter in AMS principal axes between samples, whereas sites GC01 and GC03H1 showed well defined AMS fabrics with no relationship to dyke orientation (Figure

A21iv-v). Sites COV01, GC04 and GC05 showed very poorly defined AMS fabrics with no relationship to dyke orientations (Figure A21vi-viii). On the other hand results from the gabbro sites showed only random AMS fabrics, which reflect the lack of preferred orientation of crystals in the gabbro (Figures A16 and A22a).

Using a Jelinek plot to illustrate the shape of the AMS ellipsoids, both dykes and gabbros showed a mixture of oblate and prolate magnetic fabric shapes at the specimen level. The degree of anisotropy,  $P_j$ , at all dyke sites ranges from 1.006 - 1.153, and from 1.005 - 1.247 at the gabbro sites (Figure A21ix, Figure A22b and Table A1).

**Table A1.** Magnetic fabric results.

		Mean orientation of the axis															
		K1				K2				K3							
Lithology	n	Susceptibility	Dec	Inc	Conf. angles	Susceptibility	Dec	Inc	Conf. angles	Susceptibility	Dec	Inc	Conf. angles	Pj	T		
<b>Coverack</b>																	
COV01	Dyke	19	2.51E-03	323.7	39.3	32.4/11.1	2.47E-03	94.5	38.6	65.1/30.2	2.46E-03	208.8	27.3	65.0/9.7	1.021	-0.503	
COV02	Gabbro	3	Not enough records for Jelinek statistics				Not enough records for Jelinek statistics				Not enough records for Jelinek statistics				1.09	0.236	
COV03	Dyke	13	8.13E-03	315.9	46.2	30.3/15.0	7.87E-03	190	29.3	24.9/20.7	7.58E-03	81.6	29.2	29.5/13.5	1.073	0.071	
<b>Godrevy</b>																	
GC01	Dyke	10	5.47E-04	104.1	17.8	12.0/5.1	5.43E-04	349.6	52.4	16.1/5.1	5.39E-04	205.6	31.9	18.9/5.9	1.014	-0.103	
GC02	Gabbro	12	1.06E-03	39.3	29	55.1/14.8	1.04E-03	150.4	33	57.5/27.1	9.60E-04	278	43.1	39.4/15.0	1.113	0.512	
GC03	Dyke	14	5.23E-04	275.9	4.8	44.5/23.1	5.21E-04	182.7	33.6	34.1/7.5	5.14E-04	13	55.9	39.9/7.4	1.018	0.503	
GC04	Dyke	6	5.62E-04	342.3	50.2	12.6/6.8	5.50E-04	88.3	12.9	23.1/11.0	5.41E-04	188.1	36.8	22.7/7.9	1.04	-0.145	
GC05	Dyke	10	6.78E-04	319.6	9.2	34.8/3.0	6.67E-04	55.1	30.7	37.2/30.9	6.62E-04	214.8	57.7	34.0/3.8	1.024	-0.33	
GC06	Gabbro	6	7.19E-03	78.8	42.2	69.3/8.5	7.15E-03	268.1	47.5	69.4/58.5	7.11E-03	173.1	4.7	58.9/5.7	1.012	-0.028	
GC07	Dyke	10	5.96E-04	133.6	6.9	15.0/3.4	5.95E-04	39.9	28.2	19.0/7.9	5.92E-04	236.1	60.8	14.6/3.6	1.007	0.515	
GC08	Gabbro	4	Not enough records for Jelinek statistics				Not enough records for Jelinek statistics				Not enough records for Jelinek statistics				1.01	-0.751	
<b>Leggan</b>																	
LC01	Gabbro	14	4.25E-04	102.7	9.7	74.0/56.2	4.24E-04	203.5	47.5	72.9/64.5	4.23E-04	4.2	40.9	67.3/61.2	1.003	0.063	
LC02	Gabbro	12	4.67E-04	126.4	0.6	36.6/13.8	4.64E-04	218.4	72.8	39.4/36.4	4.61E-04	36.2	17.1	39.3/13.8	1.014	0.014	
LC03	Dyke	15	5.99E-04	314.6	5.5	9.0/3.6	5.97E-04	174.4	82.9	10.2/5.5	5.89E-04	45	4.5	7.3/3.6	1.018	0.523	
LC04	Dyke	14	5.47E-04	45.1	27	76.1/17.1	5.46E-04	144.1	17	76.2/12.4	5.42E-04	262.6	57.3	25.9/18.6	1.011	0.734	
LC05	Gabbro	13	5.97E-04	326.8	22.8	68.0/22.3	5.95E-04	57.6	2.1	68.0/24.7	5.87E-04	152.7	67.1	25.8/24.6	1.018	0.58	
Total		175															

**n** = number of specimens; **Pj** = corrected anisotropy degree; **T** = shape parameter; **Dec** = declination; **Inc** = inclination.

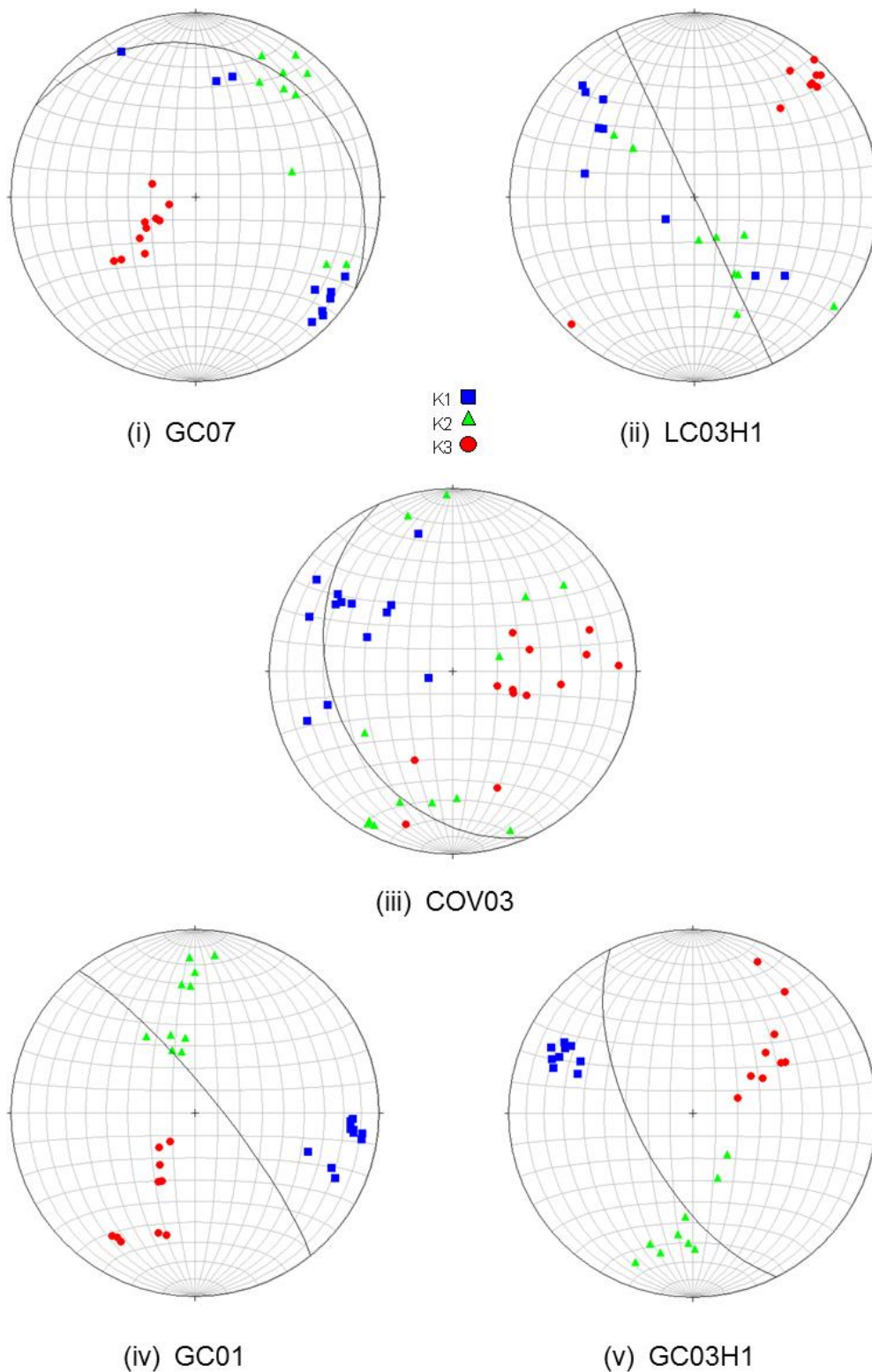
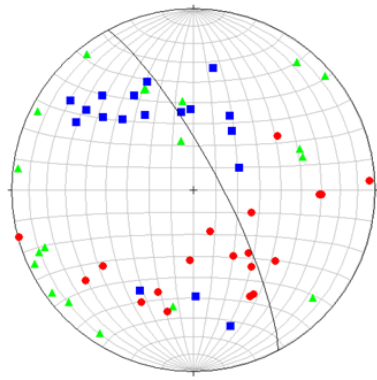
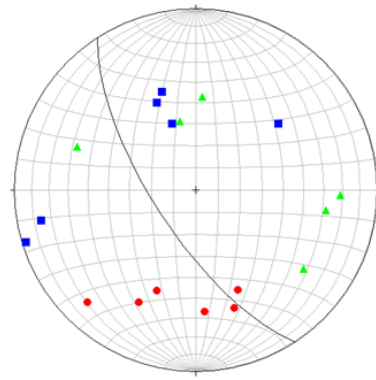


**Figure A21.** Representation of AMS of the dykes from the east coast of the Lizard. (i-viii) Stereographic projections of principal anisotropy axes ( $K_1$ ,  $K_2$ , and  $K_3$ ). (ix) Degree of anisotropy  $P_j$  versus shape parameter  $T$  diagram (Jelinek, 1981) for all dyke sites.

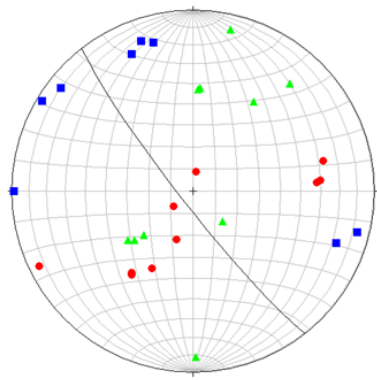


(vi) COV01

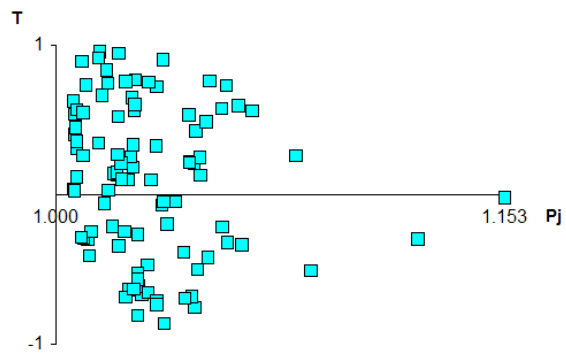


(vii) GC04

K1 ■  
K2 ▲  
K3 ●

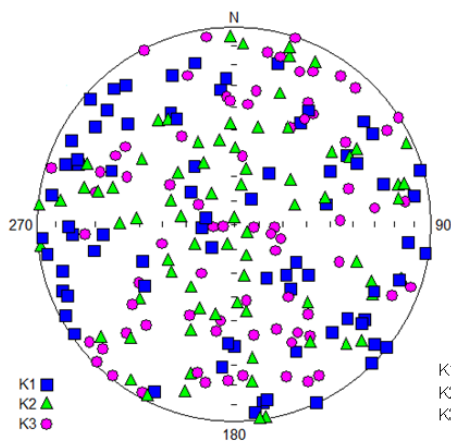


(viii) GC05

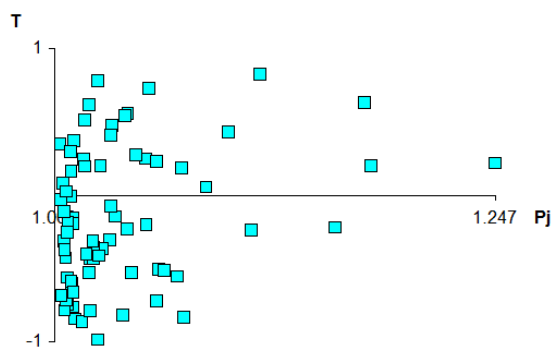


(ix)

Figure A21. (Continued)



(a)



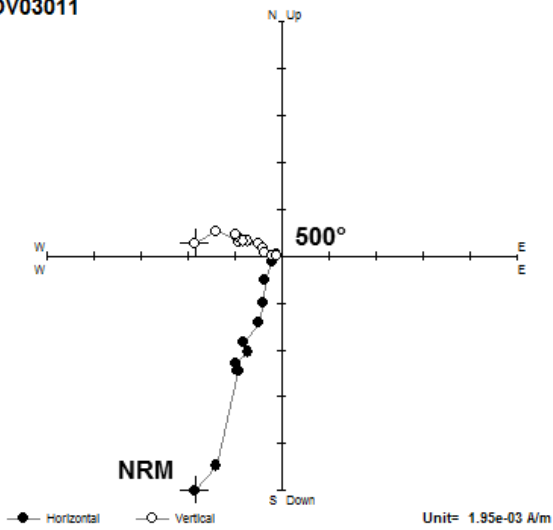
(b)

Figure A22. Representation of AMS of the gabbros from the east coast of the Lizard. (a) Stereographic projections of principal anisotropy axes ( $K_1$ ,  $K_2$ , and  $K_3$ ). (b) Degree of anisotropy  $P_j$ , versus shape parameter  $T$  diagram (Jelinek, 1981) for all gabbro sites.

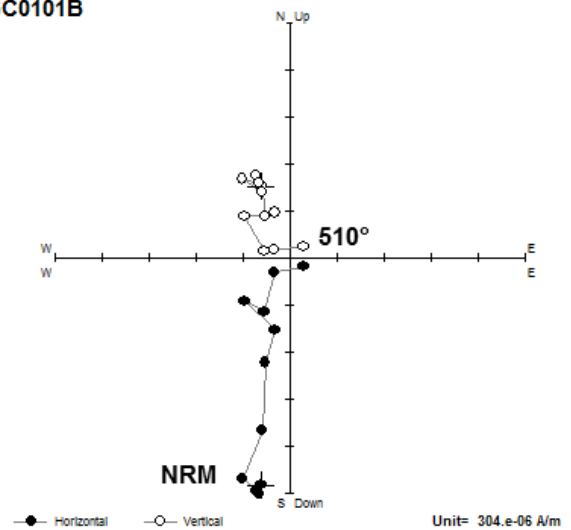
#### **A6.4 Remanent magnetization results**

The nature of the remanent magnetization of 175 specimens collected at 16 sites throughout the Coverack – Leggan region has been determined using laboratory demagnetization techniques. Typical examples of demagnetization behavior are shown in Figures A23 and A24. *In situ* and tilt corrected mean directions from all sites are listed in Table A2. Both alternating field and thermal techniques were used to identify the remanence directions, although alternating field demagnetization data are sometimes noisier than the thermal data. During the demagnetization treatments, the majority of the samples reveal a stable component, specified by straight paths in orthogonal projections trending towards the origin at elevated temperatures and alternating fields. During alternating field treatments a relatively stable component is isolated using fields up to 100 mT. Thermal demagnetization isolated stable components with maximum unblocking temperatures of 580°C, consistent with remanence carried by magnetite.

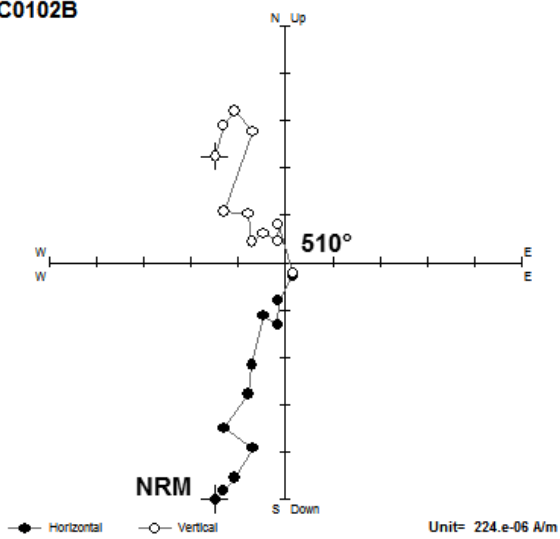
COV03011



GC0101B



GC0102B



GC0103B

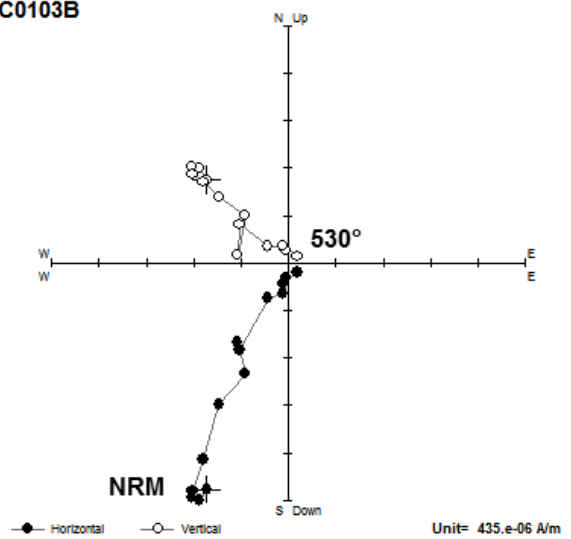
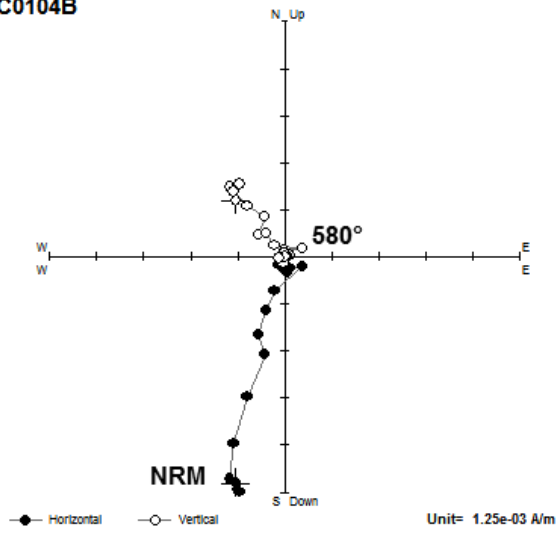
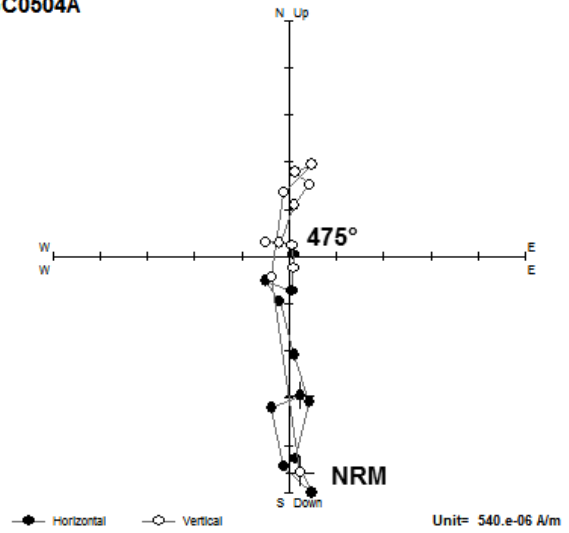


**Figure A23.** Zijderveld diagrams (orthogonal vector plots) of demagnetization data for selected samples. Solid/open symbols = projection on to the horizontal/E-W vertical planes, respectively.

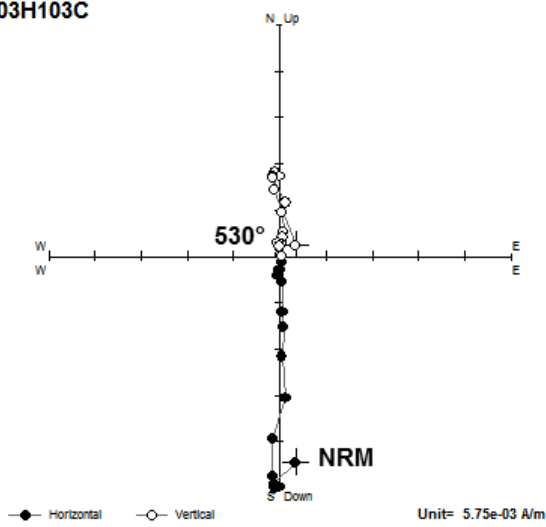
GC0104B



GC0504A



LC03H103C



LC03H203

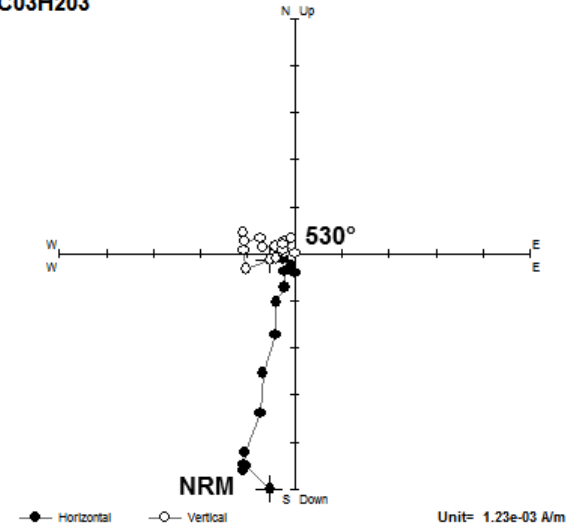
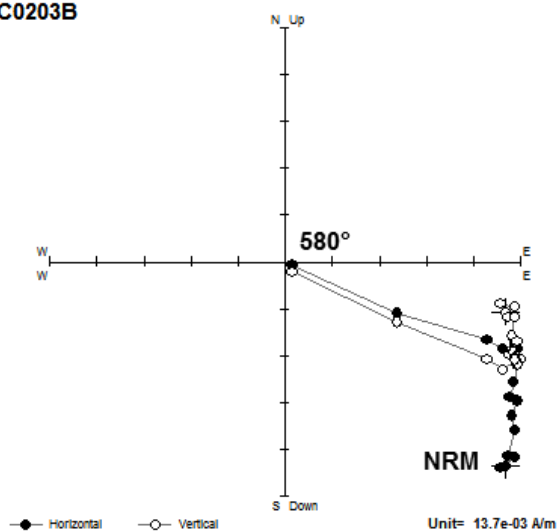
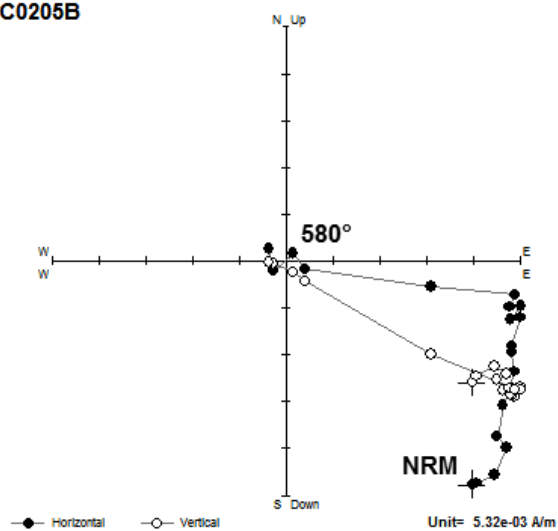


Figure A23. (Continued)

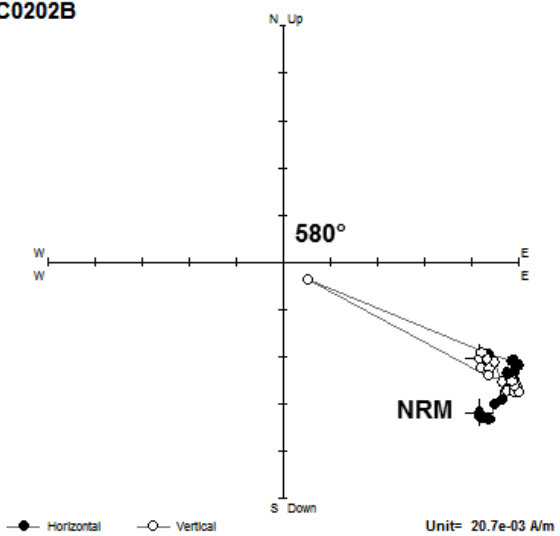
GC0203B



GC0205B



GC0202B



GC0204B

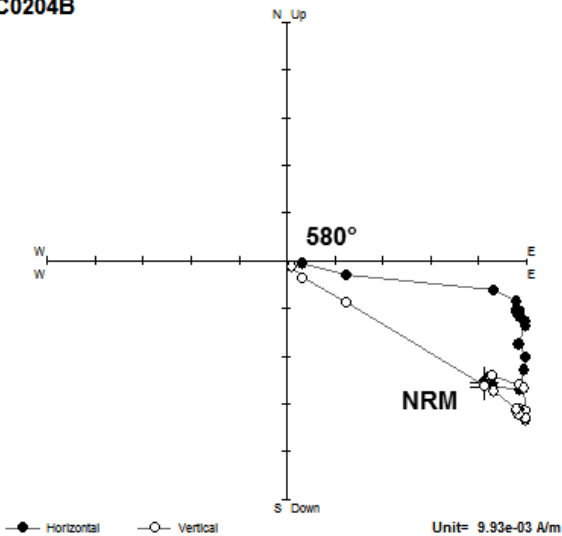
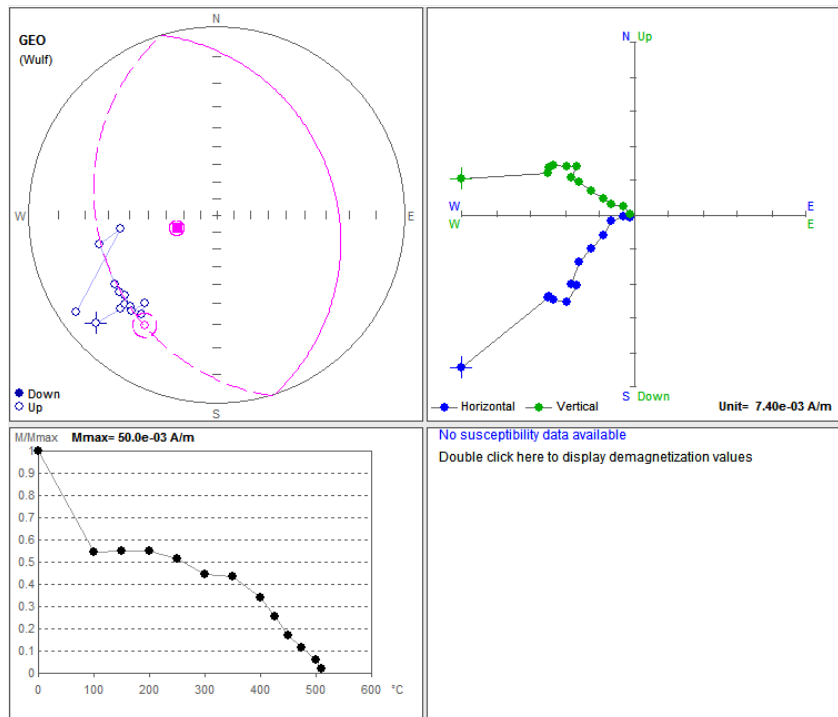
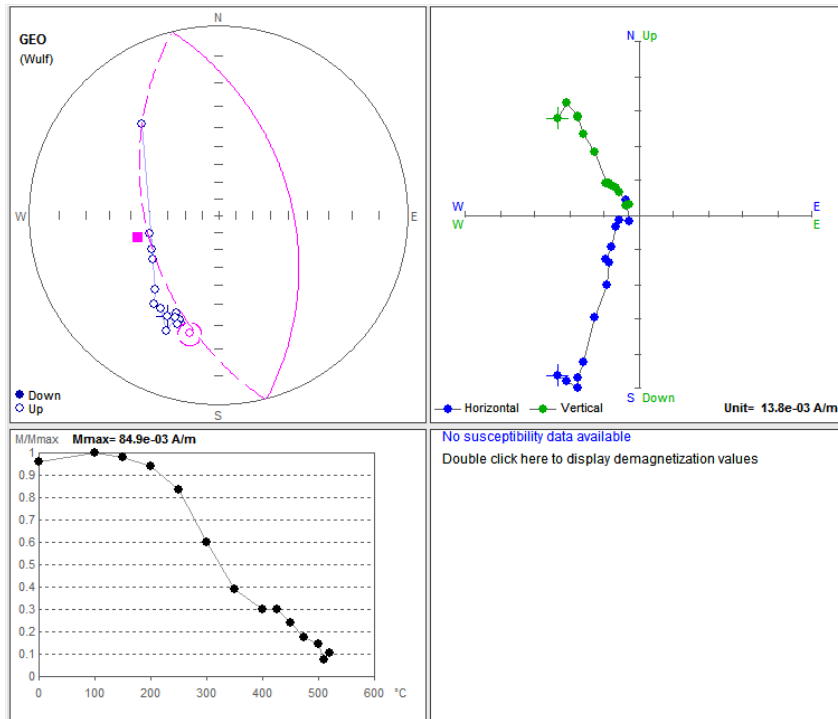


Figure A23. (Continued)



**Figure A24.** Zijderveld plots, stereographic projections and great circle demagnetization trends for selected samples.

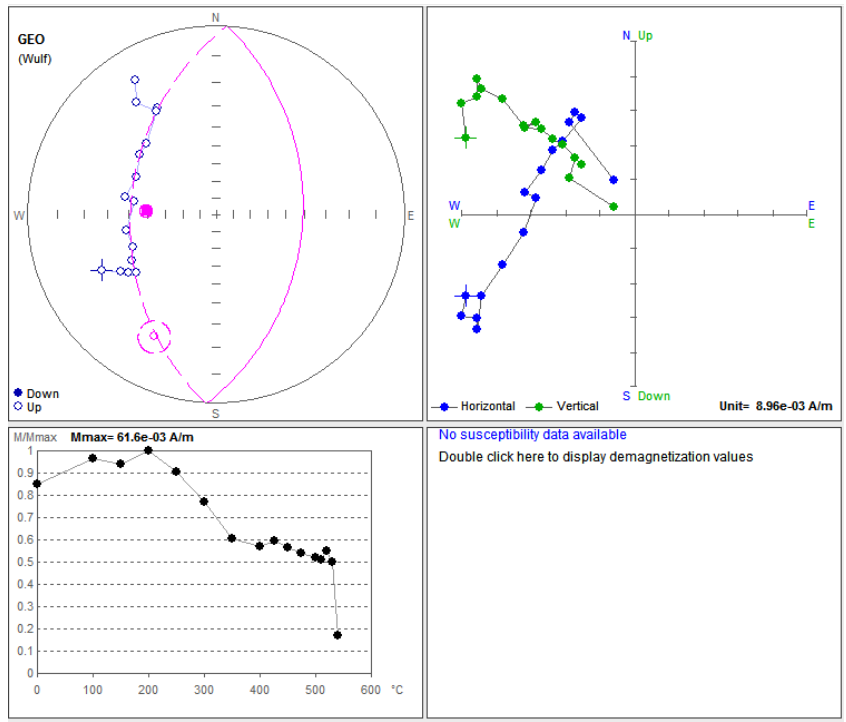
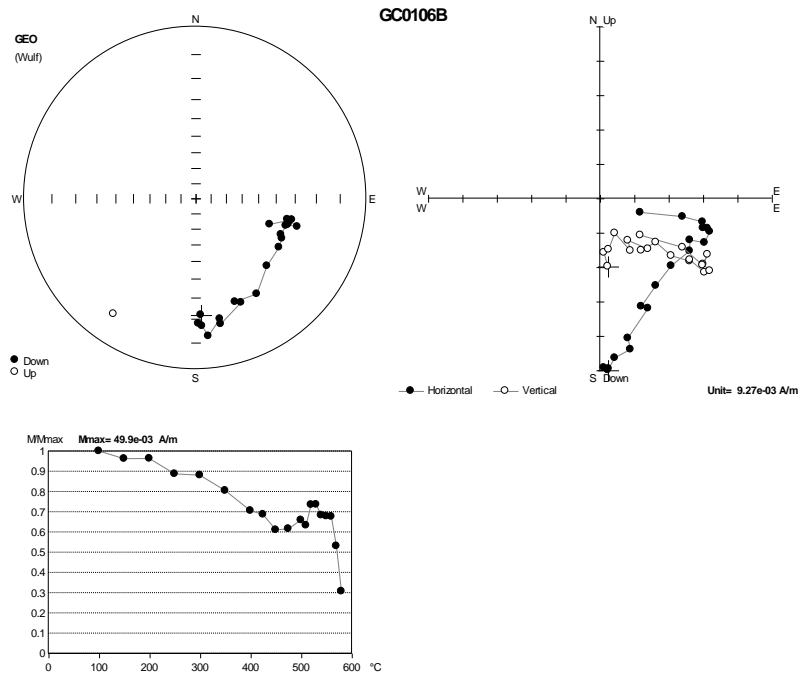


Figure A24. (Continued)



**Figure A25.** Zijderveld plots, stereographic projections and thermal demagnetization trends for sample GC0106B showing both an intermediate-high unblocking temperature overprint with a SSW declination and negative inclination and a high blocking temperature (presumably primary) component with an ESE declination and positive inclination.

**Table A2.** Palaeomagnetic results from sites displaying stable magnetizations.

Site	Lithology	DD/D	n	Mean remanence							
				<i>In situ</i>				Tilt corrected			
				Dec	Inc	$\alpha 95$	<i>k</i>	Dec	Inc	$\alpha 95$	<i>k</i>
<b>Coverack</b>											
COV01 *	Dyke	062/78	7	197.9	-18	10.4	34.4	194.3	-26.3	10.4	34.5
COV03 *	Dyke	246/34	5	186.2	-16.9	20.6	14.8	187.7	13.7	20.6	14.8
<b>Godrevy</b>											
GOC01 *	Dyke	051/80	6	198.1	-15.7	8.3	66.1	196.1	-24	8.3	66.1
GOC02	Gabbro		6	104.2	27.3	5.3	158.6	—	—	—	—
GOC04 *	Dyke	237/71	1	188.3	-16.3	—	—	190.8	-3.4	—	—
GOC05 *	Dyke	232/84	6	179.8	-17.7	5.3	161.4	181.1	-14	5.3	161.4
GOC06 *	Gabbro		3	194.7	-25.2	16.1	59.5	—	—	—	—
GOC07 *	Dyke	030/20	7	230.6	6.4	7.1	72.4	249.6	-56.8	7.1	72.5
<b>Legann</b>											
LC01 *	Gabbro		1	225.2	-30.6	—	—	—	—	—	—
LC02 *	Gabbro		1	241.4	-4.6	—	—	—	—	—	—
LC03 *	Dyke	vertical/strike 335-155	8	185.8	-10.3	6.3	78.9	185.8	-10.3	6.3	78.9
LC04 *	Gabbro		1	198.6	-11.5	—	—	—	—	—	—
LC05 *	Gabbro		1	192.6	-6.5	—	—	—	—	—	—

The mean of site means with SSW components

N	Dec	Inc	$\alpha 95$	K
12	201.3	-14.6	11.7	14.6

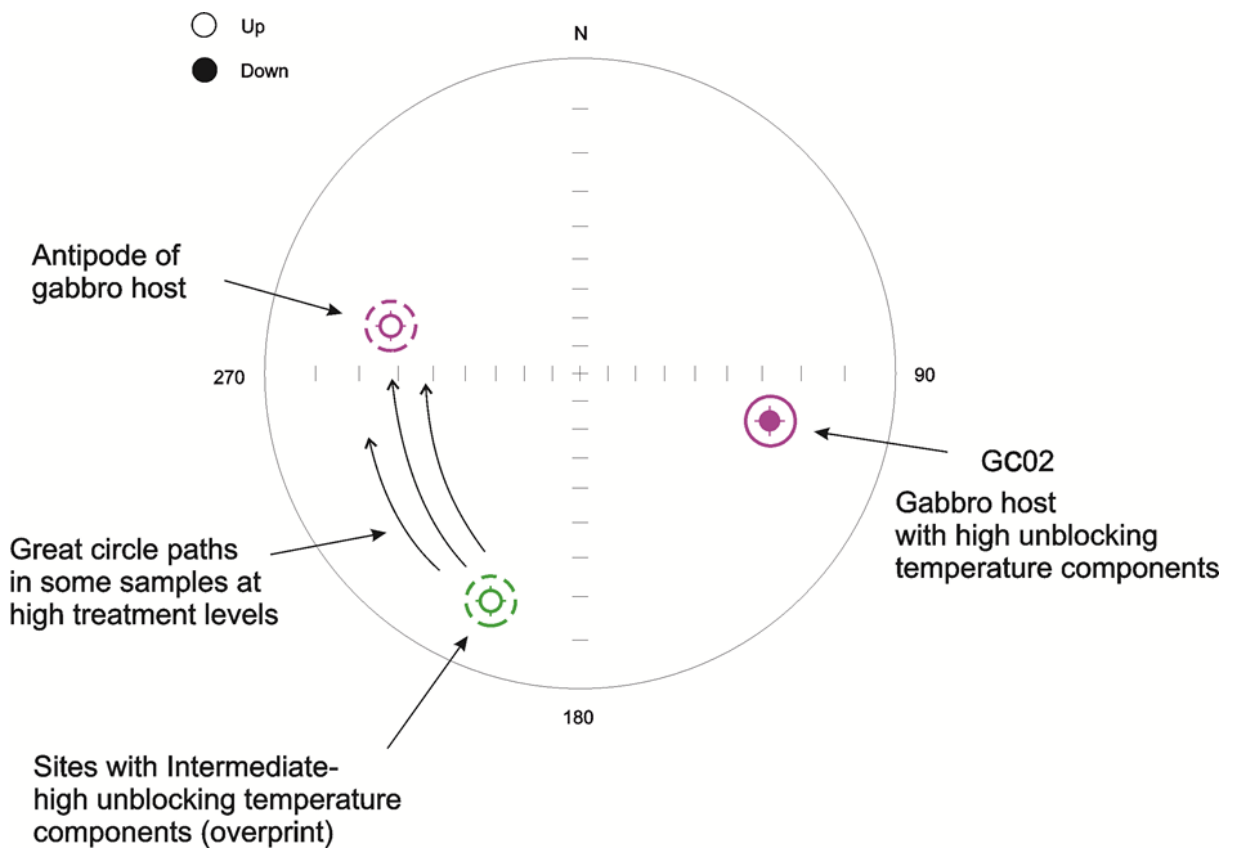
N=number of sites; n=number of specimens; Dec=declination; Inc=inclination;  $\alpha 95$ =semi-angle of 95% cone of confidence; K=Fisher precision parameter. \* sites with SSW components

## A7. Interpretation and discussion

Dyke sites from Coverack showed stable components of magnetization that have SSW declinations and shallow negative inclinations (Table A2). The same direction is isolated at the majority of sites from Godrevy and Leggan (Table A2). These SSW components of magnetization identified from individual samples were subsequently combined at the site level to give an overall mean direction of  $D = 201.3^\circ$ ,  $I = -14.6^\circ$  (Table A2). However, at these sites, higher demagnetization levels sometimes reveal a drift of remanence directions towards the NW quadrant. In these samples, the remanence migrates along great circle paths towards the NW but does not reach an endpoint direction (Figure A24). This suggests that a higher coercivity/unblocking temperature component is also present at these sites, but the direction of this component cannot be defined before either the remanence reduces to the noise level of the magnetometer or the magnetization becomes unstable.

In contrast, one of the gabbro sites at Godrevy (site GC02) records a very different ESE remanence with a positive inclination (Table A2). Gabbro specimens from this site that were demagnetized with thermal demagnetization produce clear linear demagnetization trends towards the origin (Figure A23). Most of these gabbro samples reach this stable ESE-directed endpoint component after removal of a small, lower stability SSW-directed component. One sample (GC0106B; Figure A25) in particular is especially informative though: during sampling this core was found to have penetrated through a dyke margin into the host gabbro. Demagnetization of this core shows the strong SSW-directed low stability component observed at Godrevy and a very clear ESE-directed high stability component (Figure A25). This implies that the ESE-

component is the original remanence carried by the gabbros and that the SSW-component represents a later magnetic overprint. Overall these observations suggest that the dykes at Godrevy are almost completely remagnetized but that the gabbros occasionally preserve an earlier magnetization. This is further supported by the drift of dyke samples towards a direction that is antipodal to the stable gabbro direction, suggesting that the original remanence of these dykes was of opposite polarity to that of the host gabbros (Figure A26).



**A26.** Schematic summary of remanence data from the Lizard ophiolite.

Hailwood *et al.* (1984) also observed SSW-directed magnetizations with negative inclinations in these rocks, which they interpreted as primary magnetizations acquired during formation of the ophiolite. The results from

samples in this study suggest that this is a misinterpretation, and that these directions represent a remagnetization. The correspondence of this direction with the Permian geomagnetic field direction in SW England strongly suggests that the dykes were largely remagnetized in the Permian, possibly as a result of fluid flow associated with the intrusion of the Cornubian granite batholith. These observations are supported by petrographic analyses of collected samples, which are discussed in the section A6.1.

Assuming that the ESE-directed remanence in gabbros at site GC02 is an original, primary magnetization, this direction may be used to estimate the original orientation of the dykes that cut the host gabbros, using the net tectonic rotation method described in the main thesis. In the Devonian, SW England was located in the southern hemisphere (Stampfli *et al.*, 2002; Figure A2). In this case the positive inclination at the gabbro site would represent a reversed polarity that could be assumed to be originally directed southwards (assuming an axial geocentric dipole field).

A reference inclination for this original magnetization may be calculated from the 390Ma palaeomagnetic pole from the Laurussia/Laurasia APWP of Torsvik *et al.* (2012). This pole (latitude = 1.4°, longitude = 322.5°) yields a reference inclination of 54° for a sampling site at latitude 50°N, longitude -5°W. Using the *in situ* remanence direction from gabbros at site GC02 of Dec/Inc = 104.2/27.3, a reference direction of Dec/Inc = 180/54, and the present day orientation of the dyke sampled at GC01 yields the net tectonic rotation parameters listed in Table A3.

Two solutions are found that are capable of restoring the site GC01 dyke to the vertical. However, the second (alternative) solution requires an unrealistically

large rotation of 166°, in contrast to the 90° rotation required by the first (preferred) solution (which better fits the angular difference between the observed and expected remanence directions). The initial dyke strike associated with the preferred solution is 229°. This NE-SW strike is compatible with the trend of the Rheic Ocean in palaeogeographic reconstructions (e.g. Stampfli *et al.*, 2002; Figure A2). This tentative result therefore suggests that the dykes at Godrevy Cove were emplaced along a NE-SW striking spreading axis, in contrast to some existing tectonic models (e.g. Cook *et al.*, 2002).

**Table A3.** Net tectonic rotation parameters for restoration of dykes at site GC01 using the remanence direction of their host at site GC02.

<b>Net tectonic rotation analysis of data from sites GC01 and GC02</b>	<b>Solution 1 (preferred)</b>	<b>Solution 2 (alternative)</b>
<b>Net tectonic rotation pole (azimuth/plunge)</b>	075.2/69.3	129.8/50.5
<b>Net tectonic rotation angle</b>	89.5 CCW	165.9 CCW
<b>Original dyke strike (for initially vertical dyke)</b>	229.1	310.9

## References

- Akay, E. & Uysal, Ş. (1988) 'Post-Eocene tectonics of the central Taurus Mountains', *Bull. MTA*, 108, pp. 23-34.
- Al-Riyami, K. & Robertson, A. (2002) 'Mesozoic sedimentary and magmatic evolution of the Arabian continental margin, northern Syria: evidence from the Baer-Bassit Melange', *Geological Magazine*, 139 (4), pp. 395-420.
- Al-Riyami, K., Robertson, A., Dixon, J., & Xenophontos, C. (2002) 'Origin and emplacement of the Late Cretaceous Baer-Bassit ophiolite and its metamorphic sole in NW Syria', *Lithos*, 65 (1-2), pp. 225-260.
- Alexander, A. C. & Shail, R. K. (1995) 'Late variscan structures on the coast between Perranporth and St Ives, Cornwall'. In Williams, B.J. (ed.) *Proceedings of the Ussher Society*, Vol 8, Exeter: Ussher Soc, pp. 398-404.
- Allerton, S. (1989 a) 'Distortions, rotations and crustal thinning at ridge transform intersections', *Nature* 340, pp. 626 – 628.
- Allerton, S. (1989 b) 'Fault block rotations in ophiolites: results of palaeomagnetic studies in the Troodos Complex, Cyprus. In: Kissel, C., Laj, C. (Eds.), *Palaeomagnetic Rotations and Continental Deformation*, *NATO ASI Series C*, vol. 254, pp. 393–410.
- Allerton, S. & Vine, F. (1987) 'Spreading structure of the Troodos ophiolite, Cyprus: Some paleomagnetic constraints', *Geology*, 15 (7), pp. 593-597.
- Allerton, S. & Vine, F. (1990) 'Palaeomagnetic and structural studies of the southeastern part of the Troodos complex'. In: Malpas, J., Moores, E.M., Panayiotou, A., Xenophontos, C. (Eds.), *Ophiolites: Oceanic Crustal Analogues*. *Cyprus Geological Survey Department, Nicosia*, pp. 99 –11.
- Allerton, S. & Vine, F. (1991) 'Spreading evolution of the Troodos ophiolite, Cyprus', *Geology*, 19 (6), pp. 637-640.
- Anonymous (1972) 'Penrose field conference report', *Geotimes*, 17 (12), pp. 24-25.
- Argyle, K. S., Dunlop, D. J. & Xu, S. (1994) 'Single-domain behaviour of multidomain magnetite grains'. In *Rock magnetism: Fundamentals and frontiers*. Cambridge University Press, New York: 573 pp.

- Bağcı, U., Parlak, O. & Höck, V. (2006) 'Geochemical character and tectonic environment of ultramafic to mafic cumulate rocks from the Tekirova (Antalya) ophiolite (southern Turkey)', *Geological Journal*, 41 (2), pp. 193-219.
- Bağcı, U., Parlak, O. & Höck, V. (2005) 'Whole-rock and mineral chemistry of cumulates from the Kizildag (Hatay) ophiolite (Turkey): clues for multiple magma generation during crustal accretion in the southern Neotethyan ocean', *Mineralogical Magazine*, 69 (1), pp. 53.
- Bağcı, U., Parlak, O. & Höck, V. (2008) 'Geochemistry and tectonic environment of diverse magma generations forming the crustal units of the Kızıldağ (Hatay) ophiolite, Southern Turkey', *Turkish Journal of Earth Sciences*, 17, pp. 43-71.
- Barnes, R. P. & Andrews, J. R. (1986) 'Upper Paleozoic ophiolite generation and obduction in South Cornwall', *Journal of the Geological Society*, 143, pp. 117-124.
- Barth, M. G., & Gluhak, T. M. (2008) 'Geochemistry and tectonic setting of mafic rocks from the Othris Ophiolite, Greece', *Contributions to Mineralogy and Petrology*, 157 (1), pp. 23-40.
- Beard, J. S. (1986) 'Characteristic mineralogy of arc-related cumulate gabbros: implications for the tectonic setting of gabbroic plutons and for andesite genesis', *Geology*, 14 (10), pp. 848-851.
- Beccaluva, L., Coltorti, M., Giunta, G. & Siena, F. (2004) 'Tethyan vs. Cordilleran ophiolites: a reappraisal of distinctive tectono-magmatic features of supra-subduction complexes in relation to the subduction mode', *Tectonophysics*, 393 (1), pp. 163-174.
- Benn, K. & Allard, B. (1989) 'Preferred mineral orientations related to magmatic flow in ophiolite layered gabbros', *Journal of Petrology*, 30 (4), pp. 925-946.
- Besse, J. & Courtillot, V. (2002) 'Apparent and true polar wander and the geometry of the geomagnetic field over the last 200 Myr', *Journal of Geophysical Research*, 107 (B11), pp. 2300.
- Billor, M. Z. & Gibb, F. (2002) '*The Mineralogy and Chemistry of the Chromite Deposits of Southern (Kızıldağ, Hatay and Islahiye, Antep) and Tauric Ophiolite Belt (Pozanti–Karsanti, Adana), Turkey*', Paper presented at the 9th International Platinum Symposium, Billings, Montana, USA.
- Bonhommet, N., Roperch, P. & Calza, F. (1988) 'Paleomagnetic arguments for block rotations along the Arakapas fault (Cyprus)', *Geology*, 16 (5), pp. 422-425.

- Borradaile, G. & Gauthier, D. (2003) 'Emplacement of an Archean gneiss dome, northern Ontario, Canada: Inflation inferred from magnetic fabrics', *Tectonics*, 22 (2).
- Borradaile, G. & Gauthier, D. (2006) 'Magnetic studies of magma-supply and sea-floor metamorphism: Troodos ophiolite dikes', *Tectonophysics*, 418 (1), pp. 75-92.
- Borradaile, G. J. (2001) 'Magnetic fabrics and petrofabrics: their orientation distributions and anisotropies', *Journal of Structural Geology*, 23 (10), pp. 1581-1596.
- Boulton, S. J., Robertson, A. H. & Ünlügenç, U. C. (2006) 'Tectonic and sedimentary evolution of the Cenozoic Hatay Graben, Southern Turkey: a two-phase model for graben formation', *Geological Society, London, Special Publications*, 260 (1), pp. 613-634.
- Bozkurt, E. & Mittwede, S. (2001) 'Introduction to the geology of Turkey—a synthesis', *International Geology Review*, 43 (7), pp. 578-594.
- Brenchley, P. J. & Rawson, P. F. (2006) *The geology of England and Wales*. 2<sup>nd</sup> edn. Geological Society of London. 561pp.
- Burianek, D., Hanžl, P., Erban, V., Gilikova, H. & Bolorma, K. (2008) 'The Early Cretaceous volcanic activity in the western part of the Gobi-Altay rift (Shiliin Nuruu, SW Mongolia)', *Journal of Geosciences*, 53 (2).
- Burns, L. E. (1985) 'The Border Ranges ultramafic and mafic complex, south-central Alaska: Cumulate fractionates of island-arc volcanics', *Canadian Journal of Earth Sciences*, 22 (7), pp. 1020-1038.
- Butler, R. F. (1998) Paleomagnetism: Magnetic domains to geologic terranes, *Electronic edition*, pp. 1-238.
- Cande, S. C. & Kent, D. V. (1992) 'A new geomagnetic polarity time scale for the Late Cretaceous and Cenozoic', *Journal of Geophysical Research: Solid Earth* (1978–2012), 97 (B10), pp. 13917-13951.
- Cande, S. C. & Kent, D. V. (1995) 'Revised calibration of the geomagnetic polarity timescale for the Late Cretaceous and Cenozoic', *Journal of Geophysical Research: Solid Earth* (1978–2012), 100 (B4), pp. 6093-6095.
- Cann, J. (1970) 'Rb, Sr, Y, Zr and Nb in some ocean floor basaltic rocks', *Earth and Planetary Science Letters*, 10 (1), pp. 7-11.
- Çelik, Ö. (2008) 'Detailed Geochemistry and K-Ar Geochronology of the Metamorphic Sole Rocks and Their Mafic Dykes from the Mersin Ophiolite, Southern Turkey', *Turkish Journal of Earth Sciences*, 17 pp. 685-708.

- Çelik, Ö., Delaloye, M. & Feraud, G. (2006) 'Precise  $^{40}\text{Ar}$ – $^{39}\text{Ar}$  ages from the metamorphic sole rocks of the Tauride Belt Ophiolites, southern Turkey: implications for the rapid cooling history', *Geological Magazine*, 143 (02), pp. 213-227.
- Çelik, Ö., Faruk & Delaloye, M. F. (2003) 'Origin of metamorphic soles and their post-kinematic mafic dyke swarms in the Antalya and Lycian ophiolites, SW Turkey', *Geological Journal*, 38 (3-4), pp. 235-256.
- Celik, Ö. F. (2007) 'Metamorphic sole rocks and their mafic dykes in the eastern Tauride belt ophiolites (southern Turkey): implications for OIB-type magma generation following slab break-off', *Geological Magazine*, 144(05), pp. 849-866.
- Chukwu, A. & Obiora, S. C. (2014) 'Whole-rock geochemistry of basic and intermediate intrusive rocks in the Ishiagu area: further evidence of anorogenic setting of the Lower Benue rift, southeastern Nigeria', *Turkish Journal of Earth Sciences*, pp. 23.
- Clague, D. A. & Straley, P. F. (1977) 'Petrologic nature of the oceanic Moho', *Geology*, 5 (3), pp. 133-136.
- Clube, T. (1985) *The palaeorotation of the Troodos microplate*, University of Edinburgh (PhD thesis).
- Clube, T., Creer, K. & Robertson, A. (1985) 'Palaeorotation of the Troodos microplate, Cyprus', *Nature*, 317 (6037), pp. 522-525.
- Clube, T. M. M. & Robertson, A. (1986) 'The palaeorotation of the Troodos microplate, Cyprus, in the Late Mesozoic-Early Cenozoic plate tectonic framework of the Eastern Mediterranean', *Surveys in Geophysics*, 8 (4), pp. 375-437.
- Cocks, L. & Torsvik, T. (2002) 'Earth geography from 500 to 400 million years ago: a faunal and palaeomagnetic review', *Journal of the Geological Society*, 159 (6), pp. 631-644.
- Coleman, R. G. (1986) 'Ophiolites and accretion of the North American Cordillera', *Bulletin de la Société Géologique de France*, 2 (6), pp. 961-968.
- Condie, K. C. (2005) *Earth as an evolving planetary system*. Academic Press, 447 pp.
- Cook, C. A., Holdsworth, R. E. & Styles, M. T. (1998) 'The tectonic evolution of peridotites in the Lizard ophiolite complex, South-West England', *Proceedings-Ussher Society*, 9 pp. 182-187.

- Cook, C. A., Holdsworth, R. E. & Styles, M. T. (2002) 'The emplacement of peridotites and associated oceanic rocks from the Lizard Complex southwest England', *Geological Magazine*, 139 (1), pp. 27-45.
- Crawford, A. J., Beccaluva, L. & Serri, G. (1981) 'Tectono-magmatic evolution of the West Philippine-Mariana region and the origin of boninites', *Earth and Planetary Science Letters*, 54 (2), pp. 346-356.
- Davies, G. (1984) 'Isotopic evolution of the Lizard Complex', *Journal of the Geological Society*, 141 (1), pp. 3-14.
- Delaloye, M. & Wagner, J. J. (1984) 'Ophiolites and volcanic activity near the western edge of the Arabian plate', *Geological Society, London, Special Publications*, 17 (1), pp. 225-233.
- Dietrich, D. & Spencer, S. (1993) 'Spreading-induced faulting and fracturing of oceanic crust: examples from the Sheeted Dyke Complex of the Troodos ophiolite, Cyprus', *Geological Society, London, Special Publications*, 76 (1), pp. 121-139.
- Dilek, Y. & Flower, M. F. (2003) 'Arc-trench rollback and forearc accretion: 2. A model template for ophiolites in Albania, Cyprus, and Oman', *Special Publication-Geological Society of London*, 218, pp. 43-68.
- Dilek, Y. & Furnes, H. (2011) 'Ophiolite genesis and global tectonics: Geochemical and tectonic fingerprinting of ancient oceanic lithosphere', *Geological Society of America Bulletin*, 123 (3-4), pp. 387-411.
- Dilek, Y. & Moores, E. M. (1990) 'Regional tectonics of the eastern Mediterranean ophiolites In: Malpas, J., Moores, E. M., Panayiotou, A. & Xenophontos, C. (eds) Ophiolites." Oceanic Crustal Analogues. Cyprus', *Proceeding of the Symposium "Troodos 1987"*, *The Geological Survey Department, Nicosia, Cyprus*, pp. 295-309.
- Dilek, Y., Moores, E. M., Delaloye, M. & Karson, J. A. (1991) 'Amagmatic Extension and Tectonic Denudation in the Kizildağ Ophiolite, Southern Turkey: Implications for the Evolution of Neotethyan Oceanic Crust', *Ophiolite genesis and evolution of the oceanic lithosphere. Springer*, pp. 485-500.
- Dilek, Y. & Thy, P. (1998) 'Structure, petrology and seafloor spreading tectonics of the Kizildag ophiolite, Turkey', *Geological Society, London, Special Publications*, 148 (1). pp 43-69.
- Dilek, Y. & Thy, P. (2009) 'Island arc tholeiite to boninitic melt evolution of the Cretaceous Kizildag (Turkey) ophiolite: Model for multi-stage early arc-forearc magmatism in Tethyan subduction factories', *Lithos*, 113 pp. 68–87.

- Dilek, Y., Thy, P., Hacker, B. & Grundvig, S. (1999) 'Structure and petrology of Tauride ophiolites and mafic dike intrusions (Turkey): Implications for the Neotethyan ocean', *Geological Society of America Bulletin*, 111 (8), pp. 1192.
- Dunlop, D. & Ozdemir, R. M. (1997) 'Rock Magnetism: Fundamentals and Frontiers, Cambridge University Press New York: 573 pp.
- Dunn, R. A., Lekić, V., Detrick, R. S. & Toomey, D. R. (2005) 'Three-dimensional seismic structure of the Mid-Atlantic Ridge (35 N): Evidence for focused melt supply and lower crustal dike injection', *Journal of Geophysical Research: Solid Earth* (1978–2012), 110 (B9).
- Ealey, P. J. & James, H. C. L. (2011) 'Loess of the Lizard Peninsula, Cornwall, SW Britain', *Quaternary International*, 231 (1-2), pp. 55-61.
- Edmonds, E., McKeown, M., Williams, M. & Dewey, H. (1975) *British regional geology: south-west England*. 4<sup>th</sup> edn. HM Stationery Office.
- Fleet, M. E., Bilcox, G. A. & Barnett, R. L. (1980) 'Oriented magnetite inclusions in pyroxenes from the Grenville Province', *Canadian Mineralogist*, 18 pp. 89-99.
- Flett, J. S. & Hill, J. B. (1946) *Geology of the Lizard and Meneage*:(explanation of Sheet 359). HM Stationery Off.
- Floyd, P. A., Exley, C. S. & Styles, M. (1993) *The igneous rocks of south-west England*. Springer. 256 pp.
- Fossen, H. (2010) *Structural geology*. Cambridge University Press. 463 pp.
- Garcia, M. O., Pietruszka, A. J. & Rhodes, J. M. (2003) 'A Petrologic Perspective of Kīlauea Volcano's Summit Magma Reservoir', *Journal of Petrology*, 44 (12), pp. 2313-2339.
- Gass, I. (1968) 'Is the Troodos massif of Cyprus a fragment of Mesozoic ocean floor', *Nature*, 220 pp. 39-42.
- Gee, J. S. & Kent, D. V. (2007) 'Source of oceanic magnetic anomalies and the geomagnetic polarity time scale', *Treatise on Geophysics*, vol. 5: Geomagnetism, pp. 455-507.
- Gill, R. (2011) *igneous rocks and processes: a practical guide*. John Wiley & Sons. 428 pp.
- Gillis, K. (2002) 'The rootzone of an ancient hydrothermal system exposed in the Troodos ophiolite, Cyprus', *The Journal of geology*, 110 (1), pp. 57-74.

- Girardeau, J. & Nicolas, A. (1981) 'The structures of two ophiolite massifs, Bay-of-Islands, Newfoundland: A model for the oceanic crust and upper mantle', *Tectonophysics*, 77 (1), pp. 1-34.
- Granot, R., Abelson, M., Ron, H., Lusk, M. W. & Agnon, A. (2011) 'Direct evidence for dynamic magma supply fossilized in the lower oceanic crust of the Troodos ophiolite', *Geophysical Research Letters*, 38 (16).
- Gunnarsdóttir, E. L. (2012) *The Earth's Magnetic Field*. University of Iceland: Háskólaprent, Fálkagata 2, 107 Reykjavík. 44 pp.
- Hacker, B. R. (1991) 'The role of deformation in the formation of metamorphic gradients: Ridge subduction beneath the Oman Ophiolite', *Tectonics*, 10(2), pp. 455-473.
- Hailwood, E., Gash, P., Andresen, P. & Badham, J. (1984) 'Palaeomagnetism of the Lizard Complex, SW England', *Journal of the Geological Society*, 141 (1), pp. 27.
- Hari, K., Rao, N. C., & Swarnkar, V. (2011) 'Petrogenesis of gabbro and orthopyroxene gabbro from the Phenai Mata Igneous Complex, Deccan volcanic province: Products of concurrent assimilation and fractional crystallization', *Journal of the Geological Society of India*, 78 (6), pp. 501-509.
- Harris, C. & Chaumba, J. B. (2001) 'Crustal contamination and fluid-rock interaction during the formation of the Platreef, northern limb of the Bushveld Complex, South Africa', *Journal of Petrology*, 42 (7), pp. 1321-1347.
- Harrison, R. J. & Feinberg, J. M. (2009) 'Mineral magnetism: Providing new insights into geoscience processes', *Elements*, 5 (4), pp. 209-215.
- Hatcher, R. D. (1990) *Structural geology: Principles, concepts, and problems*. Merrill Publishing Company. 531 pp.
- Hefferan, K., & O'Brien, J. (2010) *Earth materials*: John Wiley & Sons. pp. 608.
- Holder, M. T. & Leveridge, B. E. (1986) 'A model for the tectonic evolution of South Cornwall', *Journal of the Geological Society*, 143 pp. 125-134.
- Humphreys, D. R. (2002) 'The earth's magnetic field is still losing energy', *Creation Research Society Quarterly*, 39 (1), pp. 3-13.
- Hunter, A. & Easterbrook, G. (2004) *The geological history of the British Isles*. The Open University. 143 pp.

- Hurst, S. D., Verosub, K. L. & Moores, E. M. (1992) 'Paleomagnetic constraints on the formation of the Solea graben, Troodos ophiolite, Cyprus', *Tectonophysics*, 208 (4), pp. 431-445.
- Inwood, J. (2005) '*The tectonic evolution of the Hatay ophiolite of southeast Turkey*'. University of Plymouth (PhD thesis).
- Inwood, J., Anderson, M. W., Morris, A. & Robertson, A. H. F. (2009a) 'Successive structural events in the Hatay ophiolite of southeast Turkey: Distinguishing oceanic, emplacement and post-emplacement phases of faulting', *Tectonophysics*, 473 (1-2), pp. 208-222.
- Inwood, J., Morris, A., Anderson, M. W. & Robertson, A. H. F. (2009b) 'Neotethyan intraoceanic microplate rotation and variations in spreading axis orientation: Palaeomagnetic evidence from the Hatay ophiolite (southern Turkey)', *Earth and Planetary Science Letters*, 280 (1-4), pp. 105-117.
- Jackson, E. D., Green, H. W. & Moores, E. M. (1975) 'The Vourinos ophiolite, Greece: Cyclic units of lineated cumulates overlying harzburgite tectonite', *Geological Society of America Bulletin*, 86 (3), pp. 390-398.
- Jackson, M. (1991) 'Anisotropy of magnetic remanence: a brief review of mineralogical sources, physical origins, and geological applications, and comparison with susceptibility anisotropy', *Pure and Applied Geophysics*, 136 (1), pp. 1-28.
- Jaffey, N. & Robertson, A. H. (2001) 'New sedimentological and structural data from the Ecemiş Fault Zone, southern Turkey: implications for its timing and offset and the Cenozoic tectonic escape of Anatolia', *Journal of the Geological Society*, 158 (2), pp. 367-378.
- Jelinek, V. (1981) 'Characterization of the magnetic fabric of rocks', *Tectonophysics*, 79: 63-67.
- Johnson, H. P., Kent, D. V., Tivey, M. A., Gee, J. S., Largon, R. L. & Embley, R. W. (1997) 'Conference on the magnetization of the oceanic crust steers future research', *Eos, Transactions American Geophysical Union*, 78 (19), pp. 199-202.
- Jones, K. A. (1997) 'Deformation and emplacement of the Lizard Ophiolite Complex, SW England, based on evidence from the Basal Unit', *Journal of the Geological Society*, 154 pp. 871-885.
- Judd, J. W. (1885) 'On the Tertiary and older peridotites of Scotland', *Quarterly Journal of the Geological Society*, 41(1-4), pp. 354-418.
- Juteau, T. (1980) 'Ophiolites of Turkey'. *Ophioliti*, 2 pp. 199-237.

- karaođlan, F. K., Parlak, O., Kloöetzli, U., Thoöeni, M. & Koller, F. (2013) 'U–Pb and Sm–Nd geochronology of the Kızıldag (Hatay, Turkey) ophiolite: implications for the timing and duration of suprasubduction zone type oceanic crust formation in the southern Neotethys', *Geol. Mag.* 150 (2), pp. 283–299.
- Kearey, P., Brooks, M. & Hill, I. (2002) *An introduction to geophysical exploration*. 3<sup>rd</sup> edn. Wiley. com. 262 pp.
- Kidd, W. (1977) 'The Baie Verte Lineament, Newfoundland: ophiolite complex floor and mafic volcanic fill of a small Ordovician marginal basin', *Maurice Ewing Series*, pp. 407-418.
- Kirby, G. (1984) 'The petrology and geochemistry of dykes of the Lizard Ophiolite Complex, Cornwall', *Journal of the Geological Society*, 141 (1), pp. 53.
- Kirschvink, J. (1980) 'The least-squares line and plane and the analysis of palaeomagnetic data', *Geophysical Journal International*, 62 (3), pp. 699-718.
- Knecht, D. J. (1972) Handbook of Geophysics and Space Environments. The Geomagnetic Field. DTIC Document. *Air Force Surveys in Geophysics*, no. 246. 120 pp.
- Koç, H., Tasli, K. & Özer, E. (2013) 'Revised Late Campanian-Danian age of the melange-related turbiditic sequence in the Mersin area (Central Taurides, S. Turkey)', *Turkish Journal of Earth Sciences*, 22 (2), pp. 239-246.
- Kroner, U., Hahn, T., Romer, R. L. & Linnemann, U. (2007) 'The Variscan orogeny in the Saxo-Thuringian zone-heterogenous overprint of Cadomian/Paleozoic Peri-Gondwana crust', *Special Papers-Geological Society of America*, pp.
- Le Maitre, R. R. W. (2002). *Igneous rocks: a classification and glossary of terms: recommendations of the International Union of Geological Sciences, Subcommission on the Systematics of Igneous Rocks*: Cambridge University Press. 236 pp.
- Lee, P. E., Jessup, M. J., Shaw, C. A., Hicks III, G. L. & Allen, J. L. (2012) 'Strain partitioning in the mid-crust of a transpressional shear zone system: Insights from the Homestake and Slide Lake shear zones, central Colorado', *Journal of Structural Geology*, 39 pp. 237-252.

- Leveridge, B. & Hartley, A. (2006) 'The Variscan Orogeny: the development and deformation of Devonian/Carboniferous basins in SW England and South Wales'. In: The geology of England and Wales/edited by PJ Brenchley and PF Rawson. London: *Geological Society of London*, 2006 pp. 225-255.
- Leveridge, B. E. & Shail, R. K. (2011) 'The Gramscatho Basin, south Cornwall, UK: Devonian active margin successions', *Proceedings of the Geologists' Association*, 122 (4), pp. 568-615.
- Lowrie, W. (2007) *Fundamentals of geophysics*. 2<sup>nd</sup> edn. Cambridge University Press. 381 pp.
- Lytwyn, J. N. & Casey, J. F. (1995) 'The geochemistry of postkinematic mafic dike swarms and subophiolitic metabasites, Pozanti-Karsanti ophiolite, Turkey: Evidence for ridge subduction', *Geological Society of America Bulletin*, 107 (7), pp. 830-850.
- MacDonald, W. D. (1980) 'Net tectonic rotation, apparent tectonic rotation, and the structural tilt correction in paleomagnetic studies', *Journal of Geophysical Research: Solid Earth (1978–2012)*, 85 (B7), pp. 3659-3669.
- MacLeod, C., Allerton, S., Gass, I. & Xenophontos, C. (1990) 'Structure of a fossil ridge–transform intersection in the Troodos ophiolite', *Nature*, 348 (6303), pp. 717-720.
- MacLeod, C., Boudier, F., Yaouancq, G. & Richter, C. (1996) 'Gabbro fabrics from Site 894, Hess Deep: Implications for magma chamber processes at the East Pacific Rise', *Proceedings-Ocean Drilling Program Scientific Results. National Science Foundation*, pp. 317-328.
- MacLeod, C. & Murton, B. (1995) 'On the sense of slip of the Southern Troodos transform fault zone, Cyprus', *Geology*, 23 (3), pp. 257-260.
- MacLeod, C. J. & Yaouancq, G. (2000) 'A fossil melt lens in the Oman ophiolite: Implications for magma chamber processes at fast spreading ridges', *Earth and Planetary Science Letters*, 176 (3), pp. 357-373.
- McElhinny, M. W. & McFadden, P. L. (2000) *Paleomagnetism: continents and oceans*. vol. 73. Academic Press. 386 pp.
- Merrill, R. T., McElhinny, M. W. & McFadden, P. L. (1996) *Magnetic Field of the Earth*. vol. 63. Academic Press. 531 pp.
- Metcalf, R. V. & Shervais, J. W. (2008) 'Suprasubduction-zone ophiolites: Is there really an ophiolite conundrum?', *Special Papers-Geological Society of America*, 438 pp. 191.

- Moix, P., Beccaletto, L., Kozur, H. W., Hochard, C., Rosselet, F. & Stampfli, G. M. (2008) 'A new classification of the Turkish terranes and sutures and its implication for the paleotectonic history of the region', *Tectonophysics*, 451 (1-4), pp. 7-39.
- Moix, P., Kozur, H., Stampfli, G. & Mostler, H. (2007) 'New paleontological, biostratigraphic and paleogeographic results from the Triassic of the Mersin Mélange, SE Turkey', *New Mexico Museum of Natural History and Science Bulletin*, 41 pp. 282-311.
- Monroe, J. S. & Wicander, R. (2009) *The Changing Earth: Exploring Geology and Evolution*. 5th edn. Canada: Brooks/Cole. 735 pp.
- Moores, E. (1982) 'Origin and emplacement of ophiolites', *Reviews of Geophysics*, 20 (4), pp. 735-760.
- Moores, E. & Twiss, R. (1995) *Tectonics*. W. H. Freeman and Company, New York. 415 pp.
- Moores, E. & Vine, F. (1971) 'The Troodos Massif, Cyprus and other ophiolites as oceanic crust: evaluation and implications', *Philosophical Transactions of the Royal Society of London, Series A, Mathematical and Physical Sciences*, 268 (1192), pp. 443-467.
- Morales, L. F., Boudier, F., & Nicolas, A. (2011) 'Microstructures and crystallographic preferred orientation of anorthosites from Oman ophiolite and the dynamics of melt lenses', *Tectonics*, 30 (2).
- Morris, A. (1996) 'A review of palaeomagnetic research in the Troodos ophiolite, Cyprus', *Geological Society, London, Special Publications*, 105 (1), pp. 311-324.
- Morris, A. (2003) 'A palaeomagnetic and rock magnetic glossary', *Tectonophysics*, 377 (1-2), pp. 211-228.
- Morris, A. & Anderson, M. W. (2002) 'Palaeomagnetic results from the Baër-Bassit ophiolite of northern Syria and their implication for fold tests in sheeted dyke terrains', *Physics and Chemistry of the Earth, Parts A/B/C*, 27 (25-31), pp. 1215-1222.
- Morris, A., Anderson, M. W., Inwood, J. & Robertson, A. H. F. (2006) 'Palaeomagnetic insights into the evolution of Neotethyan oceanic crust in the eastern Mediterranean', *Geological Society, London, Special Publications*, 260 (1), pp. 351.
- Morris, A., Anderson, M. W. & Robertson, A. H. F. (1998) 'Multiple tectonic rotations and transform tectonism in an intraoceanic suture zone, SW Cyprus', *Tectonophysics*, 299 (1-3), pp. 229-253.

- Morris, A., Anderson, M. W., Robertson, A. H. F. & Al-Riyami, K. (2002) 'Extreme tectonic rotations within an eastern Mediterranean ophiolite (Baër-Bassit, Syria)', *Earth and Planetary Science Letters*, 202 (2), pp. 247-261.
- Morris, A., Creer, K. M. & Robertson, A. H. F. (1990) 'Palaeomagnetic evidence for clockwise rotations related to dextral shear along the Southern Troodos Transform Fault, Cyprus', *Earth and Planetary Science Letters*, 99 (3), pp. 250-262.
- Morris, A., Gee, J. S., Pressling, N., John, B. E., MacLeod, C. J., Grimes, C. B. & Searle, R. C. (2009) 'Footwall rotation in an oceanic core complex quantified using reoriented Integrated Ocean Drilling Program core samples', *Earth and Planetary Science Letters*, 287 (1-2), pp. 217-228.
- Mukasa, S. B. & Ludden, J. N. (1987) 'Uranium-lead isotopic ages of plagiogranites from the Troodos ophiolite, Cyprus, and their tectonic significance', *Geology*, 15 (9), pp. 825-828.
- Mullen, E. D. (1983) ' $\text{MnO}/\text{TiO}_2/\text{P}_2\text{O}_5$ : a minor element discriminant for basaltic rocks of oceanic environments and its implications for petrogenesis', *Earth and Planetary Science Letters*, 62 (1), pp. 53-62.
- Murphy, J. B., Keppie, J. D., Nance, R. D. & Dostal, J. (2010) 'Comparative evolution of the Iapetus and Rheic Oceans: a North America perspective', *Gondwana Research*, 17 (2), pp. 482-499.
- Nance, R. D., Gutiérrez-Alonso, G., Keppie, J. D., Linnemann, U., Murphy, J. B., Quesada, C., Strachan, R. A. & Woodcock, N. H. (2012) 'A brief history of the Rheic Ocean', *Geoscience Frontiers*, 3 (2), pp. 125-135.
- Nance, R. D. & Linnemann, U. (2008) 'The Rheic Ocean: origin, evolution, and significance', *GSA Today*, 18 (12), pp. 4-12.
- Nicolas, A., Reuber, I. & Benn, K. (1988) 'A new magma chamber model based on structural studies in the Oman ophiolite', *Tectonophysics*, 151 (1), pp. 87-105.
- Okay, A. I. (2008) 'Geology of Turkey: a synopsis', *Anschnitt*, 21 pp. 19-42.
- Okay, A. I. & Tüysüz, O. (1999) 'Tethyan sutures of northern Turkey', *Geological Society, London, Special Publications*, 156 (1), pp. 475-515.
- Okay, A. I. & Whitney, D. L. (2010) 'Blueschists, eclogites, ophiolites and suture zones in northwest Turkey: a review and a field excursion guide', *Ophioliti*, 35 (2), pp. 131-172.

- Parlak, O. (1996) *Geochemistry and geochronology of the Mersin ophiolite within the eastern Mediterranean tectonic frame (southern Turkey)*. University of Genève (PhD thesis).
- Parlak, O., Bozkurt, E. & Delaloye, M. (1996 a) 'The obduction direction of the Mersin Ophiolite: structural evidence from subophiolitic metamorphics in the Central Tauride Belt, Southern Turkey', *International Geology Review*, 38 (8), pp. 778-786.
- Parlak, O. & Delaloye, M. (1996) 'Geochemistry and timing of post metamorphic dyke emplacement in the Mersin Ophiolite (southern Turkey): New age constraints from  $^{40}\text{Ar}/^{39}\text{Ar}$  geochronology', *Terra Nova*, 8 (6), pp. 585-592.
- Parlak, O. & Delaloye, M. (1999) 'Precise  $^{40}\text{Ar}/^{39}\text{Ar}$  ages from the metamorphic sole of the Mersin ophiolite (southern Turkey)', *Tectonophysics*, 301 (1-2), pp. 145-158.
- Parlak, O. & Delaloye, M. (2001) *Mersin Ophiolite*, in *Field Excursion A2 GuideBook*. Çukurova University, Adana –Turkey, 1-15 pp. Available.
- Parlak, O., Delaloye, M. & Bingöl, E. (1996 b) 'Phase and cryptic variation through the ultramafic-mafic cumulates in the Mersin Ophiolite (Southern Turkey)', *Ophioliti*, 21 (2), pp. 81-92.
- Parlak, O., Delaloye, M. & Bingöl, E. (1995) 'Origin of subophiolitic metamorphic rocks beneath the Mersin ophiolite, southern Turkey', *Ophioliti*, 20 (2), pp. 97-110.
- Parlak, O., Delaloye, M. & Bingöl, E. (1996 c) 'Mineral chemistry of ultramafic and mafic cumulates as an indicator of the arc-related origin of the Mersin ophiolite (southern Turkey)', *Geologische Rundschau*, 85 (4), pp. 647-661.
- Parlak, O., Höck, V. & Delaloye, M. (2000) 'Suprasubduction zone origin of the Pozanti-Karsanti ophiolite (southern Turkey) deduced from whole-rock and mineral chemistry of the gabbroic cumulates', *Geological Society, London, Special Publications*, 173 (1), pp. 219.
- Parlak, O., Höck, V. & Delaloye, M. (2002) 'The supra-subduction zone Pozanti-Karsanti ophiolite, southern Turkey: evidence for high-pressure crystal fractionation of ultramafic cumulates', *Lithos*, 65 (1-2), pp. 205-224.
- Parlak, O., Karaoğlan, F., Rızaoğlu, T., Klötzli, U., Koller, F. & Billor, Z. (2013) 'U-Pb and  $^{40}\text{Ar}$ - $^{39}\text{Ar}$  geochronology of the ophiolites and granitoids from the Tauride belt: Implications for the evolution of the Inner Tauride suture', *Journal of Geodynamics*, (65), pp. 22– 37

- Parlak, O. & Robertson, A. (2004) 'The ophiolite-related Mersin Melange, southern Turkey: its role in the tectonic–sedimentary setting of Tethys in the Eastern Mediterranean region', *Geological Magazine*, 141 (03), pp. 257-286.
- Parlak, O., Yilmaz, H. & Boztuğ, D. (2006) 'Origin and tectonic significance of the metamorphic sole and isolated dykes of the Divriği ophiolite (Sivas, Turkey): evidence for slab break-off prior to ophiolite emplacement', *Turkish Journal of Earth Sciences*, 15 (1), pp. 25-45.
- Parrot, J. F. (1977) *Assemblage ophiolitique du Baër-Bassit et termes effusifs du volcano-sédimentaire: pétrologie d'un fragment de la croûte océanique téthysienne charriée sur la plate-forme syrienne*, vol. 72. IRD Editions, pp.333.
- Passchier, C. W. & Trouw, R. A. (2005) *Microtectonics*. 2<sup>nd</sup> edn. Springer: 366 pp.
- Pearce, J., Lippard, S. & Roberts, S. (1984) 'Characteristics and tectonic significance of supra-subduction zone ophiolites', *Geological Society, London, Special Publications*, 16 (1), pp. 77.
- Perrin, M., Plenier, G., Dautria, J.-M., Cocuau, E. & Prévot, M. (2000) 'Rotation of the Semail ophiolite (Oman): additional paleomagnetic data from the volcanic sequence', *Marine Geophysical Researches*, 21 (3-4), pp. 181-194.
- Petrovský, E. & Kapička, A. (2006) 'On determination of the Curie point from thermomagnetic curves', *Journal of Geophysical Research*, 111 (B12), pp.1-10.
- Piper, J. (1987) *Palaeomagnetism and the continental crust*. Open University Press. 434 pp.
- Piper, J., Gürsoy, H., Tatar, O., Beck, M., Rao, A., Koçbulut, F. & Mesci, B. (2010) 'Distributed neotectonic deformation in the Anatolides of Turkey: A palaeomagnetic analysis', *Tectonophysics*, 488 (1), pp. 31-50.
- Rajesh, H., Santosh, M. & Yoshida, M. (1998) 'Exsolution features in pyroxene phenocrysts from an anorthosite massif in northern Kerala, South India', *Journal of Geosciences-Osaka City University*, 41 pp. 85-108.
- Raposo, M. I. B., D'Agrella-Filho, M. S. & Pinese, J. P. P. (2007) 'Magnetic fabrics and rock magnetism of Archaean and Proterozoic dike swarms in the southern São Francisco Craton, Brazil'. *Tectonophysics*, 443 (1). pp 53-71.

- Reeve, W. D. (2010) 'Geomagnetism Tutorial', Reeve Observatory Anchorage, Alaska, USA. pp.33
- Renne, P. R., Scott, G. R., Glen, J. M. & Feinberg, J. M. (2002) 'Oriented inclusions of magnetite in clinopyroxene: Source of stable remanent magnetization in gabbros of the Messum Complex, Namibia', *Geochemistry Geophysics Geosystems*, 3 (12), pp. 1079.
- Ricou, L. (1971) 'Le croissant ophiolitique péri-arabe. Une ceinture de nappes mises en place au Crétacé supérieur', *Revue de géographie physique et de géologie dynamique*, 13 (4), pp. 327-349.
- Ricou, L., Marcoux, J. & Whitechurch, H. (1984) 'The Mesozoic organization of the Taurides: one or several ocean basins', *Geological Society, London, Special Publications*, 17 (1), pp. 349-359.
- Roberts, S., Andrews, J. R., Bull, J. M. & Sanderson, D. J. (1993) 'Slow-spreading ridge-axis tectonics: evidence from the Lizard complex, UK', *Earth and Planetary Science Letters*, 116 (1-4), pp. 101-112.
- Robertson, A. (1975) 'Cyprus umbers: basalt-sediment relationships on a Mesozoic ocean ridge', *Journal of the Geological Society*, 131 (5), pp. 511-531.
- Robertson, A. (1990) 'Tectonic evolution of Cyprus. In: Malpas, L., Moores, E.M., Panayiotou, A., Xenophontos, C. (Eds.), *Ophiolites: Oceanic Crustal Analogues. Cyprus Geological Survey Department*, Nicosia, pp. 235–252.
- Robertson, A. (2004) 'Development of concepts concerning the genesis and emplacement of Tethyan ophiolites in the Eastern Mediterranean and Oman regions', *Earth-Science Reviews*, 66 (3-4), pp. 331-387.
- Robertson, A., Parlak, O. & Ünlügenç, U. (2013 a) 'Editorial introduction to 'Geological Development of Anatolia and the Easternmost Mediterranean Region' Geological Society, London, *Special Publications*, 372, pp.1-7.
- Robertson, A., Pickett, E. & Ustaömer, T. (1999) 'Inter-relationships between Palaeotethys and Neotethys in the Eastern Mediterranean region: possible role of changing subduction polarity', *Journal of Conference Abstracts, EUG*, 10(4), pp. 315.
- Robertson, A. & Woodcock, N. (1980) 'Tectonic setting of the Troodos massif in the east Mediterranean. In: Panayiotou, A. (Ed.). "Ophiolites: Proceedings of the International Symposium, 1979, Cyprus Geological Survey Department. pp. 261- 272.

- Robertson, A. & Xenophontos, C. (1993) 'Development of concepts concerning the Troodos ophiolite and adjacent units in Cyprus', *Geological Society, London, Special Publications*, 76 (1), pp. 85-119.
- Robertson, A. H. (1998) 'Mesozoic-Tertiary tectonic evolution of the easternmost Mediterranean area: integration of marine and land evidence', *Proceedings of the Ocean Drilling Program Scientific Results*, pp. 723-782.
- Robertson, A. H. (2000) 'Mesozoic-Tertiary tectonic-sedimentary evolution of a south Tethyan oceanic basin and its margins in southern Turkey', *Geological Society, London, Special Publications*, 173 (1), pp. 97-138.
- Robertson, A. H. & Dixon, J. (1984) 'Introduction: aspects of the geological evolution of the Eastern Mediterranean'. *Geological Society, London, Special Publications*, 17 (1), pp. 1-74.
- Robertson, A. H., Parlak, O. & Ustaömer, T. (2012) 'Overview of the Palaeozoic–Neogene evolution of Neotethys in the Eastern Mediterranean region (southern Turkey, Cyprus, Syria)', *Petroleum Geoscience*, 18 (4), pp. 381- 404.
- Robertson, A. H., Parlak, O. & Ustaömer, T. (2013 b) 'Late Palaeozoic–Early Cenozoic tectonic development of Southern Turkey and the easternmost Mediterranean region: evidence from the inter-relations of continental and oceanic units', *Geological Society, London, Special Publications*, 372, pp. 9-48.
- Robertson, A. H. F. (2002) 'Overview of the genesis and emplacement of Mesozoic ophiolites in the Eastern Mediterranean Tethyan region', *Lithos*, 65 (1-2), pp. 1-67.
- Robinson, P. & Malpas, J. (1990) 'The Troodos ophiolite of Cyprus: New perspectives on its origin and emplacement', *Ophiolites, Oceanic Crustal Analogues*, pp. 13-26.
- Rochette, P., Aubourg, C. & Perrin, M. (1999) 'Is this magnetic fabric normal? A review and case studies in volcanic formations', *Tectonophysics*, 307 (1), pp. 219-234.
- Rochette, P., Jackson, M. & Aubourg, C. (1992) 'Rock magnetism and the interpretation of anisotropy of magnetic susceptibility', *Reviews of Geophysics*, 30 (3), pp. 209-226.
- Sarıfakıoğlu, E., Özen, H., & Winchester, J. A. (2009) 'Petrogenesis of the Refahiye Ophiolite and its Tectonic Significance for Neotethyan Ophiolites Along the zmir-Ankara-Erzincan Suture Zone', *Turkish Journal of Earth Sciences (Turkish J. Earth Sci.)*, 18, pp. 187-207.

- Sarıfakıoğlu, E., Dilek, Y., & Winchester, J. A. (2012) 'Late Cretaceous subduction initiation and Palaeocene–Eocene slab breakoff magmatism in South-Central Anatolia, Turkey', *International Geology Review*, 55(1), pp. 66-87.
- Schöbel, S. & Wall, H. d. (2011) *Die Anisotropie der magnetischen Suszeptibilität (AMS) zur Bestimmung von Lavafießrichtungen in Flutbasalten*, Hannover. 27 pp.
- Selwood, E. B., Durrance, E. M. & Bristow, C. M. (1998) *The geology of Cornwall: and the Isles of Scilly*, Univ. of Exeter Press. 298 pp.
- Sengör, A. & Yilmaz, Y. (1981) 'Tethyan evolution of Turkey: a plate tectonic approach', *Tectonophysics*, 75 (3), pp. 181-241.
- Şengör, A., Yılmaz, Y. & Sungurlu, O. (1984) 'Tectonics of the Mediterranean Cimmerides: nature and evolution of the western termination of Palaeo-Tethys', *Geological Society, London, Special Publications*, 17 (1), pp. 77-112.
- Shervais, J. W. (1982) 'Ti-V plots and the petrogenesis of modern and ophiolitic lavas', *Earth and Planetary Science Letters*, 59 (1), pp. 101-118.
- Simonian, K. t. & Gass, I. (1978) 'Arakapas fault belt, Cyprus: A fossil transform fault', *Geological Society of America Bulletin*, 89 (8), pp. 1220-1230.
- Simpson, C. & Schmid, S. M. (1983) 'An evaluation of criteria to deduce the sense of movement in sheared rocks', *Geological Society of America Bulletin*, 94 (11), pp. 1281-1288.
- Stampfli, G. & Borel, G. (2002) 'A plate tectonic model for the Paleozoic and Mesozoic constrained by dynamic plate boundaries and restored synthetic oceanic isochrons', *Earth and Planetary Science Letters*, 196 (1), pp. 17-33.
- Stampfli, G., Marcoux, J. & Baud, A. (1991) 'Tethyan margins in space and time', *Palaeogeography, Palaeoclimatology, Palaeoecology*, 87 (1), pp. 373-409.
- Stampfli, G. M., von Raumer, J. F. & Borel, G. D. (2002) 'Paleozoic evolution of pre-Variscan terranes: From Gondwana to the Variscan collision', *Variscan-Appalachian dynamics: the building of the late Paleozoic basement*, 364 pp. 263–280.
- Staudigel, H., Gee, J., Tauxe, L. & Varga, R. J. (1992) 'Shallow intrusive directions of sheeted dikes in the Troodos ophiolite: Anisotropy of magnetic susceptibility and structural data', *Geology*, 20 (9), pp. 841-844.

- Tarling, D. & Hrouda, F. (1993) *Magnetic anisotropy of rocks*. Chapman and Hall: 217 pp.
- Tarling, D. H. (1971) *Principales and Applications of Palaeomagnetism*. Chapman and Hall: 164 pp.
- Tarling, D. H. (1983) *Palaeomagnetism: Principles and applications in geology, geophysics, and archaeology*. Chapman and Hall London. 379 pp.
- Tauxe, L. (1998) *Paleomagnetic principles and practice*. Springer. 299 pp.
- Tauxe, L., Butler, R. F., Van der Voo, R. & Banerjee, S. K. (2009) Essentials of paleomagnetism. vol. 723. *University of California Press Berkeley*.
- Tekeli, O. & Erendil, M. (1986) 'Geology and Petrology of the Kizildağ Ophiolite (Hatay)', *Bulletin of Mineral Research and Exploration*, 107 pp. 21-37.
- Thayer, T. (1963) 'Flow-layering in alpine peridotite-gabbro complexes', *Spec. Publ. Mineral. Soc. Am*, 1 pp. 55-61.
- Torsvik, T. H., Van der Voo, R., Preeden, U., Mac Niocaill, C., Steinberger, B., Doubrovine, P. V., van Hinsbergen, D. J., Domeier, M., Gaina, C. & Tohver, E. (2012) 'Phanerozoic polar wander, palaeogeography and dynamics', *Earth-Science Reviews*, 114 (3), pp. 325-368.
- Twiss, R. J. & Moores, E. (1992) *Structural Geology*. W. H. Freeman. 532 pp.
- Van der Voo, R. (1993) *Paleomagnetism of the Atlantic, Tethys and Iapetus oceans*. Cambridge University Press. 411 pp.
- Varne, R., Brown, A. V. & Falloon, T. (2000) 'Macquarie Island: Its geology, structural history, and the timing and tectonic setting of its N-MORB to E-MORB magmatism'. *Special Papers-Geological society of America*, pp. 301-320.
- Varne, R., Gee, R. D. & Quilty, P. G. (1969) 'Macquarie Island and the cause of oceanic linear magnetic anomalies', *Science*, 166 (3902), pp. 230-233.
- Vernon, R. (2000) 'Review of microstructural evidence of magmatic and solid-state flow', *Visual Geosciences*, 5(2), pp. 1-23.
- Vine, F. & Moores, E. (1969) 'Paleomagnetic Results for Troodos Igneous Massif Cyprus', *Transactions-American Geophysical Union, American Geophysical Union*, pp. 131.
- Wakabayashi, J. & Dilek, Y. (2003) 'What constitutes 'emplacement' of an ophiolite?: Mechanisms and relationship to subduction initiation and formation of metamorphic soles', *Geological Society, London, Special Publications*, 218 (1), pp. 427-447.

- Weiler, P. D. (2000) 'Differential rotations in the Oman Ophiolite: paleomagnetic evidence from the southern massifs', *Marine Geophysical Researches*, 21 (3-4), pp. 195-210.
- Westaway, R. (2002) 'Discussion on new sedimentological and structural data from the Eceemis Fault Zone, southern Turkey: implications for its timing and offset and the Cenozoic tectonic escape of Anatolia', *Journal-Geological Society London*, 159 (1), pp. 110-112.
- Whitney, D. L. & Hamilton, M. A. (2004) 'Timing of high-grade metamorphism in central Turkey and the assembly of Anatolia', *Journal of the Geological Society*, 161 (5), pp. 823-828.
- Wilson, B. M. (1989) *Igneous petrogenesis a global tectonic approach*. Chapman and Hall. 466 pp.
- Winkler, A., Alfonsi, L., Florindo, F., Sagnotti, L. & Speranza, F. (1997) 'The magnetic anisotropy of rocks: principles, techniques and geodynamic applications in the Italian peninsula', *Annals of Geophysics*, 40 (3).
- Wright, T. L. (1971) *Chemistry of Kilauea and Mauna Loa lava in space and time*. US Government Printing Office. Geological Survey Professional Paper 735, 40 pp.
- Yanagi, T. (2011) 'Island Arc Volcanic Rocks and the Upper Continental Crust'. Arc Volcano of Japan, *Springer*, pp. 77-102.
- Yaouancq, G. & MacLeod, C. (2000) 'Petrofabric investigation of gabbros from the Oman ophiolite: comparison between AMS and rock fabric', *Marine Geophysical Researches*, 21 (3-4), pp. 289-306.
- Yetiş, C. (1984) 'New observations on the age of the Ecemiş Fault', *Proc. of International Symposium on the Geology of the Taurus Belt, Ankara-Turkey*, pp.159–164.
- Yilmaz, A. & Yilmaz, H. (2013) 'Ophiolites and Ophiolitic Mélanges of Turkey: A Review', *Geological Bulletin of Turkey*, 56 (2).
- Yilmaz, Y. (1993) 'New evidence and model on the evolution of the southeast Anatolian orogen', *Geological Society of America Bulletin*, 105 (2), pp. 251-271.
- Zhu, Y. & Ogasawara, Y. (2001) 'Clinopyroxene Phenocryst from the Kokchetav Shoshonitic Volcanic Rocks: Implications for the Multi-Stage Magma Processes', *UHPM Workshop at Waseda University*, PP. 170-173.